UNIVERSITY OF SOUTHAMPTON
Faculty of Engineering and Physical Sciences
School of Electronics and Computer Science

A Thesis for the Degree of Doctor of Philosophy

Optimal Rectenna Design for Textile, Flexible, and Printed Radio Frequency Energy Harvesting

by
Mahmoud Ashraf Hassan Wagih Mohamed

April, 2021

UNIVERSITY OF SOUTHAMPTON

ABSTRACT

FACULTY OF ENGINEERING AND PHYSICAL SCIENCES
SCHOOL OF ELECTRONICS AND COMPUTER SCIENCE

Doctor of Philosophy

Optimal Rectenna Design for
Textile, Flexible, and Printed Radio Frequency Energy Harvesting

by Mahmoud Ashraf Hassan Wagih Mohamed

The growing energy demands of the Internet of Things (IoT) highlight the need for battery-free methods to remotely power pervasive IoT devices. Emerging electronics fabrication techniques such as electronic textiles (e-textiles) and additive manufacturing can be utilized to realize low-cost Radio Frequency (RF) components. Far-field propagation of radio waves enables the remote delivery of power using rectifying-antennas (rectennas). Rectennas emerged in the 1950s for drone-powering, and more recently for harvesting ambient RF power and for wireless-powering IoT networks. Optimizing a rectenna is a multi-variate problem imposing constraints on the materials, fabrication process and size of the rectenna. This work investigates and optimizes different rectenna architectures for wearable and flexible electronics, achieving Power Conversion Efficiencies (PCEs) surpassing State-of-the-Art (SoA) rectennas of higher complexity.

Rectennas are proposed based on 50 Ω matching networks and matching network-elimination, showing that material properties do not hinder high-PCE rectennas. Antenna-rectifier co-design is proposed as an antenna-based solution for simultaneous wireless information and power transfer (SWIPT), demonstrating high PCE and uncompromised off-body radiation properties. The scalability of low-cost textile-based rectennas for millimeter-wave (mmWave) bands is then demonstrated through a novel broadband microstrip antenna design and analytical analysis showing up to an order of magnitude performance gains at mmWave bands compared to Ultra High Frequency (UHF) bands. The first implementation of a textile-based mmWave rectenna is presented based on a novel broadband antenna with high efficiency based on a compact radiator. At UHF, the proposed design methodologies are applied to two application-oriented implementations. Firstly: an e-textile coplanar waveguide thin and flexible rectenna integrated with a textile supercapacitor is presented, showing the highest reported end-to-end efficiency; secondly: a compact rectenna is proposed for low-resolution printing, representing the first meshed co-designed rectenna and showing PCE-improvements over SoA while having the lowest complexity. It is concluded that rectennas can be demonstrated with SoA PCEs using low-cost materials and components, presenting RF energy harvesting as a highly-practical solution for powering future IoT.

Contents

List of Figures

List of Tables

Nomenclature

α	Path-loss exponent
A	Area
β	Propagation constant
Γ	Reflection coefficient
c	Speed of light
C	Capacitance
d	Distance
D	Antenna directivity
ϵ	Permittivity of free space
ϵ_r	Relative permittivity (Dielectric Constant)
E	Electric field
f	Frequency
f_0	Fundamental tone
f_n	n^{th} harmonic
f_r	Resonant frequency
G	Antenna gain
H	Magnetic field
$\eta_{\text{Rad.}}$	Antenna radiation efficiency
$\eta_{\text{App.}}$	Antenna aperture efficiency
θ	Elevation angle
k_{mn}	Wave number of the mn mode
λ	Wavelength
λ_0	Free-space wavelength
l	Length
L	Inductance
P	Power
P_{TX}	Transmitted, i.e. total radiated, power
P_{RX}	Received RF power
P_{DC}	DC power
μ_0	Permeability of free space
μP	Microprocessor
R	Resistance ($\Re\{Z\}$)

$R_{\text{Rad.}}$	Radiation resistance
r	Radius
σ	Conductivity
S	RF power density (Poynting vector)
S_{ij}	Element ij of a scattering-parameters matrix
τ	Capacitor RC time constant
TM_{mn}	The mn transverse magnetic mode
T	Time period of a wave
$\tan\delta$	Dissipation Factor (loss tangent)
φ	Azimuthal angle
ϕ	Phase delay
V	Voltage
V_{Br}	Diode breakdown voltage
V_{F}	Diode forward voltage drop
Z	Impedance
Z_0	Characteristic Impedance

Acronyms

AM Amplitude Modulation. 15

AVA Antipodal Vivaldi Antenna. 146, 147, 149, 151, 161, 162, 163

BAN Body Area Networks. 39, 52, 53, 120, 123, 134, 137, 140, 142, 218

CMOS Complementary Metal Oxide Semiconductor. 13, 17, 23, 24, 35, 36, 39, 40, 42, 43, 44, 47, 50, 51, 53, 66, 169, 194, 215, 217, 218, 238

CP Circularly Polarised. 19, 21, 24, 25, 26, 28, 29, 30, 31, 32, 34

CPW Coplanar-Waveguide. 8, 21, 26, 37, 169, 170, 172, 183, 190, 206

CW Continuous Wave. 78, 81, 86, 89, 91, 103, 114, 158, 160, 161, 162, 164, 175, 201, 202, 204, 211, 217

DC Direct Current. 2, 27, 30, 31, 38, 57

DTV Digtial Telivision. 15, 16, 32

EDA Electronics Design Automation. 22, 37, 66

EH Energy Harvesting. 2, 8, 13, 170, 213, 214

EIRP Equivalent Isotropically Radiated Power. 3, 34, 39, 41, 74, 139, 140, 161, 162, 164, 167, 184

EIS electrochemical impedance spectroscopy. 178, 182

EM Electro-Magnetic. 2, 18, 32, 34, 35, 37, 38, 55, 56, 58, 65, 98, 99, 100, 103, 104

EMC Electro-Magnetic Compatibility. 33

ESD Electro-Static Discharge. 48, 49

FCC Federal Communication Commission. 3

FDA Folded-Dipole Antenna. 100, 101, 116, 193, 194, 197, 200

FET Field-Effect Transistor. 23

FoM Figure of Merit. 4, 13, 19, 26, 28, 59, 65, 134

GC galvanostatic cycling. 178, 180

GSM Global System for Mobile. 15, 18

HB Harmonic Balance. 34, 37, 48, 65, 100, 139, 140, 155, 174, 201

IC Integrated Circuit. 13, 24, 33, 36, 42, 111, 179, 194

IoE Internet of Everything. 4, 5, 6, 167, 213, 216

IoT Internet of Things. 1, 4, 5, 6, 14, 16, 41, 213, 214, 215, 217, 218

ISM Industrial Scientific Medical. 28, 97, 110, 169, 183, 194

LCP Liquid Crystal Polymer. 50, 52

LNA Low-Noise Amplifier. 18, 24, 218

LOS Line-of-Sight. 59, 122, 140, 215

LP Linearly-Polarised. 19, 21, 24, 25, 28, 29, 30, 31, 71, 89

MCU Micro-Controller Unit. 34, 106

MIMO Multi-In Multi-Out. 46

mmWave Milli-Meter Wave. 2, 6, 7, 8, 13, 22, 27, 28, 32, 33, 36, 39, 40, 41, 42, 43, 44, 45, 46, 47, 48, 50, 51, 52, 53, 54, 57, 60, 63, 121, 122, 123, 124, 127, 128, 130, 133, 134, 137, 138, 139, 140, 142, 145, 146, 149, 150, 154, 157, 158, 160, 161, 162, 164, 167, 213, 214, 215, 217, 218

MoM Method of Moments. 48, 100

MOS Metal-Oxide Semiconductor. 37, 218

MPPT Maximum Power Point Tracking. 37, 81, 116, 182

PA Power Amplifiers. 18, 34, 41, 132, 161, 162, 163, 218

PCB Printed Circuit Board. 22, 23, 43, 47, 49, 50, 69, 77, 80

PCE Power Conversion Efficiency. xiii, 1, 4, 5, 6, 8, 14, 15, 17, 18, 19, 22, 23, 29, 34, 35, 36, 37, 38, 39, 40, 41, 46, 48, 50, 51, 53, 56, 58, 61, 62, 63, 64, 65, 67, 69, 71, 75, 76, 77, 78, 80, 81, 82, 84, 85, 87, 88, 89, 90, 91, 93, 94, 95, 97, 98, 99, 100, 101, 103, 104, 105, 107, 108, 115, 116, 117, 118, 120, 139, 140, 142, 154, 157, 158, 160, 162, 163, 164, 175, 176, 177, 182, 183, 184, 185, 188, 190, 191, 194, 197, 200, 201, 202, 203, 204, 206, 207, 211, 213, 214, 215, 238

PMIC Power Management Integrated Circuit. 16, 24, 170, 182, 188, 190

PML Polarization Mismatch Loss. 71, 89

PSD Power Spectral Density. xi, 15, 16, 17, 19, 26, 209, 216

RF Radio Frequency. v, xiii, 1, 2, 3, 4, 5, 14, 15, 17, 35, 36, 37, 39, 40, 55, 61, 62, 64, 65, 79, 81, 82, 84, 87, 89, 183, 217

RFEH Radio Frequency Energy Harvesting. 1, 2, 3, 4, 5, 6, 13, 14, 16, 21, 25, 26, 27, 28, 29, 30, 32, 33, 35, 36, 38, 39, 54, 55, 56, 58, 59, 60, 61, 63, 65, 67, 69, 71, 75, 76, 81, 95, 112, 117, 140, 145, 151, 157, 167, 169, 170, 183, 185, 190, 191, 194, 197, 206, 207, 209, 211, 213, 214, 215, 216, 217, 218

RFIC Radio Frequency Integrated Circuit. 18, 35, 41

RFID Radio Frequency Identification. 1, 13, 24, 25, 27, 33, 201, 216, 217

SAR Specific Absorption Rate. 15, 74, 109, 130, 133

SIW Substrate-Integrated Waveguide. 26, 30, 43, 44, 137

SoA State-of-the-Art. 5, 8, 15, 17, 28, 54, 67, 81, 89, 95, 97, 117, 191, 204, 206, 211, 213, 216

SoI Silicon-on-Insulator. 24

SOLT Short Open Load Through. 151

SoS Silicon-on-Sapphire. 36

SPICE Simulation Program with Integrated Circuit Emphasis. 37

SWIPT Simultaneous Wireless Information and Power Transfer. 2, 8, 36, 97, 106, 110, 117, 118, 120, 213, 214, 216, 217

TRL Through Reflect Line. 49

TSC textile supercapacitor. 169, 178, 179, 180, 181, 182, 183, 184, 185, 186, 187, 190, 214

UHF Ultra-high Frequency. 1, 2, 13, 15, 17, 31, 41, 60, 61, 122, 137, 139, 140, 142, 192

UV Ultra-Violet. 192

UWB Ultra-Wide Band. 21, 218

VNA Vector Network Analyser. 23, 38, 46, 48, 49, 57, 69, 71, 78, 81, 86, 87, 89, 91, 110, 114, 125, 137, 151, 158, 172, 175, 180, 182, 197

WLAN Wireless Local Area Network. 15

WPT Wireless Power Transmission. 1, 2, 4, 5, 6, 13, 16, 19, 22, 23, 24, 26, 27, 28, 29, 31, 32, 38, 40, 41, 43, 46, 47, 54, 56, 57, 59, 63, 89, 106, 122, 134, 137, 139, 140, 142, 169, 194, 213, 214, 215, 217, 218

Declaration of Authorship

I declare that this thesis and the work presented in it is my own and has been generated by me as the result of my own original research.

I confirm that:

1. This work was done wholly or mainly while in candidature for a research degree at this University;
2. Where any part of this thesis has previously been submitted for a degree or any other qualification at this University or any other institution, this has been clearly stated;
3. Where I have consulted the published work of others, this is always clearly attributed;
4. Where I have quoted from the work of others, the source is always given. With the exception of such quotations, this thesis is entirely my own work;
5. I have acknowledged all main sources of help;
6. Where the thesis is based on work done by myself jointly with others, I have made clear exactly what was done by others and what I have contributed myself;
7. Parts of this work have been published as listed in Section 1.4, and are cited in their respective chapters.

Signed:..... Date:.....

Acknowledgements

I would like to thank my supervisors, Prof. Steve Beeby and Dr. Alex Weddell, for their continuous support throughout this research project, and for offering me the full flexibility in planning and managing this research project. I would also like to thank Dr. Mohammed El-Hajjar and Prof. Harold Chong for their feedback and insights, as internal examiners, in addition to Prof. Yang Hao for his comments as an external examiner. I finally acknowledge the anonymous peer-reviewers and journal editors, whose criticism and commentary helped significantly improve the quality of my work.

I would like to thank Dr. Geoffrey Hilton, from the University of Bristol, for his extensive support with the antenna measurements, the useful feedback and insights, and for providing access to the necessary millimeter-wave test facilities. I thank Prof. John Bandler, from McMaster University, for his extensive mentoring and exceptional enthusiasm, which helped me with effective research communication. I also acknowledge Dr. Christopher R. Valenta from Georgia Tech Research Institute for giving permission to reuse his code in the rectifier analysis.

The current and previous PhD students and research fellows in the SEMS Research Group, including but not limited to Dr. Abiodun Komolafe, Dr. Bahareh Zaghari, Dr. Russel Torah, Dr. Sheng Yong, Dr. Zeeshan Ahmed, Nicholas Hillier, Watcharapong (Boyd) Paosangthong, and Ashwini Valavan, thanks for your support, motivation, and for creating a pleasant work environment. My friends in Southampton, namely those from the Southampton University Hillwalking Club, thank you for your company. Finally, I thank Dr. Mihai Rotaru for being my first mentor in the world of microwave engineering.

I acknowledge the European Commission for financially supporting this work through the EnABLES Project: European Infrastructure Powering the Internet of Things, funded under H2020-EU.1.4.1.2, grant number: 730957, alongside the School of Electronics and Computer Science for co-funding my studies. I thank Arm Research, for offering me an extended remote research internship during an increasingly difficult time, allowing me to bring my research closer to solving real-world challenges.

To my parents.

Chapter 1

Introduction

> *"The economic transmission of power without wires is of all-surpassing importance to man"*
>
> – Nikola Tesla [1],

The Internet of Things (IoT) market has undergone major growth, with predictions of reaching a trillion connected devices by 2035, contributing significantly to the global gross domestic product (GDP) [2]. Multiple design challenges, such as deployment cost, sustainability, and the utilization of existing infrastructure to support the wide-scale deployment of distributed data acquisition nodes, as well as enabling edge computing remain unsolved. Remote-powering of IoT nodes can be achieved through Wireless Power Transmission (WPT) and Radio Frequency Energy Harvesting (RFEH). First proposed as a mean of transferring power using the high-voltage Tesla coils by Nikola Tesla [1], WPT evolved to employ non-coupled radiative means to transfer power using radio waves [3]. Wireless Power Transmission (WPT) can take place simultaneously with information transmission at RF bands, regardless of the transmission medium [4]; power can be extracted from wireless communication systems using detector-like circuitry focusing on maximizing the PCE as opposed to preserving and amplifying the signal for high receiver sensitivity.

WPT was first proposed by Tesla in the 1900s as a mean of transferring thousands of horse-power [1]. Commercial WPT evolved into using near-field non-radiative power transfer for consumer electronics wireless charging, and radiative far-field WPT for Radio Frequency Identification (RFID) at the Ultra-high Frequency (UHF) bands [5]. Contradicting the well-known assumption that free-space propagation losses are proportional to the square of distance, multiple research efforts were devoted to realizing lower-loss RF wireless links using reflectors, waveguides and finally, phased arrays [3]. In his review, W. C. Brown described the assumption that power density *always* decreased with the

square of the distance as a "*widespread but incorrect assumption*" [3]. His conclusions were backed by the WPT efficiency, η_2 in (1.1), approaching 100% by the mean of a beam guided using lenses and reflecting mirrors in 1961 [3]. Furthermore, the practical demonstration of RF-powered drones in the 1960s, with end-to-end efficiencies around 14% over tens of meters, acted as a confirmation that high-power RF power transfer is not limited in range or efficiency [3].

1.1 Rectennas: A Power Source for Unobtrusive IoT

To receive the RF power, a rectifying antenna (rectenna) is required to convert the RF Electro-Magnetic (EM) waves to steady DC power. In its simplest form, a rectenna is composed of an EM resonator: an antenna, and a rectifying element: a diode. Rectennas are highly-scalable for different power levels, from nano-watts to watts of RF power, and for different frequency bands, from the lower UHF bands to Milli-Meter Wave (mmWave), sub-THz, and up to optical frequencies [6]. Therefore, rectennas can be utilized for a variety of applications and can be scaled to different frequency bands based on the application. Since their early emergence in the 1950s, rectennas have re-attracted significant research interest with the emergence of "Energy Harvesting (EH)" as a mean of powering electronic devices. Fig. 1.1 shows the number of research papers published, indexed in IEEEXplore, investigating rectennas, showing an increased interest since the rise of EH for battery-free electronics in the 2000s.

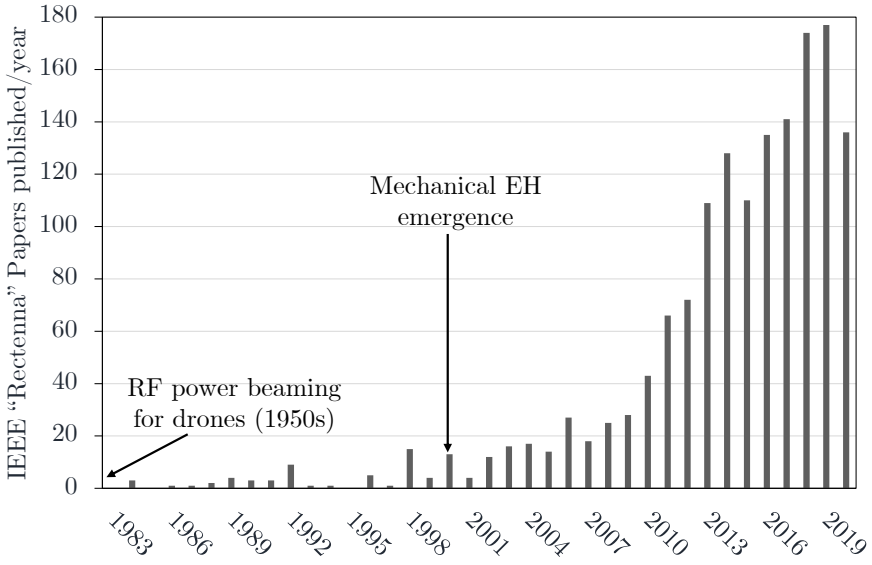

FIGURE 1.1: The number of research papers published on rectennas, indexed in IEEEXplore, showing the increased research interest.

Nowadays, the wide-scale deployment of RF base-stations in areas with high population density makes a significant amount of EM power available in air. In an EH context,

the available radio waves, microwaves, and in future networks: mmWaves, may be "*recycled*" and converted to Direct Current (DC) power. Hence, a low-power device can sustain operation or recharge its battery using the available energy. WPT and Simultaneous Wireless Information and Power Transfer (SWIPT) using a range of power-optimized algorithms and transceiver architectures are increasingly presented as enablers of future wireless networks [7, 8]. Future "RFEH networks" are broadly defined as networks utilizing a dedicated RF transmitter to power multiple nodes or devices, using rectennas, transmitting power-specific wave-forms or information and power using the same wave using SWIPT [7].

In order to describe the focus points of this work, the power-conversion stages in an RFEH system need to be outlined. When harvesting energy from existing sources or a dedicated RF power transmitter, multiple uncontrollable factors affect the available power density. To illustrate, the transmitted power level and propagation channel can significantly change the available power density by orders of magnitude. Furthermore, the Equivalent Isotropically Radiated Power (EIRP) of the transmitter is limited by regulatory bodies such as the Federal Communication Commission (FCC) and the Office of Communications (Ofcom). On the other hand, the receiving antenna, the rectifier, and the rest of the RF-powered node can be designed to maximize the power reception and conversion for certain operation conditions, such as the RF power level, the incident wave's properties (direction and polarization), as well as the desired output impedance, voltage sensitivity, and RF-DC efficiency. Fig. 1.2 shows the architecture of a typical RFEH system.

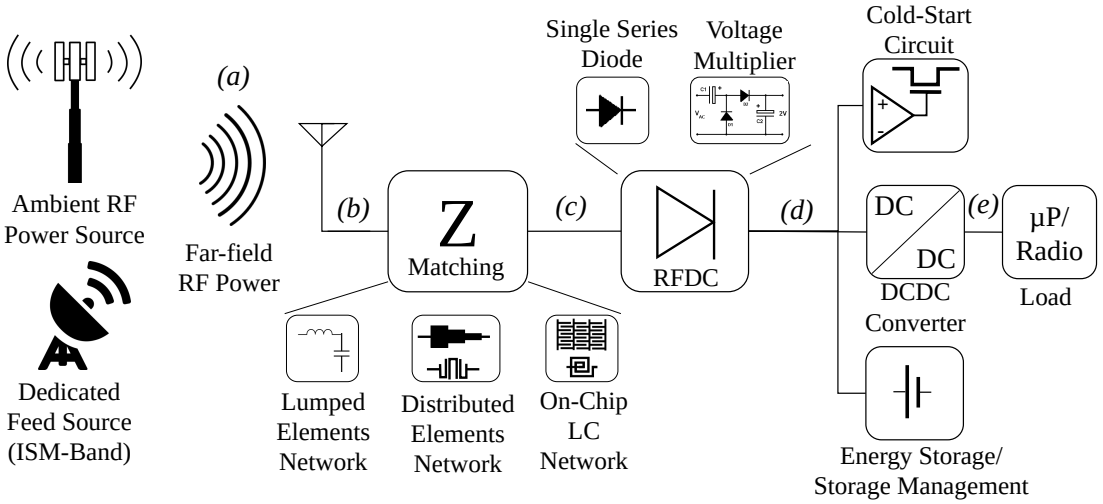

FIGURE 1.2: System architecture of a RFEH wireless node, showing the power sources and conversion stages, as well as commonly reported implementations.

In a wireless-powered network, the end-to-end DC efficiency from the transmitter to the load needs to be considered. To put RF-powered networks in a more standardized form, Clerckx *et al.* discussed the need for a wireless power 1G concept [9], where the

end-to-end efficiency η is defined as

$$\eta = \underbrace{\frac{P_{\mathrm{RF}}}{P_{\mathrm{DC}}}}_{\eta_1\text{: PA}} \times \underbrace{\frac{P_{\mathrm{RF-RX}}}{P_{\mathrm{RF-TX}}}}_{\eta_2\text{: Channel+gains}} \times \underbrace{\frac{P_{\mathrm{DC}}}{P_{\mathrm{RF}}}}_{\eta_3\text{: Rectenna}} \times \underbrace{\frac{P_{\mathrm{DC-Load}}}{P_{\mathrm{DC-RX}}}}_{\eta_4\text{: DC PowerManagement}} . \tag{1.1}$$

Linking (1.1) to Fig. 1.2, point (a) shows the RF plane wave that is available to be received by the rectenna, $P_{\mathrm{RF-RX}}$, where the power at point (b) can be approximated using a propagation model and the transmitter and receiver gains. The rectenna's PCE (η_3) is the ratio of the rectified DC power delivered to a resistive load, at (d), to the received RF power, at (b). Finally, the power delivered to the active load (e), i.e. a microprocessor or a sensor node, is the final parameter in the system, which can be considered to calculate the end-to-end DC to DC efficiency. At a system and application level, performance metrics such as the sensor node active time and the number of transmitted and received data packets can be utilized to evaluate the overall functionality of the RF-powered node.

In the earliest rectenna experiments by W. C. Brown at Raytheon Company for RF-powered drones, the DC end-to-end efficiency exceeded 13% [3]. Techniques such as beamforming using real-time electrically-steerable antenna arrays can be utilized to overcome the bottle-neck of the system: *propagation losses* [9]. From a receiver's point of view, the antenna's radiation properties determine how much power is received from an incident plane-wave, and the rectifier's impedance matching determines the percentage of power absorbed or reflected back. Brown's rectennas were formed of large highly-directive antenna arrays, with rectifier diodes designed to approach "near-unity" efficiencies at power levels in the order of 10 W, to be able to sufficiently power drones.

Whether a rectenna is to receive power from a dedicated transmitter or recycle ambient RF power, a key performance metric that needs to be maximized is the RF to DC Power Conversion Efficiency (PCE). This is a direct function of the rectifying diode and its source and load impedances. Moreover, certain antenna parameters such as the peak gain, beamwidth, and polarization can be regarded as a Figure of Merit (FoM) based on the application and the WPT medium, affecting the power conversion from a to b in Fig. 1.2. The DC circuitry, from point d in Fig. 1.2, can be considered as an equivalent circuit of a certain impedance. This impedance could then be utilized in the rectenna design. Alternatively the power management circuitry could be designed according to the optimal load impedance of the rectenna. Thus, designing a rectenna achieving the maximum RF to DC PCE is crucial to enabling RF-powered wearable and flexible electronics and is *the main objective of this research.*

1.2 Textile, Printed and Flexible RF Electronics

To enable the low-cost pervasive distributed IoT networks to benefit from the advances in WPT and RFEH, rectennas need to be fabricated using a variety of low-cost methods, on common materials such as polymers, textiles, and paper. Such materials were not intended as a substrate for RF system and posses undesirable dielectric properties such as high dielectric losses. Moreover, rectennas may need to be flexible, conformable, integrated in compact or transparent structures, or wearable, operating in proximity of human tissue. Therefore, powering the next generation of low-cost Internet of Everything (IoE) devices using rectennas is subject to being able to design high-performance rectennas within the material and packaging limitations.

Recent advances in flexible and printed RF front-ends and antennas can be exploited to fabricate low-cost rectennas. For example, different additive manufacturing techniques such as inkjet, 3D, screen, and dispenser printing have been used to print antennas on a variety of substrates [10]. Additive manufacturing allows rapid prototyping and reducing the fabrication costs compared to standard photolithography, as well as enables fabrication of circuits on unusual substrates.

RF electronic textiles (e-textiles) have been widely investigated for wearable applications, with recent fully-textile antenna implementations achieving radiation efficiencies approaching their rigid counterparts [11]. Textile-based antennas allow unobtrusive integration of antennas in garments and wearables. Compared to being limited to a compact footprint in a device such as commercial wearable smart-watches and glasses, textile antennas can utilize the garments large area to improve the antennas' performance in terms of gain and bandwidth.

The key challenge in flexible, wearable and low-cost antenna design, is the trade-off between the material choice, desired form-factor, and antenna performance. Despite the breadth of literature on textile, flexible, and transparent antennas, textile antenna designs are still limited to thicker substrates, with limitations on their bandwidth or radiation efficiency. Moreover, textile-based and flexible rectennas have consistently produced a lower PCE compared to their rigid counterparts, owing to their lossy substrates. Therefore, research into high-efficiency rectennas fabricated using flexible and wearable low-cost materials is essential to enable efficient RF-powered IoT [12].

1.3 Summary of This Work

In this thesis, novel antenna designs, matching networks, and adaptations of existing techniques for efficient textile-based and flexible rectennas are proposed to enable full adoption of RFEH and WPT in future IoE. Different flexible and textile-based RF

electronics fabrication techniques are utilized to realize rectennas specifically-designed to achieve the maximum PCE, compared to prior art, despite being implemented using low-cost materials. Multiple rectenna topologies are investigated to demonstrate flexible and textile-based rectennas, achieving significant PCE improvements over State-of-the-Art (SoA) rectennas while maintaining the lowest overall system complexity.

From the rectenna design perspective adopted in this work, "RFEH" is defined broadly as any effort to scavenge DC power from an incident plane-wave, in the far-field region of a transmitter. When the transmitter is a radio source not designed specifically for WPT, such as smartphones or cellular base-stations, the term *"Ambient RFEH"* is used [13].

1.3.1 Research Objectives

The endeavor to realize high-efficiency rectennas for wearable applications and low-cost unobtrusive IoT and IoE devices can be summarized in the following *research objectives*:

1. Being able to design rectifiers on unusual and low-cost materials with high-PCEs (>50%) and sufficient DC potential (330 mV [14]) to power off-the-shelf devices, from sub-μW/cm^2 power densities at UHF bands;
2. Demonstrating the feasibility of using low-cost flexible and textile-based rectennas as DC power supplies at mmWave bands (beyond 20 GHz), for wireless networks beyond 5G;
3. Showing the scalability of the developed rectenna design methodologies to various fabrication methods and packaging requirements based on application-specific rectenna designs.

The next section introduces the structure of this thesis, and outlines how each chapter proposes new solutions to achieve these research objectives.

1.3.2 Research Challenges

Hindering the adoption of rectennas as power supplies for wearable, printed, and flexible IoE devices are several research challenges which are addressed in this thesis. The key *research challenges* can be summarized as:

1. Low sensitivity of existing flexible rectennas: rectennas need to efficiently harvest sub-μW/cm^2 radiation to enable long range WPT or ambient RFEH;
2. Material-induced losses: the undesirable conductive and dielectric properties (tanδ) of low-cost conductors and substrates limit their suitability for RF applications, especially in the mmWave spectrum;

3. Low-resolution manufacturing: antennas need to be designed to match the low resolution of commercial additive manufacturing and e-textiles, especially at mmWave frequencies where the features are under 1 mm;

4. Human proximity effects: antennas operating in vicinity of the body need to overcome $\Re\{\epsilon_r\}$-induced detuning and $\Im\{\epsilon_r\}$-induced absorption.

1.3.3 Thesis Structure and Contributions

This thesis follows a systematic structure of designing and optimizing rectennas for textile-based and flexible printed electronics using different rectenna topologies, as shown in Fig. 1.3. The arrows in Fig. 1.3 indicate where a method or a technique introduced or developed in the previous chapter is adapted and extended. The publications arising from each chapter, listed in the following section, are referenced in Fig. 1.3.

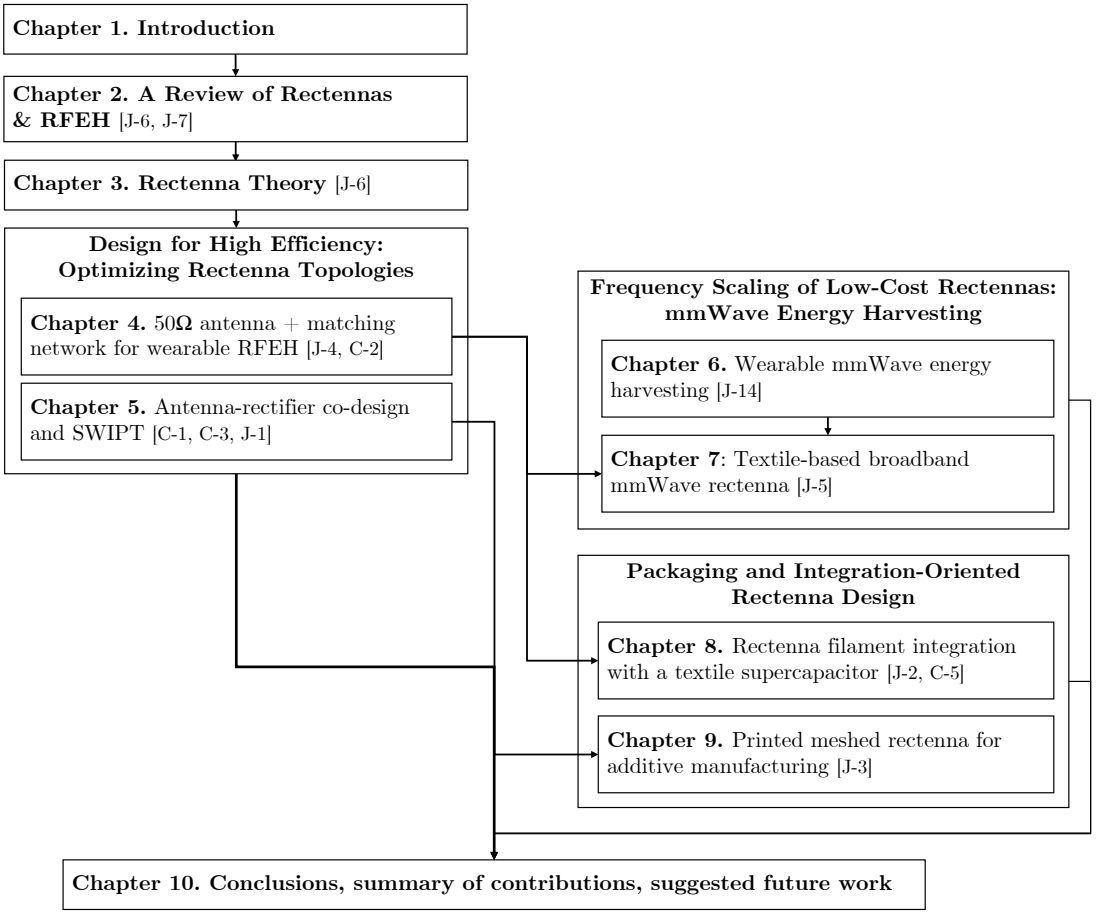

FIGURE 1.3: Structure of the thesis.

In Chapter 2, a literature review is presented, spanning the full breadth of rectenna design. An in-depth categorization of rectennas based on their bandwidth and radiation properties is presented in Section 2.4, and published in [15], followed by a review

of mmWave rectennas in Section 2.8, and published in [12]. Chapter 3 follows by presenting an overview of the theoretical fundamentals of antenna design, rectification, and impedance matching, governing the operation of rectennas, and presents a range of guidelines which are then followed in the practical rectenna development.

Chapter 4 explores the most common rectenna topology, a 50 Ω antenna with a matching network, and proposes a textile wearable rectenna with SoA PCE from sub-μW/cm^2 power densities, concluding that lossy textile substrates do not hinder high-PCE rectification. In Chapter 5, antenna-rectifier co-design is explored to mitigate the losses of lumped components by eliminating the impedance matching network, and is then proposed as an antenna-based solution for SWIPT, based on a high-isolation dual-port microstrip antenna. Both chapters show how the first research objective of this work can be achieved using low-cost materials for wearable applications.

In Chapters 6 and 7, the second research objective of enabling mmWave EH using low-cost textile rectennas is investigated. Wearable mmWave EH is analyzed and a broadband microstrip antenna is proposed and a wireless-powered mmWave network is evaluated analytically showing the potential for up to an order of magnitude performance gains over UHF harvesting. In Chapter 7, the first implementation of a broadband rectenna operating between 20 and 26.5 GHz (the K-band) is proposed based on a novel off-body antenna design, representing the first mmWave antenna designed specifically for lossy substrates such as textiles.

Chapters 8 and 9 fulfill the third research objective of this thesis, showing the scalability of the rectenna design methodologies optimized in Chapters 4 and 5, in two application-oriented demonstrators. Firstly, a high-voltage thin and flexible Coplanar-Waveguide (CPW) rectenna is proposed for concealed e-textiles, and demonstrated directly charging a textile supercapacitor with the highest end-to-end charging efficiency compared to all reported energy harvesters. In Chapter 9, a compact high-impedance antenna is proposed for co-designed rectennas, limited to low-resolution additive manufacturing. Meshing of the antenna is investigated for applications requiring optical transparency, demonstrating high-PCE for various mesh densities. Both chapters show that high-PCE rectennas are not limited by the dielectric or conductor used, and can be realized using a range of fabrication techniques and integrated with other flexible components. The thesis is finally concluded in Chapter 10, summarizing the research findings and contribution, and suggesting new research directions enabled by this work.

1.4 List of Publications

The following publications have been produced based on the material and contributions in this thesis, in addition to work on wireless power transfer, energy harvesting, and wearable antennas carried out during the candidature period. Publications J-8. and

C-1., cited in different parts of this thesis, are included in Appendix A. The publications arising from the work described in the thesis' chapters are cited in the introduction of each respective chapter.

Journal Papers:

J-1. **Mahmoud Wagih**, Geoffrey S. Hilton, Alex S. Weddell, Steve Beeby "Dual-Band Dual-Mode Textile Antenna/Rectenna for Simultaneous Wireless Information and Power Transfer (SWIPT)" *IEEE Transactions on Antennas and Propagation*, 2021.

J-2. **Mahmoud Wagih**, Nicholas Hillier, Sheng Yong, Alex S. Weddell, Steve Beeby "RF-Powered Wearable Energy Harvesting and Storage Module based on E-Textile Coplanar Waveguide Rectenna and Supercapacitor" *IEEE Open Journal of Antennas and Propagation*, 2021.

J-3. **Mahmoud Wagih**, Alex S. Weddell, Steve Beeby "Meshed High Impedance Direct-Write Printed Rectenna Optimized for Additive Manufacturing" *IEEE Open Journal of Antennas and Propagation*, 2020.

J-4. **Mahmoud Wagih**, Alex S. Weddell, Steve Beeby "Omnidirectional Dual-Polarized Low-Profile Textile Rectenna with over 50% Efficiency for Sub-μW/cm^2 Wearable Power Harvesting " *IEEE Transactions on Antennas and Propagation*, 2020.

J-5. **Mahmoud Wagih**, Geoffrey S. Hilton, Alex S. Weddell, Steve Beeby "Broadband Millimeter-Wave Textile-Based Flexible Rectenna for Wearable Energy Harvesting" *IEEE Transactions on Microwave Theory and Techniques*, 2020.

J-6. **Mahmoud Wagih**, Alex S. Weddell, Steve Beeby "Millimeter-Wave Power Harvesting: A Review" *IEEE Open Journal of Antennas and Propagation*, 2020.

J-7. **Mahmoud Wagih**, Alex S. Weddell, Steve Beeby "Rectennas for RF Energy Harvesting and Wireless Power Transfer: A Review of Antenna Design" *IEEE Antennas and Propagation Magazine*, 2020.

J-8. **Mahmoud Wagih**, Oktay Cetinkaya, Bahareh Zaghari, Alex S. Weddell, Steve Beeby "Real-World Performance of Sub-1 GHz and 2.4 GHz Textile Antennas for RF-Powered Body Area Networks" *IEEE Access*, 2020.

J-9. **Mahmoud Wagih**, Yang Wei, Abiodun Komolafe, Russel Torah Steve Beeby "Reliable UHF Long-Range Textile-Integrated RFID Tag Based on a Compact Flexible Antenna Filament" *Sensors* 2020.

J-10. **Mahmoud Wagih**, Abiodun Komolafe, Bahareh Zaghari "Dual-Receiver Wearable 6.78 MHz Resonant Inductive Wireless Power Transfer Glove using Embroidered Textile Coils" *IEEE Access*, 2020.

J-11. **Mahmoud Wagih**, Abiodun Komolafe, Bahareh Zaghari "Separation-Independent Wearable 6.78 MHz Near-Field Radiative Wireless Power Transfer using Electrically-Small Embroidered Textile Coils" *Energies*, 2020.

J-12. Watcharapong Paosangthong, **Mahmoud Wagih**, Russel Torah, Steve Beeby "Textile-based Triboelectric Nanogenerator with Alternating Positive and Negative Freestanding Grating Structure" *Nano Energy*, 2019.

J-13. **Mahmoud Wagih**, Yang Wei, Steve Beeby "Flexible 2.4 GHz Node for Body Area Networks with a Compact High-Gain Planar Antenna" *IEEE Antennas and Wireless Propagation Letters*, 2019. (edited during candidature based on 2017/18 work)

J-14. **Mahmoud Wagih**, Geoffrey S. Hilton, Alex S. Weddell, Steve Beeby "Higher-Order Mode Broadband Textile-Based Microstrip Antenna for Compact Wearable Millimeter-Wave Wireless Power Transmission". **(In Preparation)**

Conference Papers:

C-1. **Mahmoud Wagih**, Geoffrey S. Hilton, Alex S. Weddell, Steve Beeby "2.4 GHz Wearable Textile Antenna/Rectenna for Simultaneous Information and Power Transfer" *15th European Conference on Antennas and Propagation*, Dusseldorf, Germany, 2021.

C-2. **Mahmoud Wagih**, Alex S. Weddell, Steve Beeby "Analyzing and Maximizing the Power Harvesting Efficiency of a Textile Rectenna Through Reflector-Based Shielding" *15th European Conference on Antennas and Propagation*, Dusseldorf, Germany, 2021.

C-3. **Mahmoud Wagih**, Alex S. Weddell, Steve Beeby "High-Efficiency Sub-1 GHz Flexible Compact Rectenna Based on Parametric Antenna-Rectifier Co-Design" *IEEE MTT-S International Microwave Symposium*, Los Angeles, U.S.A., 2020. (**Best 3MT Presentation, 2$^{\text{nd}}$ place**)

C-4. **Mahmoud Wagih**, Nicholas Hillier, Sheng Yong, Alex S. Weddell, Steve Beeby "Wearable E-Textile Wireless RF Power Supply based on a Textile Supercapacitor and a Flexible Rectenna Filament" *IEEE International Conference on Flexible and Printable Sensors and Systems*, Manchester, U.K., 2020.

C-5. **Mahmoud Wagih**, Alex S. Weddell, Steve Beeby " Sub-1 GHz flexible concealed rectenna yarn for high-efficiency wireless-powered electronic textiles" *14th European Conference on Antennas and Propagation*, Copenhagen, Denmark, 2020.

C-6. **Mahmoud Wagih** "Direct-Write Dispenser Printing for Rapid Antenna Prototyping on Thin Flexible Substrates" *14th European Conference on Antennas and Propagation*, Copenhagen, Denmark, 2020.

C-7. **Mahmoud Wagih**, Abiodun Komolafe, Bahareh Zaghari, Alex S. Weddell, Steve Beeby "A Broadband Outlook on Flexible and Textile RF Energy Harvesting and Wireless Power Rransfer: from Near-Field to 5G" *InnoLAE* 2020, Cambridge, U.K., 2020. (Oral abstract)

C-8. **Mahmoud Wagih**, Alex S. Weddell, Steve Beeby "Powering E-Textiles Using a Single Thread Radio Frequency Energy Harvesting Rectenna" *Proceedings*, 2020, 65.

C-9. **Mahmoud Wagih**, Alex S. Weddell, Steve Beeby "Broadband Millimeter-Wave Textile-Based Flexible Rectenna for Wearable Energy Harvesting" *IEEE Wireless Power Transfer Conference (WPTC)*, London, U.K., 2019. (**Best Student Paper Award**)

C-10. **Mahmoud Wagih**, Abiodun Komolafe, Bahareh Zaghari "Position Independent Wearable 6.78 MHz Near-Field Radiative Wireless Power Transfer using Electrically-Small Embroidered Textile Coils" *PowerMEMS* 2019, Krakow, Poland. (**Best Oral Paper Award**)

C-11. **Mahmoud Wagih**, Alex S. Weddell, Steve Beeby "Characterizing and Modelling Non-linear Rectifiers for RF Energy Harvesting" *PowerMEMS*, Krakow, Poland, 2019.

C-12. **Mahmoud Wagih**, Alex S. Weddell, Steve Beeby "Overcoming the Efficiency Barrier of Textile Antennas: a Transmission Lines Approach" *Proceedings: E-Textiles*, London U.K., 2019.

C-13. **Mahmoud Wagih**, Abiodun Komolafe, Bahareh Zaghari "Wearable Wireless Power Transfer using Direct-Write Dispenser Printed Flexible Coils" *IEEE International Conference on Flexible and Printable Sensors and Systems* 2020, Manchester, U.K.

C-14. Abiodun Komolafe, **Mahmoud Wagih**, Ashwini Valavan, Zeeshan Ahmed, Alexas Stiukas, Bahareh Zaghari "A smart cycling platform for textile-based sensing and wireless power transfer in smart cities " *Proceedings: E-Textiles*, 2019, London, U.K.

C-15. Watcharapong Paosangthong, **Mahmoud Wagih**, Russel Torah, Steve Beeby "Textile Manufacturing Compatible Triboelectric Nanogenerator with Alternating Positive and Negative Freestanding Grating Structure" *Proceedings: E-Textiles*, 2019, London, U.K.

Chapter 2

Rectennas and RFEH: A Review

2.1 Introduction

In this chapter, background literature, spanning the RFEH system discussed in Chapter 1 is reviewed. The early beginnings of WPT using rectennas is reviewed in Section 2.2, followed by the work on ambient RFEH and existing power sources in Section 2.3. Section 2.4 then reviews and categorizes antenna design form an impedance matching and bandwidth, radiation properties, and polarization perspectives using standard antenna parameters as FoM in rectenna design for both RFEH and WPT, these sections have been published in [15]. Textile-based and wearable antenna design is reviewed in Section 2.5. Rectifiers, devices and architectures for efficient RF-DC conversion are reviewed in Section 2.6. mmWave-specific WPT and EH techniques and challenges are reviewed in Section 2.8, published in [12]. Finally, concluding remarks and a summary are provided in Section 2.9.

2.2 WPT and RFEH: The History and Motivation

N. Tesla proposed WPT in the 1900s as a mean of transferring thousands of horsepower [1]. The term "*rectenna*", describing an antenna connected to a rectifier for harvesting Radio Frequency (RF) power, emerged in the 1950s for powering autonomous drones [3], and later for space power beaming [16]. Long-range RF and microwave WPT has been hindered by the spherical spreading of RF radiation in free space. Thus, commercial WPT has been mostly limited to near-field non-radiative power transfer for wireless consumer electronics charging [5]. Radiative UHF Radio Frequency Identification (RFID) represents the only pervasive application where rectennas have been utilized in an unobtrusive manner [17]. RFID tags are a unique case of rectennas where RFID

TABLE 2.1: Power Conversion Stages in a RFEH System, and Existing Literature Surveys Covering Each Component

Conversion stage	Power source	Focus element	Literature surveys
a-b	Radiated RF plane wave	Antenna radiation characteristics	This survey
b-c	RF guided wave	Antenna and matching network bandwidth	This survey, 2013 [20], 2018 [22], 2019 [24]
c-d	Z-matched RF wave	Rectifier topology and technology	2013 [20], 2014 [17], 2016 [23], 2018 [22]
d	Unregulated DC power	Power management circuitry	2015 [21], 2016 [23]
e	Regulated DC power	Load, network architecture	2013 [20], 2014 [7]

antennas are often described purely as antenna and not rectennas [18, 19], with the rectifier concealed on a Complementary Metal Oxide Semiconductor (CMOS) Integrated Circuit (IC), as discussed in more detail in Section 2.4.4.2.

As the power consumption of semiconductor devices and wireless sensor nodes continuously scales down, it became more feasible to power sensors using ambient RFEH, or using distributed low-power omnidirectional transmitters [7, 20]. An ultra-low power wireless-powered system is typically composed of the RF-harvesting front-end, DC power and storage management, and a low-power microprocessor and transceiver.

Fig. 1.2 shows the architecture of an RF-powered IoT node, and the commonly reported implementations of the RF front-end. The end-to-end efficiency of a wireless-powered system, is dependent on the performance of individual components: the antenna, rectifier and power management circuit. Multiple literature surveys have been carried out focusing on different components of the system. Table 2.1 outlines the power conversion stages, the key component for efficient power conversion, and the relevant literature surveys focusing on each part. Recent surveys focused on the power conversion techniques [17, 20, 21], rectifier topologies [21, 22], or RFEH from a networking perceptive [7, 23]. However, antenna design for RFEH has not been considered as a key parameter in reported reviews. While some surveys considered the antenna's bandwidth and efficiency from a holistic perspective, or specific antenna designs for niche applications such as miniaturized or wearable antennas [22, 24], no detailed analysis has been presented on the impact of certain antenna parameters on the power reception and PCE.

2.3 Ambient RF Power

Wireless communication infrastructure has been widely deployed in urban and suburban environments, producing a considerable amount of RF power, previously described

as electro-pollution [25], making it attractive for energy harvesting as a result of being widely-deployed, and more predictable than environmental energy harvesting sources. In this section, a review of the different mobile and stationary power sources previously utilized for RFEH is presented.

2.3.1 Base-station RF Power Density Surveys

Cellular networks [26], Amplitude Modulation (AM) radio broadcast [27, 28], Digtial Telivision (DTV) broadcast [29], and Wireless Local Area Network (WLAN) [11], are examples of the available RF power sources in urban environments. Broadband surveys of available RF power were performed in London, United Kingdom [13], Shunde, China [30], in addition to an indoor survey in an office environment [31, 32]. To add, surveys of specific bands, such as DTV, have also been presented [29].

The measurement approach can be summarized in measuring the Power Spectral Density (PSD) over the frequency band of interest, commonly the full UHF spectrum, using a broadband antenna [13,31,32]. Fig. 2.1 shows a good agreement between the PSDs measured in different locations for the Global System for Mobile (GSM) bands, additional ambient power peaks have can be observed with the introduction of 4G/LTE (Europe) and CDMA (China) around 800 MHz and 2.65 GHz. Only in [13], a more detailed measurement approach has been discussed; the approach used in measuring Specific Absorption Rate (SAR) and exposure has been used where the measurements are performed in different directions while retaining the maximum value, while repeating the frequency sweeps within a time-frame. Furthermore, while [30,33] took place in urban districts, [13] extends the survey to cover semi-urban locations with more than 270 measurement spots around London suburbs.

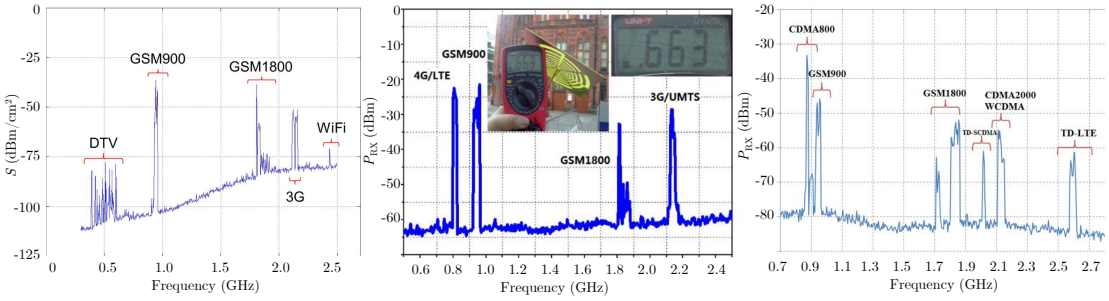

(a) (b) (c)

FIGURE 2.1: Reported measured PSDs in: (a) outdoor, London, UK, 2012 (before 4G deployment) (reproduced from [13], ©IEEE 2013); (b) Outdoor, Liverpool, UK, 2015, (reproduced from [33], ©IEEE 2016); (c) Outdoor, Shunde, China, 2015. (reproduced from [30], ©IEEE 2015)

By observing the single channel PSDs, it can be concluded that no single ambient frequency can be utilized for power conversion using SoA rectifiers [21], as the power can be lower than −40 dBm. However, when combining multi-band power, −15 dBm was

measured on a power meter in [33] using a frequency-independent antenna covering the spectrum in Fig. 2.1-C. Hence, the reported PCE in [33, 34] focused on P_{RX}=−15 dBm described by Song *et. al.* as "ambient power level". From Fig. 2.1-a, it can be seen that a rectenna needs to have a sensitivity better than −30 dBm/cm^2 (S <1 μW/cm^2), to harvest ambient signals, as outlined in the research objectives of this thesis.

While some spectral surveys reported averaging over a short period of time (<1 minute) [13, 31], none of the surveys considered the impact of low-network activity periods such as weekends or nigh-time on the available power density. In [35], it was shown that the network activity varies significantly overtime as observed in Fig. 2.2. It can be predicted that the available base-station power varies depending on the network activity [36]. For example, at night or on weekends, for a varying load network, the traffic could decline by over 80% implying that the harvested energy will decrease during these time-periods. Therefore, despite ambient RFEH being described as a time-invariant energy resource, this is only true in a network that maintains a certain level of traffic over time.

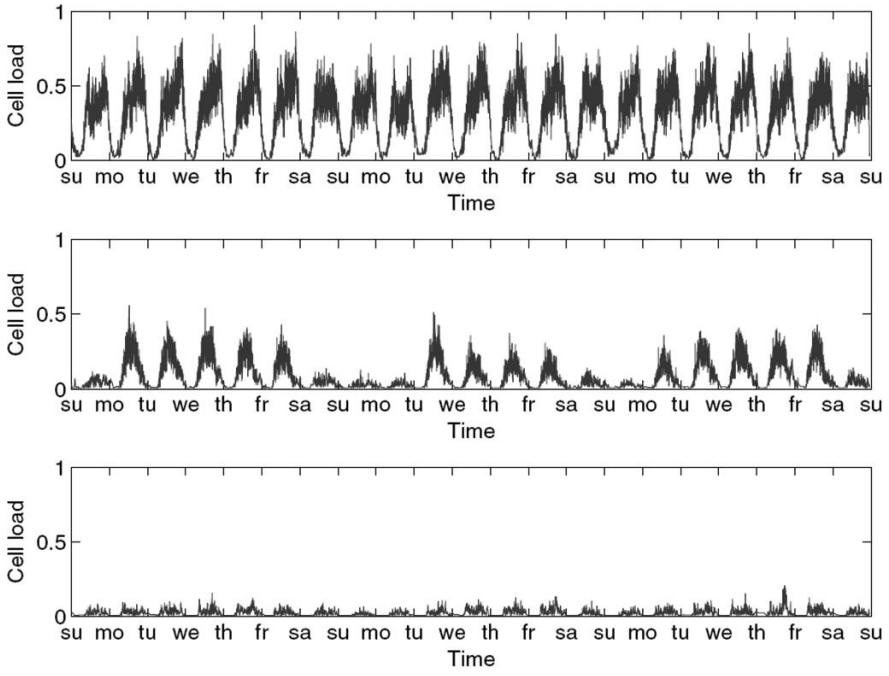

FIGURE 2.2: Normalized network activity of a high-load (top), varying load (middle), and low-load (bottom) network over a three week period in California, USA (reproduced from [35], ©IEEE 2008)

Complete systems were reported functioning off recycled ambient RF power from base-stations including cellular networks [13], DTV [29], and FM radio broadcast [37]. [13] relied on harvesting the power from all frequency bands shown in Fig. 2.1-b. However, the −29 dBm quoted sensitivity reported by Pinuela *et al.* [13] was questioned by Bito *et al.* [14], where −29 dBm is lower than the power threshold required for the Power Management Integrated Circuit (PMIC) used for cold-start, even when excluding the rectification losses. This could imply a higher actual PSD when the measurements

were performed in [13]. In addition to RFEH, FM radio broadcast waves were used for low-power backscattering communications, as far as 34.5 km from the base-station [38]. Nevertheless, the system was powered using a flexible solar cell, as the RF power density is too low for a rectenna, where the more recently reported FM harvester had a range of up to 6.5 km away from the base-station [37]. In [39], it was stated that ambient RFEH is becoming increasingly difficult with the reduced RF emissions from cellular networks, owing to the adoption of more energy-efficient transmitters as opposed to continuously radiating power in an omnidirectional manner. Therefore, Okba *et al.* suggested that WPT using dedicated transmitters is used instead, which enables more energy-efficient communications within an IoT network [39].

The most recent and the most extensive survey of ambient RF power, its applicability fo low-power computing, as well as the possibility of converting it to DC using SoA rectennas was presented in [40]. Gu *et al.* performed a survey of the UHF spectrum in Montreal, covering varying locations and times, as observed in Fig. 2.3. The PSD in [40] closely follows the previously reported PSDs, some of which are shown in Fig. 2.1

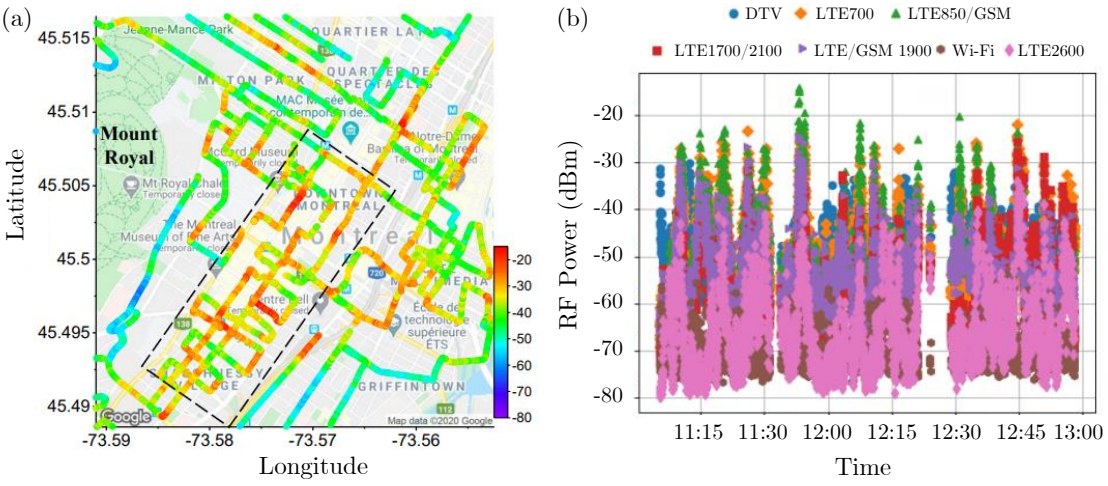

FIGURE 2.3: Measured RF power in Montreal, 2020, showing the spatial variation in GSM900 power (a) and time variations of all bands in the UHF spectrum (b) [40], ©IEEE 2008)

In Fig. 2.3-a, it can be observed that the ambient GSM900 power exceeds −20 dBm in most outdoor locations in the survey, a power level at which several SoA rectennas can operate. For example, the flexible dipole rectenna proposed in Chapter 5 was quoted in [40] owing to its highest PCE at −20 dBm. In [40], it was also shown that the energy/computation in CMOS nodes smaller than 180 nm can be powered based on the DC power output of SoA rectennas based on the measured RF power levels. However, the DC voltage output of rectennas still remains a bottleneck where most high-PCE rectennas do not produce enough DC potential for the CMOS logic to operate.

2.3.2 Mobile Power Sources

An alternative approach to harvest ambient power is to harvest from mobile transmitters, such as mobile-phones [41], or license-free sources [42, 43]. Harvesting from mobile devices has been studied in the context of on-body RF harvesters, due to the significantly lower distance between the power source and the harvester, pushing the available power to levels above 0 dBm. P_{RF}=1.88 dBm was measured using a smart-lens flexible dipole (of −28 dB on-eye gain) at 18 cm from a smartphone [41]. In [44], it was shown that harvesting from the GSM up-link band in an indoor busy environment, such as a commuter train, can outperform harvesting from the down-link by multiple times.

In [42], 3D EM field simulation was used to estimate the electric and magnetic (E- and H-) near-fields power from a long-range two-way radio for a wrist-wearable. The simulation has been validated through measurements using E- and H-probes as shown in Fig. 2.4. In, [43] the proposed multi-band rectenna is demonstrated at 2.4 GHz using the near-field radiation leaking from a microwave-oven, as well as in contact with a ringing mobile phone.

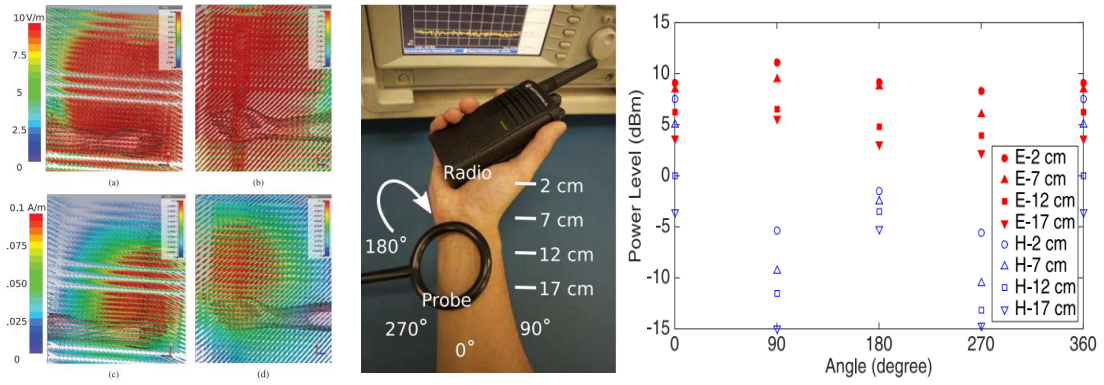

(a) (b) (c)

FIGURE 2.4: Simulation and measurement of available near E- an H- field from a 433 MHz radio on-body: (a) 3D EM simulated E- and H- fields; (b) testing setup; (c) measured RF power at different distances (reproduced from [14], ©IEEE 2017).

Studies harvesting from mobile have focused on GSM, due to the higher achievable PCE around 900 MHz [21], and due to the higher available power from GSM compared to 3G calls. While [45] studied the effect on different waveforms to improve the PCE there has been no report on the effect of harvesting from different communication protocols relating the efficiency to specific protocols.

2.4 Antenna Design from an RFEH Perspective

2.4.1 Bandwidth and Matching in Rectennas: A Non-50 Ω RF Network

For a rectenna to receive power and rectify it efficiently, an impedance match between the antenna's impedance and the rectifier is crucial to prevent the power from being reflected back to air. The standardization of the characteristic impedance to the 50Ω constant has been derived as a compromise between attenuation and power-handling in the early-days of microwave engineering [46]. In antennas, the impedance bandwidth, is defined as the range of frequencies where the reflected power is less than 10% ($S_{11} < -10$ dB). This has been traditionally referenced to a 50 Ω source, due to the fact that a Low-Noise Amplifier (LNA), a Power Amplifiers (PA), or a detector are conventionally designed with 50 Ω input impedance matching, integrated on the Radio Frequency Integrated Circuit (RFIC).

In rectennas, where the antenna's output is fed directly into a rectifier, the non-linearity of the diode results in a highly-varying input impedance, with a dominant capacitive component [33, 47]. Assuming a 50 Ω antenna is used, the main challenge lies in designing an additional RF matching-network to transform the input impedance to the rectifier's at the frequencies of interest, and optimizing it for a certain power level. In this case, an end-to-end impedance bandwidth is required to ensure efficient RF to DC conversion. Thus, although an antenna could achieve a theoretical infinite or ultra-broad bandwidth using periodic elements or self-complementary geometry, the rectenna's bandwidth will be bottle-necked by the rectifier's matching network.

Multiple rectenna topologies have been presented to maximize the power transfer between the antenna and the rectifier, through minimizing reflection, for single- and multi-band harvesting or WPT. Figure 2.5 shows a summary of the reported rectenna topologies categorized by their impedance matching architectures. Examples of high performance rectennas, in terms of end-to-end bandwidth (the FoM in this case), from each category are compared in Appendix B in Table B.1.

While WPT from a dedicated feed and ambient RFEH are distinct rectenna applications, from a bandwidth perspective, achieving an end-to-end match between the antenna, the rectifier and the load is fundamental to achieving high PCE. Nevertheless, WPT rectennas have been more focused on achieving a higher-Q match (lower S_{11}) to improve the single-tone PCE for certain power levels (topologies a, e and f), hence, in single-tone WPT may not be a FoM on its own. However, a broad bandwidth in single-tone WPT improves the systems immunity to detuning, fabrication imperfections and packaging parasitics. On the other hand, RFEH rectennas have prioritized multi-band operation, due to the often low PSD in single bands, falling into topologies b-d and g.

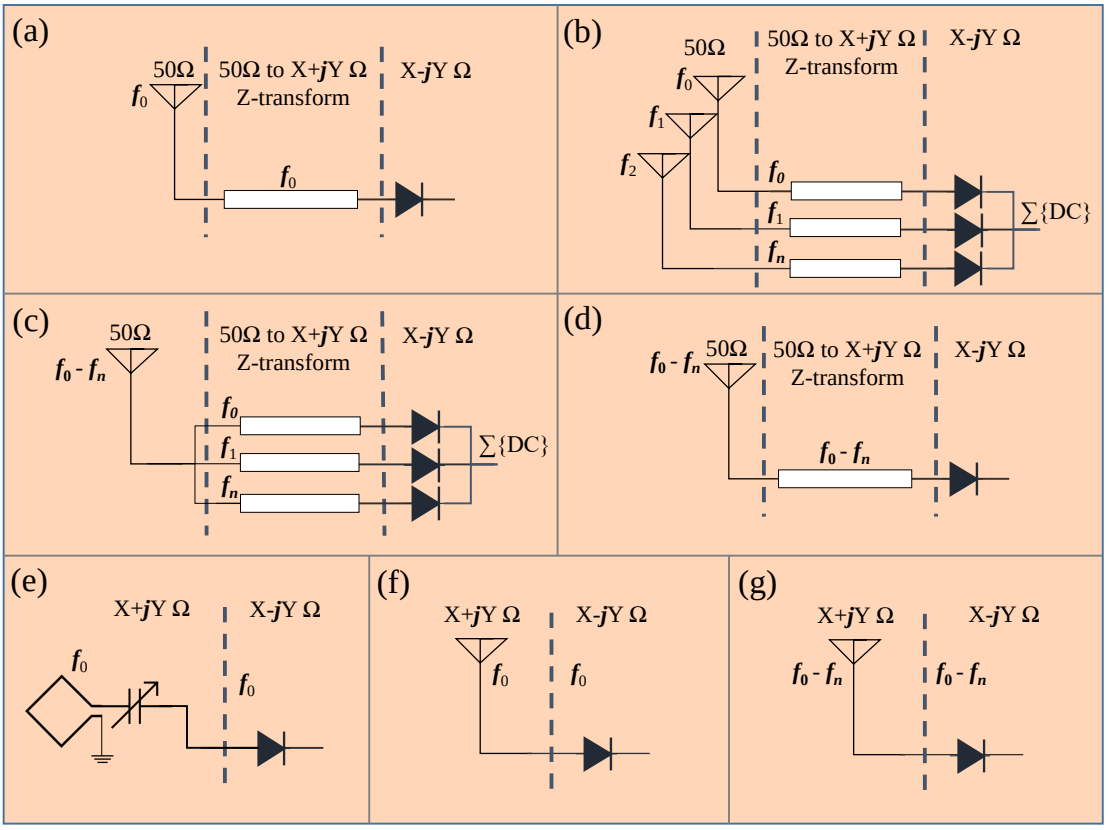

FIGURE 2.5: Rectenna topologies from a bandwidth and impedance matching perspective. (a): Single band rectenna with standard antenna. (b): Multi-band rectenna (formed of multiple mutually coupled antennas) with one rectifier and matching network per band. (c): Broadband rectenna with multiple RF-ports and separate matching networks for each band. (d): Broadband rectenna with a broadband antenna and a broadband matching network. (e): Single band rectenna using an electrically small antenna directly matched to the rectifier. (f): Single band electrically large antenna with complex impedance to conjugate the rectifier. (g): Broadband rectenna with complex impedance to conjugate the rectifier over a range of frequencies. The dashed line represents the measurement plane where a $S_{11} < -10$ dB bandwidth needs to be maintained.

2.4.2 50 Ω Rectennas

2.4.2.1 Single-Band 50 Ω Antennas in Rectennas

Antenna design for 50 Ω single band rectennas (topology A) has been based mostly on standard antenna designs, such as a Linearly-Polarised (LP) or a Circularly Polarised (CP) radiator patch over a ground plane [11,48–51], dipole antennas [13,52] and inverted-F monopoles [53–56]. Differential single-band rectennas have been based on multiple antenna elements configured as an array with DC combining [48], or hybrid DC and RF combining of multiple patch elements [57]. The effect of size reduction on the rectenna's PCE has been discussed in [39].

As many of the presented 50 Ω antennas are single band, which meets the requirements of single-tone WPT, when ambient multi-band RFEH is sought, multiple single-band antennas have been combined to form multi-band rectennas with suppressed mutual coupling (topology B) [13,53], with independent DC combining, after the power management circuit stage, making it entirely isolated from the RF harvesting and conversion circuit, requiring multiple power management circuits for each bands, which may decrease the efficiency of the boost converters [11], due to the low DC power from individual bands.

2.4.2.2 Multi- and Broad-band RFEH Antennas

Ambient RFEH is usually associated with multi-band harvesting, thus, multiple methods of improving the bandwidth of standard antenna designs, or methods of forming dual or triple-band antenna arrays have been presented. In this section, bespoke antenna design for RFEH is reviewed, along with classic multi-band antennas with the potential of being employed as rectennas. In this context, the terms "multi-band" and "broadband" antennas are differentiated through the continuity of their bandwidth ($S_{11} < -10dB$) outside the bands of interest.

CPW monopoles, occupying smaller areas than their microstrip patch antenna counterpart at the same frequency, and producing a LP or a CP wave, are commonly used in broadband ambient rectennas [58–60]. A reflector plane can be used for increased isolation, and improved gain resulting in a similar radiation pattern to patch antennas [60]. Slotted-CPW antennas were used to improve the impedance-bandwidth across multiple bands such as the 1.8-2.7 GHz [59] or 1-3 GHz [58, 61].

Slot rectennas, with aperture-proximity feed were designed to have increased bandwidth, as well as multiple proximity feeds for different rectifiers and matching networks targeting different bands. [43, 62, 63]. Patch rectennas have also been presented for dual-band operation using asymmetric corner trimming resulting in dual-resonance [63]. Figure 2.6 shows some of the reported multi-band antennas utilizing more than one bandwidth improvement technique.

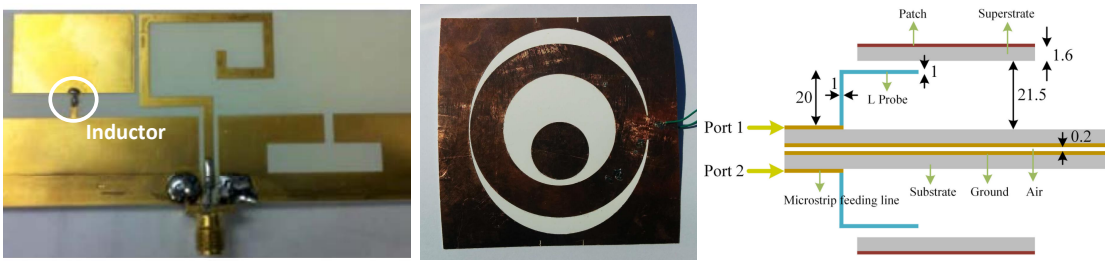

FIGURE 2.6: Multi-band UHF RFEH antennas: (left) triple band antenna with a lumped inductor and three radiator elements (reproduced from [64], ©IEEE 2013); (center) triple band slotted patch (reproduced from [43], ©IEEE 2018); (right) L-probe-fed dual-band patch (reproduced from [65], ©IEEE 2017)

Conventional broadband antenna designs, including frequency-independent antennas, have been used in ambient RFEH as well as proposed for mmWave applications [66]. Spiral antennas: a single element textile rectenna with a single band matching network [67], a spiral array [68], and a log-periodic antenna [33] have been presented. A triangular spiral antenna has also been presented for harvesting energy from 1-3 GHz [69]. A spiral antenna, with unfolded dipole ends was presented for dual-band operation at 900 MHz and the Ultra-Wide Band (UWB) (3-5 GHz) bands [70]. Ref. [71] presents triple band operation using a multi-port rectenna formed of an array of "pixel" elements, with DC combining, with the "pixel" connections optimized through simulation to tune the antenna, the "pixel" rectenna has been compared to $\lambda/4$ monopoles .

2.4.3 Antenna-Rectifier Impedance Matching

Matching the 50 Ω antenna to a non-linear rectifier presents a challenge due to the wide variation in its input impedance with frequency. In topologies A and B (Fig. 2.5), a common matching network topology is LC matching using lumped components [72, 73], however, the fractional bandwidth is typically lower than most communication bands [13]. Single band stub matching has been commonly used at sub-6 GHz microwave [11, 71, 74] as well as at mmWave bands [75, 76], usually paired with RF-short quarter-wave stubs at the fundamental frequency and the 2^{nd} harmonic. Therefore, the reported mmWave rectennas have inherently narrow band due to their PCE bandwidth being bottle-necked by the harmonic rejection at the outuput, which makes them specific to single-tone WPT applications in the 24 GHz license-free band. A comparison of lumped and distributed stub matching has been reported in order to numerically defining a maximum PCE of a rectenna [77].

Rectennas in topologies C and D have been presented with more complex matching networks. Full-distributed-line matching networks have been presented for broadband operation [78, 79], with an RF-block-DC-short (DC-pass filter) at the output port [26] or a DC-block capacitor acting as a return path for the diode's harmonics [65]. Rectifier components, such as capacitors in a voltage doubler, have been replaced in [78] by Printed Circuit Board (PCB) interdigitated capacitors, synthesized using commercial Electronics Design Automation (EDA) tools. Other reported broadband rectenna matching networks combine lumped components, for matching the lower frequencies, and distributed elements for creating RF shorts at the input [80]. Varying the load's observed input impedance by the source, known as source-pull technique, has been utilized to design a broadband rectifier of 57% fractional bandwidth (1.25 to 2.25 GHz) with up to 10% higher PCE compared to a lumped or distributed line matching network [81]. While matching networks have commonly been designed to match the antenna across its full 50 Ω bandwidth, in [67, 82] broadband antennas have been connected to narrow-band rectifiers. Hybrid lumped and distributed elements matching networks have been widely

used in topologies C and D [33, 43, 65, 80], avoiding complex structures such as interdigitated capacitors which require more accurate modeling and fabrication than standard microstrip lines.

The input power to the rectifier affects the input impedance due to the diodes' non-linearity. Therefore, rectennas have been designed to maximize the PCE for specific input power levels as well as load impedances [11, 71]. In [33], the matching network for the six-band rectenna, following topology C, has been designed to match the rectifier at power levels from -30 dBm to -10 dBm and for loads between 1 and 100 kΩ, based on a complementary conjugate resistance compression network. Moreover, as a result of the predominately capacitive high impedance of the diodes at sub-3 GHz frequencies, broadband rectennas without matching networks [34, 83, 84], or minimized simplified matching circuits [85], focused on $P_{\mathrm{RF}} > 0$ dBm, and frequencies higher than 1 GHz [84–87] due to the lower capacitive impedance of the diode enabling a good match with the antenna, avoiding designing antennas with input reactance >1000 Ω.

Adaptive, or reconfigurable, impedance matching has been presented in CMOS rectennas, where the matching network is formed of an on-chip capacitor bank and inductors [88]. Static CMOS matching networks have also been presented for standard 50 Ω antennas [88] as well as co-designed antennas [89, 90]. In [91], a passive CMOS power-detector has been used to control the switches directing the antenna's output to different rectifiers and matching networks based on the available power. A design-time reconfigurable matching network has been presented using lumped adjustable capacitors, tuned by trimming while measuring the input impedance using a Vector Network Analyser (VNA) [92]. On-board switches, controlled by an external micro-controller, were utilized in [93] to tune the on-PCB matching network capacitors at 900 MHz, demonstrating up to 10% performance improvement. In a reconfigurable microstrip matching network, a Field-Effect Transistor (FET) switch has been used to tune matching stubs for dual-frequency operation [94].

2.4.4 Antenna and Rectifier Co-design

Rectennas following topologies E-G in figure 2.5 are characterized by the antenna's direct match to the rectifier, instead of the 50 Ω standard, requiring a minimized or eliminated-matching circuit to deliver power to the rectifier. This section reviews state-of-the-art rectennas employing non-50 Ω antennas, in addition to the advantages of matching-network-less rectennas.

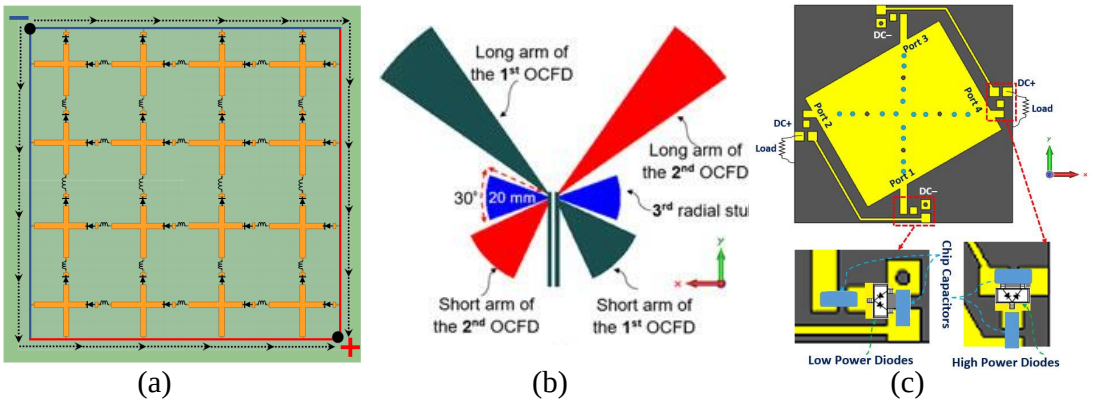

FIGURE 2.7: Rectennas directly matching the diode's impedance: (a) 4×4 RFEH cross-dipole surface (reproduced from [84], ©IEEE 2019); (b) broadband inductive off-center fed dipole (OCFD) (reproduced form [34], ©IEEE 2017); (c) dual-polarization frequency-selectable off-set patch (reproduced from [83], ©IEEE 2018).

2.4.4.1 Electrically Small Antennas

LC resonant loop antennas have been widely used in applications where the system's size is critical. At sub-1 GHz frequencies, where the wave-length could result in a standard distributed-elements antenna occupying more space than the system's overall dimensions, applications such as fully-integrated transceivers for body-implants particularly benefit from using electrically small antennas for WPT [95].

The highly inductive impedance, near resonance, of a small-antenna can be utilized to directly conjugate the rectifier [96], or with an additional on-chip capacitive matching network [97]. Electrically small antennas, down to $ka = 0.645$, compared to $ka = 5.91$ in a normal dipole ($ka = 2\pi r/\lambda_0$), have been reported for sub-1 GHz WPT with LP and CP [96], using Huygens dipole antennas [98].

Multiple on-chip LC coils for radiative WPT have been presented for microwave and sub-1 GHz fully-integrated rectennas. In a fully-integrated 915 MHz CMOS rectenna, a dipole antenna has been directly tuned to match a 3.4 Ω source using slot-termination to inductively load the antenna [99]. CMOS rectennas with a PMIC and a LNA were also presented with on-chip loop antennas in a standard Silicon-on-Insulator (SoI) chip [100]. A power-harvesting RFID 5.8 GHz transceiver with an integrated coil-antenna has been presented for near-field powering [101]. A dual-band antenna, for 7 GHz WPT and 1 GHz communication have been presented with on-chip tuning capacitors [102].

2.4.4.2 Rectifier-Conjugate Antennas

The typical input impedance of the rectifier is highly capacitive, and therefore requires an inductive antenna to directly conjugate its impedance [33, 47]. High-impedance inductive antennas have been widely used in RFID tags due to the RFID IC's capacitive

impedance [18]. In antenna literature, RFID ICs are often discussed as a black-box with an equivalent circuit of Z_{IC}, where an antenna is designed to achieve a $Z_{\mathrm{In}} = Z_{\mathrm{IC}}^{*}$ [18,19]. Few mentions of rectifiers is presented in the discussion, as the reason behind the capacitive Z_{IC}, in most RFID antennas and propagation literature [18, 19, 103]. However, the input impedance of an RFID tag is fundamentally that of a rectifier, implemented in a CMOS process using diode-connected transistors [104], and integrated with a backscattering modulator in the form of a shunt shorting switch. As Z_{IC} is obtained from a datasheet of a commercial part, it is difficult to provide a solid description of the process used to report that figure by the IC's manufacturer. Nevertheless, several recent studies described antenna co-design based on the extracted $Z_{\mathrm{Rectifier}}$ from non-linear simulation packages [105]. Therefore, RFID tags are a very pervasive example of matching network-free rectennas which are often unnoticed, simply due to the fact that the antenna and the rectifier are designed in two different stages, by the tag and the IC designers, respectively, and that the rectifier is "concealed" in a commercially-available CMOS IC.

The same approach can be utilized to design a RFEH antenna to directly conjugate the rectifier's impedance. Dipole antennas, recently becoming a trend in complex-impedance RFID antennas [18], exhibit high impedance (resistance and reactance) near their resonant frequency. For example, [106] reports one of the earliest dipoles designed to match the resistance of the diode with a low-impedance load. However, only the resistance of the dipole is partially matched to the rectifier. A similar approach was reported when measuring the reception efficiency of polarization-independent arrays using a resistive load simulating the rectifier's real-impedance [107, 108], achieving an impedance bandwidth from 6 to 20 GHz with respect to the purely-resistive dummy load in [108].

Inductive dipoles [34, 109, 110] have been used to match the high capacitance of the rectifier at the band of interest. In a folded dipole antenna, the dual shorted lines (dipole-folds), act as an impedance transformer allowing the design of very high impedance antennas [109]. Alternatively, the offset feed, [34,83], is responsible for increasing the inductive reactance as well as the real impedance. Combining multiple offset dipole elements with imbalanced bow-tie radial stubs resulted in the dual-broadband high impedance of the antenna in [34], proposed for multi-band RFEH. Nevertheless, the efficiency of such a generic high-impedance rectenna will be lower than a specifically co-designed dipole for a single frequency and power level such as [111]. A hybrid filter-matching network structure has been incorporated in the antenna in [112] and a cross dipole array [113] represent the highest frequency direct antenna-rectifier matching rectenna (Ku band). Cross-dipole RFEH surface arrays have been also reported with a real impedance match [108, 114] or a complex impedance match to the rectifier [84]. Figure 2.7 shows some of the reported rectifier conjugate antennas.

Other antenna structures, such as dual-LP [77, 83] and CP patches [87] have also been used to directly conjugate the rectifier's impedance, providing higher gain compared to omni-directional dipoles. The off-center feed in [83] produces additional narrow-band

resonances allowing three bands of operation, as opposed to a standard single-band patch, using shorting vias. A rectenna array exhibiting only a real-impedance match has been previously presented for a simpler antenna design [48]. In more recent implementations, both dual-polarization metasurfaces, [115], and electrically-small loops, [116], were used to realize dual-band rectennas with no matching network. In both cases, the resonator was designed to achieve an input impedance conjugating the rectifiers' at the frequencies of interest.

2.4.5 Radiation Properties in RFEH and WPT

The power received is a direct function of the receiver and the transmitter gain (G_{RX}, G_{TX}). While the gain, on its own is often regarded as a FoM , it does not provide a complete picture on the anticipated reception of the rectenna, due to the gain's angular-dependence $G(\theta, \varphi)$ [117]. Furthermore, antenna properties such as main-lobe directivity and polarization directly impact the amount of power harvested from an incident wave. Antenna radiation properties are the key parameter where ambient RFEH and WPT can be distinguished. While in both applications the propagation medium may be unknown, and its impact on the received wave needs to be considered, knowledge of the transmitting antenna can be exploited. Table 2.2 identifies the key parameters reviewed in this section, and their applicability to RFEH and WPT, distinguishing where how the FoM changes with application.

Table 2.2: Key Radiation Properties in WPT and RFEH Rectennas

Parameter	Ambient RFEH	Dedicated WPT
Gain	Insignificant [53]	FoM
Beam-width	Wide (Omnidirectional)	FoM: Narrow, directional LoS
Polarization	Arbitrary: Dual LP/CP	Single-Pol, CP

2.4.5.1 Directivity and Gain

In most RFEH and WPT applications, it is assumed that the direction of the incident radiation is unknown by the harvester, with no LoS path. In this effort, multiple antenna designs and placements have been investigated to maximize the received power from an unknown source, independent of main-lobe alignment between the transmitter and the receiver.

Omni-directional rectennas have been widely presented in ambient RFEH rectennas [13,53]. In [13,30], the PSD has been reported to vary based on the antenna's orientation. Nevertheless, the variation in power has not been explained and hence it is impossible to identify if the change is due to the antenna's radiation pattern, or due to a polarization mismatch.

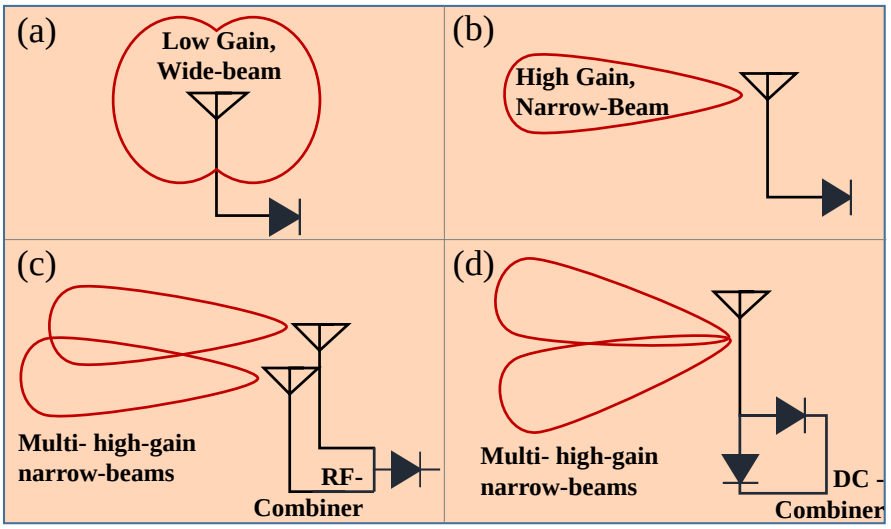

FIGURE 2.8: Rectenna topologies based on the antennas' radiation patterns. (a): Omni-directional antenna. (b): High-gain directional. (c): Multi- high-gain beam antenna with RF combining. (d): Multi- high-gain beam with DC combining.

High gain directional antennas and arrays have been widely-reported for microwave WPT and beaming [118], improving the harvesting efficiency from low RF power-densities and overcoming the propagation losses. Yagi-Uda rectenna arrays [26, 119], bow-tie array [120], a spiral array [68], tightly-coupled-Vivaldi array [121], a CPW CP array [122] and a wide-area patch array [48] were among the scalable rectenna implementations for maximizing the incident power density, where the area permits. Other approaches to improve the antenna's gain included Substrate-Integrated Waveguide (SIW) techniques at microwave and mmWave bands, specific to WPT [123–125]. However, high-gain rectennas are characterized by narrow-beam width, making receiving arbitrarily-directed waves inefficient. An investigation into the number of antenna elements and ports concluded that higher directivity does not correspond to higher harvested power in ambient RFEH assuming a 3D random incident field, this has been validated through field measurements in urban environment [53]. Based on [53], high gain arrays can be restricted to WPT applications.

In the effort of porting the benefits of higher gain antennas to arbitrary RFEH, packaging or layout solutions have been utilized to overcome directionality problems. A double-patch-antenna wrist-band was presented to harvest power from both directions, for ambient Wi-Fi RFEH [11]. Ambient cellular RFEH antennas have also been designed as 3D boxes [126], and printed or adhered to the walls of an enclosure [74, 127, 128], for reducing the system's area and enabling multi-direction harvesting. In [128], the cubic rectenna structure demonstrates higher energy-reception probability in ambient RFEH, due to the improved antenna diversity.

Improvements to antenna designs to increase the beam-width included auxiliary parasitic patch elements to improve the WPT of a 2.4 GHz 4×1 array [129]. A 6 GHz

Mesh-like antenna with multiple beaming-regions was also proposed demonstrating multiple beams for each port [130, 131]. Multi-port multi-rectifier surface rectennas and energy harvesting antennas of omni-directional radiation patterns have been presented for multi-direction and multi-polarization RFEH [84, 86, 107, 108]. Multi-rectifier with beamforming matrices [132, 133], and multi-port antenna arrays [131] have also been presented for high-gain, multi-direction energy harvesting. A comparison of RF-, DC-, and hybrid power combining from multiple antennas have been presented in [134]. At mmWave bands where more compact antennas are more feasible, large microstrip arrays were integrated with Rotman beamforming lenses to achieve wide angular-coverage and high-gain for rectennas and RFID transponders [135, 136].

In conclusion, although high-gain antennas are preferred to improve the harvested power from low RF densities, highly-directional receivers can be undesirable in applications with unknown transmitter direction, such as ambient RFEH or WPT through an unknown propagation channel. In this effort, multiple methods of multi-beaming were proposed for multi-direction high gain WPT and RFEH.

2.4.5.2 Antenna Polarization for Maximum RFEH and WPT Efficiency

Antenna polarization describes the motion of the field vectors referenced to the direction of propagation from the antenna. Polarization mismatch results in reduced transmission/reception between antennas even with main lobe direction alignment. For instance, no power is received if a vertically LP antenna is used for transmission, and a horizontally LP antenna is used for reception. In this section, reported approaches to maximize the wireless reception efficiency and avoid polarization mismatch losses are reviewed, in this regard, attention is paid to the antenna's ability to receive a wave (maintain higher gain) both through its primary and secondary polarizations, hence the FoM is the polarimetric gain, observed through the antenna's immunity to variation in the polarization angle of incidence, which can be quantitatively compared through the antenna's primary and secondary gains (e.g. left- and right-hand CP) being equally high. A summary of the proposed rectennas' architecture, in terms of polarization, is given in figure 2.9 with SoA examples compared in table B.2 in Appendix B.

In cellular communications, where linear-polarization alignment between the base-station and the mobile phone is very unlikely, base-station antennas have been designed to be dual-polarized [137, 138], or multi-polarized [139], avoiding polarization-mismatch losses when being received by a phone's LP antenna, regardless of its angle. However, variation in a LP wave's polarization due to multi-path effects remain an unresolved issue. Based on the assumption of multi-polarized mobile base-station and a highly-varying polarization at the rectenna, cellular RFEH antennas have been designed as LP antennas, as reported in most ambient RFEH literature [13, 53, 71, 80].

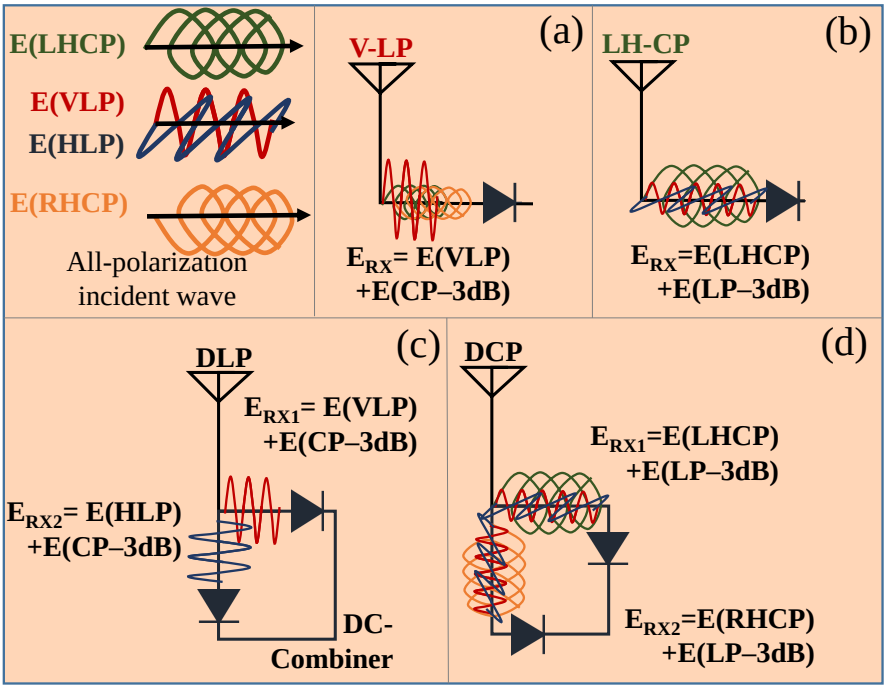

FIGURE 2.9: Rectenna topologies based on antenna polarization, showing the total received power by each antenna from an all-polarized incident wave: (a) single LP antenna; (b) single CP; (c) Dual LP; (d) Dual CP.

Circularly Polarised (CP) rectennas have been mainly proposed for WPT due to their relative immunity to being mispositioned [68, 76, 140]. CP antennas enable reception of CP radiation with the same direction of rotation (left- or right-hand-side CP) without power losses, in addition to all LP waves with a 3 dB loss (50% power loss) regardless of the polarization angle. Thus, multiple WPT rectennas employed CP antennas to achieve rotation-independence with a CP transmitter. CP rectennas have been reported for the 900 MHz, 2.4 [61, 141], and 5.8 GHz Industrial Scientific Medical (ISM)-bands [140, 142, 143] as well as for mmWave rectennas [76, 144]. CP antennas based on asymmetric geometry have been reported has been reported with wider-beam axial ratio to improve the immunity to mis-positioning in WPT applications [145] along with beam switching for improved angular coverage [133].

In RFEH from arbitrarily polarized waves, polarization-diversity represents a potential solution to polarization mismatch losses [126]. Dual LP rectennas have been demonstrated using imbalanced slotted radiating elements [141], as well as slotted ground planes [146] in proximity fed antennas; rotated feed slots are used to achieve dual LP. Cross dipoles have also been reported for dual-LP rectennas for RFEH [80] along with dual-port patches [83]. It is expected that with dual-LP, the antenna could receive a similar amount of power regardless of the polarization angle. For instance, a stable PCE has been achieved by a dual-LP patch while varying the polarization orientation by 360° [147]. The dual-port/dual-rectifier architecture has been widely reported in

ambient RFEH or random-polarization in LP rectennas WPT [59, 63, 83, 148] and CP rectennas [49, 61, 68, 144].

All-polarization, also-known-as multi-polarization, rectennas have been presented for entirely overcoming polarization mismatch losses, enabling the reception of CP and LP waves [85, 149], where the two dual polarization-orthogonal LP elements effectively harvest all LP and CP waves. To illustrate, the net vertical and horizontal voltages (V_V and V_H), (2.1), remain unchanged regardless of the polarization angle

$$P_{RX}(\varphi = 90^o) = \frac{V_V^2}{2Z_0} = P_{RX}(\varphi = 0^o) = \frac{V_H^2}{2Z_0}. \tag{2.1}$$

In (2.1) Z_0 is the antenna's characteristic impedance and φ is the angle of the receiving antenna on the polarization plane [149].

A right-hand E_{RHCP} and left-hand E_{LHCP} CP-wave follow in

$$E_{\text{LHCP}} = \frac{1}{\sqrt{2}}(E_x + jE_y), \tag{2.2}$$

$$E_{\text{RHCP}} = \frac{1}{\sqrt{2}}(E_x - jE_y), \tag{2.3}$$

for the right-hand ($RHCP$) and left-hand ($LHCP$) CP incident fields. where the power from each linear polarization is harvested twice (once by each element) resulting in full reception of the CP component [149], overcoming the 3 dB polarization mismatch loss. Finally, through DC-combining arbitrarily polarized incident waves can be harvested. The dual-port antenna in [150] achieves left- and right-hand CP and LP using a dual-mode SIW cavity. Orthogonal Dual-LP and DCP were both reported to achieve similar net harvested power regardless of the incident polarization after combining the power from both ports [85, 149]. Figure 2.10 shows the geometry of reported all-polarization rectennas, based on microstrip patches in Fig. 2.10-a and b, and using a metasurface and E/H-antennas in Fig. 2.10-c and d, respectively.

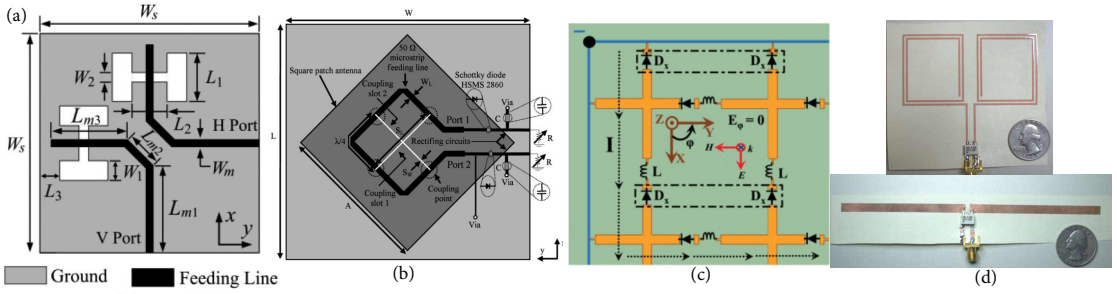

FIGURE 2.10: Polarization independent rectennas: (a) dual-LP slot (reproduced from [73], ©IEEE 2016); (b) dual-CP slot (reproduced from [61], ©IEEE 2011); (c) dual-LP cross-dipole array (reproduced from [84], ©IEEE 2019); (d) dual antennas for harvesting near field H- (top) and E- (bottom) fields (reproduced from [42], ©IEEE 2015).

Polarization independent surfaces have been presented using a cascaded cross-dipole rectenna array [84], meta-material surface rectenna [107], and receiving meta-material antennas with a dummy resistive-load [108, 114] or a microstrip-transformer connected to a 50 Ω RF power meter [151]. A frequency selective surface has also been used to harvest arbitrarily polarized waves [152]. Surface rectennas have been reported at a variety of frequencies and recently extended to dual-band energy harvesting at 2.4 and 5.8 GHz [115]. Using a complex-impedance dual-polarized surface combines the benefits of eliminating the matching network with those of dual-polarization RFEH, realizing a simple yet alignment-independent energy harvesters.

Dual dipoles have also been utilized to achieve all-polarization operation at UHF (0.75 - 0.95 GHz), receiving up to 13 dB higher RF power by using only 4-dipole elements compared to a single dipole rectenna [153]. Dual orthogonal slotting of the patch's ground plane has been reported for the aperture feed of dual LP rectennas [85, 149], harmonics rejection has also been achieved using the slotted feed in [85] omitting the need for an independent filter.

Where all-polarization is achieved using dual antenna feeds, the rectifier has been used to combine the incident arbitrarily-polarized wave with the two ports connected as a signal and ground to the voltage doubler or shunt diode [149, 154]. An alternative topology has been presented in [149, 153] where every output is rectified independently with DC combining. A modified charge pump has been presented in [148] to mitigate the effect of imbalance between the vertically and horizontally LP incident power.

To summarize, in WPT applications with a dedicated power source, CP is preferred due to the improved WPT efficiency regardless of antenna's polarization angle, but it can still be prone to variations in the polarization, from RHCP to LHCP or vice-versa, due to multi-path reflections. On the other hand, in multi-source harvesting, specifically from ambient sources, all-polarization antennas can achieve better overall reception and maximum portability; a multi-port/multi-rectifier architecture is required to combine the all-polarization power at RF or DC.

2.4.6 Antennas for RFEH and WPT: *Summary*

In the previous sections, recent advances in antenna design for RF energy harvesting and WPT are reviewed, presenting a standard categorization of RFEH and WPT antenna design, not presented previously in literature. The three fundamental antenna requirements for achieving high RF to DC efficiency have been identified as:

1. Antenna-rectifier impedance bandwidth at RFEH and WPT bands of interest.
2. Main-lobe alignment between the transmitter and receiver in WPT from a dedicated feed.

3. Polarization match between the rectenna and the incident wave, regardless of the angle and position.

Based on their impedance, rectennas have been classified into 50 Ω and rectifier-conjugate, rectennas, with emphasis on the impedance matching across different frequency bands and loads, along with the efficiency of each matching approach.

The radiation properties, from a directivity and polarization perspective, have been reviewed in state-of-art rectennas. Methods of improving the gain through beamforming and packaging to overcome the narrow beamwidth were reviewed. Finally, CP rectennas for WPT were reviewed along with various implementations to achieve polarization-independent reception both for WPT and RFEH.

2.5 Textile-Based Wearable Antennas and RFEH

2.5.1 Body-Centric Antennas and Propagation

A plethora of research has been carried out into textile-based antennas for wearable and body-centric communications [155]. Textile-based antennas have been proposed spanning the full EM spectrum and its applications from DTV [156] up to mmWave sensing and imaging [157]. Wearable antennas can be classified into three categories, off-body, on-body, and in-body, based on the position of the transceiver the wearable device is communicating with [155].

First of all, off-body, where the wearable antenna communicates with a device or a base-station off the body [158–162]. Off-body antennas typically have broadside radiation patterns to minimize interaction with the body. The second mode is on-body communications, where two antennas mounted on the same user communicate across the body [163–165], these antennas typically have omnidirectional radiation patterns with vertical polarization, or end-fire radiation patterns for point-to-point applications [164]. The final mode is in-body, where the wearable antenna communicates with an implant or is used for medical imaging [166].

Multiple wearable antenna designs, based on textile and non-textile materials, such as buttons and accessories, have been proposed for off-, on- and in-body applications. A ground plane or reflector backing is often implemented to direct the antenna's main beam away from the body for off-body applications. On the other hand, on-body/omnidirectional antennas often resemble monopoles and have omnidirectional radiation patterns [167]. As for in-body antennas, either omnidirectional radiation patterns or high gain beams directed into the body are used. For example, in [168] an off-/in-body antenna combines two patch elements, one facing off the body and the other facing into the body, with a ground plane in between.

To improve the versatility of the wearable antennas, making them suitable for different off-, on-, and in-body applications simultaneously, multi-mode antennas have been proposed. Multiple antennas have been developed using textile dual and multi-mode antennas [167–176]. This has been achieved using multi-port antennas [167, 173], single-port antennas with multiple radiating elements [168, 169] as well as antennas with multiple resonant modes for multi-band and multi-mode operation with reconfigurable elements [177].

A wearable rectenna is often perceived as an off-body antenna, where the power is received from a transmitter off the body. Despite the breadth in the textile-based rectenna implementations, textile rectennas have been mostly based on conventional antenna designs, namely the microstrip patch [11, 178–180], owing to its off-body radiation. Multi-mode antennas were not investigated thus far for RFEH. While recently an unshielded matching network-free rectenna was proposed in [181], based on a large-area array of bow-tie elements, its RFEH efficiency was low due to the broad bandwidth, resulting in reduced impedance matching quality, and due to absorption by the body. In addition, despite textile RFID antennas being previously reported, [182, 183], high-impedance textile antennas were only demonstrated with off-the-shelf RFID ICs and antenna rectifier co-design was not investigated for textile rectennas.

2.5.2 Wearable Antennas Fabrication and Textile Characterization

Wearable garment-integrated antennas have been presented both using textile substrates and conductors, using embroidery [182, 184], conductor-plated e-textiles used in Electro-Magnetic Compatibility (EMC)-shielding [11, 164], flexible copper foils and laminates [159, 185] as well as non-flexible or textile components such as buttons [186], logos [187, 188] and accessories, such as a RFEH necklace [189], potentially improving the radiation efficiency of the antenna and immunity to human-proximity effects. Additive manufacturing through conductor printing has been widely used to produce wearable antennas including inkjet printing [75, 190], screen-printing [191], and dispenser printing [192]. Although printing fulfills the accuracy requirements up to mmWave bands [75], when printed on fabrics, the surface resistance is constantly higher than the copper-plated or copper laminated antenna surfaces [190]. Recent advances in microwave smart textiles, as well as wearable circuits and systems were previously reviewed [193–195].

To design textile-based rectennas, knowledge of the textile substrate's relative permittivity (ϵ_r) and the dissipation factor ($\tan\delta$) is essential. Multiple methods have been presented in literature to characterize the dielectric characteristics of different materials [196], a summary of the most widely used methods can be found in [197, 198]. More recent studies investigated the application of such methods to textile substrates and proposed similar methods [11, 199]. The two line method, originally presented by Lee *et. al.* for broadband dielectric characterization [196], has been utilized in [200] to evaluate the

performance of transmission lines on textiles. [199] proposed an adaptation to the two-line method; overcoming the uncertainties introduced by the material inhomogeneity, at the coax-microstrip interface. [201] presented a simpler method of determining the real component of the relative permittivity, as $\Im\{\epsilon_r\}$ will not affect the frequency-tuning of the antenna.

2.5.3 Textile-Based Rectifiers and Rectennas

Following on the rich literature on textile-based antennas, multiple implementation of flexible and textile-based rectennas have been reported for wearable applications. As power in a wearable scenario will likely come from an off-body source, broadside microstrip patch antennas were the most common antenna design adopted in wearable rectennas [11, 178–180, 191]. While this improves the antenna's shielding from the body, rectennas were subsequently limited to textile substrates thicker than 1 mm, and having lowest possible tanδ, such as felt [11], to enable the microstrip patches to achieve a higher radiation efficiency [117].

In the earliest fully-textile rectenna implementations, a sub-1 GHz textile rectenna was demonstrated based on a proximity coupled rectifier [178]. The rectenna however, was only able to achieve a PCE between 40% and 50% for S>3 μW/cm^2. A 2.4 GHz CP rectenna was also realized using conductive fabrics for the antenna, and an FR4 board for the rectifier [180]. While the PCE and the DC output were not reported in [180], the rectenna was able to power an Micro-Controller Unit (MCU) at 1.7 m from a 29.1 dBm EIRP source, i.e. S≈2.2 μW/cm^2. Screen printing was later utilized in [191] to realize a dual-polarization rectenna, following on the realization of inkjet printed patch antennas on textiles in [190]. However, owing to the higher surface roughness of printed conductors compared to conductive fabrics, and the sub-0.5 mm thickness of the woven polyester substrate, the rectenna's radiation efficiency was 11%.

In [11], a "best-in-class" PCE was achieved in a wearable rectenna, surpassing all its counterparts at 2.4 GHz. Nevertheless, the rectifier in [11] was implemented on a low-loss Duroid substrate, and utilized fully-distributed matching which results in very low losses in the matching network. The rectifier was coupled to a wearable patch antenna using broadside coupling with a shared ground plane. Adami *et al.* concluded that the high PCE was only achievable due to the careful rectifier design using non-linear EM-Harmonic Balance (HB) co-optimization, implementing the matching network on a low-loss substrate, and the harmonics termination. Comparing Adami *et al.* microstrip antenna design in [191] and [11], the radiation efficiency exceeding 60% in [11] was achieved by using a 3.2 mm-thick felt substrate and highly conductive fabrics instead of screen-printed silver in their earlier implementation [191].

More recent implementations focused on utilizing the large area of textiles [179, 181]. A patch rectenna array was used for 2.4 GHz harvesting from a Wi-Fi source with an intermediate PA relay. In [181], a 2-5 GHz rectenna was demonstrated with no isolation from the body based on dual-polarized bow-tie antenna elements with individual rectifying diodes for each cell. [179] can be directly compared to the preceding work in [11], as both rectennas were based on the same diode (Skyworks SMS7630) and operate at the same frequency (2.4 GHz). While Vital *et al.* achieved a high peak PCE of 70% at 8 dBm using a fully-textile rectifier and a lumped inductor [179], the −20 dBm PCE was over 46% lower than that achieved by Adami *et al.* using the low-loss rigid rectifier. This further demonstrates that achieving a high PCE on textiles, at power levels below −10 dBm is increasingly challenging, due to the impedance matching network implementations being limited by the insertion losses in a textile transmission line.

2.6 RF to DC Power Conversion Techniques

In the previous section, methods of harvesting RF energy from EM-waves and delivering it to a power-conversion-circuit have been discussed. This section reviews the power conversion techniques utilized to maximize the PCE through rectifier design.

2.6.1 Schottky Diode Rectifiers

Schottky diodes have been used for RF voltage detectors in wireless receivers. Schottky diodes have been integrated in standard CMOS processes for improved integration with mixed-signal CMOS RFIC [202, 203], commercially-available discrete Schottky diodes have been widely-used in rectennas [7, 17]. At low power levels, a Schottky diode's PCE is limited by its junction potential, due to the low voltage of the RF input. As the RF power, and subsequently voltage, increases, the potential approaches the diode's break-down voltage which limits the high-power PCE [204]. The PCE of hypothetical diodes was analytically calculated in [17] (using the methods in [204]) for varying diode parameters.

When selecting or designing a Schottky-based rectifier for RFEH, low series resistance and junction capacitance are the key characteristics in a RF Schottky diode. To explain, the cut-off frequency is defined in this work as the frequency where the resistance and the reactance of the diode are equal. This can be calculated using the diode's total capacitance C_T and the series resistance R_S (2.4) [205, 206] using

$$f_{cut-off} = \frac{1}{2\pi R_S C_T}. \tag{2.4}$$

While in [206] only the junction capacitance is considered due to the devices being measured on-wafer, when the diodes are packaged the total (junction+packaging) capacitance needs to be considered.

2.6.2 Rectifier Architecture

The topology of the power conversion circuit, the rectifier, varies significantly based on multiple factors such as the diode technology and the target-power levels. A comparative analysis of different rectifiers is in [17], and a discussion of different topologies is in [21].

A single series diode rectifier (half-wave rectifier) has been widely reported in multiple ambient and low power rectennas [11, 13, 33, 42, 43, 62, 77, 80] as well as mmWave rectennas [75, 76]. Single shunt-diode rectennas have also been reported with increasing popularity among dipole rectennas [34, 106, 131]. The main motivation behind single-diode rectifiers' is minimizing the power lost as V_d, which contributes significantly to PCE at approximately $P_{RF} < -10$ dBm. At higher power levels, the break-down voltage V_{Br} of the diode reduces the PCE due to the maximum achievable voltage output of the rectifier.

Voltage multipliers have been widely used in studies presenting an integrated system (up to the load) due to the ease of directly using the output voltage of the rectifier to power standard electronics; overcoming the low voltage output [29, 92] [26, 59, 74, 78, 82, 83]. A mmWave dual-frequency harmonic recycling voltage doubler has been presented in [207] demonstrating 12% PCE improvement, compared to a conventional voltage doubler without harmonic recycling.

2.6.3 CMOS Rectifiers

Fully-integrated rectifiers in digital and mixed-signal CMOS processes have attracted significant interest. A number of studies have presented custom CMOS implementations for RFEH, where either the rectifier and matching network, or the full system where integrated in the same IC [88, 208].

A Dickson voltage multiplier [209], is a commonly selected rectifier architecture in CMOS RFEH implementations. Either with a fixed number of stages [89, 210, 211], or reconfigurable through changing the number of stages [88], or through adjusting the threshold voltage of the individual transistors forming the rectifier [208].

Alternative CMOS processes such as Silicon-on-Sapphire (SoS) have been previously used to demonstrate RFEH rectifiers of high efficiency at RF power levels lower than -20 dBm; through minimizing V_{TH} [212]. Where efficiencies of up to 30% at power levels as low as -40 dBm have been achieved by a rectifier of a near-zero V_{TH} [212].

In studies involving transceiver design, the incoming RF signal has to be directed not only to the rectifier but also to the transceiver, either for down-link communication in SWIPT applications [211], or for clock or carrier generation [208, 211].

A reconfigurable rectifier, with an integrated on-chip LC matching network, has been presented by Abouzied *et al.* [88]. The second order LC matching network contains two capacitors which can be digitally tuned to match the antenna's impedance to the rectifier. An N-stage rectifier (N: Number of stages) is proposed, with the output voltage proportional to N, and is dynamically reconfigurable based on the available RF power level. A boosting rectifier dynamically matches the impedance of the rectenna to the load based on the available RF power (Maximum Power Point Tracking (MPPT)). Xia *et. al.* presented a rectifier with a reconfigurable threshold voltage, based on the runtime power conversion efficiency [208]. A sub-threshold 50-stage rectifier, using low-threshold transistor achieves a -32 dBm 1V sensitivity with 155 ms charging time of 1 nF capacitor [213]. Reconfigurability has been investigated in changing the transistor connections, at run-time, to control the voltage threshold of the devices [214]. This enables a significantly improved dynamic range compared to static cross-coupled rectifier (with a fixed threshold cancellation scheme); the rectifier proposed by Almansouri *et al.* was able to reach a PCE over 40% down to -35 dBm (when excluding mismatch), such performance was only achievable using custom devices such as the tunnel diode in [215].

2.6.4 Custom Rectifiers

Custom diodes have been presented for high-frequency rectification, for detection as well as power conversion, towards low-cost implementation on unusual materials, or improved performance. For example, a spintronic diode has been presented demonstrating 26 μV higher Zero-bias responsivity compared to the high-sensitivity Schottky Skyworks SMS7630 [216]. Furthermore, the spin-diode demonstrates 10% PCE compared to the SMS7630's 1% at 30 GHz at P_{RF}=30 μW. This is attributed to the ultra-low capacitance and resistance of the spin-diode of 10 fF and 1 Ω respectively compared to the SMS7530's 90 fF and 20 Ω.

At 28 GHz, a detector rectenna based on a Graphene diode achieves approximately 1% PCE at P_{RF}=500 μW after integration with a 2×2 patch array [217]. A backward tunnel heterojunction diode achieves 5.5 times improvement in efficiency over the SMS7630 with PCE=18.2% at $P_{RF}=-30$ dBm [215]. Fully-flexible rectennas based on flexible diodes have been recently presented. CPW devices fabricated on low-cost flexible substrates have been fabricated on silicon and organic materials for HF applications [205]. A fully-flexible rectenna has been recently presented based on a 2D Metal-Oxide Semiconductor $(MOS)_2$ diode achieving up to 40% PCE at P_{RF}=5 dBm at 2.4 GHz [218].

2.7 Rectenna Integration

2.7.1 Simulation and Modeling

3D and 2.5D EM simulation have been used to design the antennas and the microstrip matching networks [11] and to model the RF power source [42]. HB simulation, considers the steady-state solution of a non-linear active circuit which cannot be simulated using transient Simulation Program with Integrated Circuit Emphasis (SPICE) [219]. Due to the fact that harmonic balance simulation enables large-signal modeling of active circuits, reported rectenna simulations relied entirely on HB using commercial EDA tools (namely Keysight ADS) [11,33,41,207,220], enabling simultaneous simulation of the rectifier and the distributed matching networks.

Analytical estimation of the diode's impedance using Ohm's law, from the DC IV relation is possible using the diode's current. The approach has been cross-validated using harmonic balance simulation and measurement [154]. Analytical models of a Schottky diode were used to fully model and predict a rectenna's performance [221]. Simplified methods, based on co-simulation of the transistor-rectifier circuit and the matching network [222]. A similar approach has been outlined for iterative optimization of the rectenna in full-wave EM simulation utilizing the diode's impedance as a port impedance, establishing an accurate simulation of the rectenna's bandwidth, from a similar perspective to the proposed in section 2.4.2 [223]. A numerical model, for optimizing the load impedance and smoothing capacitor has been presented based on a commercial Schottky diode (HSMS286c) at different ambient RFEH frequencies, with an eliminated-matching network [77].

2.7.2 Testing and Evaluation Methods

Power-calibrated signal generators are the most commonly used instrument to quantify the PCE of the rectifiers, after measuring 50-Ohm rectifier's bandwidth using a VNA at the power levels of interest [11]. Rectennas mismatched to 50-Ohm (directly matched to the rectifier) have been tested in an anechoic chamber, using a reference antenna as a power source and a propagation-model to quantify the amount of power incident at the rectenna [84], or in an indoor environment using the calculated received power [224].

Different methods of expressing the efficiency of rectennas and WPT systems have been proposed based on traditional antenna parameters were presented. A 3D voltage-pattern measurement was presented in [225], providing the rectenna's DC output in a format similar to antenna radiation patterns. Measuring the 3D voltage pattern has demonstrated that a rectifier can alter the radiation patterns of the rectenna. A similar testing approach has been reported in [68] plotting a radar-plot of the DC power as a function of the incident wave's angle. The two-port network approach in [226] enables

prediction of the end-to-end WPT efficiency in the same format as non-radiative coupled systems. A similar two-port approach was followed in [42] when harvesting power from a near-field 433 MHz license-free walkie-talkie. In [45], a number of incident waveforms has been compared to present an waveform optimized for WPT.

2.7.3 High-Efficiency Low-Power Rectennas

Combining low-V_F diodes, optimized input impedance matching or antenna-rectifier co-design, and an optimal load impedance (DC current draw), multiple rectennas have been reported achieving high PCE from ultra-low power densities. Antenna rectifier co-design was used in [111], where the rectifier was designed to achieve the a high $\Im\{Z_{\text{in}}\}$ to $\Re\{Z_{\text{in}}\}$ ratio, and matched using a high-Z loop antenna. The same antenna was utilized in [89] to match a CMOS cross-coupled rectifier, showing the versatility of antenna-rectifier co-design, and its suitability for both discrete and integrated rectifiers. In [227] a 6-stage cross-coupled CMOS rectifier, was matched to small loop antenna achieving a 3 V DC output from -22 dBm with a high-impedance load. Nevertheless, the high-PCE dynamic range of the rectifier will be very limited due to the reverse leakage in a cross-coupled rectifier [214].

As discussed and implemented in [11], presenting the rectifier with Z_{in} which results in a maximum PCE could be achieved using either a co-design antenna with a complex impedance, or using a low-loss matching network. One of the highest reported PCEs, using lumped components, was achieved using a co-designed stripline dipole backed by a large reflector was reported in [228] at 2.45 GHz with over 50% at S=0.22 μW/cm^2, and a peak PCE of 83%. Likewise, at 868 MHz, the highest PCE in prior art was achieved using a co-designed dipole [111]. Therefore, while theoretically both a matching network and a co-designed rectenna can achieve the same PCE, matching network-free rectennas are more suited to low-power applications due to having lower parasitics, and reducing the overall system losses.

For ambient RFEH a range of energy harvesters was presented using multi-port rectennas [53,71,229]. The output of such systems is substantially higher than a single rectenna element, owing to combining the DC output of multiple rectenna elements [53], and in some implementations a combination of RF-combining and DC combining, to increase the RF power available at a rectifier's input.

2.8 mmWaves for RFEH and WPT

The broad spectrum at mmWave bands has attracted significant interest for a breadth of applications, with 5G communications being the main commercial drive for mmWave

networks [230,231], motivating research in broadband high-gain antenna design [232], antenna arrays, and beam-forming techniques [230]. Emerging applications such as gesture detection [233], and high-speed Body Area Networks (BAN) [159], have also been investigated at the 60 GHz license-free bands. While mmWave communications have not yet made it to full commercial deployment, efforts to realize mmWave rectennas have been motivated by the small micro-cells size and high EIRP limits [234]. Moreover, numerical analysis of an RFEH network at 28 GHz has shown that the end-to-end efficiency of the network surpasses sub-6 GHz networks, due to the improved energy coverage [235].

In this section, recent advances enabling mmWave WPT and RF-powered networks are reviewed. mmWave-specific rectification challenges are identified and emerging platforms for mmWave rectennas, from fully-integrated CMOS to flexible printed mmWave rectennas, are reviewed. Although the term mmWave means the frequency spectrum from 30-300 GHz, where the wavelength is between 10 and 1 mm, 5G and license-free bands between 20 and 30 GHz are commonly referred to as mmWave bands. As a result, the term mmWave bands will be used in this thesis to describe rectennas and antennas operating above 20 GHz.

2.8.1 mmWave Space Power Beaming

W. C. Brown's earliest drone-powering rectennas operated at microwave bands below 10 GHz [3]. The additional atmospheric attenuation of mmWave signals due to air and water vapor was considered a major hindrance to mmWave WPT. Yoo and Chang were motivated by the miniaturization potential at mmWave to realize a rectenna operating at 35 GHz for space WPT applications [204, 236]. In space, mmWave signals will not be attenuated and hence high end-to-end efficiencies can be maintained with more compact transmitting arrays and rectennas. They developed a theoretical framework with numerical and experimental validation comparing the rectifier design process at 10 and 35 GHz [204]. Their theoretical analysis is used in Chapter 3.2.2-A to evaluate commercially-available diodes up to 100 GHz.

Although the 35 GHz rectenna in [204] achieved a 39% PCE, the maximum theoretical PCE of the rectenna is calculated to be 60%, if the antenna was matched to the rectifier's impedance to minimize the reflection. Therefore, it can be concluded that mmWave rectennas can be designed without an ideal impedance matching stage while still maintaining performance. The diode's cut-off frequency was calculated to be 155 GHz based on the parameters utilized in the simulation [204]. Therefore, harmonics propagation to the output could be ignored at 35 GHz. Hence the relatively-high 39% PCE can be achieved without stand-alone harmonic termination.

Rectenna development at mmWave bands was focused on presenting diodes of high breakdown voltage V_{Br}, to enable efficient reception of high power densities [16]. As with

[204], Koert and Cha discussed the miniaturization potential of 35 and 94 GHz rectenna arrays for space applications, making higher gain antennas more realistic at mmWave compared to sub-6 GHz bands. They then developed rectennas in GaAs processes with fringed diodes with higher V_{Br}. Koert *et al.* developed rectennas operating at 35 and 94 GHz [237]; 35 GHz is the frequency where the atmospheric attenuation reduces from the peak reached around 28 GHz, due to absorption by water-vapour. At 94 GHz, the rise in absorption at 60 GHz, due to oxygen, reduces to its lowest point above 50 GHz. The work by Koert and Cha was developed at an industrial lab (ARCO Power Technologies) which later became part of E-Systems and acquired by Raytheon Company, where the earliest WPT systems were developed [3].

Following the feasibility studies showing the ability to realize rectennas beyond 30 GHz for mmWave WPT, the diode design was identified as a key challenge facing the development of mmWave rectennas [16]. The conclusion drawn about hybrid rectennas, i.e. a GaAs RFIC diode mounted on a printed circuit as opposed to a fully-integrated diode, is that hybrid rectennas are better suited for applications around 35 GHz. Beyond 94 GHz, a fully-integrated rectenna is essential. While the diode's junction would not be different in a fully-integrated rectenna, this shows that the critical bottle-neck to the rectenna is the parasitic capacitance introduced by the transition from a printed circuit to a GaAs die. The issue of estimating and factoring in the diode's packaging parasitics was revisited in more recent rectenna designs [75, 76, 238]. Parasitic capacitance of packaged devices is also more widely regarded as a challenge in mmWave components such as PAs [239].

As interest in mmWave power harvesting has re-emerged for IoT applications [235,240], it is essential to reflect upon the developments in high-power space WPT. The main difference between the work in [16, 236, 241], and practical commercial deployment of mmWave rectennas is the power densities. The high PCE, which approaches 90% in [204], requires a high mmWave power input, exceeding 10 mW/cm^2. While such an energy density is plausible in power beaming in space, it is highly impractical for WPT to IoT devices in a dense urban environment due to the limits on the EIRP. Thus, efficient rectification at mW and sub-mW power levels is essential to realize a mmWave-powered IoT.

2.8.2 The Rectenna at mmWave

A rectenna at mmWave bands, where diodes approach their cut-off frequencies and packaging and layout parasitics cannot be ignored, requires careful harmonic termination, which plays a dominant role in determining the rectenna's performance. Fig. 2.11 shows the structure of typical UHF and microwave rectenna compared to mmWave rectennas.

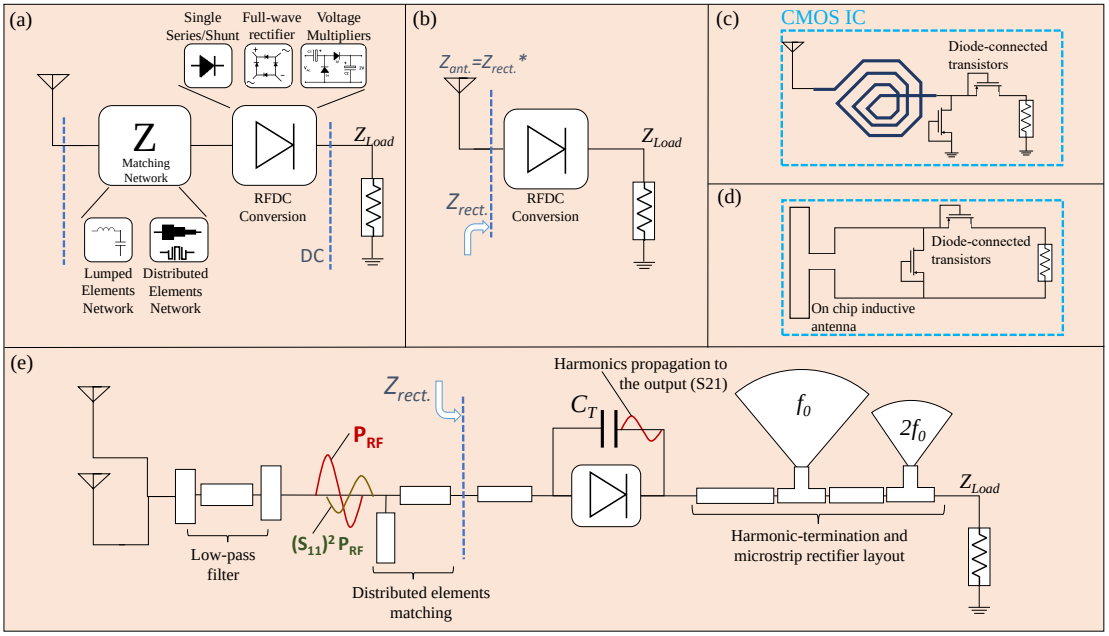

FIGURE 2.11: The typical sub-6 GHz rectennas topologies contrasted to mmWave rectennas: (a) sub-6 GHz rectenna with a 50 Ω antenna and a matching network, (b) sub-6 GHz rectenna with antenna-rectifier co-design, (c) mmWave fully-integrated rectenna with on-chip matching, (d) fully-integrated mmWave rectenna with no standalone matching stage (e) Schottky-based mmWave rectenna, showing the rectifier's parasitic capacitance and the harmonic-termination microstrip stubs at the output.

The mmWave rectenna, in Fig. 2.11-e, requires additional components to prevent the high frequency harmonics from propagating to the output. The diodes' non-linearities are more evident and can result in significant power being generated at higher harmonics, which, if not terminated properly, can adversely lower the DC output [207]. In addition, the rectifier design, simulation and matching stages are more uncertain and discrepancies between the datasheet and real-world performance need to be tackled. Fig. 2.11-e shows the additional components of a mmWave rectenna such as filters and harmonic termination, often not seen in sub-6 GHz rectennas, as well as the main challenge, the integration of the antenna and the rectifier at the $Z_{Rect.}$ plane.

The rectifier/antenna interface ($Z_{Rect.}$ plane in Fig. 2.11-e) is the main source of uncertainty. mmWave rectenna design can involve multiple design iterations to experimentally characterize the rectifier's impedance and diode parameters [76]. It is also not uncommon to see additional prolonged antenna or rectifier feed-lines [159, 242], modified designs post-fabrication [243], as well as a generally higher discrepancy margin between simulation and measurements [238, 244]. The antenna and rectifier design are commonly treated as separate matters and are reviewed separately in Sections 2.8.3 and 2.8.4.

Fully-integrated rectennas at mmWave bands, motivated by the miniaturization of the antenna, follow a different architecture. Given the sub-mm scale of CMOS IC, the parasitics of the entire system are significantly lower and hence harmonic termination and layout consideration are not of great significance as in discretes. On-chip antennas are

also different in their design requirements where balanced antennas are more common compared to discrete rectennas. Furthermore, more attention is given to circuit-level simulation to extract the rectifier's input impedance compared to discrete rectennas, where it is not possible to prototype and measure the rectifier separately. Integrated antenna design for mmWave rectennas is reviewed in Section 2.8.4.2.

2.8.3 Antenna Design for mmWave Rectennas

To counter the high propagation losses and the additional atmospheric attenuation, mmWave rectennas rely on high gain antennas to maximize the harvested power. A variety of antenna design and fabrication methods have been reported in literature, from wave-guide, to PCB, and fully-integrated antennas in CMOS processes. In this section, recent trends and advances in antenna design for mmWave rectennas are reviewed. Section 2.8.5 is dedicated to additively-manufactured antennas and rectennas on low-cost substrate, where they are reviewed from a holistic rectenna perspective rather than being purely focused on the antenna design. A comparison of the antennas reported for mmWave rectennas is presented in Tables B.3 and B.4 in Appendix B.

2.8.3.1 Antennas and Arrays in mmWave Rectennas

High gain antennas have historically been developed using waveguide components and horn antennas, due to their power handling capabilities and low losses [245]. mmWave rectennas have been developed based on waveguide antennas [243], or with a waveguide-to-microstrip interface for integration with waveguide components [246]. Such rectennas will have the highest gain ($>$ 15 dB) and can be demonstrated with linear, [246], or circular polarization [243], which may be preferred in directional WPT applications.

Nevertheless, waveguide components are 3-dimensional and more expensive compared to planar antennas. Arrays are the most common method to improve the directivity of microstrip antennas [247]. The majority of PCB antennas reported are based on arrays with at least two elements [234], and as many as 4×4 elements [220, 248]. However, wireless communication antennas, e.g. [232], have been reported with higher gain than some of the reported arrays for mmWave rectennas [75]. While patch antennas have the advantage of not requiring vias, a via may still be required at the rectifier stage. Although microstrip patch antennas can achieve high gain and radiation efficiency on low-loss substrates, they are inherently narrow-band, especially on thinner substrates [76, 117]. An advantage of planar microstrip antennas is that they can be realized on a variety of unconventional substrates using printing and photolithography [10]. mmWave harvesting antennas implemented on lossy substrates and using additive manufacturing are reviewed in detail in Section 2.8.5.

SIW transmission lines have significantly advanced the development of planar antennas at mmWave bands. SIW antennas benefit from suppressed surface waves which improves the antenna elements' isolation, and subsequently the radiation properties [76, 249]. A 4×4 rectenna array was proposed in [220] based on the SIW slot array detailed in [250]. To interface the SIW with the microstrip rectifier in [76], a SIW-microstrip transition was developed. The length of the tapered transition microstrip line is 16.7 mm (1.33λ) highlighting that a standard SIW transition can significantly increase the area of a mmWave rectenna. To reduce the size of SIW rectennas, a 24 GHz rectenna was realized in a 15×22.9 mm^2 area based on a rectifier integrated inside the SIW cavity [251]. A vertically-stacked double-element rectenna based on two 10 dBi 35 GHz SIW Vivaldi antennas with microstrip rectifiers was proposed in [252].

While SIW rectennas have only been implemented on low-loss high-frequency substrates [76, 220, 251, 252], SIWs have previously been demonstrated on unusual substrates. For wearables, SIWs based on conductive threads are used to realize low-loss high-isolation SIW antennas and transmission lines for wearable applications [253]. Rigid threads woven into fabrics have been used to demonstrate transmission lines up to 37 GHz [254], the proposed textile waveguide to standard waveguide transition allows the development of mmWave rectennas based on SIW textile antennas integrated with microstrip components such as rectifiers.

2.8.3.2 Fully-Integrated mmWave EH Antennas

At mmWave bands, the miniaturization of antennas enables their integration in standard CMOS processes or semiconductor packages with the associated communication [255], or in this case energy harvesting, circuitry. Multiple on-chip antennas have been proposed for mmWave rectennas and mmWave-ID [256–260]. Fig. 2.14 shows the micrographs of reported on-chip antennas for power harvesting in the 24 to 94 GHz spectrum.

Folded dipole antennas were used for 24 GHz fully-integrated rectennas for RFID applications [256, 258]. With a length of 1.6 and 3.7 mm for [258] and [256], the dipoles achieve a gain of −8.7 and −1 dB, respectively. As [256] uses the 60 GHz band for up-link, a $\lambda/2$ dipole was integrated on the same chip for communications at 60 GHz. In CMOS, differential balanced antennas such as dipoles are generally preferred to single-ended ones, dipoles can connect to differential circuits eliminating baluns [255]. Such implementations enable fully-integrated pad-less radio transceivers, which do not require any external components to function. To account for the multi-antenna integration in [256], the positioning of the 60 GHz antenna and the energy storage capacitors (shown in Fig. 2.12-a) was optimized to prevent mutual coupling with the 24 GHz dipole. The 24 GHz dipole had a simulated impedance of 60 Ω and a radiation efficiency approaching 30% [256].

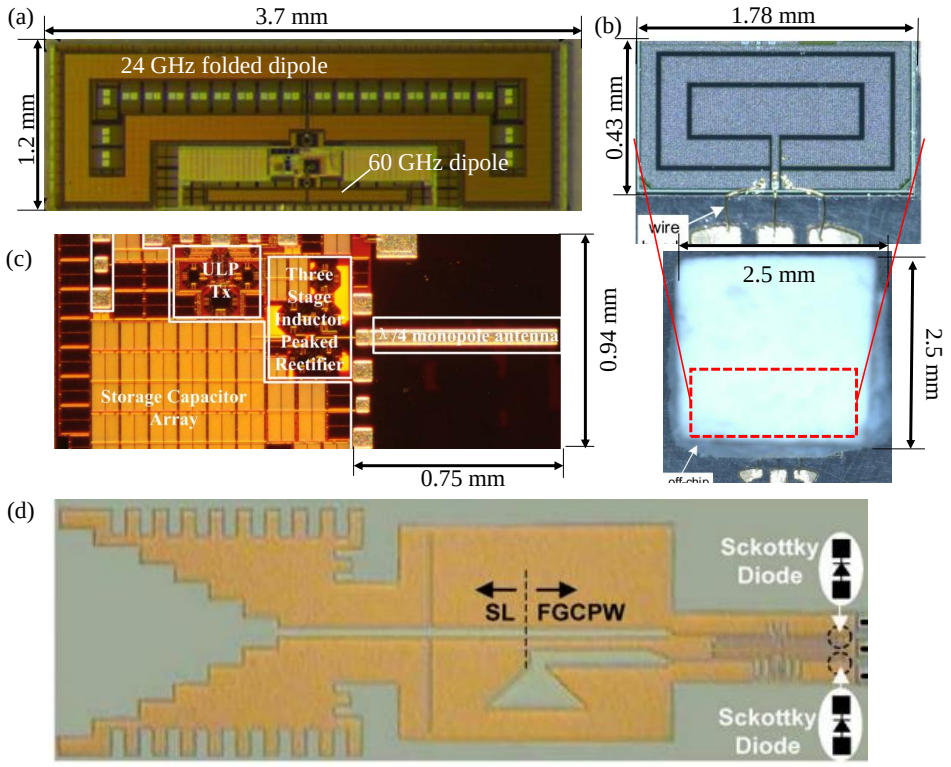

FIGURE 2.12: Micrographs of the on-chip energy harvesting and mm-ID antennas: (a) 24 GHz folded dipole rectenna and 60 GHz $\lambda/2$ communications dipole, (reproduced from [256], ©IEEE 2015), (b) 71 GHz $\lambda/4$ monopole rectenna with inductor matching, (reproduced from [259], ©IEEE 2013), (c) 24/40 GHz slot with off-chip dielectric resonator, (reproduced from [257], ©IEEE 2017), (d) 35/94 GHz (2.9 mm^2) rectenna, (reproduced from [261], ©IEEE 2010).

A similar design was presented in [259] with an on-chip 71 GHz $\lambda/4$ monopole. The antenna was directly connected to a single-ended inductive-matched rectifier, as shown in Fig. 2.12-c. Although the gain was not reported, it is expected that the antenna's gain approaches 0 dB as with [256], as the monopole is $\lambda/4$ in length. A comparison of CMOS mmWave power harvesting antennas [256,258,259] was presented in [240] concluding that the Q-factor of the matching component is equally significant to the antenna's dimensions when evaluating the performance, in terms of received DC power, of mm-sized far-field power receivers.

2.8.3.3 Beamforming and Phased Arrays for mmWave EH

In 5G and mmWave communications, phased arrays are employed to steer the main beam of the receiving antenna. Phased array transceivers have been proposed with low power consumption down to 10s of mW for active reception [262]. Such power overhead is mainly due to the amplifiers in the system but also due to the tunable phase-shifters. In a mmWave rectenna aimed at high-power applications, such overhead for phased-array tuning could be accommodated without significantly reducing the net DC output.

However, for low-power harvesting systems, complex active array tuning circuits are not feasible and hence mmWave rectennas did not employ phased arrays.

In [263], a method of employing a rectenna to tune a phased antenna array was proposed at 60 GHz. Although the rectifier's performance is not discussed in details, the radiation patterns of the retro-directive array can be reconfigured successfully from a mmWave incident power density of 0.013 mW/cm^2, providing a bias voltage of 5 V and allowing the local oscillator to produce 5 dBm of power. Such efforts could be combined with more recent low-power phased-array controllers to realize a steerable phased array rectenna for long-range high-power mmWave WPT.

Beamforming on the other hand allows quasi-omnidirectional energy harvesting using high gain antenna arrays and a Multi-In Multi-Out (MIMO) beamforming network [135]. Beamforming techniques were used for sub-6 GHz energy harvesting based on full RF combining with a butler matrix and 1×4 patch antenna arrays at 2.4 GHz [132]. Low-loss coaxial cables are used to connect the 3D cylindrical patch array to the butler matrix which connects directly to the rectifiers [132]. The system in [132] achieves wide angular coverage with four main beams each having over 6 dB higher gain compared to dipoles. Nevertheless, the structure is very complex and requires low-loss interconnects as well as occupying a large volume ($290\times130^2\pi$ mm^3). At mmWave bands, implementing such large area arrays is straightforward on planar flexible substrates [135, 136]. Therefore, beamforming networks can enable long-range wide-beamwidth energy harvesters beyond 24 GHz.

2.8.4 Diodes and Rectification for mmWave EH

2.8.4.1 Schottky Diodes at mmWave Bands

A rectifier's PCE is limited by the forward bias threshold voltage V_F at lower power levels, and by the breakdown voltage V_{Br} at higher power levels. An additional loss is incurred due to the harmonics generated due to the non-linearity of the diode [204]. At mmWave frequencies, the fundamental-tone and harmonics propagation to the output becomes the major limiting factor to the PCE, due to approaching the cut-off frequency of the diode. It was found that a significant proportion of the input power (66%) can exist at the first and second harmonics at the output of the rectifier, with only 32% of the output power being DC [207]. Most commercially-available silicon (Si) Schottky diodes have a junction cut-off frequency around 20 GHz, which can be adversely reduced by the packaging and mounting parasitics. Therefore, Gallium Arsenide (GaAs) diodes, capable of switching beyond 100 GHz, are typically chosen for rectennas beyond 20 GHz.

Other than commercially-available Schottky diodes, multiple diodes have been proposed in literature showing potential for efficient rectification at mmWave bands. In [215],

although the low-barrier tunnel diode was demonstrated at 2.4 GHz with the highest low-power (sub −30 dBm) PCE surpassing commercially-available diodes, measurements show that the diode can be used for efficient rectification beyond 40 GHz. From the VNA impedance measurements at −30 dBm, the diode maintains a predominantly reactive impedance showing the potential for mmWave rectification. In [217], a self-switching graphene diode was proposed and integrated with a 2×2 patch antenna array on a silicon/silicon-dioxide substrate. For a 50 Ω probe-feed, the diode has a voltage sensitivity (responsivity) of 7.04 V/W at 28 GHz from a 1.22 mW input [217]. In [264], a Mott diode was used in a 93 GHz rectenna, showing over 5× PCE improvement over the Microsemi MS8151 GaAs diode. However, the commercial diode in comparison does have a very high V_F which will result in the lowest PCE compared to other GaAs diodes such as the Macom MA4E and the Virginia Diodes ZBD.

2.8.4.2 Fully-Integrated mmWave Rectifiers

CMOS rectifiers have been widely used for fully-integrated on-chip RF-DC conversion at sub-6 GHz and mmWave bands. The high $f_{\text{cut-off}}$ of CMOS diode-connected transistors enables efficient rectification at mmWave bands. Furthermore, the fully-integrated nature of the devices implies no influence from the packaging parasitics, which were previously shown to significantly reduce $f_{\text{cut-off}}$ of Schottky diodes [75]. However, such parasitics will still exist once a CMOS rectifier is integrated with a PCB antenna. On the other hand, multiple CMOS mmWave rectifiers were reported with power-sensitivity (on-wafer) below 0 dBm [256,260], which is not typically achieved by discrete Schottky-based rectifiers.

As reviewed in Section 2.8.3.2, multiple antennas have been proposed in CMOS processes to enable improved integration of mmWave rectifiers. For example, at 24 GHz a folded dipole antenna was directly connected to the CMOS rectifier in [256] without separate impedance matching. At 62 GHz [265], and 71 GHz [259], Gao *et al.* proposed an inductor-peaked rectifier for threshold voltage cancellation. The series inductor connecting the gate of the diode-connected transistor was used to resonate with the transistor's capacitance. A series inductor was also used to match the rectifier showing a $S_{11}<-20$ dB bandwidth from 54 GHz to over 64 GHz. The design of fully-integrated CMOS mmWave-powered systems is described in detail in [266]. Another topology used for rectification at 60 GHz is a cross-coupled rectifier [260]. The flip-chip CMOS rectifier was connected to a grid array antenna-on-package with a transformer balun resulting in a predominately real rectifier impedance, which results in resonance at the operation frequency.

Realizing rectifiers in standard digital CMOS processes allows large-scale and low-cost production of high-efficiency rectifiers operating above 60 GHz. In addition, the 60 GHz power amplifier, with 24.6 dBm output, demonstrated by [260] as part of a complete WPT system shows that complete mmWave WPT can be realized in standard digital

CMOS as well as integrated with off-chip compact antennas. As opposed to Schottky-based rectennas (Fig. 2.11), discussed in the next section, a harmonic termination or low pass filtering stage was not required to realize high-efficiency rectifiers, due to the high level of integration, high $f_{\text{cut-off}}$ and overall compactness. Table B.5 in Appendix B compares the recent mmWave CMOS rectifiers.

2.8.4.3 Design and Matching of mmWave Rectifiers

To achieve high PCE, it is essential to match the impedance of the generator (i.e. the antenna) to the rectifier's input impedance at the frequency, load current, and power level of interest. At UHF and microwave, this could be achieved using antenna rectifier co-design or impedance transformers [15]. As shown in Fig. 2.11, Schottky-based mmWave rectennas often have a standalone impedance matching stage, and the antenna or array are matched to 50 Ω characteristic impedance. The key challenge in matching rectennas at mmWave bands is obtaining an accurate estimate of the diode's parameters, especially the packaging parasitics. Such knowledge will enable the use of commercial simulation software and non-linear circuit analysis methods such as HB to evaluate the optimum $Z_{rect.}$ at the rectifier's transition plane. The transition plane, shown in Fig. 2.11, marks the transformation of the 50 Ω antenna impedance to the rectifier's. Furthermore, the rectifier design will include additional stages when designing the "DC" side of the circuit to properly terminate the harmonics and prevent PCE degradation. The layout of the circuit beyond the diode will still significantly impact the input impedance and the propagation of harmonics to the output.

The theoretical analysis provided by Yoo and Chang's mmWave rectenna can be used to evaluate the input impedance of shunt diodes using closed form equations [204]. At 10 GHz, the theoretical calculations have shown a good agreement (<10% discrepancy) between the calculations and Method of Moments (MoM) simulations. However, at 35 GHz the discrepancies increase to approximately 50%. The MoM simulations showed a close agreement with the measurements for a 400 Ω load but not for a 100 Ω load. This demonstrates that the higher-current diode parameters were not characterized as accurately as the low-current ones. Yoo and Chang attributed the discrepancies and the lower efficiency at 35 GHz to impedance mismatch. As the S_{11} of the rectifier was not measured due to the coplanar structure which is hard to interface with a single-ended VNA, it is hard to evaluate the impedance matching of the 35 GHz rectifier. On the other hand, using a tunable open stub tuner at 10 GHz has improved the 10 GHz rectenna's PCE from 45% to over 60% to approach the theoretical maximum. This supports the assumptions that the 35 GHz rectenna was limited by an impedance mismatch at the diode interface. Finally, it is key to note that the rectifier had a simple layout with no open stubs terminations and only used a DC-pass filter to prevent harmonics propagation to the output.

In more recent rectenna implementations by Ladan *et al.* [76,207,267], a more empirical approach was adopted to design and match the rectifier. The rectifier was first designed including harmonic termination at the fundamental tone f_0 and the second harmonic $2\times f_0$. To account for the high Electro-Static Discharge (ESD) susceptibility of GaAs diodes, ESD protection was included using a shunt 200 kΩ resistor at the diode's input. To minimize the influence of the ESD protection on the mmWave signal path, $\lambda/4$ at f_0 butterfly radial stubs were added to the ESD protection branch. Including ESD protection is essential especially for the GaAs diodes which are the most costly component in the system and are difficult to replace. Yet, apart from [207], ESD protection remains uncommon in mmWave rectennas which use highly ESD-sensitive devices. At 94 GHz, Hemour *et al.* used both on-wafer measurements, with a TRL calibration, and DC IV-curve measurements to measure the VDI W-ZBD characteristics [238]. Nevertheless, the performance of the rectenna was underestimated in simulation due to over-estimating the diode's parasitics based on the empirical characterization [238]. At 24 GHz, Bito *et al.* used DC IV curve measurements to optimize the models of the MA4E1317 [75]. As with [238], the rectifier's measured output surpassed the HB-simulated output due to over-estimating the diode's losses [75].

When considering the distributed microstrip layout of the rectifier in [207] after adding the harmonic termination, ESD protection, and in [207]: the extra stage for harmonics recycling, the rectifier's impedance can no longer be analyzed using simple analytical formulas as in [204]. To explain, the size of the rectifier and the additional component will result in multiple Smith chart rotations significantly varying the diode's impedance at individual tones. As a result, Ladan *et al.* resorted to fabricating Through Reflect Line (TRL) calibration standards on the same PCB. The bespoke calibration "kit" is then used to transfer the VNA calibration plane to the rectifier's input (the $Z_{rect.}$ plane in Fig. 2.11-e) allowing the coax-microstrip transitions to be calibrated out. The VNA is then used to directly measure Z_{rect} for which a microstrip matching network is then designed and implemented on a second PCB. As the rectifier is matched to 50 Ω, a standard band-pass filter (BPF) was added between the patch array and the matching network. The measured S_{11} of the rectifier shows a good impedance match at both the design frequencies of 24 and 35 GHz in [76] and [207], respectively. In a more recent rectifier design at 35 GHz, Mei *et al.* proposed a shunt-diode rectifier based on microstrip series matching [243]. The microstrip feedline connecting the shunt diode to the negative DC terminal of the rectifier was responsible for canceling the rectifier's capacitance at 35 GHz, as measured using a VNA.

A common feature among most rectifiers is the use of vias for single-series [76], self-biased [267], and voltage-doubler rectifiers [207, 242]. However, for printed and flexible electronics, vias involve complicated fabrication processes and additional steps [75]. Thus, via-free rectifiers with single-sided current return paths have been proposed for single-ended microstrip-fed single-series rectifiers [75, 135, 268]. The current return path

would typically include some form of harmonic termination such as radial stubs. The DC terminals of the rectifier are then both present on the top layer. For shunt diodes, the process is more straightforward as the positive and negative terminals of the rectifier are on the same layer [204, 243].

Although at mmWave bands beyond 60 GHz, the majority of implementations are based on fully-integrated CMOS devices (Table B.5), Hemour *et al.* proposed the highest PCE rectenna at 94 GHz with over 3× PCE improvements over CMOS implementations [238]. Despite being implemented on a very low loss alumina substrate (alumina's 60 GHz tanδ<0.001 [269]), it was observed that the surface current losses peaked in the matching network [238]. The rectenna had an overall size of $0.55\lambda_0^2$ which, despite being larger than fully-integrated CMOS rectennas, is still usable for applications such as swarm micro-robotics. This is a particularly interesting example where a Schottky-based rectenna outperforms its CMOS counterparts, based on a diode with very low parasitics and V_F, on a very low-loss substrate.

2.8.5 Additive Manufacturing and Low-Cost mmWave Rectennas

2.8.5.1 Rectenna Topologies and Motivation

Many of the mmWave rectenna implementations can be leveraged in space and defense applications, where the materials and diodes cost is negligible. However, for ubiquitous mmWave-powered networks to become a reality, several research challenges need to be overcome to allow high-efficiency low-cost rectennas. This section reviews the advances in additively-manufactured and flexible low-cost rectennas, as well as the viability of mmWave rectennas on lossy substrates. More broadly, low-cost and unusual mmWave antenna designs proposed for wireless communications are also reviewed based on their suitability for enabling new mmWave power harvesting applications.

To properly evaluate flexible and printed mmWave rectennas they need to be categorized based on their various components as in Fig. 2.13. The first class (Fig. 2.13-a) of flexible and conformable rectennas are those involving low-cost fabrication techniques to realize the rectenna on a flexible high frequency substrate. This substrate could be commercially available Liquid Crystal Polymer (LCP) which has tanδ<0.005. Various implementations have been presented using this fabrication method and all implementations were based on common geometry microstrip patch antennas [75, 135]. Such rectennas can achieve a DC output close to or surpassing their counterparts on rigid PCBs as in [136]. However, they cannot be classified as fully low-cost components as they still rely on expensive high-frequency substrates which can be over 90× more expensive than fiberglass or plastics [270].

The second class of low-cost rectennas are those implemented on lossy conventional substrates (Fig. 2.13-b). Such implementations are more suited to real-life applications

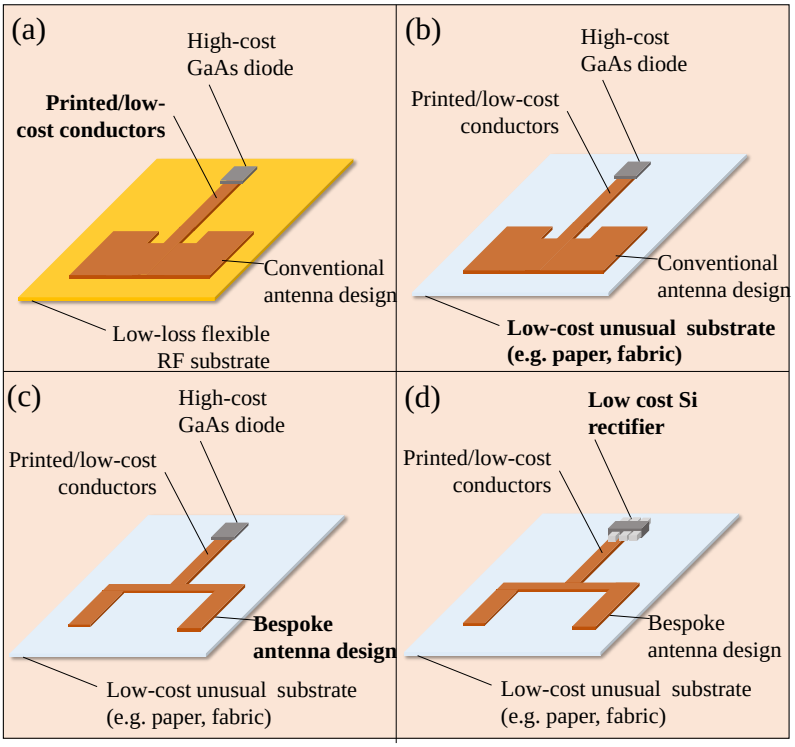

FIGURE 2.13: Low-cost mmWave rectenna categories: (a) low-cost conductors on flexible RF substrates [75], (b) low-cost conductors and substrate [234], (c) bespoke antenna design for high efficiency on lossy substrate, (d) the all low-cost components rectenna concept avoiding the use of costly mmWave GaAs diodes.

as their performance is not dependent on using low-loss substrates to realize complex impedance matching networks. For example, the rectenna in [234] is a demonstration of a mmWave-powered system-in-package. However, as the design is based on conventional antenna designs, the performance may be further improved through higher radiation efficiency antennas designed specifically for a lossy substrate.

The third class of low-cost rectennas is based on novel antenna design for maximizing the radiation efficiency on a lossy substrate (Fig. 2.13-c). Thus far, to the best of the author's knowledge, no implementation has been reported for a mmWave rectenna in this topology other than [244], which is proposed in Chapter 7.

The only fully low-cost mmWave topology not only employs bespoke antennas on low-cost substrates but also requires robust and low-cost rectifiers, as in Fig. 2.13-d. While Schottky diodes for mmWave applications will remain on GaAs to avoid operating near the cut-off frequency, the advances in CMOS mmWave rectifiers could be leveraged to realize low-cost printed rectennas. From a research and development perspective, the cost and time barrier of custom CMOS design for mmWave rectifiers contributes to the drive towards using off-the-shelf Schottky diodes, albeit being a costly component. However, for mass production, the high-efficiency rectifiers realized in standard CMOS processes could be used as the rectifying elements in future ubiquitous mmWave rectennas [266]. A recent rectenna array implementation at 94 GHz, showing high PCE approaching 25%

using miniaturized PCB antennas and CMOS rectifiers, further demonstrates the feasibility of large-area mmWave energy harvesting using large-area hybrid systems [271]. Nevertheless, the antennas in [271] were still implemented on a low-loss high-cost substrate.

2.8.5.2 Design, Fabrication and Performance

A variety of fabrication techniques have been developed based on additive manufacturing, photolithography, and hybrid methods to realize flexible mmWave antennas and systems. For example, direct inkjet printing of antennas directly on flexible substrates using conductive inks is a straightforward process of printing multi-layered aperture coupled antennas using printable dielectrics [272]. Furthermore, inkjet masking has been used to deposit photoresistive inks to allow the etching of commercially-available polyimide copper laminates without the use of masks and precision mask aligners [42]. Fig. 2.14 shows photographs of mmWave rectennas fabricated using a variety of low-cost techniques such as printing on flexible and 3D printed substrates, these implementations were all presented by the same research group.

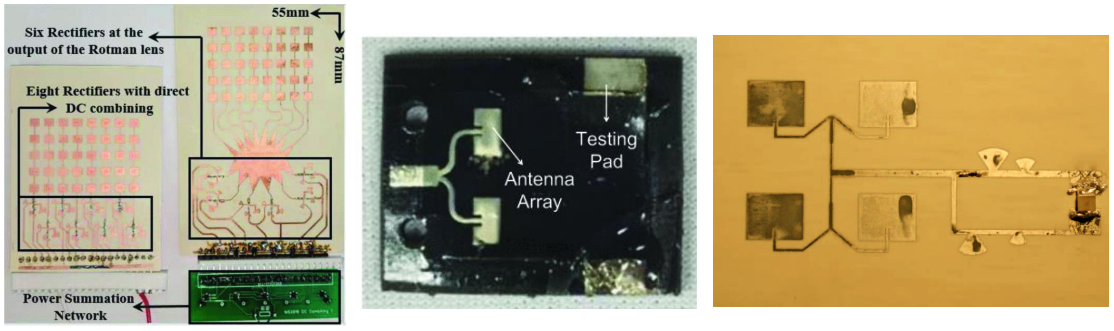

FIGURE 2.14: Photographs of flexible and printed mmWave rectennas: (a) high gain and wide-beam inkjet-masked rectenna (reproduced from [135], ©IEEE 2019), (b) 3D printed system-in-package rectenna (reproduced from [234], ©IEEE 2019), (c) flexible inkjet-printed rectenna (reproduced from [75], ©IEEE 2017)

The majority of mmWave rectennas were based on 50 Ω antennas. Thus, flexible and printed antennas proposed for 5G and license-free communications beyond 24 GHz can be employed in mmWave power harvesting. Examples of flexible and printed antennas developed for wireless communications have shown the possibility of achieving very high radiation efficiency (>80%) and a wide-bandwidth for 5G applications in [232]. Similarly, BAN flexible antennas have been demonstrated at 60 GHz based on flexible PCBs [273]. However, as for the LCP-based rectennas in [75, 135], these antennas were implemented on substrates with $\tan\delta$<0.005. Hence, they cannot be considered as fully low-cost components and the designs may need to be optimized to achieve high radiation efficiencies on lossy substrates.

Eid *et al* proposed flexible beamforming arrays based on Rotman lenses (Fig. 2.14-b) as an enabler of long range power harvesting [135] and backscattering [136]. The inkjet masking fabrication technique used, first presented in [42], is fairly low-cost and well-suited for rapid prototyping. However, the systems are implemented on low-loss Rogers LCP substrates. It is unclear how the performance of such a system, considering the complex Rotman lens, will vary if it was implemented on a lossy dielectric such as FR4, lossy polymers, or textiles. Considering only the microstrip feeds dielectric losses, based on the formulas in [274], the 55 mm-length microstrip rectenna feed will incur over 6 dB insertion losses at 28 GHz for a tanδ=0.02. tanδ=0.02 is a conservative estimate based on the properties of materials such as fabrics [159,244] or 3D printable dielectrics [234], tanδ of substrates such as paper can exceed 0.04 [43]. It is expected that the dielectric losses will be also higher in the Rotman lens due to the unusual geometry and the larger area over a lossy dielectric. Similar conclusions could be drawn on rectenna arrays printed or etched on flexible low-loss substrates such as [75], where the net DC output will degrade significantly should the system be transferred to a lossy substrate.

A particularly common example of antenna substrates which have a high tanδ are textiles. Driven and parasitic mmWave antenna arrays have been recently presented as high as 77 GHz with 11.2 dB gain [157]. mmWave antennas on textiles have also been developed for on/off-body BAN applications [159, 164]. Considering the 41% efficiency patch array in [159] and the end-fire 48% quasi-Yagi in [164], meaningful conclusions can be drawn upon the effect of the antenna design on a lossy substrate at mmWave bands can be drawn. Both antennas, by Chahat *et al.* have been fabricated using the same conductors and on the same cotton substrate by the same group. Yet, the endfire antenna achieves over 1 dB higher efficiency.

The rectifier in [135] achieve the highest PCE of ≈33%, only 21% lower than the high efficiency rectenna implemented on a rigid PCB in [76]. [135] uses a solid metal sheet for the antenna and the ground plane to improve the conductivity above 20 GHz. Thus, as discussed in section 2.8.5.1, such implementations are on low-loss substrates and can hence achieve a high PCE using optimal matching network design. Yet, it is hard to verify this assumption as the rectifier's S_{11} is not reported for any of the reported rectennas. Table B.7, in Appendix B, compares the recent flexible rectifiers' performance.

2.8.6 mmWave EH: *Summary*

From the literature reviewed in this section, the key requirements for efficient mmWave power transmission may be summarized as:

1. Efficient high gain antenna and array designs not limited to low-loss RF substrates.
2. Impedance matched, high sensitivity and PCE rectifiers, based on accurate diode and package models, enabling rapid design and simulations.

3. Antenna-rectifier fabrication and packaging techniques to allow reliable and scalable integration of high-$f_{\mathrm{cut-off}}$ Schottky or CMOS rectifiers with high-gain low-cost antennas.

Holistic design of mmWave rectennas involving both antenna and rectifier co-design based on low-cost semiconductors and packaging techniques will be needed for reliable high-efficiency harvesters.

2.9 Summary and Conclusions

In this chapter, technologies, architectures and different approaches to rectenna design for RFEH and WPT were reviewed. Rectennas were categorized and evaluated based on standard antenna parameters. Furthermore, rectification and power conversion techniques were reviewed, with emphasis on rectennas operating at mmWave bands as well as wearable and flexible rectennas.

Despite the advances in antenna design, matching networks, and antenna-rectifier co-design techniques, wearable and low-cost rectennas still pose additional research challenges. For example, textile antennas in particular have been limited in their topologies and in their performance, compared to their conventional counterparts, and have not yet been implemented using innovative topologies such as multi-mode antennas and antenna-rectifier co-design. In addition, mmWave low-cost rectennas still pose significant challenges and have not been realized based on novel antenna designs to overcome the material-induced losses. The practical work carried out, described in the following chapters, follows on exploring the reviewed rectenna topologies demonstrating that they can be applied to realize high-efficiency textile, flexible and printed rectennas, surpassing SoA performance, up to mmWave bands.

Chapter 3

Rectenna Design: A Theoretical Overview

In this chapter, the theory governing the design and operation of rectennas is presented. The required steps for component-level optimizations are highlighted for the antenna, rectifier, and impedance matching stages. These design-guidelines are followed in the later chapters and are discussed from a theoretical perspective.

3.1 Antenna Design for Energy Harvesting

3.1.1 Antenna Fundamental Parameters from an RFEH Perspective

In this section, antenna fundamentals are revisited from an RFEH perspective, understanding the physical parameters which affect the RF EM power which can be harvested by a rectenna.

To begin with, the time-average EM power density S (W/m^2) of a time-varying Poynting vector is given by

$$S = \frac{1}{2} \times E_0 \times H_0, \tag{3.1}$$

where E_0 and H_0 are the peak amplitudes of the complex electric (V/m) and magnetic (A/m) field vectors, respectively [117]. In free space, the ratio of $|E_0|$ and $|H_0|$ is related by the wave impedance, and is a function of the permittivity and permeability of the propagation medium [275],

$$Z_0 = \frac{|E_0|}{|H_0|} = \sqrt{\frac{\mu}{\epsilon}}. \tag{3.2}$$

Z_0 is approximately 377 Ω and is often approximated as 120π [224]. S can subsequently be calculated from a measured or simulated E-field [181, 224], using

$$S = \frac{E^2}{Z_0}. \tag{3.3}$$

For an isotropic transmitting antenna, the EM power density S_i at the surface of a closed sphere of radius r is given by

$$S_i = \frac{P_{\mathrm{TX}}}{4\pi r^2}, \tag{3.4}$$

where P_{TX} is the total power radiated by the antenna. However, as any practical antenna will have a directional radiation pattern with an angular gain $G(\theta, \varphi)$ [117], S is given by

$$S = \frac{P_{\mathrm{TX}} G_{\mathrm{TX}}}{4\pi r^2}, \tag{3.5}$$

where G_{TX} is the realized gain of the transmitting antenna.

From (3.5), the EM power density at a given distance, r, is independent of frequency. Moreover, in space, the radiated power is conserved and does not "*dissipate*" in the propagation medium; the observed $1/r^2$ relation between the transmitted and received power is however due to the radiation of the EM waves to cover a sphere of a radius r, following the inverse-square law. It can also be observed how a directional transmitter can be used to overcome the $1/r^2$ reduction in the received power, as advocated in the early WPT experiments [3].

On the receiving end, the effective area $A_{\mathrm{eff.}}$ of the antenna is where the frequency-dependence manifests, when receiving power from a certain transmitter. $A_{\mathrm{eff.}}$ is given by

$$A_{\mathrm{eff.}} = G\frac{c^2}{4\pi f^2}, \tag{3.6}$$

where f is the frequency, and c is the speed of light. Therefore, while the power density available is not frequency-dependent, the power received, P_{RX}, delivered to the antenna's termination, given by

$$P_{\mathrm{RX}} = A_{\mathrm{eff.}} \times S \tag{3.7}$$

(assuming ideal matching), is frequency-dependent.

In RFEH and WPT, the antennas are typically studied in their far-field (Fraunhofer) region, where their radiation patterns are independent of r. The far-field region is defined as the region between the minimum radius $r_{\mathrm{min.}}$, from the antenna, and infinity. $r_{\mathrm{min.}}$ is given by

$$r_{\mathrm{min.}} = \frac{2D^2}{\lambda}, \tag{3.8}$$

where D is the largest dimension of the antenna [117]. The PCE of a rectenna operating at distance $r > R$ can subsequently be calculated as

$$\text{PCE} = \frac{P_{\text{DC}}}{P_{\text{RX}}} = \frac{V_{\text{DC}}^2}{Z_L P_{\text{RX}}}, \tag{3.9}$$

where P_{DC} (W) is the harvested DC power calculated using the DC voltage V_{DC} (V) across an Ohmic load Z_L (Ω). Using (3.5)-(3.7), the power available at a rectenna's input can be estimated in far-field WPT. By using the antenna's realized gain as G in (3.9), the losses due to impedance mismatch between the antenna and its load, typically 50 Ω when measured using a standard VNA, in addition to the losses in the antenna (conductor and dielectric losses) are factored in P_{RX}.

By substituting (3.5) and (3.6) into (3.7), equation (3.7) can be written in its most common form: the Friis free space path loss [276], where the received power is given by

$$P_{\text{RX}} = P_{\text{TX}} G_{\text{TX}} G_{\text{RX}} (\frac{c}{4\pi f r})^2. \tag{3.10}$$

While (3.10) shows that the received power is inversely proportional to the frequency-squared, such statement assumes that G_{TX} and G_{RX} are frequency-independent. However, (3.6) can be rewritten in terms of the physical area $A_{\text{phys.}}$ using the aperture efficiency term $\eta_{\text{App.}}$, where $\eta_{\text{App.}} = A_{\text{eff.}}/A_{\text{phys.}}$. The gain/area relation, assuming a fixed $\eta_{\text{App.}}$, can then be expressed as

$$G = \frac{4\pi \eta_{\text{App.}} f^2}{c} \times A_{\text{phys.}}. \tag{3.11}$$

From (3.11), it can subsequently be seen that for an antenna with a fixed physical area and aperture efficiency, the antenna's gain is proportional to f^2. Equation (3.11) can be substituted in (3.10) giving

$$P_{\text{RX}} = A_{\text{TX}} A_{\text{RX}} \eta_{\text{TX}} \eta_{\text{RX}} \frac{f^2}{c^2 r^2}, \tag{3.12}$$

where A is the physical antenna area and η is the aperture efficiency for the transmitter (TX) and the receiver (RX), respectively. Equation (3.12) gives a physical explanation to the previously reported conclusion that WPT at mmWave bands can result in an improved end-to-end efficiency over sub-6 GHz networks [16,235,240], and further motivates research in mmWave rectenna design.

To showcase the frequency-dependence of the received power, a physical example is presented. A fixed area transmitter and receiver antennas, A_{TX} =A_{RX}=10×10 cm^2, are considered for fixed separation, r=100 m. The frequency is swept from 1 to 100 GHz. The calculated received power, path loss, and antenna gains using (3.11) and (3.12) are shown in Fig. 3.1. This calculation does not account for the additional atmospheric attenuation at mmWave bands, which results in reduced penetration capabilities. However, the

attenuation of mmWaves, at sea level, is less than 1 dB/km below 50 GHz and above 70 GHz [231].

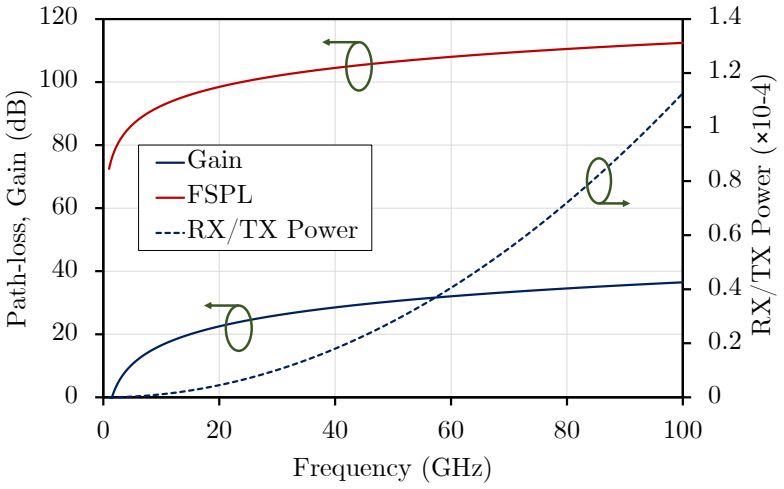

FIGURE 3.1: Calculated path loss and gain from 1 to 100 GHz and the received power ratio for a directional transmitter and receiver of a fixed area and aperture efficiency.

3.1.2 The Wire Antenna for RFEH

The gain of an antenna is limited by its physical size as in (3.11). From an RFEH perspective, it is desirable to minimize the area of the antenna while not reducing its $A_{\text{eff.}}$, not to reduce the RFEH efficiency from low S. For an aperture-type antenna, $A_{\text{eff.}} < A_{\text{phys.}}$ and $\eta_{\text{App.}} < 1$ [117]. On the other hand, the effective area is significantly larger than the physical aperture (the surface area) for wire-type antennas, such as dipoles and monopoles [19, 117].

Dipoles are typically designed with $l \approx \lambda/2$, to achieve an impedance close to 73 Ω, which can be matched to 75 or 50 Ω lines with $S_{11} < -10$ dB [19]. The half-wave wire dipole has an inductive $\Im\{Z\}$ for $l_{\text{dipole}} > \lambda/2$, where $\Im\{Z\}$ is a function of the wire's radius [19]. Therefore, it is possible to use the dipole antenna as a starting point for designing a high-Z rectenna eliminating the rectifier's matching network, as reviewed in Chapter 2.4.4. As in [18], the equivalent circuit of a dipole could be loaded with additional inductance, through a mutually-coupled inductive feed or an inductive slot, embedded within the dipole. Fig. 3.2 shows the layout and the simplified (unbalanced) equivalent circuit of inductive-fed dipoles. While the simple wire and planar dipoles can be analyzed and designed using analytical models [19], such as the transmission line model [111], more complex dipole antenna designs for co-designed rectennas, such as the antennas proposed in Chapters 5 and 9, are typically analyzed in numerical full-wave EM simulators [19].

Both antennas shown in Fig. 3.2 are characterized by using an inductive feed. By tuning their dimensions, Z_{Antenna} can be designed to match the desired value which

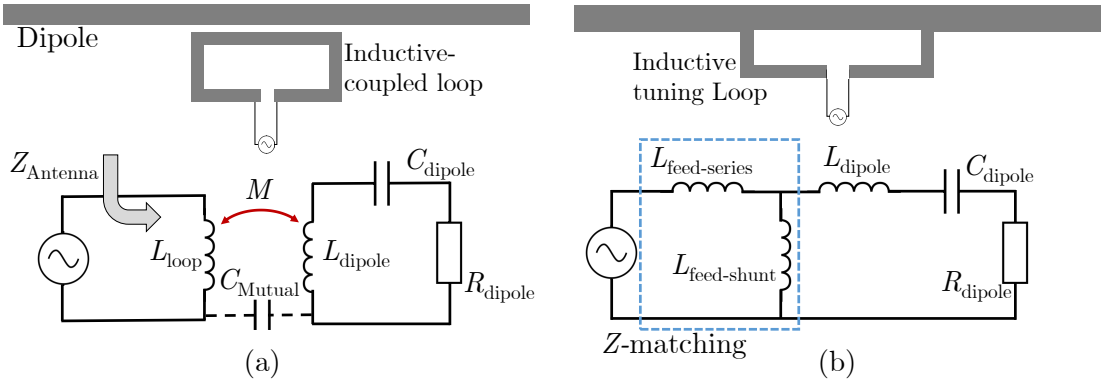

FIGURE 3.2: Inductive dipole antennas layout (top) and simplified equivalent circuits (bottom): (a) inductive coupling-fed dipole [277]; (b) shunt-fed dipole [278].

maximizes the rectifier PCE. The equivalent circuits represent high-level abstractions of the dipole's feed inductance, and its operation as a matching network.

As for monopoles, the large ground-plane available in most electronic systems typically satisfies the conditions of the large ground in the image theory [19], enabling the miniaturization of monopole antennas used to power RFEH systems. Therefore, monopole antennas can be considered a more compact alternative to their dipole counterparts. Broadband antennas can be realized using "fat" monopoles [19], such as the disc antenna [279] adapted in Chapter 4, where the curved edge and the continuous current path allow the antenna to achieve multiple resonant modes.

3.1.3 High-Efficiency and Broadband Antennas

Intuitively and from (3.10), a high directivity D and gain G ($G = \eta_{\text{Rad.}} \times D$), translate to higher power reception. D is given by

$$D = \frac{4\pi U}{P_{\text{TX}}}, \tag{3.13}$$

where U is the radiation intensity per steradian (solid angle) [117]. In ambient RFEH, or WPT with a non-Line-of-Sight (LOS) source, a uniform power distribution over the sphere surrounding the rectenna can be assumed [53]. Subsequently, the average harvested power, from [53], is given by

$$P_{\text{RF}} = \frac{\eta_{\text{Rad.}}\lambda^2 S}{4\pi} \int_{\Omega} D(\Omega)\mathrm{d}\Omega = \eta_{\text{Rad.}}\lambda^2 S. \tag{3.14}$$

From (3.14), it is observed that, assuming a uniform distribution of the received power or an unknown direction of incidence of the power, the radiation efficiency $\eta_{\text{Rad.}}$ is the

main FoM. For a small, simple monopole with no dielectric susbtrate, $\eta_{\text{Rad.}}$ is given by

$$\eta_{\text{Rad.}} = \frac{R_{\text{Rad.}}}{R_{\text{Antenna}}} = \frac{R_{\text{Rad.}}}{R_{\text{Rad.}} + R_{\text{Loss}}}, \tag{3.15}$$

where $R_{\text{Rad.}}$ is the radiation resistance and R_{Loss} is the antenna's Ohmic resistance. For a planar antenna with a lossy conductor and dielectric, $\eta_{\text{Rad.}}$ cannot be fully-described by the series resistors model (3.15), due to the tanδ losses [117], and is given by

$$\eta_{\text{Rad.}} = \frac{P_{\text{TX}}}{P_{\text{Accepted}}} = \frac{P_{\text{TX}}}{P_{\text{TX}} + P_{\sigma-\text{loss}} + P_{\text{DK}-\text{loss}}} \tag{3.16}$$

where P_{Accepted} is the accepted power after any reflection (S_{11}) and $P_{\sigma-\text{loss}}$ and $P_{\text{DK}-\text{loss}}$ represent the power dissipated in the conductor and dielectric, respectively [117, 280].

To maximize $\eta_{\text{Rad.}}$, $R_{\sigma-\text{loss}}$ and $R_{\text{DK}-\text{loss}}$ need to be minimized. For a high-σ material such as copper, the σ loss resistance does not exceed 0.1 Ω in the microwave bands. In a microstrip antenna, the dielectric (tanδ) loss is the main source of losses. The dielectric losses $P_{\text{DK}-\text{loss}}$ arise from $|E|$ dissipating in the substrate and is given by

$$P_{\text{DK}-\text{loss}} = \frac{\omega\epsilon''}{2}\int\int\int_V |E|^2 dV = \frac{1}{2}|E_0|^2 \frac{Wt\tan\delta}{240}\sqrt{\frac{\epsilon_r}{\mu_r}}, \tag{3.17}$$

where W and t are the width and thickness of the microstrip cavity, and E_0 is the E-field amplitude at the radiating slot [280].

To reduce $P_{\text{DK}-\text{loss}}$, substrates with a very low tanδ are used for microwave and mmWave antennas [19]. As this is not possible for textiles [11], paper [43], and other low-cost materials [270], equation (3.17) implies that a microstrip antenna with a compact radiator, i.e. smaller W, will reduce $P_{\text{DK}-\text{loss}}$ improving $\eta_{\text{Rad.}}$. While (3.17) is valid for a microstrip antenna above and parallel to a large ground plane, the same principal can be applied for a planar dipole or monopole on a substrate, where E can be computed by the means of a full-wave simulator. Therefore, compact antennas are more desirable on lossy substrates. This concept is explored and validated numerically and experimentally in Chapter 7, for a mmWave textile-based rectenna.

For broadband antennas to be realized with high radiation efficiency ($\eta_{\text{Rad.}}$), multiple resonant modes can be utilized. The antenna can then be modeled using multiple radiative "resistors" for each f_r, as shown in Fig. 3.3 [19, 281]. Using a fixed radiation resistance $R_{\text{Rad.}}$ and tunable L and C elements, the single-resonance antenna equivalent circuit in Fig. 3.3 was tuned for f_r=3 GHz. By tuning the L and C elements of antenna-2, the $S_{11} < -10$ dB bandwidth could be improved by a factor of 3.5, as shown in the reflection coefficient in Fig. 3.3 when matched to a 50 Ω source. Likewise, multiple resonators can be utilized to realize a broadband complex-Z rectenna with no matching network [34]. By utilizing an antenna design with multiple elements, a high $\eta_{\text{Rad.}}$ can

be achieved for all the resonances, resulting in a broadband high-efficiency RFEH performance. Practical development of broadband antennas is presented in Chapter 4 and in Chapters 6 and 7, for UHF and mmWave textile-based antennas, respectively.

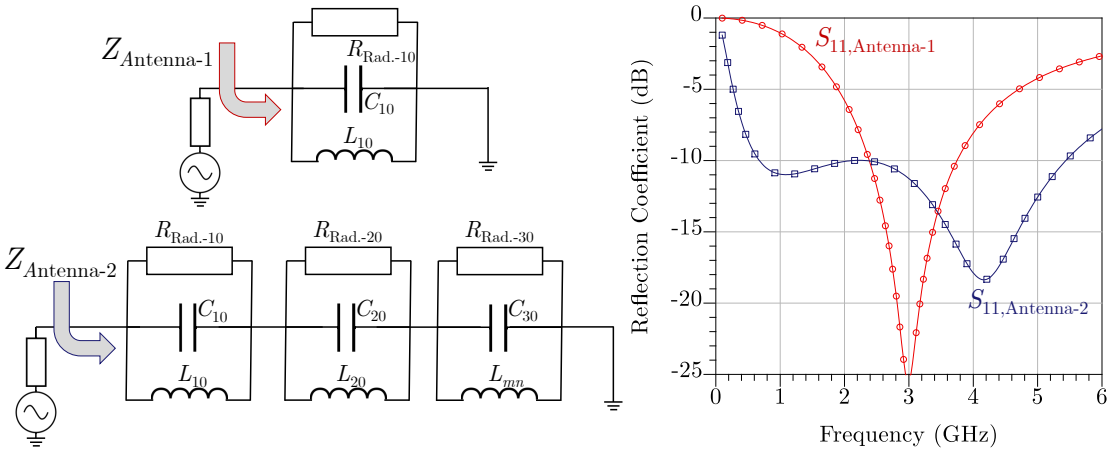

FIGURE 3.3: The equivalent circuit of a single-mode 3 GHz antenna (Antenna-1) and a triple-mode antenna (Antenna-2), and their reflection coefficient.

3.2 RF Rectification

3.2.1 Rectifier Topologies and Efficiency

From the reported rectifier topologies in Chapter 2.6, the Schottky-based single-series and the voltage doubler rectifier are discussed in this analysis, and utilized in the next chapters in rectenna design. From a time-domain perspective, the maximum PCE of these topologies can be established using an analytical method as in [282]. A transient simulation of an ideal diode fed using a UHF (1 GHz) voltage source (4 V amplitude) is utilized to demonstrate the RF rectification mechanism in time-domain. Fig. 3.4 shows the schematic of a single-series rectifier, and the simulated waveforms for various smoothing capacitor values. Z_{Load}=1000×Z_{Source}=1 kΩ, both have no imaginary component in consistence with reported theoretical analysis of rectifiers in time domain [204, 283]. As Z_{Load} in a typical RFEH application will always exceed 100 Ω, the "half-wave" nature of the single-series rectifier is not a limit to high-PCE.

From Fig. 3.4, it can be seen that a high C_{Smooth} value is crucial for efficient and steady rectification. 100 pF, combined with a load of 1 kΩ, correspond to τ=100×T, where T is the time period at 1 GHz. The same requirement holds for a voltage doubler, where a large C_1 is essential to store the charges on the negative half-cycle, ahead of "charge-pumping" it to create the doubling effect at the output. Fig. 3.5 shows the schematic and waveforms of the voltage doubler rectifier, where it is evident in the waveforms that unless C_1 and C_2 are sufficiently large, no charge-pumping will take place. The DC

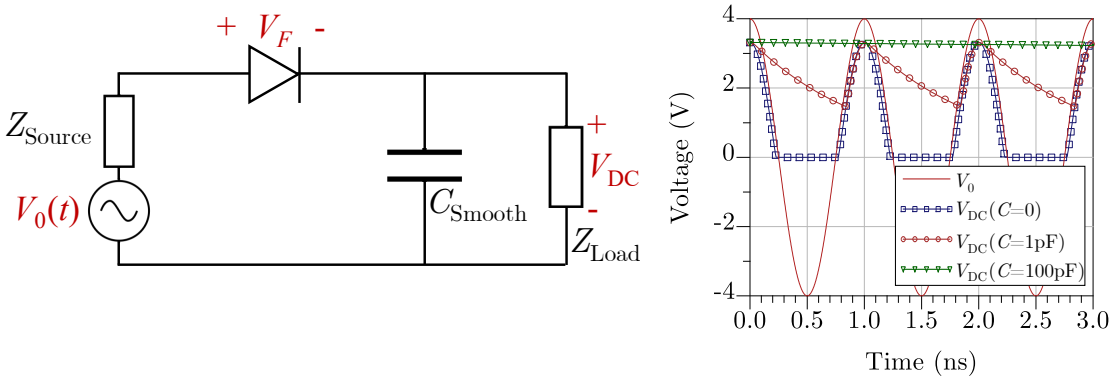

FIGURE 3.4: Schematic of a single-series rectifier and the transient waveforms for varying C_{Smooth} values.

voltage output of a voltage doubler can be approximated using

$$V_{\text{DC}} = 2 \times V_0 \sin \omega t - 2 \times V_F, \tag{3.18}$$

highlighting the significance of the forward voltage drop V_F when V_0 is small [33].

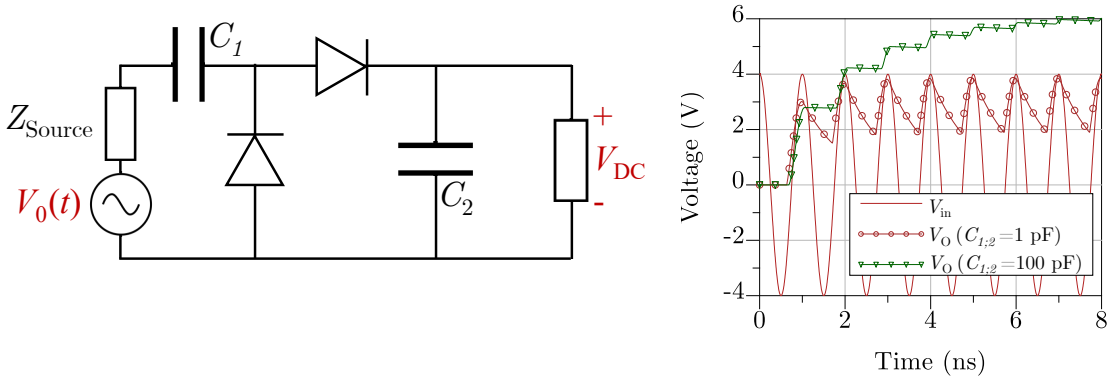

FIGURE 3.5: Schematic of a voltage doubler rectifier and the transient waveforms for varying $C_1 = C_2$ values.

In [282], it was shown that the maximum PCE of a single-series and a voltage doubler is 81.1% and 92.3%, respectively, limited by the distortion losses, which can be improved using harmonic termination. These values were validated in Keysight ADS using the transient simulation and were found to agree within 1%. However, the analysis so far has considered ideal diodes whereas, in a real Schottky rectifier, V_F is the main limit to the PCE at low power levels, as repeatedly discussed in literature [17]. Therefore, real diodes are evaluated analytically in the next section.

3.2.2 Rectification Losses

In Chapter 2.8.4.1, the losses in a rectifier were reviewed and the forward voltage drop across the diode's junction was identified as the main source of losses at low power levels. Four commercially-available RF Schottky diodes are evaluated analytically to

investigate their losses based on the method proposed by Yoo and Chang [204]. The PCE formulation is based on [284] and the Matlab code is reproduced and modified with permission from [284]. The diodes' PCE was calculated based on their datasheet junction parameters quoted in [12]. Fig. 3.6 shows the calculated PCE, assuming $\Im\{Z_{\text{Rectifier}}\}$ is canceled with its complex conjugate, for varying loads R and input voltages V from 1 to 100 GHz. In this analysis, the PCE is defined as

$$\text{PCE} = \frac{P_{\text{DC}}}{P_{\text{DC}} + P_{\text{Loss}}}, \tag{3.19}$$

where the power loss is inclusive of the diode's forward voltage drop and resistive losses, in addition to phase distortion losses [204,283], previously analyzed in [282], and assumes no impedance mismatch losses.

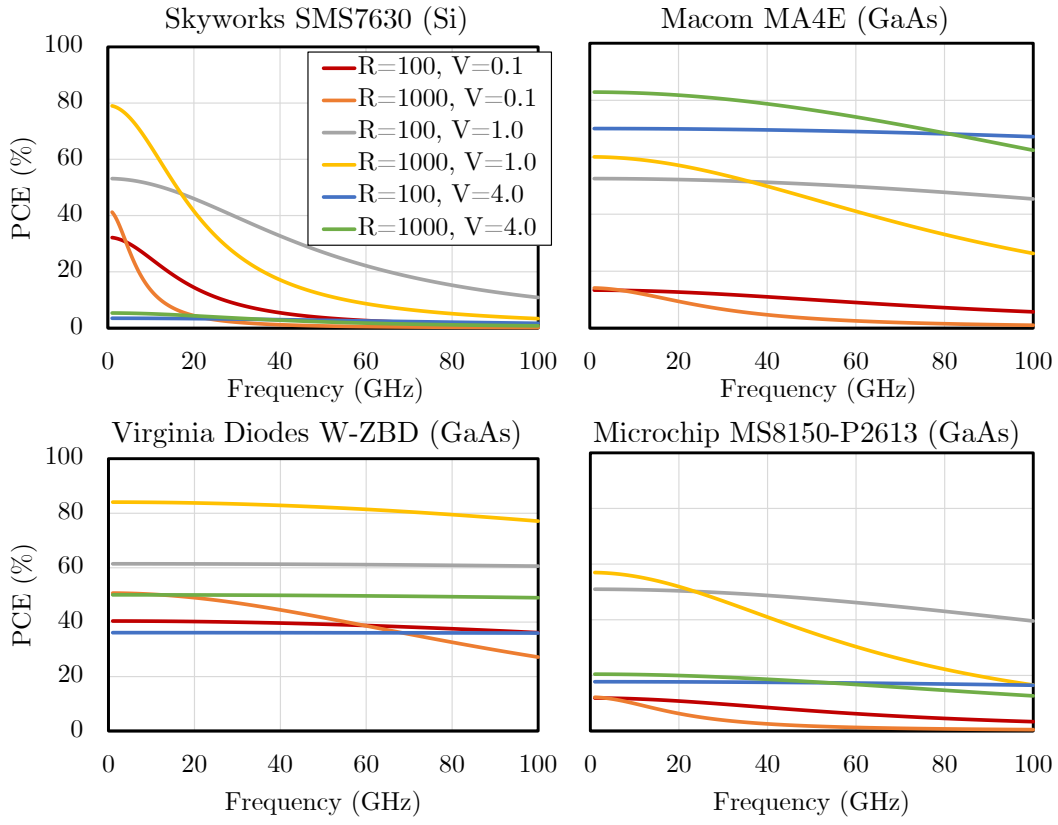

FIGURE 3.6: Analytically-calculated maximum PCE of commercial Schottky diodes from 1 to 100 GHz, for varying load R and RF input voltage V.

For low-power RFEH, a low input V is expected, for V=0.1 V it can be observed that the SMS7630 and the W-ZBD achieve over 100% higher PCE at 1 GHz, with a 1 kΩ load, due to their low V_F under 0.1 V. However, as the SMS7630 is a low-cost component implemented in Si, its switching speed is limited and will cut-off above 20 GHz, resulting in a reduced PCE. However, the GaAs W-ZBD is a very specialized component aimed towards mmWave and sub-THz applications and hence does not show any significant PCE degradation with frequency. A high V_{Br} diode on the other hand, like the MA4E, can achieve a high PCE above 80%, but only from a 4 V input which is only present

in high-power WPT, due to its relatively high V_F. Therefore, the diode choice for low-power RFEH is mainly governed by V_F, as long as $f_{\text{cut-off}}$ of the diode is higher than the rectenna's frequency of operation.

3.3 Rectenna Matching and Antenna-Rectifier Co-Design

In the previous section, rectifiers and antennas have been analyzed separately, assuming the rectifiers' reactance is canceled using "conjugate" matching [204,282,284]. In this section, the Z-matching approach required to achieve the maximum PCE for a certain power level or incident power density, and the influence of the source impedance on the rectifier's DC performance are discussed. For maximum power transfer, the antenna's impedance needs to match the rectifier. The L-matching circuit, shown in its equivalent lumped form in Fig. 3.2-b, can be used to transform the antenna's Z_{Antenna} to match Z_{Recifier}. For $Z_{\text{Antenna}} = Z_{\text{Rectifier}}$, an S_{11} very close to zero is expected at the rectifier's input. Nevertheless, a low S_{11} is not the only condition to be met for a high PCE.

The L-network, which could either be lumped, distributed as a microstrip network, or built into the antenna as in Fig. 3.2, "boosts" the RF voltage input to the rectifier [111, 278]. To explain, a receiving antenna acts as a voltage source with an amplitude given by

$$V_0 = \sqrt{8 P_{\text{RX}} Z_{\text{Antenna}}}. \tag{3.20}$$

From (3.20) [285], assuming the reactance of the load (the rectifier) is canceled using an L-network as in Fig. 3.2-b, V_0 at the rectifier's input can be increased by increasing Z_{Antenna}, for the same power input. Recalling (3.18), the voltage drop V_F is the main source of losses at low power levels [17, 204]. Hence, increasing V_0 improves the PCE at low power levels by increasing the V_0:V_F ratio.

On the other hand, from maximum power transfer basics [286], the antenna and the rectifier need to have matching $Z_{\text{Antenna}}{=}Z^*_{\text{Rectifier}}$. Therefore, $\Re\{Z_{\text{Antenna}}\}$ is not a fully-independent parameter, as it should equal $\Re\{Z_{\text{Rectifier}}\}$ [111]. $Z_{\text{Rectifier}}$ is governed by the diode parameters, which are not controllable by the rectenna's designer using commercial Schottky diodes. However, the rectifier's topology, layout, and load impedance do affect $Z_{\text{Rectifier}}$. Therefore, it is possible to design a rectifier that maximizes $\Re\{Z_{\text{Rectifier}}\}$ and subsequently the low-power PCE. Z_{in} can be evaluated analytically for a diode using

$$Z_{\text{diode}} = \frac{V_F}{I_{\text{dc}}} = \frac{V_0 \sin \omega t - 0.5 V_{\text{DC}}}{I_S \left[B_0 \left(\frac{V_0}{m V_T} \right) \exp \left(\frac{-0.5 V_{\text{DC}}}{m V_T} \right) - 1 \right]}, \tag{3.21}$$

where V_T is the diode's thermal voltage, I_S is the diode's saturation current, ω is the angular frequency, m is the diode's ideality factor and B_0 denotes the DC harmonic of the Bessel function describing the diode's current [33]. As $V_{\text{DC}} = Z_{\text{Load}} \times I_{\text{DC}}$, Z_{diode}

is dependent on the load. Therefore, while the diode parameters are limited by the commercially-available diodes, Z_{Load} can be used to tune and increase $\Re\{Z_{\text{Rectifier}}\}$, improving the PCE at low power levels.

For topologies more complex than a lumped single-series or voltage doubler rectifier, the theoretical analysis of the rectifier is increasingly complex [283, 284]. Moreover, analytical methods such as those by Yoo and Chang [204] have diminished accuracy compared to HB simulation at low power levels [283]. For instance, despite Song *et al.* presenting (3.21) for calculating Z_{diode}, in their analysis of a voltage doubler, $Z_{\text{Rectifier}}$ was evaluated using non-linear HB simulation. Hence, the rectifier optimization needs to be guided by a non-linear circuit simulation, which considers all the layout and packaging effects, as well as models the diode's junction accurately, in order to have a full control over the rectifier design and matching process from an end-to-end perspective.

Optimal PCE is achieved through maximizing the voltage gain of the complex-Z source [287], as well as optimizing the load impedance (DC current draw) for maximum power transfer between the rectenna and the load [11]. In this work, the complex-Z source matching is done through a standalone matching network, in Chapter 4 and 8, as well as through complex-Z antennas without a matching network in Chapter 5 and 9.

3.4 Conclusions

In this chapter, the theoretical fundamentals governing the operation of a rectenna were presented covering EM propagation, antenna design, rectification, and rectifier-matching and co-design. The following key points have been identified as guidelines to realizing high-efficiency rectennas:

- While a high antenna gain is an application-dependent FoM, a high $\eta_{\text{Rad.}}$ is always a requirement for optimal RFEH.
- Designing rectennas based on antennas with a high effective to physical area ratio, i.e. wire-type antennas, is an enabler of more compact RF energy harvesters.
- To realize high-$\eta_{\text{Rad.}}$ antennas on lossy substrate, a miniaturized radiator is preferred to minimize the dielectric loss.
- For broadband rectennas, based on 50 Ω or co-designed complex-Z antennas, creating multiple resonances enables high $\eta_{\text{Rad.}}$ over a wide bandwidth.
- To enable high-sensitivity RFEH, the rectifier, antenna, and load need to be co-designed to maximize the PCE from low RF power densities, through maximizing the voltage output of the antenna.

- While an impedance match is required to design a rectifier with minimal S_{11}, the optimum input impedance of the rectifier needs to be optimized numerically to achieve the best PCE, where the PCE is dependent on Z_{in} and not only the S_{11}.

The forementioned techniques are transferable to different device technologies (Schottky-based or CMOS-integrated), rectenna architectures, and frequencies. These fundamentals are used as a high-level guidance to the optimizations carried out using commercial EDA and simulation tools in the following chapters.

Chapter 4

High-PCE Wearable Textile-Based Rectenna Based on a 50Ω Antenna

By far the most common rectenna topology is a 50 Ω antenna with an impedance matching stage. The majority of textile-based rectennas reported adopt this topology utilizing standard microstrip patch antennas due to their high isolation [11, 178, 179]. Reported textile-based wearable rectennas have the following fundamental shortcomings:

1. Requiring a thick (>2 mm) substrate to improve the antenna's $\eta_{\text{Rad.}}$;
2. Being limited to narrow-band broadside RFEH due to utilizing microstrip patch antennas;
3. Achieving at least 46% lower PCE when the rectifier is implemented on textiles, in [179], compared to a low-loss substrate [11], despite using the same diode.

The analytical calculations and off-body measurements in [288], available in Appendix A, show that unisolated sub-1 GHz omnidirectional rectennas can outperform their 2.4 GHz broadside off-body rectennas by over an order of magnitude, in terms of harvested power, when modeled based on their average angular gain and using the performance of SoA high-PCE rectifiers. Therefore, a high-PCE omnidirectional rectenna design is needed to demonstrate that material properties do not limit the maximum achievable PCE of wearable rectennas.

This chapter demonstrates the feasibility of high-PCE wearable RFEH using low-profile, broadband, all-textile rectennas. A dual-polarization compact fully-textile broadband antenna is presented on a 1 mm-thick felt substrate and evaluated on the body (Sections 4.1 and 4.2). The rectenna uses a compact lumped inductive-matched rectifier achieving a best-in-class PCE of 41.8% at −20 dBm (Sections 4.3 and 4.4). To demonstrate the scalability of the matching approach, a multi-band rectifier is designed and

evaluated. Finally, time-variant s-parameter measurements are presented (Section 4.4) showing the textile-based rectifier directly charging an electrolytic capacitor as well as investigating the effect of the capacitors' charge-state on the rectifier's input impedance. In wireless testing (Section 4.5), the proposed rectenna achieves over 5× higher PCE than SoA textile rectennas at power densities less than 1 μW/cm^2. When tested on-body, the rectenna achieves over 40% PCE from an incident 1 μW/cm^2 plane-wave. The rectenna's dual-polarization harvesting capability is demonstrated along with a 360° omnidirectional half-power beamwidth. The contributions in this chapter have been published in [289].

4.1 Textile Antenna Design and Fabrication

4.1.1 Fully-Textile Rectenna Fabrication Technique

Felt suffers from lower dielectric losses compared to other woven textiles due to the increased porosity reducing its loss tangent (tanδ). Therefore, for textile antennas with the highest $\eta_{\text{Rad.}}$ felt has been used a substrate [11, 290]. Furthermore, 1 mm felt was reported to have a minimal impact on on-body propagation at 60 GHz compared to 0.2 mm cotton, despite its higher thickness due to its mostly-air composition [291].

To validate the assumptions about the felt's properties and to accurately simulate the rectenna, 1 mm-thick commercial felt has been characterized using the two-line method [196, 199]. The 1 mm felt was used as a substrate for two microstrip lines of 40 and 60 mm length and 4 mm trace width. Based on the dielectric properties reported in [11], the trace width has been selected to realize a 50 Ω microstrip line. The measured dielectric properties of felt are ϵ_r=1.12 and tanδ=0.023.

The conductor material needs to be chosen carefully to minimize the antenna's conductive losses. Printed antennas on textile suffer from around 10 μm surface roughness which reduces the conductivity at microwave bands. Flexible laminates, and metalized shielding fabrics are mechanically more reliable and resilient to cracking compared to printed traces [292, 293]. Moreover, their sheet resistance is lower than that of low-temperature conductive inks [190]. As the proposed antenna features are all larger than 1 mm, laser or die-cutting can be utilized for faster turn-around and reduced fabrication costs. Conductive fabric (P&P Microwave weave, 0.005 Ω/square, with adhesive backing) was chosen as it offers improved user comfort compared to flexible copper sheets. The fabric have been cut using a standard CO_2 laser-cutter, to create features larger than 1 mm, as shown in Fig. 4.1-a.

To fabricate a miniaturized rectifier supporting low-footprint component packages photolithography has to be utilized. The process described in [185] has been utilized to fabricate the rectifier (Fig. 4.2-c). Features down to 150 μm, such as surface mount components pads, can be resolved using a commercial copper etcher and a standard UV

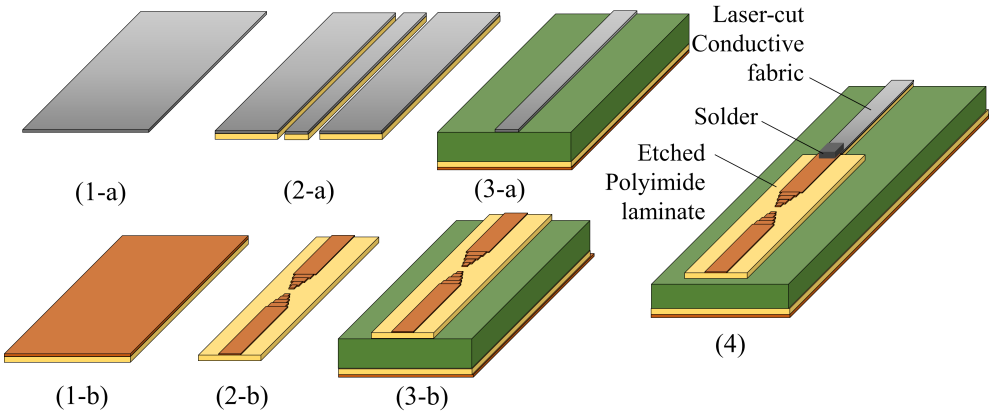

FIGURE 4.1: Textile rectenna fabrication steps: (1-a) conductive fabric prior to cutting, (2-a) laser cut antenna traces, (3-a) adhered laser-cut traces on the felt substrate. (1-b) polyimide copper laminate, (2-b) etched copper laminates, (3-b) etched traces adhered to felt, (4) integration of laser-cut and etched Polyimide laminates using a solder interface.

light source without the need for a clean room environment. For improved reliability, textile-based electronics require encapsulation [183, 293]. Fabricating flexible circuits on thin polyimide filaments for textiles integration support encapsulation techniques such as vacuum-forming [183]. Encapsulated RFID tags have been demonstrated withstanding over 30 machine washing cycles [183]. Fig. 4.2 shows photographs of the fabricated rectenna and rectifier prototypes.

The unresolved challenge in realizing a RF textile system employing two fabrication processes is in demonstrating a low-loss transition between the transmission lines. Connections between textile RF transmission lines and a standard PCB have been addressed previously using broadside coupling between a fabric and a Duroid microstrip with 0.7 dB losses at 2.4 GHz [11], and hook-on flexible interconnects of approximately 1 dB loss up to 2 GHz [294]. As the thickness of the conductive fabric and the flexible Polyimide PCB is comparable, a solder interface can be utilized at the transition between the copper and conductive fabric, as shown in Fig. 4.1 and 4.3. Low-temperature solder (melting point=170°C) is utilized to prevent damaging the metalized woven threads of the antenna, alternatively, a layer of thin conductive epoxy can be used in order to further reduce process temperatures, making this transition compatible with all textile materials.

To investigate the effect of the conductive fabric to flexible PCB transition, two 60 mm microstrip lines were fabricated, a fully flexible copper line, and a hybrid 50% copper, 50% conductive fabric with a soldered interconnect line. The insertion losses through both lines are measured using a VNA up to 2 GHz. Compared to the fully copper line, as shown in Fig. 4.3, the hybrid line experiences only 0.50, 0.41 and 0.22 dB additional insertion losses at 0.75, 1.9, and 2.4 GHz, respectively. Therefore demonstrating the lowest loss on-fabric transition compared to [11] and [294].

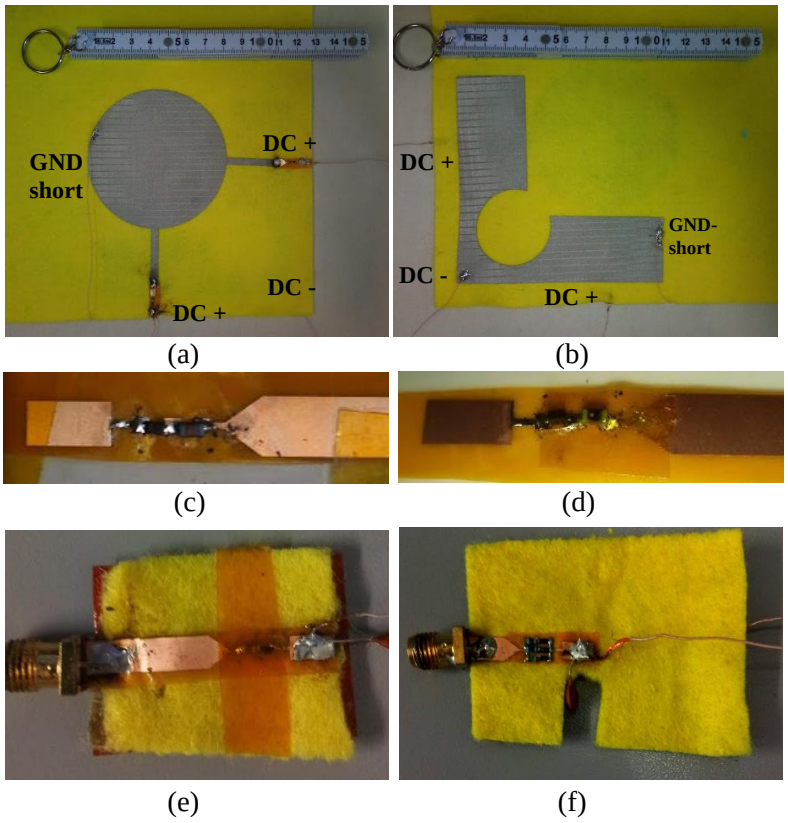

FIGURE 4.2: Photographs of the rectenna and rectifier prototypes: (a) top-side of the assembled rectenna, (b) bottom-side of the assembled rectenna, (c) close-up photo of the rectifier prior to integration with the textile substrate, (d) the rectifier following Kapton encapsulation, (e) the single band connectorized rectifier used in PCE measurements, (f) the multi-band rectifier prototype.

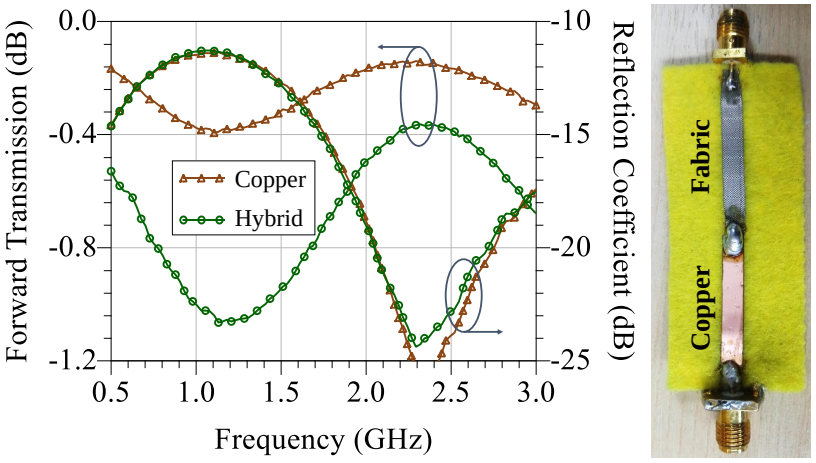

FIGURE 4.3: The textile-flexible circuit interface measured s-parameters (left) and photograph of the 60 mm-length prototype (right).

4.1.2 Dual-Polarization Broadband On-Body Antenna

In recent implementations, ambient RFEH has been synonymous with multi-band harvesting [13]. In order to harvest a considerable power density from ambient sources,

the antenna needs to radiate at multiple bands between 0.7 and 2.7 GHz [13]. Dual [26], triple [43,71], broadband [80], and six-band rectennas are becoming increasingly popular [33].

Broadband antennas, mainly developed for Ultra-Wide-Band (UWB) communication (3-10 GHz) [279], can be scaled to cover the UHF microwave bands of interest in RFEH context. A microstrip-fed design, the circular disc monopole [279], is adopted due to ease of implementation using simple fabrication techniques. Furthermore, being a wire-type antenna with no ground-plane-backing, the electric-fields dissipated in the lossy textile substrate will be minimized implying the possibility of achieving higher gain and radiation efficiency.

In order to efficiently harvest arbitrarily-propagating RF power, the antenna needs to be independent of the incident wave's polarization angle to avoid Polarization Mismatch Loss (PML), as discussed in Chapter 2.4.5.2. The circular monopole design has been modified to include two feeding points, for horizontal and vertical LP reception. Both ports are fed using 50 Ω microstrip lines for ease of testing, and for integration with 50 Ω-matched rectifiers. The ground planes of both ports overlap at the corner of the antenna, increasing the antenna's port coupling (S_{21}). The simulated surface current plot of the antenna at 900 MHz, in Fig. 4.4-b, shows that a significant portion of the current travels from the H-LP port to the V-LP port through the inner corner of the ground plane. Therefore, the antenna is modified through voiding the ground plane using a circular notch reducing the current flow between the ports. In CST simulations, the notch improves the port-isolation by 5 dB from 0.8 to 2.4 GHz. In the context of RFEH, this increases the amount of RF power at the individual port, allowing the rectifier to achieve higher PCEs.

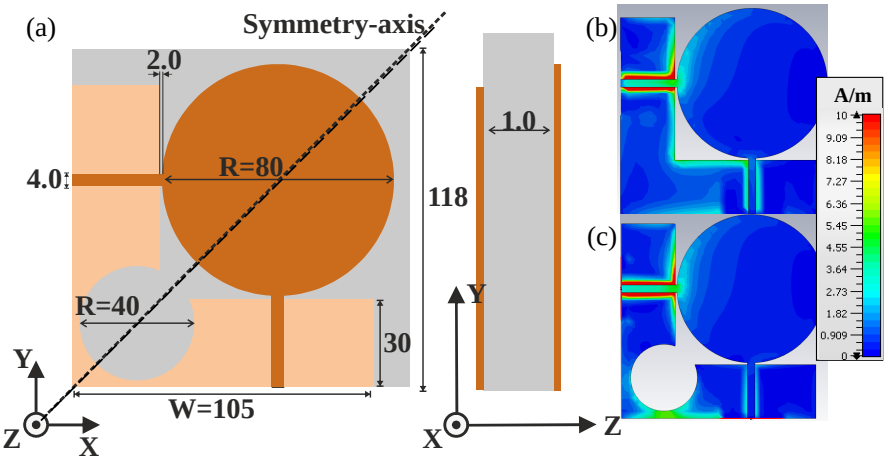

FIGURE 4.4: Dual-polarization broadband disc monopole geometry (a), dimensions in mm, and the surface current plot at 900 MHz before (b) and after (c) ground-voiding.

4.2 Antenna Simulation and Measurement

The antenna has been simulated in CST Microwave Studio, the model utilized the extracted material properties of the substrate, as well as a lossy copper model with 1 μm surface roughness, to accurately model the skin-depth losses. The s-parameters were measured using a ZVB4 VNA, Fig. 4.5 shows the simulated and measured s-parameters of the antenna, showing a $S_{11} < -10$ dB bandwidth from 800 MHz to 3.5 GHz, and more than 14.5 dB port isolation from 0.8 to 2.45 GHz. The slight discrepancy observed between the simulated and the measured s-parameters is due to the non-uniformity of the coax-microstrip interface at the SMA connector, due to the high-flexibility of the substrate.

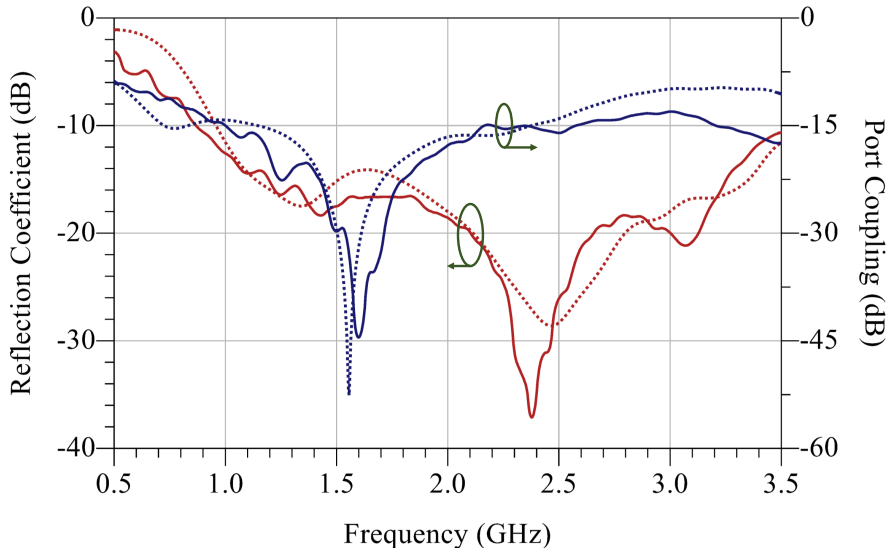

FIGURE 4.5: Simulated (dashed) and measured (solid) reflection coefficient (S_{11}) and port coupling (S_{21}) of the proposed dual-polarization textile monopole.

As the antenna is designed to maintain broadband operation, it is not possible to shield the antenna using a solid ground plane or a reflector. Such conductive-backing would result in a narrow-band response similar to a microstrip patch. In addition, it is desired to have wide angular coverage to be able to harvest arbitrarily-directed plane waves [132]. In human-proximity, it has previously been shown that the resonance of monopole antennas can shift by over 20% at 2.4 GHz [185]. Therefore, it is essential to measure the reflection coefficient of the antenna when operating on-body.

The antenna has been mounted on a user's chest with a non-uniform separation of ≈1 mm gap of clothing and air as shown in Fig. 4.6-b. A human model, AustinMan [295], was included in the antenna's 3D model in CST to simulate the gain (Fig. 4.6-a). Fig. 4.7-a compares the measured reflection coefficient of the antenna on-chest and on-leg with the simulation using the AustinMan. The measurement on-leg includes bending across a ≈7 cm radius. Both the simulation and measurement agree in showing a $S_{11}<-10$ dB

from 0.8 to 3.5 GHz. The discrepancies below −15 dBm could be attributed to additional crumpling of the antenna prototype and additional mismatch at the SMA.

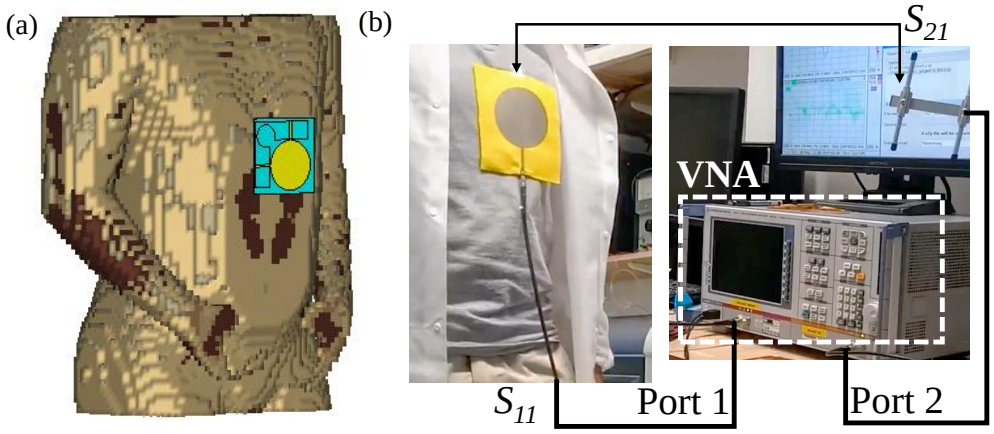

FIGURE 4.6: Antenna on-body simulation model (a), and measurement setup (b).

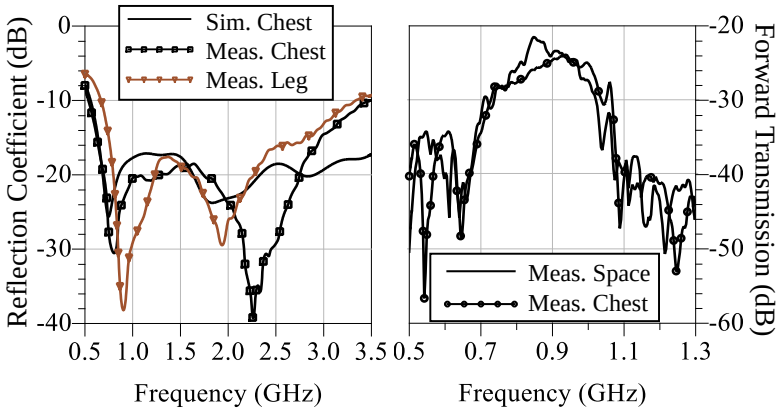

FIGURE 4.7: S-parameters of the wearable antenna: (left) simulated and measured S_{11} on-body, (right) S_{21} between the textile antenna and a 10 dBi 900 MHz log antenna at 1 m.

Certain placements on the body imply that the antenna may be bent over a sharper radius than that in Fig. 4.7, where the forward transmission was measured on-chest. In [288] (see appendix A), it is shown that placing energy harvesting antennas on the extremities of the body (i.e. arm or leg) results in improved off-body link budget [288]. Fig. 4.8 shows the antenna's S_{11} while being bent over various body parts over radii between 70 and 30 mm. It can be seen that the antenna maintains its broad bandwidth over all body placements. The antenna was simulated on the Austinman model's arm with a 50 mm bending radius showing −2.21, 2.78 and 3.07 dB gain at 0.8, 1.5, 2.2 GHz, respectively, compared to −3.87, −0.28, and −0.68 dB, when placed flat on the model's chest. The higher on-arm gain agrees with the measurements in [288] showing improved antenna gain when placed on the arm compared to on-torso placements for both a monopole and a microstrip patch.

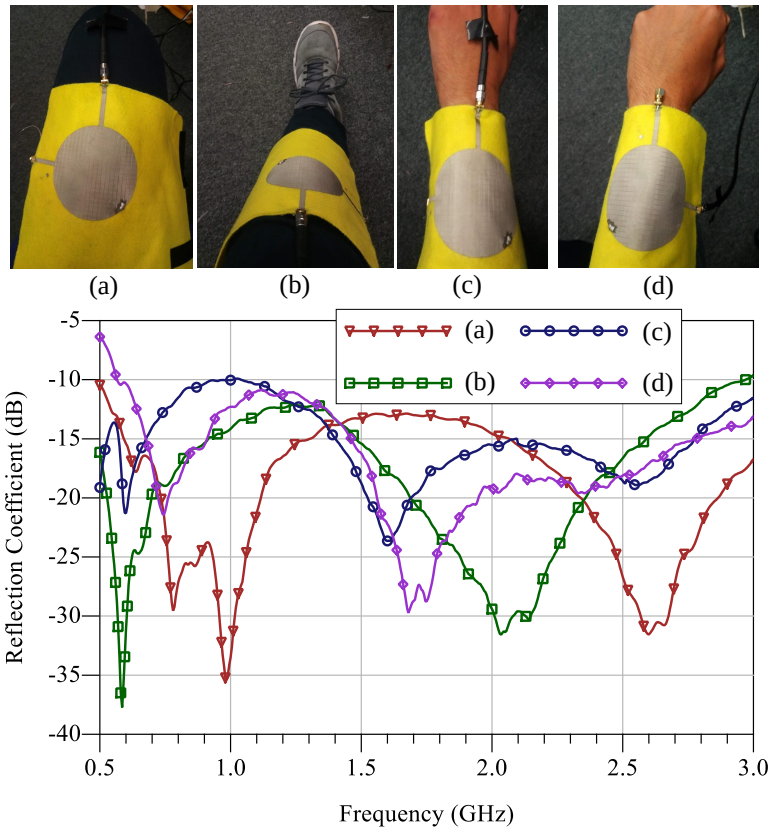

FIGURE 4.8: Measured antenna's S_{11} during bending over various body parts: (a) 70 mm bending radius the y-axis on-thigh, (b) 55 mm bending radius on the y-axis on-leg, (c) 30 mm bending radius on the y-axis on-wrist, (d) 30 mm bending radius on the x-axis on-wrist

In addition to impedance matching, the degradation in an antenna's realized gain in proximity with the human body needs to be quantified. The forward transmission (S_{21}) between the textile antenna and a 10 dBi log-periodic antenna has been measured at 1 m separation, as shown in Fig. 4.6-b. The measured S_{21} is shown in Fig. 4.7-b. At 846 MHz, the maximum degradation in the gain is observed with the on-chest S_{21} (Fig. 4.6), and is 4.4 dB lower than that measured in space.

The measured gain, based on the free-space losses at 1 m and the 10 dB log antenna gain is −4.87 dB. This shows good agreement with the simulated antenna gain of −4 dB using the AustinMan model in Fig. 4.6-a. When the measurements were repeated to reduce the uncertainty due to multi-path reflections, the measured gain varied between −6.5 dB and −4 dB, on-body. Such variation could be attributed to subtle changes in the 1 mm separation between the antenna and the body.

An additional requirement in the design of wearable antennas is compliance with the SAR regulations. This is particularly relevant as the proposed antenna is unisolated from the body. Therefore, the power levels at which the antenna can be used safely are simulated in CST Microwave Studio to calculate the antenna's SAR. Fig. 4.9 shows the simulated SAR of the on-chest antenna; the peak SAR for a received/transmitted power

of 20 and 10 dBm is 0.876 and 0.088 W/kg, respectively, when normalized to 1 gm of tissue mass. Both values are well below the 1.6 W/kg limit for mobile phones in the U.S. Recpetion of power levels exceeding 20 dBm in the far-field is very unlikely using EIRP-compliant transmitters.

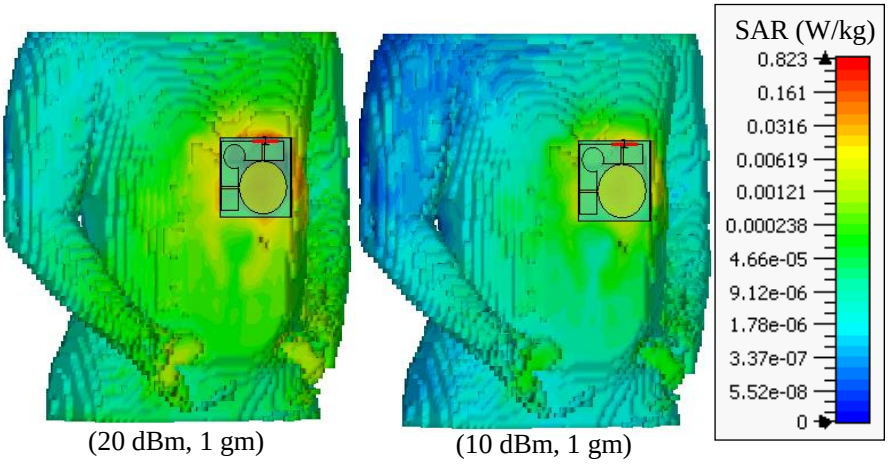

FIGURE 4.9: Simulated SAR of the antenna on the Austinman phantom at 20 and 10 dBm, normalized to 1 gm.

In the rectenna, the 50 Ω port connection is replaced with a connection to the rectifier. The rectifier requires a shunt current return path, before the diode, for the DC currents [282, 296]. Such a return path could be achieved using a shunt inductor in the matching network. However, this requires an additional through-textile via which would complicate the fabrication process. To mitigate this, the current return path is built into the antenna. As the antenna is broadband, an additional ground-shorting textile wire could be connected between the monopole's disc and the bottom ground plane, without affecting the S_{11} bandwidth. The ground shorting thread added to the antenna is shown in the photograph in Fig. 4.4-a and b (GND-short). The s-parameters in Fig. 4.7 were measured after the GND-short thread was added which does not affect the impedance matching.

4.3 Textile Microstrip Rectifier

4.3.1 Rectifier Design and Modeling

Reported rectifier designs have focused on designing a rectifier first, computing or measuring its input impedance, then designing a 50 Ω matching network or a complex conjugate antenna to match the rectifier's input impedance. While this approach achieves a good impedance match and high PCE, the design of the rectifier should not be input-impedance agnostic, as the PCE of a rectenna is not only dependent on the reflection coefficient (S_{11}) and the diode's parameters, but also on the source and load impedances, as discussed in Chapter 3.3.

The input impedance of a single series diode is typically very high, approaching open-circuit impedance at lower-frequencies. Nevertheless, the impedance values reported in RFEH studies and from diode manufacturer's measured s-parameters vary significantly between 1000 Ω to 10 Ω. This is attributed to the quarter wave transformer effect introduced by the 2-port network, i.e. feed-line, any lumped components, or packaging parasitics between the input port and the diode's junction. This network can be represented as a line of length l, and impedance Z_l, varying the observed input impedance as in (4.1),

$$Z_{in} = Z_0 \frac{Z_l + jZ_0 tan(\beta l)}{Z_0 + jZ_L tan(\beta l)}, \tag{4.1}$$

making it more difficult to achieve a broadband impedance match.

For simplicity, considering a 50 Ω air-dielectric microstrip feed-line of length l, for $0 < l < \lambda/4$ (typical for most commonly used lines below 3 GHz), any increase in l will result in a reduction of the observed input impedance, subsequently resulting in increased variation in the input impedance, due to the more variable range of frequencies to be matched in cellular RFEH. Fig. 4.10 shows the input impedance of a single-series rectifier, based on the SMS7630-079lf diode with different microstrip feed lengths, as seen by a 50 Ω port.

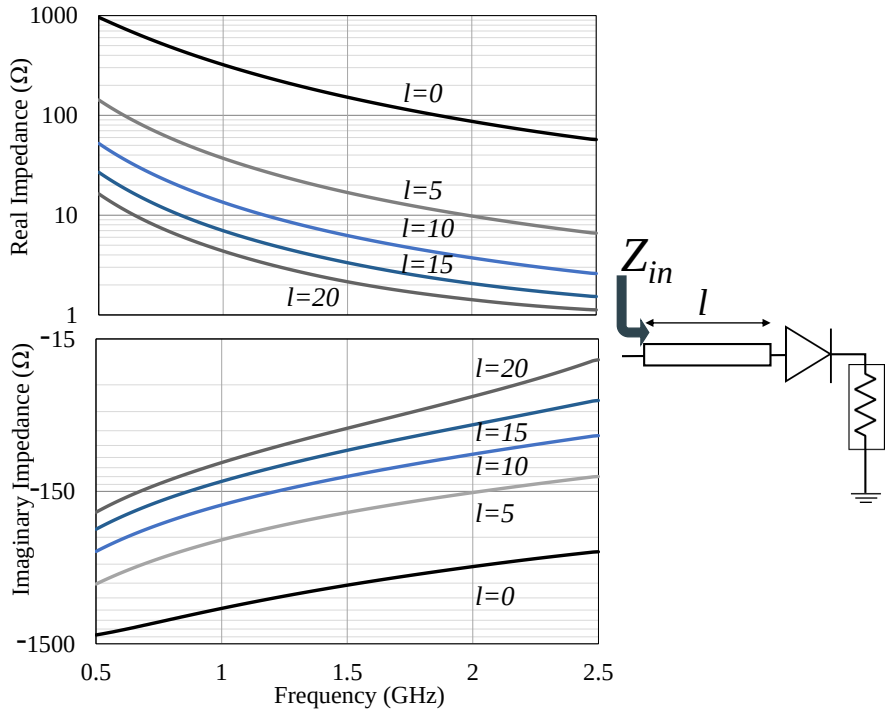

FIGURE 4.10: Single-series rectifier input impedance variation with the microstrip feed-length, l, in mm.

It can be observed that although $\Re\{Z_{in}\}$approaches short circuit impedance as l approaches $\lambda/4$, the imaginary impedance sustains a higher capacitive component due to the diode's junction and packaging parasitic capacitance. While this can be factored in

the matching process, a predominantly reactive source impedance will limit the maximum achievable PCE of the system [77]. Thus, operation in the diode's resistive region allows achieving higher PCE using the same diode. In addition, varying the length between the diode and the matching components can lower the observed input impedance. This makes matching a 50 Ω antenna or port easier.

As this rectenna is optimized for maximizing PCE rather than voltage sensitivity, the rectifier topology of choice is a single series rectifier. The low voltage output of a single-series rectifier can be boosted using a high-efficiency low-power boost converter as in [11]. Furthermore, an additional advantage of a single-series rectifier is its high impedance ($\Re\{Z\}$) compared to a voltage doubler [297], enabling easier input matching over a wider bandwidth. The chosen diode is the Skyworks SMS7630-079lf, usable up to 9 GHz, due to its low series resistance and junction, and having a very low voltage drop $0.06 < V_f < 0.12$ mV for 0.1 mA diode current. Thus, it has been widely utilized in high-efficiency low-power rectennas [11, 80, 132]. As this work focuses harvesting low power densities, the relatively low breakdown voltage of the diode which will result in reduced PCE at higher power levels does not represent a practical issue.

4.3.2 High Impedance-Transformer Matching

From Fig. 4.10, it can be seen that a feed-line of 5 mm length can transform the observed $\Re\{Z_{in}\}$ to 50 Ω. Higher order distributed element networks were avoided due to the expected insertion losses in the lossy textile substrate [43]. Furthermore, while broadband matching has been reported using complex matching networks [26,33,80,298], a triple-path rectifier is implemented to achieve the multi-band operation for harvesting power from different bands, without increasing the size or order of the matching network.

An ideal series inductor, of impedance $Z = j\omega L$, can match $\Im\{Z_{\text{in}}\}$, and the microstrip traces can match the high $\Re\{Z_{\text{in}}\}$ (Fig. 4.10). In reality, a packaged lumped inductor carries associated capacitive and resistive parasitic components, as shown in Fig. 4.11-c. Therefore, accurate modeling of the inductor's parasitics, similar to the diode's parasitics in Fig. 4.11-d (usually given by the manufacturer) is required to obtain a close match between the simulation and analytical models and the measured results.

4.3.3 Single and Multi-Band Rectifiers

Two microstrip rectifiers with 50 Ω input matching are designed for the felt substrate, to be etched as described in section 4.1.1. The rectifiers are a 820 MHz (5G and LTE frequency in the U.K.) single-band single-path rectifier, and a multi-band triple-path rectifier matched at 940 MHz, 1.5 and 2.1 GHz. The layout of the proposed rectifiers is shown in Fig. 4.11, where the 50 Ω microstrip feed is connected to the output of

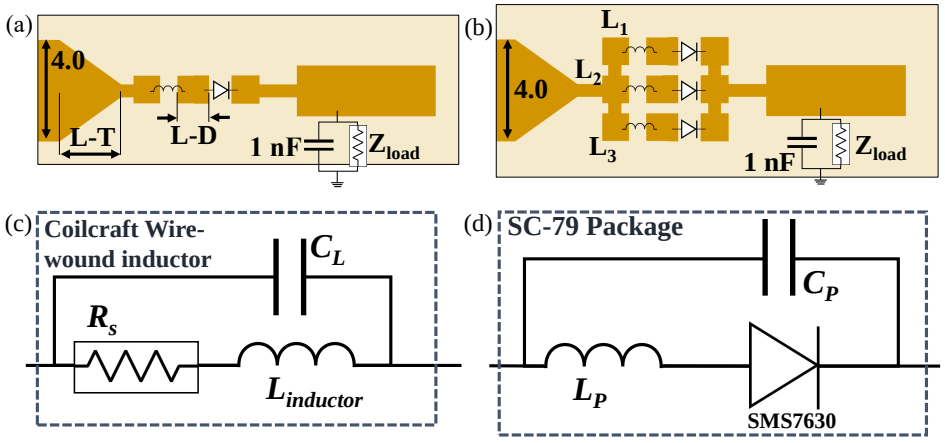

FIGURE 4.11: Layout of the proposed microstrip rectifiers: (a) single-band, (b) multi-band, (c) equivalent circuit of a lumped matching inductor, (d) equivalent circuit of a packaged diode.

the fully-textile antenna using the conductive fabric to flexible PCB transition shown in Fig. 4.3. The values of the matching inductors in Fig, 4.11 are L=82 nH for the single-band rectifier, and L_1=56 , L_2=20, L_3=11 nH for the multi-band rectifier. The choice of inductance, taper length (L-T) and separation between the indutor and diode (L-D) are discussed in the next section.

4.4 Rectifier Simulation and Measurements

4.4.1 Large-Signal Rectifiers' Performance

The rectifiers have been simulated using harmonic balance in Keysight ADS, based on the datasheet model for the diode's characteristics. The packaging parasitic inductance and capacitance have been obtained from the datasheet as well as the mismatched diode's S_{11} measurement, using a high-power VNA. The single and triple-band rectifiers have been simulated using closed-form microstrip-models for accurate modeling of the soldering pads, and the feed point from the 50 Ω source.

The initial values for L-T an L-D in Fig. 4.11-a are 2.5 and 0.5 mm, respectively. A parameter sweep of different inductances has been performed to maximize the PCE at −20 dBm as in Fig. 4.12. This process ensures a proper $\Im\{Z\}$ match is obtained. The next step is tuning the microstrip layout to maximize the $\Re\{Z\}$ match. Fig. 4.13 shows the PCE as a function of the microstrip taper and pad between the diode and the inductor. As previously shown in Fig. 4.10, a longer feed line (L-D) will result in a lower observed $\Re\{Z\}$. The optimal values for L-T and L-D demonstrate that a compact rectifier will achieve the highest PCE. Such compactness gives the additional advantage of mitigating the insertion losses associated with the fabric substrate.

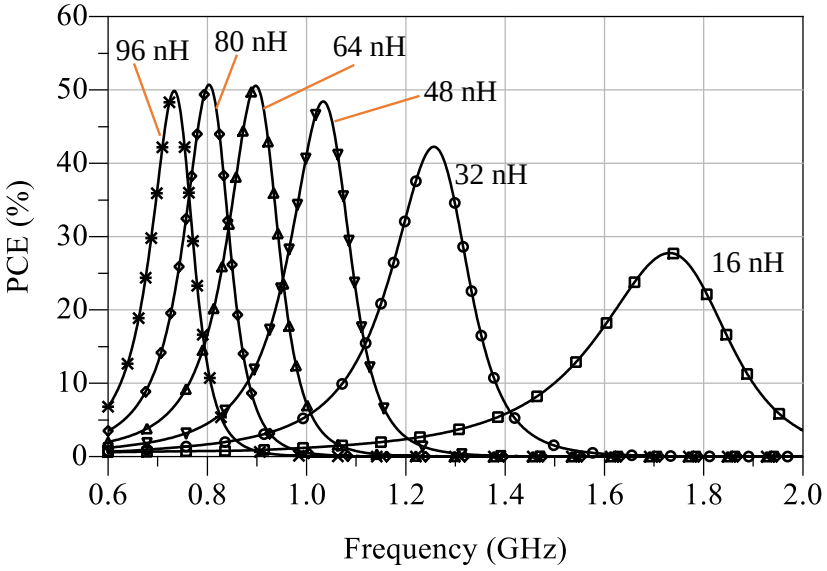

FIGURE 4.12: The rectifier's −20 dBm PCE as a function of frequency for different matching inductor values.

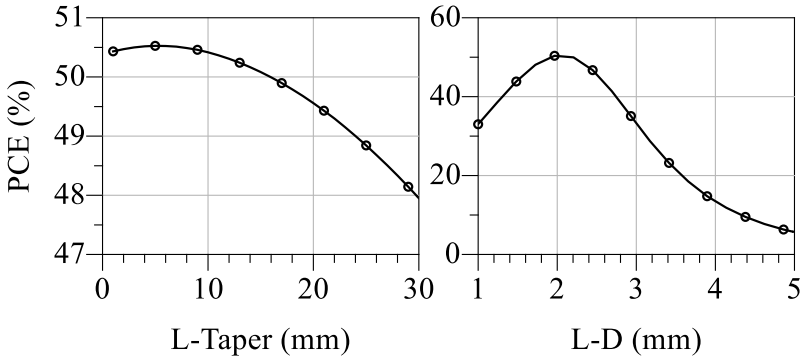

FIGURE 4.13: The rectifier's −20 dBm PCE as a function of the microstrip taper length (L-T: left) and the length between the inductor and the diode (L-D: right).

A Continuous Wave (CW) output from the VNA has been used to measure the large-signal reflection coefficient of the single-band rectifier and compare it with the simulated model, across a 7 kΩ. The matching inductors were simulated using both an ideal model with C_L=0.1 pF and the manufacturer s-parameters. An additional C_L component of 0.07 pF was added post-measurement to the s-parameters model. Fig. 4.14 shows the reflection coefficient of the rectifier, demonstrating an improved impedance-match in the low power region, corresponding to the design range of this work. Given the optimized impedance match for −20 dBm, it is expected that the proposed rectifier achieves higher PCE compared to reported rectifiers utilizing a similar diode, with a generic matching network. Fig. 4.15 shows the measured PCE of the single-band rectifier demonstrating high PCE at 10 μW power levels. Based on the simulation using an ideal inductor in Fig. 4.15, the maximum achievable PCE at −20 dBm is 50%.

To demonstrate the reliability of the proposed rectifier, the DC measurements were repeated over multiple bending cycles. Repetitive bending of textile-based electronics is

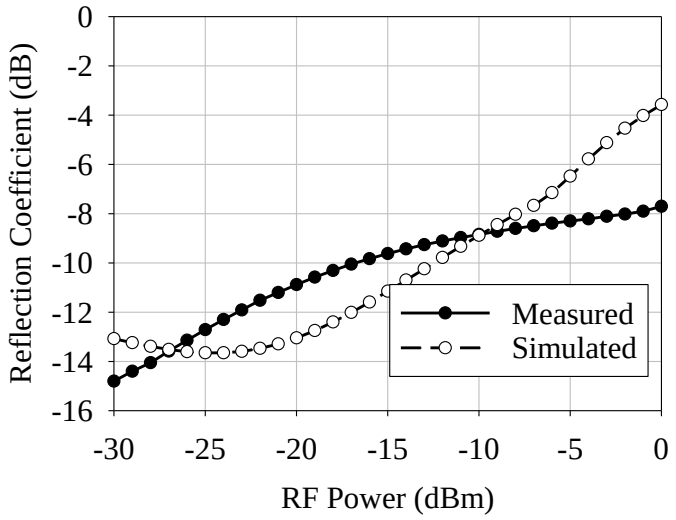

FIGURE 4.14: Simulated and measured reflection coefficient (S_{11}) of the single band rectifier at different RF power levels from the CW VNA.

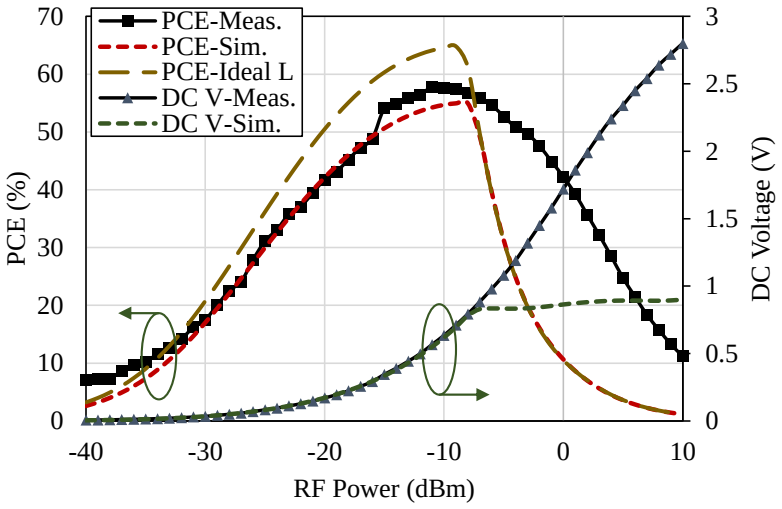

FIGURE 4.15: Simulated (dashed) and measured (solid) PCE and DC voltage output of the single-band textile rectifier, at 820 MHz, with a 7 kΩ load resistor.

widely used as a reliability test [293]. Five bending cycles of the rectifier prototype in Fig. 4.2-e were performed before the DC output was measured at −20 and −10 dBm. Fig. 4.16 shows the measured DC voltage for 250 bending cycles. Each bending cycle was performed at a sharp bending radius of <5 mm, the DC voltage was measured during and after bending and no noticeable difference was observed. The maximum variation for both −20 and −10 dBm was less than 3%, and did not resemble a permanent or cumulative degradation. Such a reliability test demonstrates the rectifier's suitability for the harshest wearable applications, and is in line with the reliability tests of electronic textiles in [293].

To investigate the losses associated with the textile-based interconnects, the single-band rectifier has been prototyped on a standard FR4 PCB. The DC voltage of the textile rectifier at −20 dBm was only 4.6% lower than that of a its rigid counterpart. This

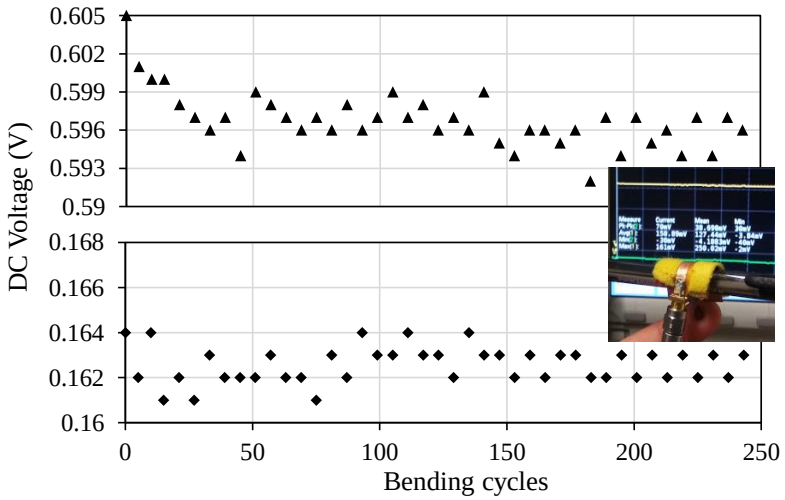

FIGURE 4.16: Measured DC output at −10 (top) and −20 dBm (bottom) for repetitive bending cycles; inset shows photograph of the bent rectifier.

translates to less around 1% PCE-improvement when migrating to a rigid FR4 substrate, concluding that compact lumped matching enables mitigation of the insertion losses associated with textile transmission lines and substrates. As FR4 is a lossy substrate, the purpose of this is to demonstrate that interconnects on textile do not affect the performance. The rectifier's has been simulated for a tanδ=0 substrate and the −20 dBm PCE was 44.5% as opposed to the 41.8% measured PCE of the proposed rectifier on the felt substrate.

A key advantage of the textile-based inductor-matched rectifier is the simple frequency tunability by varying the inductance, shown in Fig. 4.12. To further demonstrate the scalability of the proposed textile-based rectifier design, the value of the matching inductor was varied on the fabricated prototype to investigate its bandwidth and PCE. A 56 nH lumped inductor was selected to match the rectifier at 1 GHz. Fig. 4.17 shows the simulated and measured S_{11} of the rectifier, showing a close agreement and validating the previous simulated results in Fig. 4.12.

To verify that the large-signal performance of the rectifier is unaffected by the change in frequency, a power sweep was carried out at 1 GHz from the CW source. Fig. 4.18 compares the measured and simulated PCE of the rectifier matched for 800 MHz and 1 GHz. It can be observed that for the targeted power levels, −20 to −10 dBm, the rectifier maintains its PCE which surpasses SoA implementations. The lower PCE measured at 1 GHz below −21 dBm can be attributed to minor variations in the optimal load impedance of the rectifier, which could be be avoided by tuning the load for the rectifier using MPPT or a bespoke boost converter [11].

The multi-band rectifier (Fig. 4.11-b) has been connected to a VNA to measure its bandwidth and evaluate its performance, Fig. 4.19 shows the measured reflection coefficient of the rectifier at different power levels. As with the single-band rectifier, it is

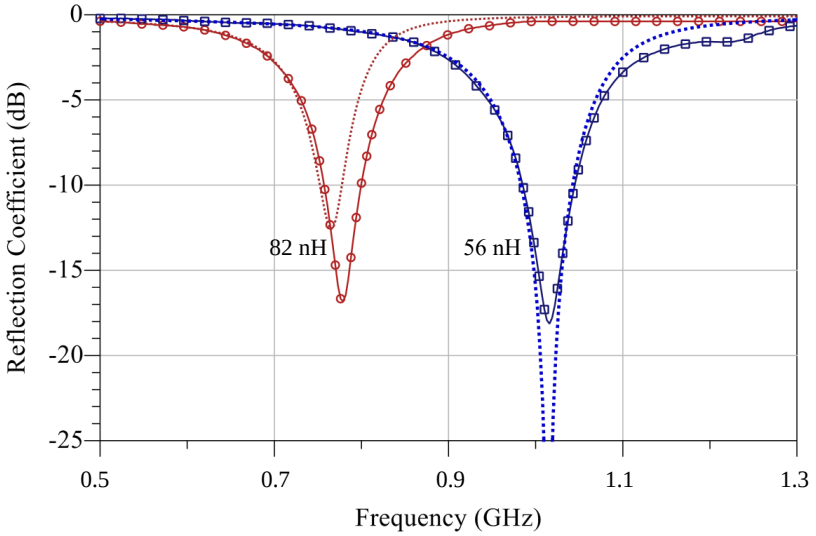

FIGURE 4.17: Simulated (dashed) and measured (solid) S_{11} of the rectifier, at −20 dBm, far two inductor values.

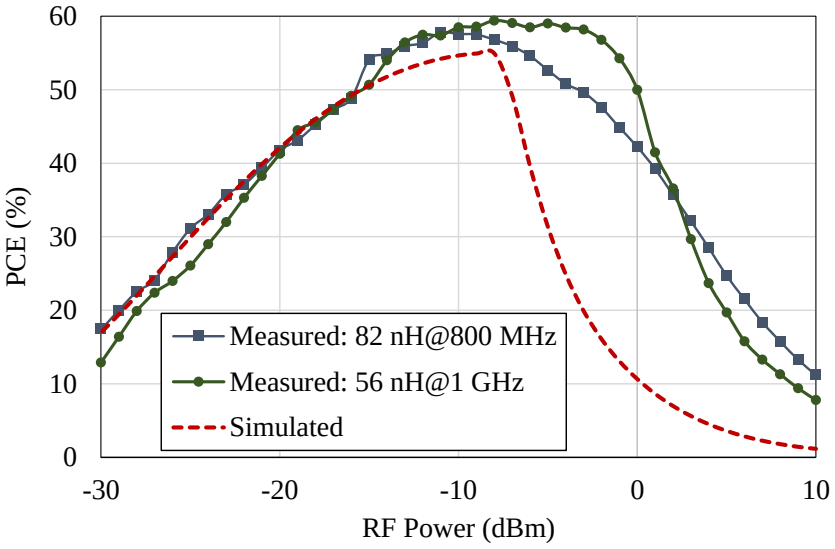

FIGURE 4.18: Simulated (dashed) and measured (solid) PCE of the single-band inductor-matched rectifier far two inductor values.

observed that the reflection coefficient changes with the available RF power, due to the variation in the diode's input impedance. For example, at 960 MHz (GSM RFEH band) it is observed that the rectifier is optimized for −20 dBm and below. On the other hand, the inductive matching at 1.5 GHz improves at higher power levels (minimum reflection is achieved at 0 dBm). This is due to the diode's lower impedance at higher frequencies and the inductors approaching their self-resonant frequencies where the inductance is higher than the datasheet values. The low self-resonant frequency is due to the lower frequency matching inductor. The 56 nH 0603 Coilcraft inductor used for matching at 960 MHz self resonates at 1.9 GHz, which may result in additional interference with the high frequency rectifier path. Fig. 4.20 shows the measured large-signal reflection coefficient of the rectifier at the four bands where a drop in the S_{11} is observed.

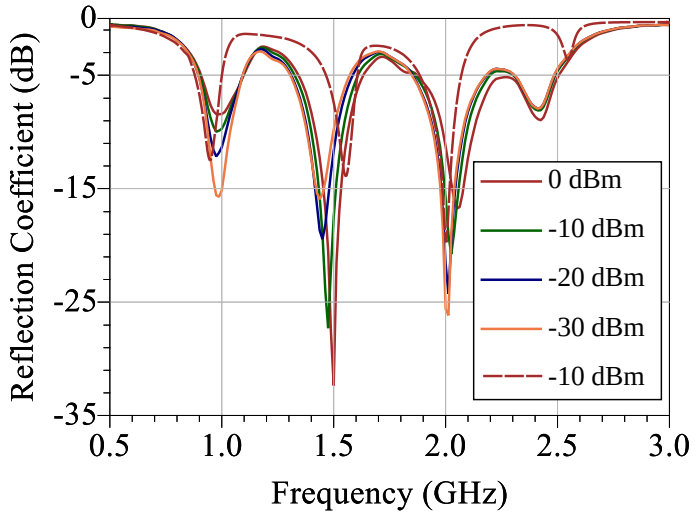

FIGURE 4.19: Measured (solid) and simulated (dashed) reflection coefficient of the multi-band rectifier.

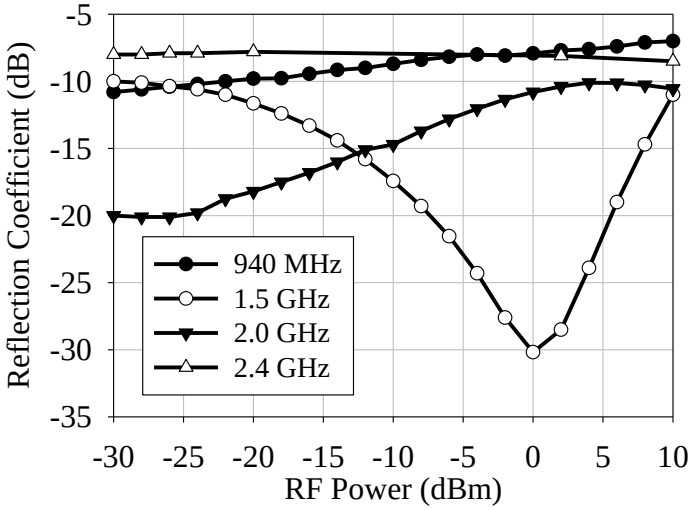

FIGURE 4.20: Measured large-signal reflection coefficient of the multi-band rectifier with variable input power levels, at the frequencies where a resonance was observed.

The multi-band rectifier, despite being well-matched at three frequency bands (cellular and ISM-bands), suffers from reduced PCE at both sub-100 μW levels (the design range of the single-band rectifier) and at their peak PCE, as a result of the additional multi-path reflection. To explain, the frequency-selective multi-path rectifier results in additional current flow of the RF signal in the microstrip network as well as the lumped components, due to the impedance mismatch of every other branch happening at the diode's plane rather than the microstrip cross-junction. This is attributed to the microstrip lines' short length compared to the wavelength, resulting in the signal traveling towards the diodes before being reflected and finally accepted by their respective branch based on the frequency. In addition, unintended resonance observed at 2.4 GHz is due to the mutual-inductance between the three paths and hence does not contribute to the DC output. While it is possible to use open stubs to suppress harmonics at the output, open stubs

are not included to keep the rectifier compact and minimize the circuitry covering the textile. Lack of harmonic termination is the reason the 2 GHz PCE degrades to about 50% of that at 0.96 and 1.5 GHz. Fig. 4.21 shows the PCE of the rectifier at variable RF power levels.

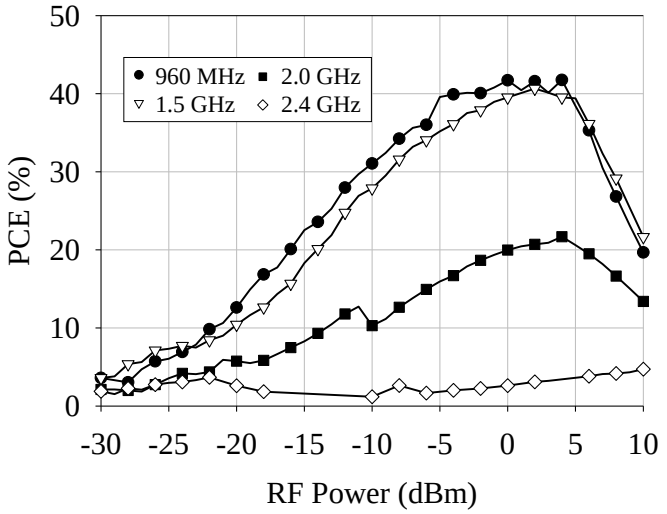

FIGURE 4.21: Measured PCE of the multi-band rectifier, at the different frequencies where a resonance is observed, with a 4.7 kΩ load.

From Fig. 4.21, it is observed that the PCE diminishes at higher frequencies, which is attributed to the mutual coupling between the tightly-positioned matching inductors. To illustrate, the higher-value inductor L_1 has a self-resonant frequency below 2 GHz, resulting in a smaller portion of the incident high-frequency signal being accepted by the diodes, hence reducing the PCE. This highlights the limitation of multi-band inductive matching using non-ideal components.

4.4.2 Resistive DC Load Sweep

As the rectifier's performance is expected to vary significantly based on the load impedance, the performance of the proposed rectifiers have been investigated for various resistive loads, as well as a capacitive load acting as an energy storage unit directly connected to the rectenna, eliminating the DC power management stage. A DC resistive load sweep has been carried out experimentally and in simulation to find the rectenna's optimal load impedance for both the single-band and multi-band rectifier. Fig. 4.22 and 4.23 show the PCE at variable load impedance at −20 and −10 dBm input power.

From Fig. 4.22, the proposed rectifier achieves a best-in-class PCE of 41.8% at −20 dBm with a 7 kΩ load, in good agreement with the simulated maximum PCE of 43% at the same frequency. The load impedance of the rectifier is in line with other rectennas such as [11] and [33] and allows a balance between the DC voltage output and a high PCE. This is achieved due to the optimized impedance matching for low RF

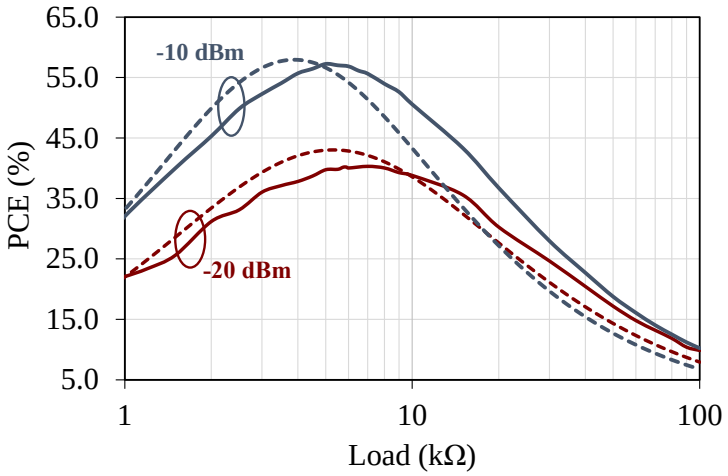

FIGURE 4.22: Measured (solid) and simulated (dashed) PCE of the proposed single-band rectifier.

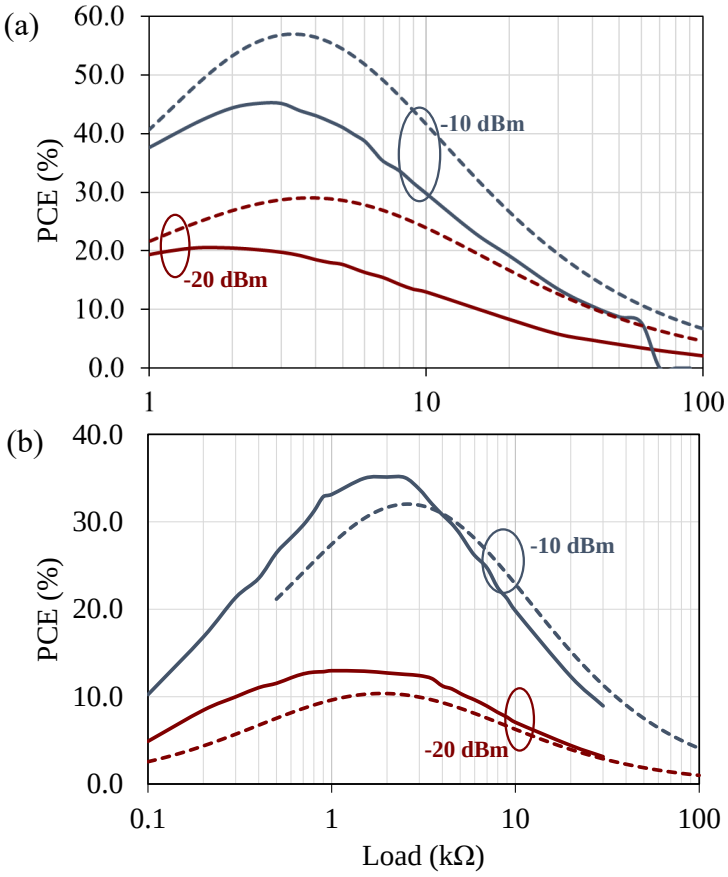

FIGURE 4.23: Measured (solid) and simulated (dashed) PCE of the multi-band rectifier at (a) 960 MHz and (b) 1.5 GHz.

power levels and the high-impedance end-to-end environment described in section 4.3.2. Additionally, more than 10% of the maximum PCE is maintained from 2.5 to 14 kΩ and 3.0 to 13.3 kΩ at −10 and −20 dBm respectively. Finally, the validity of the inductor's equivalent model proposed in Fig. 4.11-c is validated across varying Z_{load}.

The multi-band rectifier model exhibits discrepancies with the measured results especially at 960 MHz, due to the resonance shift previously observed in the S_{11} (Fig. 4.20). The fabricated rectifier prototype, despite achieving more than 20% and 45% PCE at 960 MHz which is in-line with reported values using the same rectenna, fails to achieve the simulated PCE approaching 60% at −10 dBm. This can be attributed to the tight spacing (<1 mm clearance) of the "lumped" inductors, resulting in a considerable mutual-inductance component as well as coupling between the rectifier's branches causing additional stray currents dissipating in the inductors' parasitics and the fabric substrate. The manufacturer's measured s-parameters of the coil clearly exclude the effects of other components in proximity as well as the effect of external interconnects resulting in variable C_L.

4.4.3 Rectifier Capacitive Load Analysis

Energy storage is essential in energy harvesting and intermittently-powered systems to enable cold-start of a battery-free load. Therefore, it is essential to characterize the performance of RF rectifiers directly with a capacitive load. While recent studies have investigated the charging time of a capacitor using a low-power rectenna [39], using a power-management circuit masks the capacitor's current draw and does not give any insight on the impact of the charging curve on a rectifier's S_{11}.

Motivated by keeping the component count low in the system to improve its flexibility and reliability, a discrete power management interface is avoided. Furthermore, multiple state-of-the-art low-voltage transceivers and micro-controllers have been reported with turn-on voltages as low as 250 mV [299]. Thus, the output voltage of the rectenna could be directly stored without stepping-up using a DC-DC boost converter. In Chapter 8, a similar approach is proposed to integrate a textile supercapacitor with an "e-textile" rectenna.

A storage capacitor, C_{store}, has been connected directly to the output of the microstrip rectifier replacing Z_{Load}. C_{store} is implemented using electrolytic capacitors of 1.32 mF capacitance. The performance of the single-band rectifier, with C_{Store} replacing the dummy resistive load, has been experimentally measured. The charge level in the capacitor affects its ability to be charged from a voltage source. Thus, the equivalent input impedance of the capacitor will vary during the charging cycle changing the rectifiers S_{11}. Considering the difficulty in modeling the internal DC and RF parasitics of the electrolytic capacitors, simulation of the capacitive load was not performed. A VNA has been used in CW mode as a power source to excite the single-band rectifier, while measuring the reflection at the input. As the large-signal input impedance of the capacitor is not known, it is crucial to measure the input reflection coefficient to ensure the capacitive load does not degrade the rectenna's impedance match. The DC voltage across the capacitor has been measured using an oscilloscope during the charging time

of the capacitor, until a steady state voltage is reached. Fig. 4.24 shows the charging time of the capacitor and the variation in the measured S_{11} with the amount of charge in the capacitor at −10 dBm.

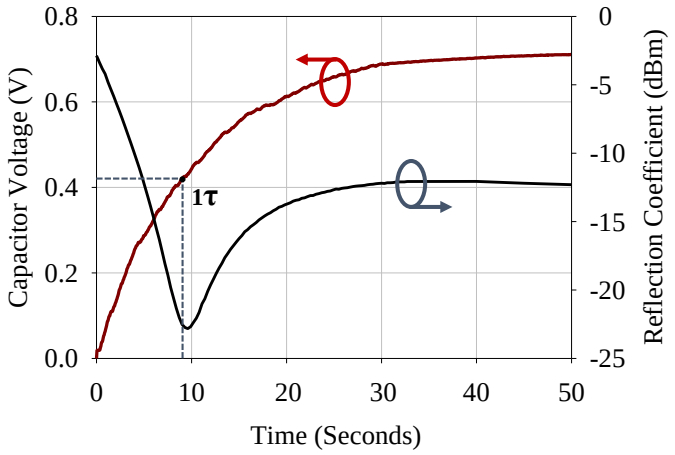

FIGURE 4.24: 1.32 mF C_{Store} charging time and the measured reflection coefficient variation with the energy stored in the capacitor over time from −10 dBm.

From the moment the VNA is turned-on (time=0), it is observed that the reflection coefficient of the diode changes significantly based on the amount of charge stored in the capacitor, implying an input impedance change. This can be explained by the charging curve of a capacitor, where initially the current (4.2) is significantly higher than the voltage. The current flowing into the capacitor given by

$$I_C = \frac{V}{R} e^{\frac{-t}{RC}} \tag{4.2}$$

will determine the load impedance and subsequently the rectifier's S_{11}.

The optimal impedance match (S_{11}=−23 dB) is achieved at time=τ, from τ=RC and the measured capacitance, the DC resistance of the circuit at that instance can be worked out to be 6212 Ω, closely approaching the optimal load impedance of the single-band rectifier shown in Fig. 4.22. The low reflection observed after the steady-state voltage is reached is due to the high leakage of electrolytic capacitors, resulting in a continuous current draw from the rectenna to maintain the energy stored.

The energy stored in the capacitor can be used to calculate the average PCE of the rectenna with capacitive loading using,

$$PCE_{average} = \frac{C_{Store} V^2}{2} \times \frac{1}{\tau} \times \frac{1}{P_{RF}} \tag{4.3}$$

where C is the storage capacitance, V is the voltage across the capacitor, and τ is the first RC time constant. P_{RF} is the power available from the generator or harvested by the antenna from a plane wave of power density S. τ could be replaced by other time periods depending on the application of the harvester.

The calculated efficiency of the capacitor-loaded rectifier at −10 dBm is 15.3% compared to 54% of the resistive-loaded rectifier at the same power level. The significantly lower PCE is attributed to the variation in the capacitor's impedance affecting both the RF impedance matching at the rectenna's input (Fig. 4.24) and the DC power transfer between the rectenna and the DC load.

An input power sweep has been carried out from −20 to 10 dBm to investigate the variation in $PCE_{Average}$ for a capacitive load. The charging curves of the load capacitor can bee seen in Fig. 4.25 for different power levels. The power sweep oscilloscope traces were used to extract the RC time constant at different power levels to calculate the average PCE using (4.3). Fig. 4.26 shows the measured peak capacitor voltage and the voltage at the first τ, in addition to the average PCE (4.3).

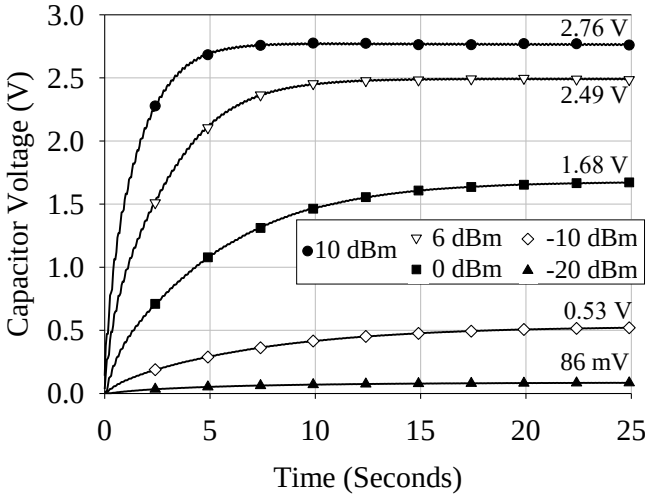

FIGURE 4.25: Measured voltage across the 1.32 mF capacitor during charging using the 970 MHz RF power, and the peak voltage reached at different power levels.

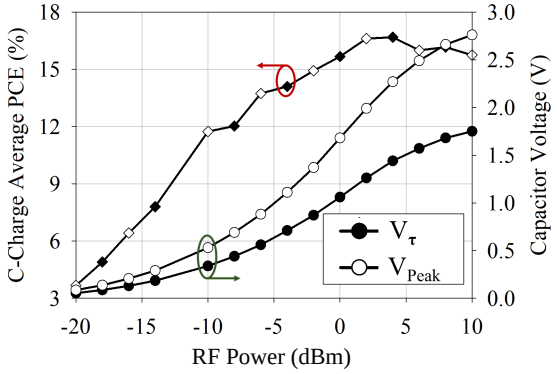

FIGURE 4.26: The measured average PCE of the capacitive-load rectifier and the capacitor voltage at the first time constant and the peak voltage.

The diminished PCE of the rectifier with the C_{store} as a load is mainly observed at lower power levels due to the wide variation in the input impedance demonstrated through the variation of the S_{11} over time in Fig. 4.24. This prohibits a high-quality

impedance match over the charging time and is due to the rectifier operating away from its optimal load.

4.5 Rectenna Wireless Testing and Evaluation

In this section, the rectenna is evaluated wirelessly in a controlled environment, with a far-field plane wave S excitation. By using a fixed S, the efficiency of the rectenna as well as the DC power output can be evaluated in a standardized manner, enabling better comparison of the performance with SoA rectennas characterized using plane wave excitation. The incident S could be directly linked to ambient S, e.g. available from cellular networks, or S available from a dedicated WPT base-station.

In order to demonstrate the performance of the whole textile rectenna (antenna and rectifier), the dual-LP broadband monopole is integrated with the proposed rectifier using the textile transition from Fig. 4.3. This section presents the wireless testing and evaluation of the integrated textile rectenna shown in Fig. 4.2-a. The tests carried out in this section demonstrate:

1. High PCE of the rectenna in space and on-body for sub-μW/cm^2 power densities.
2. Dual-polarization harvesting capabilities.
3. Omnidirectional power reception capabilities.

A standard 10 dBi LP log-periodic antenna has been used to illuminate the antenna with RF power over a fixed distance d, while varying the power available from the VNA configured to act as a CW generator. Given the VNA's maximum leveled output of 15 dBm, the distance d has been set to 1.2 m to be able to deliver power densities up to 1.75 μW/cm^2 to the rectenna. A distance of 1.2 m represents 3.3$\times\lambda$ at 820 MHz, ensuring the antennas are in their farfields. The setup is consistent with the test setups in [39] and [178], where the transmitter-rectenna separation was 1.2 and 1 m, respectively. Fig. 4.27 shows the test setup of the textile rectenna.

The power received by the rectenna, a function of the antenna's effective area A_{eff} (3.6) and the RF power density S, has been used to calculate the PCE for an incident plane wave PCE_{plane} using (3.9). The PCE from a plane wave has been calculated using $A_{\text{eff.}}$, using the measured gain G_R in space and on-body. When measuring the PCE for the misaligned polarization case, A_{eff} is halved due to the -3 dB PML. PML reduces the RF power received by each port by 50% which is then overcome by combining the power output of both ports [149]. When performing the on-body measurements, the -6.5 dB worst-case measured gain was used in the calculations of the received power.

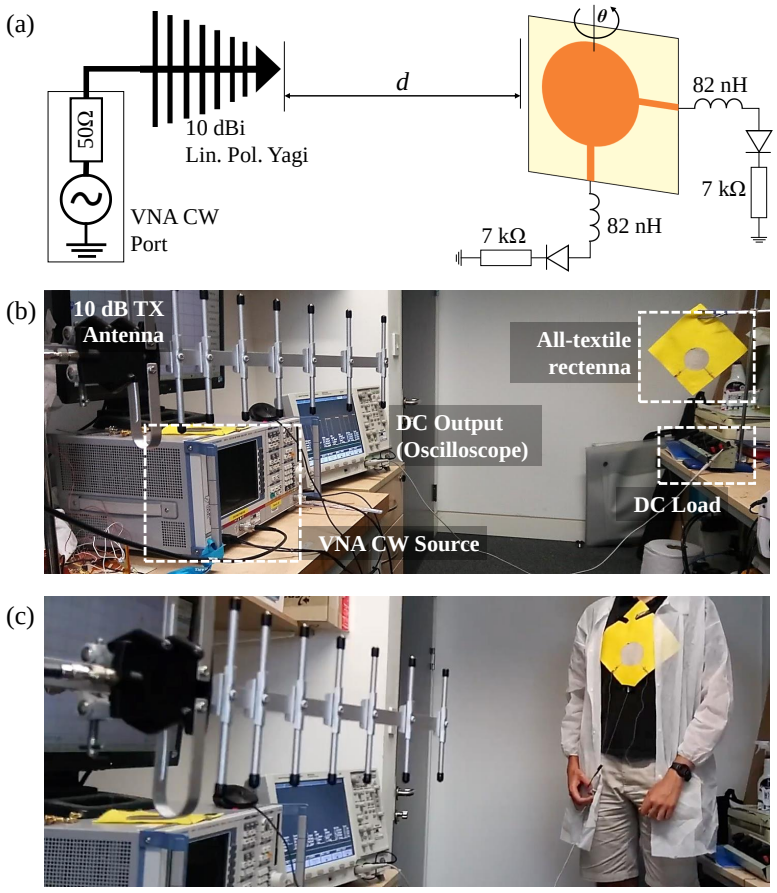

FIGURE 4.27: The wireless test setup of the textile rectenna: (a) schematic of the wireless test setup, (b) photograph of the rectenna testing in space, (c) photograph of the rectenna testing when mounted on-body.

A power sweep has been carried out to measure the received DC power and PCE at variable incident power densities. The CW input has been swept from −6 to 15 dBm. The measurements were performed with the rectenna positioned in free space and mounted on-body as in Fig. 4.27-b and 4.27-c. The antenna's position on the torso reflects the position with the lowest antenna efficiency. This was shown in the off-body measurements in [288], included in Appendix A. Thus, it is the most conservative estimate of the antenna's wearable performance.

Fig. 4.28 shows the measured PCE and DC output of the rectenna at 820 MHz for a 7 kΩ load. It is observed that the antenna achieves a PCE surpassing 50% and 45% from S <1 μW/cm^2 in space and on-body, respectively. Compared to other all-textile rectennas [178, 179, 181], this work presents the only rectenna capable of efficient power generation for power densities below 1 μW/cm^2 despite lack of shielding, having a low profile, and the smallest electrical area.

In wearable operation, it is highly likely that the antenna will move and subsequently polarization alignment with the transmitter is not guaranteed. For instance, body movements and rotations can result in over 10× reduction in the received power based on the

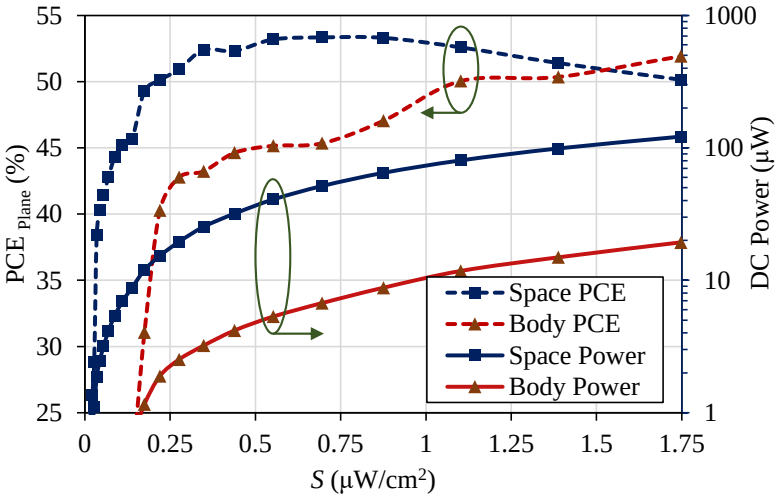

FIGURE 4.28: Measured DC output and PCE of the textile rectenna on-body and in space from varying plane-wave excitations.

V/H-polarization isolation of a single monopole. The next step in evaluating the rectenna is to validate the performance for polarization misalignments. The transmitting antenna has been rotated to have a 45° angle, over the antenna's azimuthal (polarization) plane. To verify that the incident wave is 50% misaligned with both ports of the rectenna a connectorized textile antenna was used to measure the forward transmission at both ports. The measured S_{21} at both ports was verified to be 3 dB lower than that when the polarization is fully-aligned. S has been swept while measuring the DC output of both ports. The 45° misalignment is an indicative test for the "worst-case" scenario, where the power received on each port is at its lowest, and as a result the PCE will be at its minimum. For more vertically or horizontally-polarized radiation, the power will be received predominantly at one of the dual-ports resulting in a higher PCE than in the 45° case.

Fig. 4.29 shows the measured PCE and DC output. It can be observed that, for the misaligned polarization case, the PCE is approximately 25% lower than a single-port output when the polarization is aligned. This is attributed to the mutual coupling between the ports as well as additional path losses linked to the positioning of the transmitter. The variation in the power output between the V-pol. and H-pol. could be attributed to slight variation in the polarization angle due to the transmitting antenna's position and indoor multi-path effects.

To demonstrate the omnidirectional harvesting properties of the antenna, the integrated rectenna is rotated around the axis shown in Fig. 4.27. The antenna is positioned at d=1.6 m and the VNA's CW output is set to 14 dBm, this results in a power density of 0.78 μW/cm^2. Fig. 4.30 shows the measured DC power output of the rectenna as well as the antenna's simulated gain at 820 MHz. It has previously been demonstrated that a rectenna's DC voltage patterns can vary significantly from the antenna's RF radiation

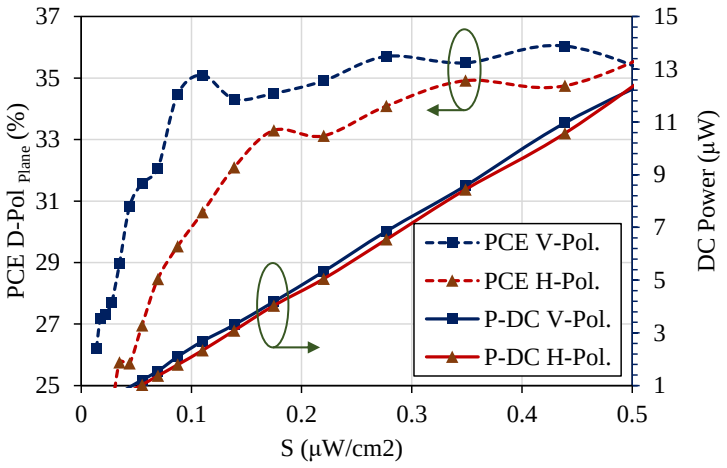

FIGURE 4.29: Measured DC output and PCE of the textile rectenna across both ports for variable incident plane waves with 45° polarization angle.

patterns due to the rectifier's size and layout [225]. In addition, planar and non-planar positioning of rectifiers was found to alter the received DC power [39].

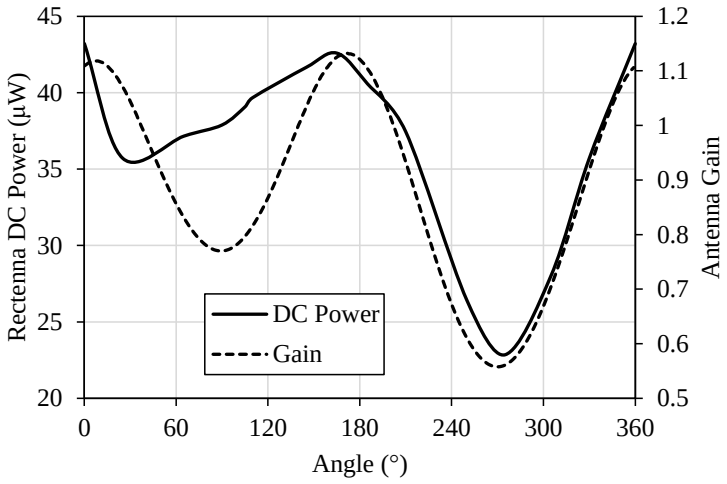

FIGURE 4.30: Measured DC output of the rectenna for variable alignment angles with the directional transmitter and the antenna's gain.

In Fig. 4.30, very close agreement between the simulated gain and the DC power is observed from 180° to 360°. From 0° to 180°, the DC power output is about 50% higher than expected from the simulated gain, this could be attributed to the indoor test setup resulting in varying multi-path effects. From Fig. 4.30, it can be concluded that the proposed rectenna maintains omnidirectional power harvesting capabilities with the half-power beamwidth covering the entire 360° angular span.

Table 4.1 compares the proposed rectenna with state-of-the-art wearable rectennas with textile antennas [11, 178–181]. Two non-textile rigid rectennas are included in the table for bench-marking. [39] is a low-profile rectenna designed for ultra-low power densities, operating at a very close frequency to this work. [132] is a wide angular coverage

2.4 GHz rectenna based on a complex 3D structure with multiple patch arrays and a beamforming network.

It is clear that the proposed rectenna, despite being implemented on textiles and utilizing lumped matching, achieves the highest reported PCE at −20 dBm, and subsequently for S<1 μW/cm^2. The PCE$_{\text{Plane}}$ presents over 5× improvement compared to reported un-isolated wearable rectennas such as [181]. The proposed rectenna also occupies the smallest electrical size compared to other textile rectenna due to its wire-type antenna structure as opposed to aperture antennas. As in Fig. 4.28, the lack of shielding did not prevent the rectenna from yielding over 10 μW from S=1 μW/cm^2. This shows that unisolated antennas can indeed be used for wearable energy harvesting.

TABLE 4.1: Comparison of the proposed textile rectenna with reported wearable and low-power rectennas.

Study	**Antenna Substrate**	**Rectifier Substrate**	**Frequency (GHz)**	**Diode**	**PCE at −20 dBm (%)**	**Loads investigated**	**PCE at S=0.5 μW/cm^2 (%)**	**DC P at S=0.5 μW/cm^2 (μW)**	**Half-power beamwidth**	**Electrical size (λ_0^3)**
This work	**Felt (all fabric)**	**Felt (polyimide on fabric)**	**0.82**	**SMS7630-079lf**	**41.8**	**Resistive/ capacitive sweep**	**53**	**35**	**360°**	**0.329 × 0.329 × 0.0027**
Monti TAP'13 [178]	Pile+Jeans (all fabric)	Jeans (all fabric)	0.876	HSMS-285X	NR	Resistive sweep	NR, 45 from 3	NR, 360 from S=2.5	80°*	0.702 × 0.556 × 0.0088
Adami TMTT'18 [11]	Felt (all fabric)	Duroid 5880	2.45	SMS7630-079lf	33.6	Resistive sweep	NR	NR	60°*	0.74 × 0.39 × 0.028
Vital TAP'19 [179]	Felt (all fabric)	Felt (all fabric)	2.4	SMS7630-079lf	18	Single resistor	NR	NR	NR, ≈65°**	0.625 × 0.6 × 0.013†
Estrada TMTT'20 [181]	Cotton (all fabric)	Cotton (all fabric)	2-5	SMS7630-079lf	NR	Resistive sweep	<5%§	9 from S=4	omni-directional	NR, >1 × 1 × 0.0006‡
Okba TMTT'19 [39]	FR4	Durroid	0.85	HSMS2850	28*	Resistive sweep	31*%	20	80°×2	0.32 × 0.17 × 0.0045
Vandelle TAP'19 [132]	RO4003	RO4003	2.4	SMS7630-079lf	NR	Single resistor	40	18	344°	2.32 × (1.04 × 1.04 × π)

*Estimated from the graphs; ** typical patch beamwidth; †antenna only; ‡ estimated from the photographs; § PCE calculated using physical area, not A_{eff}

4.6 Summary and Conclusion

This chapter presented a wearable rectenna achieving the highest reported PCE for sub-1 μW/cm^2 harvesting, showing that lossy dielectric materials are not a hindrance to realizing high-efficiency rectennas. The proposed rectifier achieves a best-in-class PCE of 41.8% at 820 MHz from -20 dBm due to careful design of the rectifier and optimized matching for sub-100 μW power levels. The key findings can be summarized as:

- To maximize the PCE, the rectifier's layout needs to be carefully designed to achieve the optimum Z_{in} for a high PCE, as opposed to only achieving a low S_{11}.
- While commercial lumped components do not reach the efficiency of their ideal counterparts, they can still be utilized to overcome material losses on high-tanδ substrates surpassing SoA implementations.
- Despite their lack of shielding, a "wire-type" broadband monopole enables a low-profile wearable rectenna which can be realized with high sub-μW/cm^2 PCE on the body, while maintaining a small footprint.
- Textile rectennas can be realized with high scalability for various requirements such as multi-band, dual-polarization, and omnidirectional RFEH.

Chapter 5

Antenna-Rectifier Co-Design and SWIPT

This chapter presents optimal rectenna design based on antenna-rectifier co-design and non-50 Ω antennas, the second rectenna topology presented in Chapter 2.4.4 and shown in Fig. 2.5-d. First of all, antenna-rectifier co-design is demonstrated in a high-efficiency rectenna for sub-1 GHz ISM-band applications, based on a flexible dipole antenna. The rectenna achieves the highest reported PCE, of 43% and 83% at −20 and −4 dBm, respectively. The rectenna does not include a matching network and occupies an area of $0.012\lambda_0^2$, enabling its seamless integration in wearable applications and battery-free active RFID tags.

Antenna-rectifier co-design is then proposed for SWIPT applications, by integrating a high-efficiency dipole-like rectenna within an off-body textile microstrip patch antenna, realizing a dual-band textile antenna for wearable SWIPT. The SWIPT antenna achieves >25 dB port-isolation, $\eta_{\text{Rad.}}$>63% (inclusive of mismatch), with and without the rectifier, and the highest reported peak RF to DC efficiency, compared to textile rectennas, of 62% from 0.8 μW/cm^2.

The motivation behind matching network elimination is first introduced in Section 5.1 along with a comparison with recent approaches to antenna-rectifier co-optimization. In Section 5.2, the design and simulation of the rectifier, used in the dipole and SWIPT antenna, is presented. The design of a parametrically-tunable dipole is presented in Section 5.3, which is then evaluated as a sub-1 GHz rectenna in Section 5.4. Antenna-rectifier co-design is then introduced for SWIPT in Section 5.5, with a stepped antenna design method. The 2.4 GHz antenna and sub-1 GHz rectenna performance is characterized in Sections 5.6 and 5.7, respectively, and compared to SoA showing the highest textile rectenna efficiency to-date, simultaneous with an uncompromised SoA off-body communications performance. The contributions in this chapter have been published in [300] and [301], and submitted for publication in [302]. The extension of this technique to

realize a single-band 2.4 GHz SWIPT antenna/rectenna, published in [301], is included in Appendix A.

5.1 Matching Network Elimination: The Motivation

A standalone matching network stage is an additional source of insertion losses and an area and cost-consuming component. Moreover, unless a matching network is optimized for certain operation conditions and is implemented on a loss-less substrate, it reduces the rectenna's PCE. The noticeable discrepancy between the simulated and measured PCE of a rectenna in literature [33,43,80] can be attributed to losses in the matching network. While a low S_{11} can still be achieved using a matching network, losses in the non-ideal components or in the distributed microstrip network cannot be avoided. To overcome the matching network losses, high impedance antennas were proposed to directly match the rectifier [111, 223, 228]. While in [34] a generic high-impedance cross-dipole was able to achieve broadband power conversion for multiple diodes, the high-impedance antennas in [111] and [228] achieve a high PCE at low power levels, owing to being optimized for a specific rectifier.

As reviewed in Chapter 2.4.3 rectenna EM-circuit co-design is an increasingly-common rectenna architecture [15]. The different approaches to EM-circuit co-design can be summarized in:

1. Designing an antenna with arbitrarily high inductive impedance to match a wide range of diodes for different operation conditions, such as power levels and frequencies [34, 83]. While this approach is portable to different applications, the low-power PCE (below -10 dBm) is particularly low and does not approach the maximum PCEs reported in literature.

2. Simulating the rectifier's input impedance for specific operation conditions, such as the power level and load resistance, and designing an antenna or an impedance transformer to match this rectifier impedance [111]. This allows achieving higher PCEs for specific power levels than the first approach, but may not fully reflect the impact of the antenna's input impedance on the rectifier which should not be neglected due to the non-linearity of the diode.

3. Considering the antenna's input impedance effect on the rectifier, through simulation or source-pull measurements, then re-designing the antenna accordingly [181, 223]. This allows an extra design iteration where the system can be tuned using antenna design to match the rectifier at realistic operation conditions. However, this approach neglects the DC load impact, which could reduce the rectenna's PCE despite achieving a low S_{11}.

4. Utilizing an optimization algorithm in conjunction with a non-linear circuit simulator to extract the optimum impedances, both for the RF source and the DC load, to maximize the PCE [11]. While this method achieves the highest PCE at its design power level (−20 dBm), it has only been used thus far to realize a rectifier with a standalone matching network, implemented on a loss-less substrate, and a 50 Ω antenna.

In the next section, antenna-rectifier co-design is presented as a two-step process: a rectifier is designed for a given power level and its source and load impedances are optimized, unlike optimization techniques where a low S_{11} is the goal, the goal is maximizing the DC power across the load. A dipole antenna is then designed with a parametrically-tunable geometry which can be optimized in EM simulation, where the antenna is tuned to match the rectifier's optimum impedance.

5.2 Rectifier Design and Simulation

When designing a high-efficiency rectenna, based on high impedance antenna-rectifier co-design, the first step is to design and optimize the rectifier separately, extracting its optimal source and load impedances, in an iterative manner. These values can then be used to guide the antenna design process. As discussed in Chapter 3.3, including the load impedance in the design and optimization process can boost the input voltage improving the low-power PCE. To improve the accuracy of the simulation models, the rectifier's layout needs to be considered when extracting its input impedance, to account for their impedance transformer effect, presented in Chapter 4.3.2. To improve the voltage sensitivity, avoiding the need for additional boost converter circuitry and to simplify the system, a voltage-doubler rectifier topology is adopted. The layout of the proposed rectifier, based on the SMS7630-079LF low-barrier Schottky diode, is shown in Fig. 5.1.

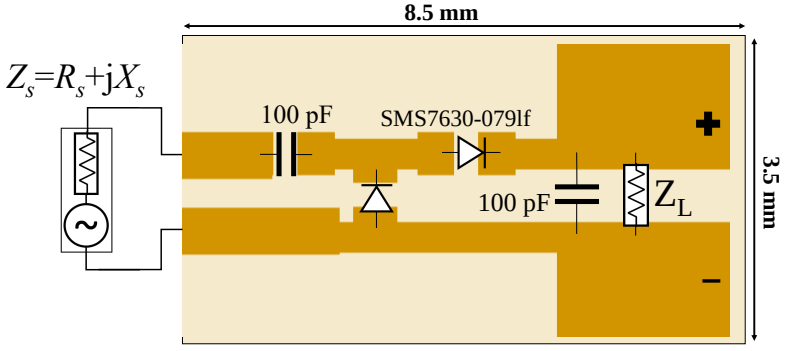

FIGURE 5.1: Layout of the differential voltage doubler rectifier. Parameters R_S, X_S and Z_L were optimized using harmonic balance simulation.

The layout in Fig. 5.1 was designed with compactness as a key objective, where the traces were kept to the minimum footprint of the components. As discussed in Chapter 4.3, this preserves the rectifier's high $\Re\{Z\}$, which is then matched through the co-designed antenna in this chapter.

The rectifier has been simulated in Keysight ADS using HB simulation along with EM Momentum MoM co-simulation, to factor in the effect of the rectifier's layout impact on the impedance. Z_S is then varied to approach the simulated Z_{in} of the rectifier. The optimization process of the source and load impedance is as follows:

1. Setting the load impedance to an arbitrary initial load in the kΩ range, reflecting a μA load;
2. Simulating the input impedance (Z_{in}) of the rectifier using non-linear HB;
3. Setting the source impedance (R_S and X_S) to the complex conjugate of the extracted Z_{in};
4. Optimizing Z_L based on the new Z_S, for maximum DC power transfer to the load;
5. Iterative tuning of R_S, X_S, and Z_L, to maximize the PCE, inclusive of mismatch.

To explain, the initially extracted Z_{in} were obtained using a mismatched source, they do not reflect the large-signal behavior of the rectifier, nor the small-signal behavior at the source power level. Therefore, an iterative optimization process has been adopted where the source impedance is varied continuously to achieve the maximum PCE at -20 dBm, ensuring the extracted impedances arise from a rectifier which absorbs most ($S_{11-\text{Rectifier}} < -10$ dB) of the incident power. The load impedance is then swept to identify the load yielding the highest PCE, as it was previously discussed in Chapter 3.3 that the PCE is not impedance-agnostic. At higher power levels the rectifier's sensitivity is expected to reduce due to the higher reflection coefficient, where the rectifier's impedance increases with power [33].

Fig. 5.2 shows the variation of the rectifier's PCE for variable R_S and X_S. As the voltage doubler's input impedance is predominantly reactive (capacitive), the source's reactance plays the dominant role in the PCE. The rectifier maintains over 50% (3 dB bandwidth) of its peak PCE with more than 230 Ω and 170 Ω variation in the input reactance and resistance, respectively, allowing for improved tolerances for antenna fabrication imperfections and simulation errors. The optimal values for the source and load impedances extracted are $R_S = 50\ \Omega$, $X_S = 340\ \Omega$ and $Z_L = 20$ kΩ. While Z_L is dependent on the current drawn by the load and can be considered as a design constraint, the identified optimal load impedance can be used to guide the design of a DC-DC converter circuit of similar input impedance to the optimal Z_L as in [11].

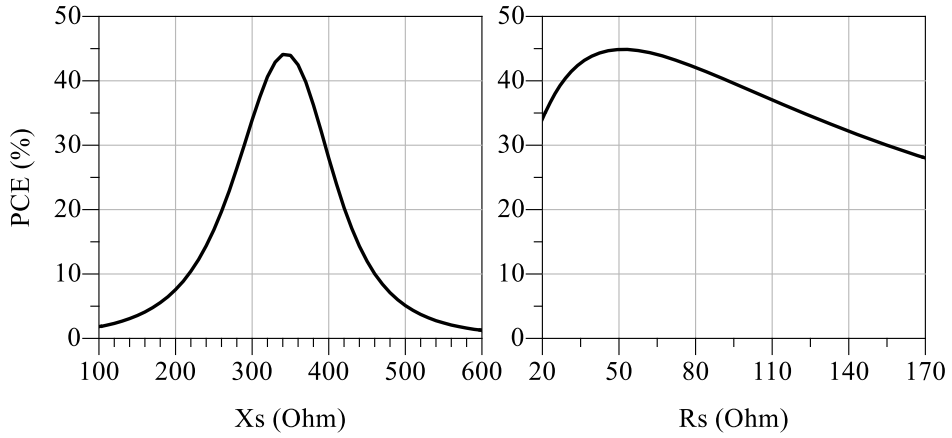

FIGURE 5.2: Simulated PCE of the voltage doubler with variable source input resistance and reactance, at −20 dBm with a 20 kΩ load.

5.3 High-Impedance FDA Design and Simulation

A Folded-Dipole Antenna (FDA) can be designed to achieve tunable Z_{Antenna}, where two shorted folds act as impedance transformers allowing impedances above 100 Ω. An FDA has been designed to allow parametric tuning of the antenna's geometry to achieve an ideal impedance match to the rectifier's input impedance. Fig. 5.3 shows the proposed FDA geometry. The parameters L, G and B were varied in the CST model to tune the antenna's input impedance Z_{ant}. While the length L is expected to vary the resonant center frequency, the impedance at resonance is a function of the impedance of the two folded lines. Hence, the gap size can be varied to tune the antenna's impedance both at and near its resonance frequency. The gap, directly influencing the parallel-plate and fringing capacitance of both arms affects mostly $\Im\{Z_{\text{Antenna}}\}$. The lines' shorting block width B can be used for finer tuning of $\Re\{Z_{\text{Antenna}}\}$ compared to the length L.

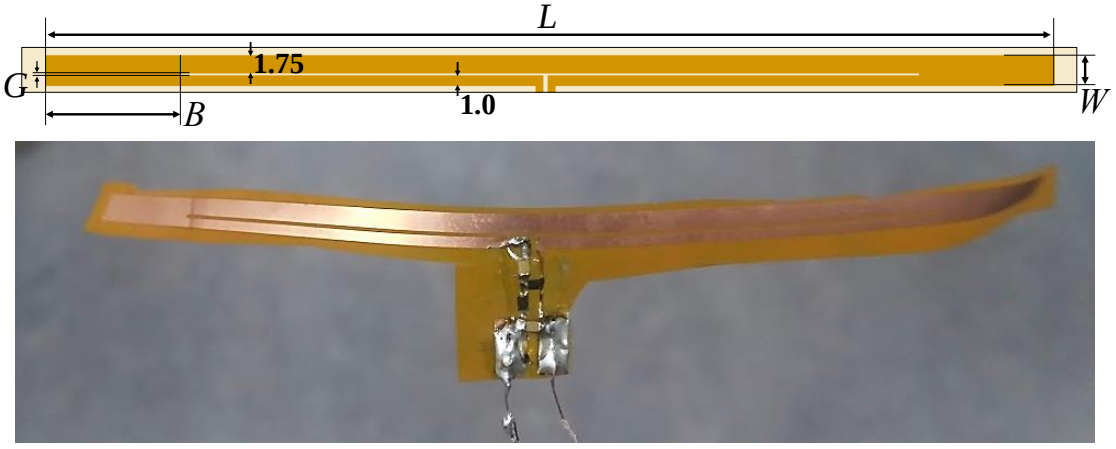

FIGURE 5.3: Layout (top) and photograph (bottom) of the high-impedance FDA, optimized dimensions (in mm): L=105, G=0.25, W=3, B=14.0.

The three parameter sweeps were performed independently with the starting parameters being $L = 100$, $B = 14$, $G = 0.3$ mm. Fig. 5.4 shows the variation in the input impedance across the swept parameters. The optimized FDA selected for this rectenna, whose dimensions are $L = 105$, $B = 14$ and $G = 0.25$, has an impedance $Z_{\text{Antenna}} = 25 + j340\ \Omega$. The antenna was designed to match the rectifier at a lower frequency than its resonance, so that the lower variation in the input impedance does not affect the impedance match, improving the broadband rectenna's response. As seen in Fig. 5.4-c, a FDA of $L < 106.25$ maintains a more stable input impedance around 860 MHz, within the rectifier's Z_S tolerance for maintaining high PCE (Fig. 5.2).

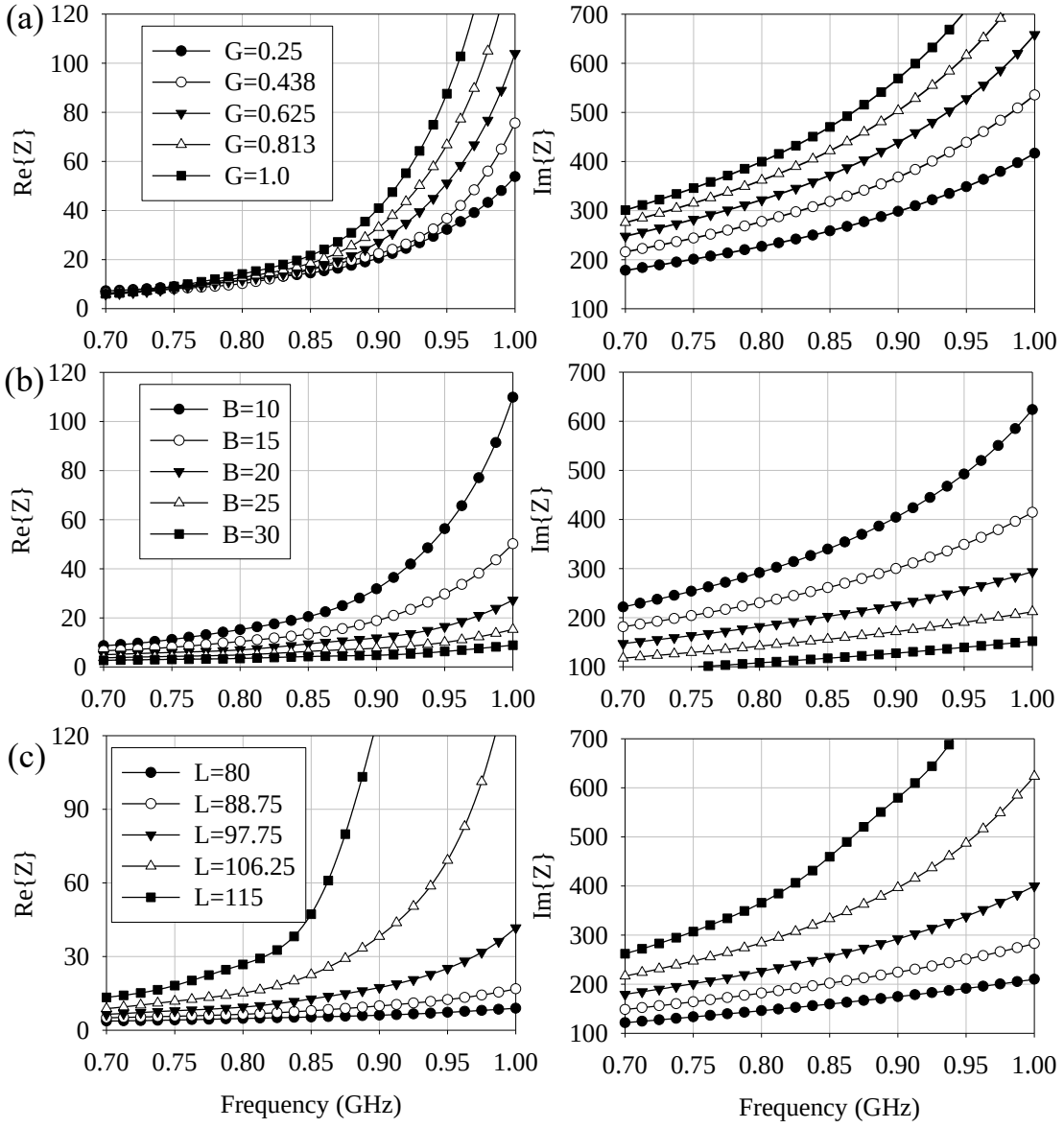

FIGURE 5.4: Simulated real (left) and imaginary (right) input impedance of the FDA for variable: (a) G; (b) B; (c) L; baseline parameters are $L = 100$, $B = 14$, $G = 0.3$ mm.

The antenna has been fabricated using standard photolithography on a commercial low-cost polyimide copper-laminate, of 25 μm thickness. The mounted components

(diodes and surface-mount capacitors) are encapsulated using UV-curable Glob-Top Epoxy, improving their mechanical reliability and resilience to repeated bending.

5.4 Rectenna Wireless Testing

5.4.1 Directional Power-Calibrated Transmitter

To investigate the integrated rectenna's performance and validate the rectifier's simulation, a directional 11 dBi antenna has been used to power the rectenna at different power levels. The transmitter antenna and the rectenna were placed at 1 m separation. The received power at the rectenna has been estimated using a standard dipole, as well as calculated using the incident plane-wave. Fig. 5.5 shows the measured PCE and DC voltage across the 20 kΩ load at variable power levels, from a 860 MHz CW input. The PCE has been calculated using the power estimated RF power using a receiver in presence and in absence of the antenna (PCE=$\frac{P_{DC}}{P_{RF}}$).

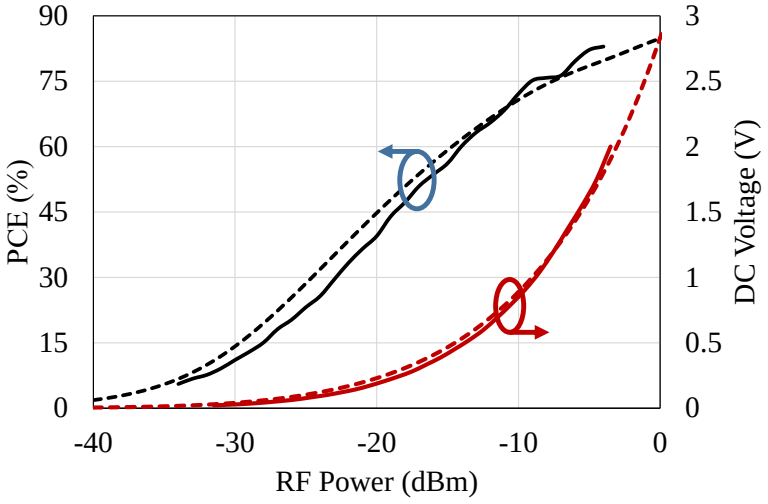

FIGURE 5.5: Measured (solid line) and simulated (dashed line) PCE of the rectenna at 858 MHz with a 20 kΩ load.

The frequency of the source has been varied to measure the rectenna's bandwidth. Fig. 5.6 shows the measured PCE and voltage output of the rectenna at −20 dBm and a 20 kΩ load. The simulated PCE has been obtained using a broadband source impedance of Z_{in}=25+j340 Ω. Therefore, the rectenna's response is more narrow-band due to the increase in the input impedance with frequency (observed in Fig. 5.4). Nevertheless, the rectenna maintains 50% of the peak PCE (3 dB bandwidth) across a 7.9% fractional bandwidth from (813 to 880 MHz), which is sufficient for sub-1 GHz applications and allows the utilization of multi-tone inputs.

Table 5.1 shows a comparison of the proposed rectenna with high-efficiency low-power rectennas with and without matching networks. It is observed that this work achieves

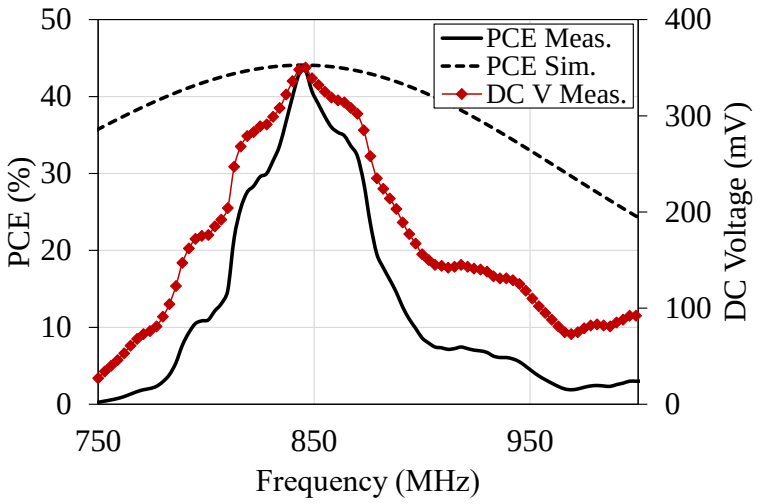

FIGURE 5.6: Simulated and measured PCE of the rectenna at variable frequencies, at −20 dBm input with a 20 kΩ load.

the highest PCE at various power levels, notably at ultra-low power levels (−20 dBm). Compared to other rectennas without matching network [34, 83], the proposed rectenna achieves higher PCE due to being designed specifically for a certain rectifier at low power levels, as well as including the load impedance in the initial iterative antenna-rectifier optimization. While [111] reported rectifier EM co-simulation and optimization of the rectifier design, the diode utilized in this work enables achieving higher PCEs due to its lower V_F. To add, this rectifier has been optimized for maximum PCE at −20 dBm, at which the input impedance was obtained.

TABLE 5.1: Comparison of the flexible dipole rectenna with reported rectennas

	This work	WPT 2017 [111]	TMTT 2018 [11]	IMS 2019 [303]	TAP 2016 [33]
Freq (GHz)	**0.868**	0.868	2.4	2.4	0.9*
Matching	**High-Z antenna**	High-Z antenna	Distrib. elements	Lumped L-network	Resistance compress network
Diode	**SMS7630**	HSMS-2852	SMS7630	SMS7630	SMS7630
PCE: −20 dBm	**43%**	33%	33.6%	15%	25%
PCE: −10 dBm	**70%**	55%	56%	35%	51%
Maximum PCE	**83%**	NR	62%	70%	67%
1 V Sensitivity at Z-load	**−9 dBm at 20 kΩ**	NR	−7 dBm† at 5 kΩ	−6.5 dBm†, load NR	−10 dBm† at 25 kΩ

*Multi-band, only 900 MHz considered for this comparison
†Calculated from the PCE curve. NR: Not reported

While the proposed high-impedance rectenna achieves the highest PCE, 50 Ω antennas with ideal impedance transformers can achieve equally high PCEs [11]. However, the parasitics of lumped components and the insertion losses of distributed elements matching will result in a non-ideal impedance match. Through careful rectifier EM co-simulation of the rectifier along with antenna-rectifier co-design, the proposed rectenna achieves the highest reported PCE using a commercial diode. The reported rectifiers with higher efficiencies, such as [304], are specifically tuned to sub-100 μW power levels and require many-stage rectifiers with innovative device-biasing techniques, where the PCE still deteriorates significantly at power levels above −10 dBm. Moreover, although [33] achieves higher DC voltage sensitivity, this is due to the resistance compression matching network, allowing higher load impedances without reducing the PCE. However, it cannot be used on a compact flexible system as it significantly increases the system's complexity, as well as reduces the measured PCE due to utilizing non-ideal lumped components [80].

5.4.2 Indoor Harvesting from an ISM-Source

The rectenna is evaluated under real operation conditions using a 3 W Powercast 915 MHz transmitter in an indoor environment. While the −20 dBm 3 dB power bandwidth does not cover the 915 MHz band (Fig. 5.6) the rectenna will still operate at 915 MHz with reduced sensitivity due to the impedance mismatch between the antenna and the rectifier at 915 MHz. This will result in reduced PCE particularly at lower RF power levels. However, this test is motivated by the availability of an off-the-shelf power transmitter at 915 MHz.

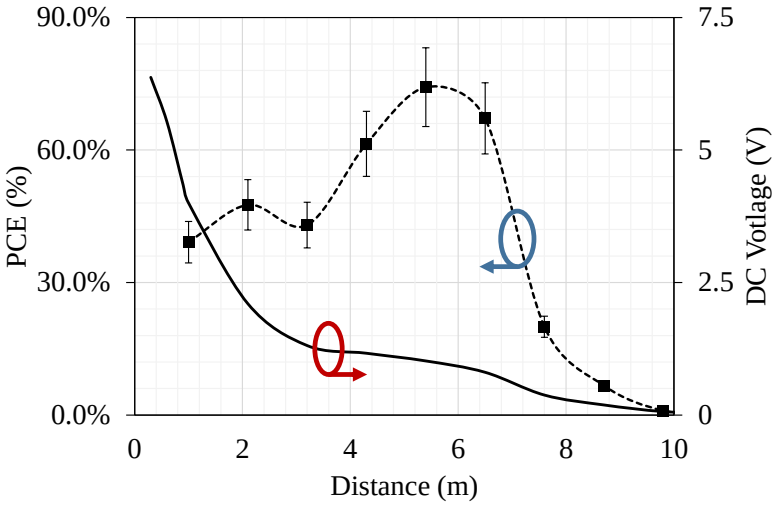

FIGURE 5.7: Measured DC output of the rectenna at varying separation from the 34.77 dBm EIRP Powercast 915 MHz transmitter.

The separation between the Powercast transmitter and the rectenna was varied and the DC voltage across the rectenna's 20 kΩ load has been measured using a multi-meter. Fig. 5.7 shows the measured DC voltage of the rectenna, the PCE has been calculated

using the Friis model with a 34.77 dBm EIRP output. The error bars indicate a ±1 dB uncertainty in the incident RF power level. The peak measured PCE is 74% at a DC voltage of 1 V at 5.4 m separation from the Powercast. Below 2 m separation from the source, the reduced PCE is due to the rectifier operating in the diodes' breakdown region. From 6 m separation and above, the drop in the PCE is due to the propagation losses, where less power to be received at the rectifier, causing it to operate in the region where V_{TH} limits the achievable PCE.

5.5 SWIPT Antenna Design and Simulation

To enable switching-free and power splitting-free SWIPT [8], a dual-port antenna can be used with high port-isolation [14]. Based on the design and implementation of a compact and very high-efficiency dipole rectenna presented earlier, it is possible to realize the WPT-port in a SWIPT antenna/rectenna as a matching network-free antenna based on a dipole.

Recently, a SWIPT rectenna has been proposed in [305] based on a high-isolation hybrid coupler. However, the size of the coupler is large compared to the antenna and a rectifier matching network is required at the antenna's input port. Furthermore, a coupler on a lossy substrate would incur significant insertion losses reducing the harvested DC power. In [14], a dual-port 2.4 GHz antenna was proposed for SWIPT, where one port is connected to the rectifier and the other connects to a wireless transceiver. Nevertheless, both antennas are fundamentally no different to a dual-port 50 Ω antenna, and a matching network is still required to achieve high-efficiency rectification.

5.5.1 Dual-Band Dual-Mode Antenna

The antenna design process is divided into two parts: the design of a 50 Ω 2.4 GHz antenna with broadside off-body radiation patterns, and the design of a broad-beam sub-1 GHz rectenna, due to the improved harvesting probability an omnidirectional antenna in sub-1 GHz bands [288]. For SWIPT to be efficient, the mutual coupling between the rectenna and the communication antenna needs to minimized. To illustrate, high mutual coupling would result in the 2.4 GHz transmitted power leaking into the rectifier, reducing the communication's range. Moreover, the rectenna's DC output may degrade if the sub-1 GHz incident power is absorbed by the 2.4 GHz transceiver instead of the rectifier.

Fig. 5.8 shows the application of a the proposed antenna. The same dual-port fully-textile antenna can be utilized as a rectenna to power wearable a MCU, sensors and a transceiver. The same antenna can then be used by the wireless transceiver to communicate with an off-body base-station.

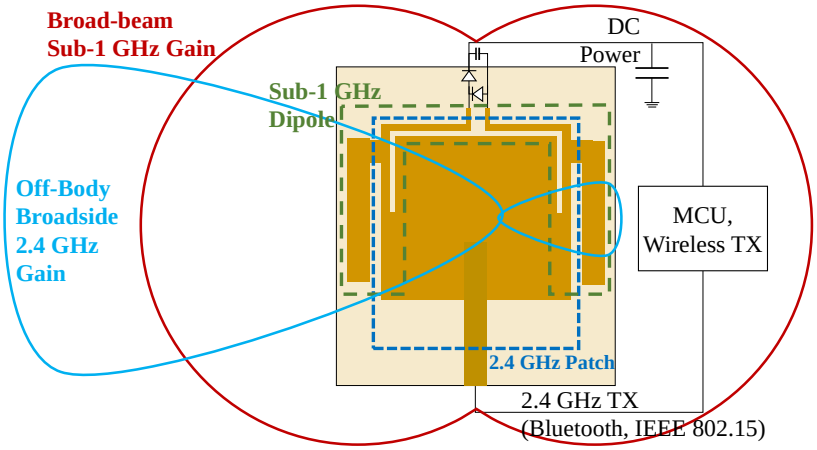

FIGURE 5.8: The architecture of the proposed SWIPT antenna for sub-1 GHz WPT and 2.4 GHz communications, with broadside and omnidirectional radiation patterns for the communication antenna and the rectenna, respectively.

5.5.2 Antenna Stepped Design and Simulations

The first step in designing the antenna is the design of a standard microstrip-fed 2.4 GHz patch. The first iteration is based on a standard geometry to resonate at 2.4 GHz. A proximity-coupled microstrip feed is selected due to the high thickness of the felt fabric (h=3.2 mm) which will result in a probe-feed having high inductance [11]. The felt fabric falls within the $h > 0.03\lambda$ margin to achieve high radiation efficiency [306]. The antenna was simulated in CST Microwave Studio to tune the length of the inset microstrip feed. Fig. 5.9 shows the design steps of the antenna, with step 1 being the common geometry patch with a proximity-coupled feed, whose parameters are quoted in Table 5.2.

TABLE 5.2: Summary of the antenna's parameters for each design stage.

	2.4 GHz S_{11}	2.4 GHz $\eta_{\text{Rad.}}$	868 MHz Z_{in} (Ω)	868 MHz $\eta_{\text{Rad.}}$ (%)
Step 1: common patch	< -20 dB	69%	single-port	single-port
Step 2: Port-2 added + loop	-1.7 dB	58%	1.4+j183	<0.01%
Step 3: GND miniaturization	-0.2 dB	54%	0.92+j182	10.1%
Step 4: dipole arms added	-3.6 dB	72%	11+j307	82%
Step 5: dipole meandering	-3.9 dB	71%	5+j337	43%
Step 6: patch stub matching	-19 dB	71%	16+j396	53%

Step 2 is to introduce a second port for connecting to the rectifier. While port-2 could be directly connected to a microstrip line and a rectifier impedance matching network, antenna-rectifier co-design could be utilized to improve the impedance matching and

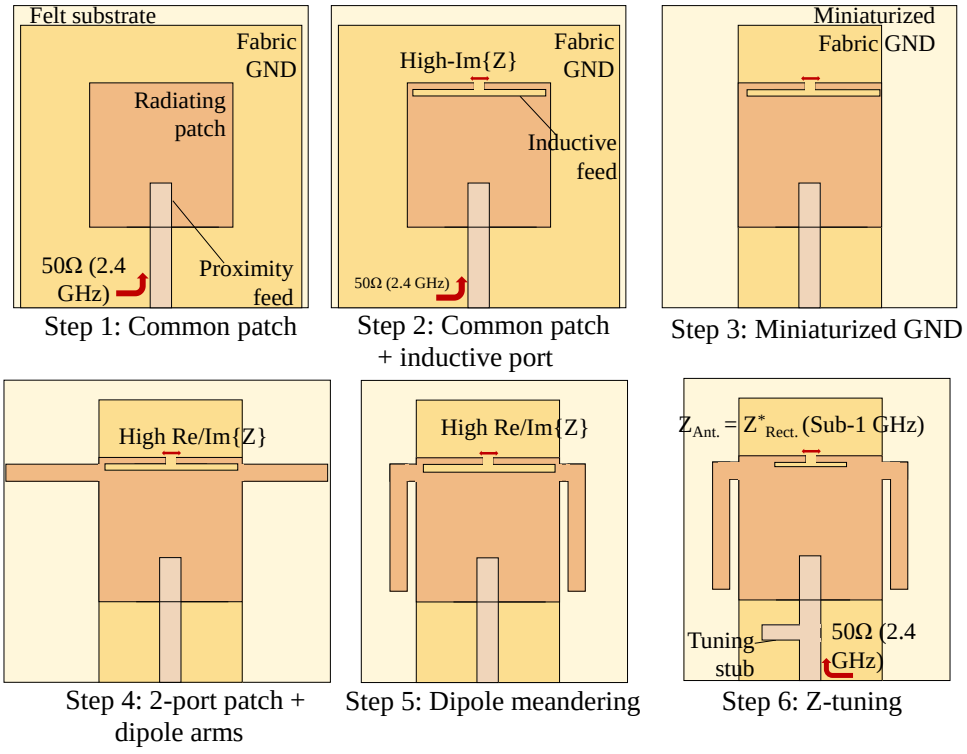

FIGURE 5.9: Design steps of the proposed dual-band SWIPT antenna.

subsequently the PCE. As discussed in Chapter 3.3, an inductive feed is required; a 1 mm-wide slot is added at 1 mm from the top of the patch to introduce an inductive matching loop. A balanced port was used to simulate the antenna's input impedance looking into the inductive loop. The simulated input impedance at port-2 shows a high complex impedance as shown in Table 5.2.

Due to the size of the patch and the ground backing, almost all the accepted power at 868 MHz at port-2 will dissipate in the dielectric substrate resulting in the very low $\eta_{\text{Rad.}}$ in step 2. To explain, the CST-simulated dielectric losses in step 2 were over 95% of the accepted power. Therefore, the ground plane is miniaturized as in step 3 in Fig. 5.9. This reduces the capacitance of the loop and allows a lower reduced input impedance. As a result, $\eta_{\text{Rad.}}$ is significantly improved as in Table 5.2.

The designed voltage doubler achieves the maximum PCE at -20 and -10 dBm with a source of $30+j330\ \Omega$ impedance, at 868 MHz. Hence, the antenna's $\Re\{Z_{\text{in}}\}$ is too low to achieve a good impedance match. Furthermore, the low $\Re\{Z_{\text{in}}\}$ implies a very low $\eta_{\text{Rad.}}$ due to the low radiation resistance. To improve $\Re\{Z_{in}\}$, half-wavelength dipole arms are added in step 4 to prolong the current path bringing the input impedance at port-2 closer to the input impedance of a standard half-wave dipole. Given that the horizontal dipole arms are not backed by the ground plane, the antenna feed at port-2 should radiate through its dipole arm with high $\eta_{\text{Rad.}}$. The length of the arms L_{Arm} can then be used to fine tune $\Re\{Z\}$. As in Table 5.2, the added dipole arms significantly improve $\eta_{\text{Rad.}}$.

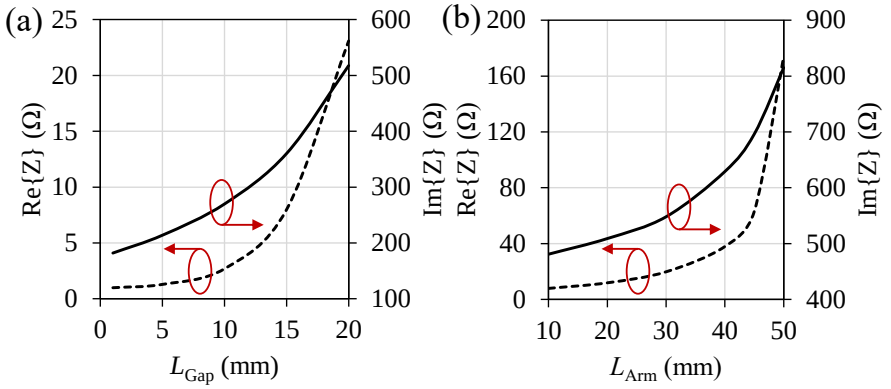

FIGURE 5.10: Tuning the rectenna's real (dashed) and imgainary (solid) impedance using (a) the gap, and (b) arm length.

While the dipole arms added bring the input impedance of port-2 to values within the range of a rectifier's input impedance, the arm's width is very long occupying additional space. The dipole arms could be redirected to make the antenna more compact without adversely reducing the radiation efficiency. In step 5, the dipole arms are folded to extend along the patch's length (E-plane), reducing the width of the whole dual-band antenna from 120 mm to 75 mm.

The final step is to tune the exact gap and dipole arms' length to match the impedance of the rectifier. The parametric tuning of Z is shown in Fig. 5.10. It is observed that L_{Gap} predominantly controls $\Im\{Z\}$ (the inductance), while L_{Arm} controls f_r and therefore affects $\Re\{Z\}$. Fig. 5.11 shows the dimensions of the proposed antenna, and the tuning parameters. The parameters included on the final antenna prototype are L_{Arm}=48 mm and L_{Gap}=2 mm.

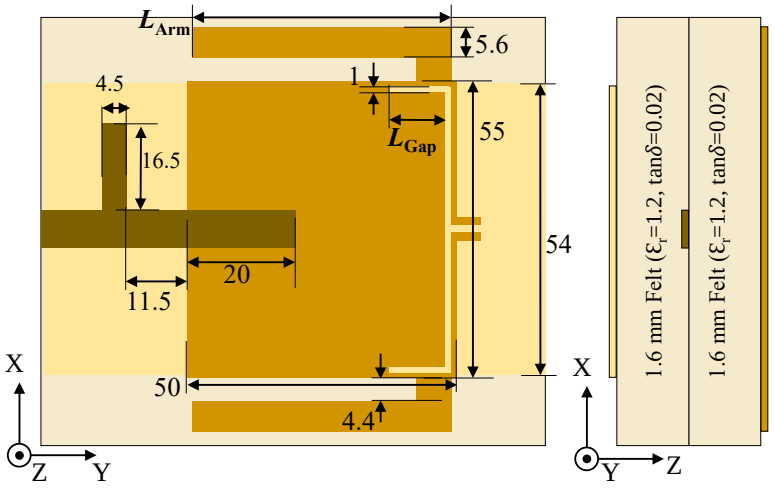

FIGURE 5.11: Layout and dimensions (in mm) of the proposed SWIPT antenna.

As the antenna's geometry has been modified to match port-2 to the rectifier, the impedance matching of the patch is altered around 2.4 GHz. Therefore, additional tuning is required to restore resonance around 2.4 GHz and match the patch to a 50 Ω

input. At 2.5 GHz, the antenna's impedance is 80 Ω, showing that it can be tuned using a real-impedance transformer. A shunt capacitive microstrip open stub is introduced on the feedline, as shown in step 6 in Fig. 5.9, to match the patch to 50 Ω. The tuned patch achieves a $S_{11}<-19$ dB at 2.4 GHz. The >30 dB simulated and measured port isolation shows that the antenna can be used for simultaneously receiving power below 1 GHz while the transceiver is active at 2.4 GHz with minimal interaction. Finally, the antenna was simulated on an Austinman model [295], showing a low SAR complying with the IEEE C95.1 regulations. The SAR is shown in Fig. 5.12 for 0.5 W of power.

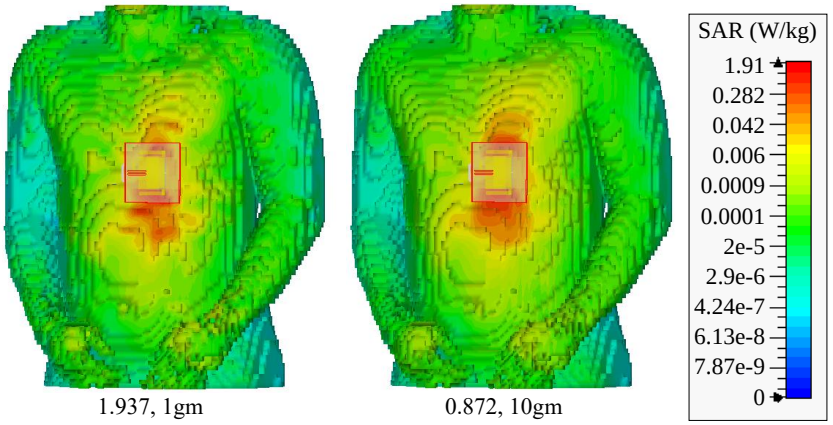

FIGURE 5.12: Simulated SAR of the antenna at 2.4 GHz showing the peak SAR, from 0.5 W, when normalized to 1 and 10 gm tissue mass.

5.6 SWIPT Antenna Fabrication and Measurements

5.6.1 Antenna Fabrication

The antenna was fabricated using adhesive-backed conductive fabric (P&P MF copper and nylon weave), patterned using laser cutting to create the antenna traces. The rectifier was fabricated on a compact 25 μm-thick flexible polyimide substrate using photolithography, adhered to the textile using a spray-mount adhesive. The process is similar to that presented in Section 4.1.1, where it was previously shown, in Fig. 4.16, that the rectifier maintains its DC output for repetitive bending, and can be waterproofed as described in [183]. Fig. 5.13-a shows the assembled antenna/rectenna prototype.

5.6.2 Antenna Input Impedance Measurements

The S_{11} at port-1 has been measured using a TOSM-calibrated VNA. The measurements have been performed with the rectifier and a DC load in place at port-2. Fig. 5.14 shows the measured reflection coefficient of the antenna with 130 MHz $S_{11}<-10$ dB bandwidth covering the 2.4 GHz ISM-band in both simulation and measurements.

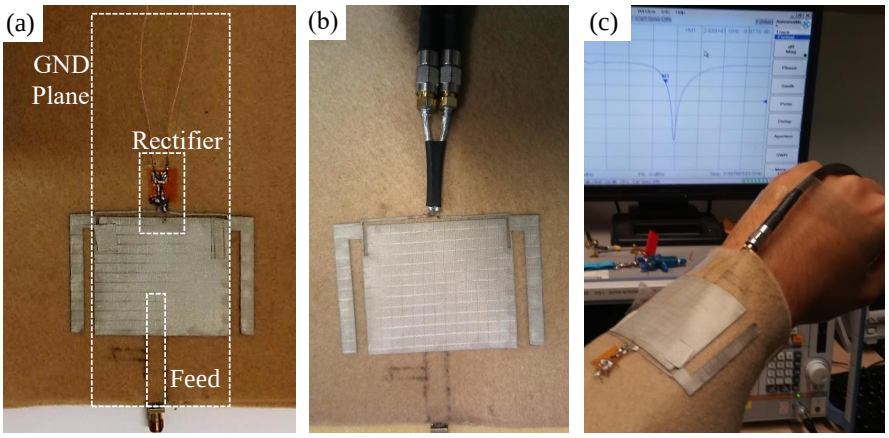

FIGURE 5.13: Photographs of the textile SWIPT antenna: (a) the assembled prototype; (b) differential dipole impedance measurement; (c) S_{11} measurement on-wrist.

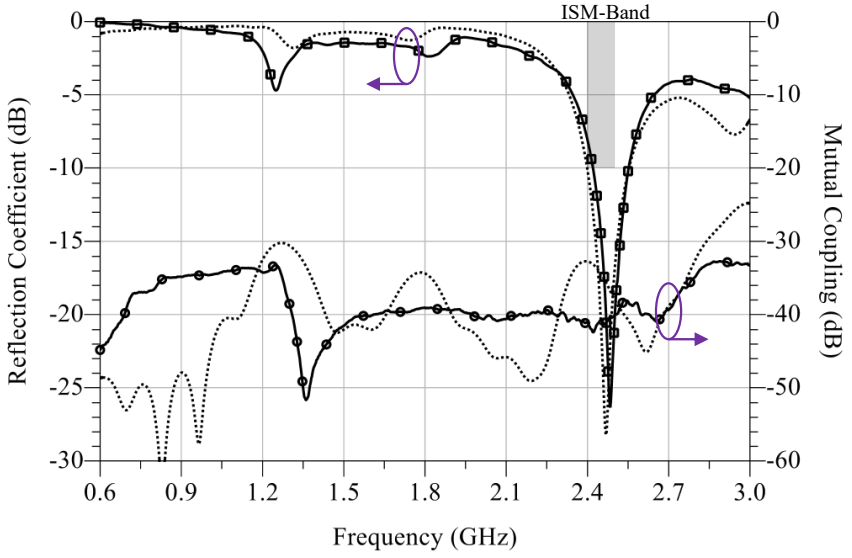

FIGURE 5.14: Simulated (dashed) and measured (solid) s-parameters of the proposed textile antenna showing the S_{11} at the 2.4 communications port.

The mutual coupling between the communication and the rectifier ports was measured using an SMA connector mounted in place of the rectifier. In Fig. 5.14, the simulated and measured mutual coupling is below -30 dB, showing minimal interference in SWIPT. For instance, less than 30 dB of the transmitted power at 2.4 GHz dissipate in the rectifier, showing that the simultaneous energy harvesting in sub-1 GHz will not reduce the radiated power.

To measure the input impedance at port-2, a two-port coaxial jig has been used to measure the differential impedance [307], as shown in Fig. 5.13-b. The simulated and measured input impedance at port-2 are shown in Fig. 5.15, demonstrating a close agreement between the simulation and measurements of $\Im\{Z\}$ below 1 GHz (the target frequency band of the rectenna). A higher discrepancy is observed in $\Re\{Z\}$ due to additional resistive losses and due to inaccuracies in measuring the radiation resistance

using balanced feeds. The impedance measurements of port-2 have been performed with port-1 terminated using a 50 Ω SMA termination, to mimic the effects of an active impedance-matched transceiver IC.

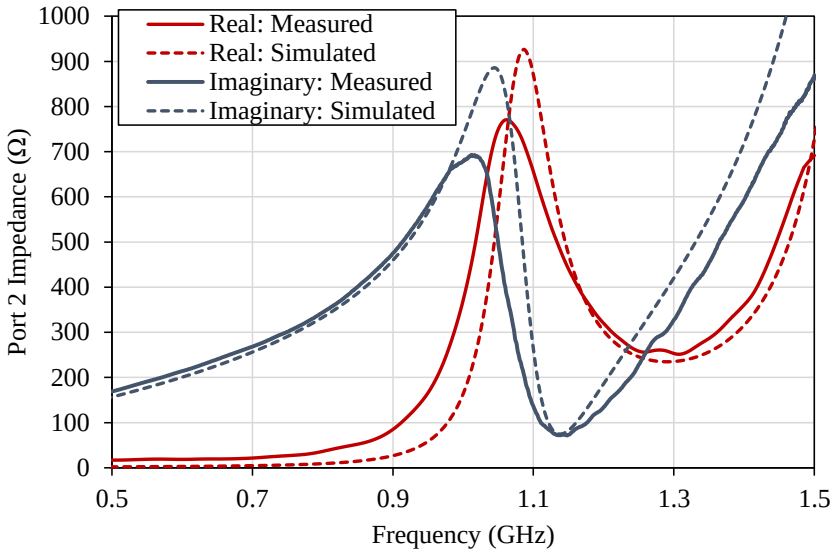

FIGURE 5.15: Simulated (dashed) and measured (solid) input impedance at port-2.

The antenna, under flat and bent conditions, has been measured in human proximity as shown in Fig. 5.13-c. Fig. 5.16 shows the reflection coefficient and impedance of the antenna while bent around the arm on the XZ axis (H-plane) and YZ axis (E-plane), and when positioned on a user's chest. On-wrist, the antenna is bent over a ≈3 cm radius. For all configurations, it is observed that the input bandwidth, at port-1, is mostly unaffected. This demonstrates that the miniaturized ground plane-backing does not have a detrimental effect of the wearable performance of the 2.4 GHz patch.

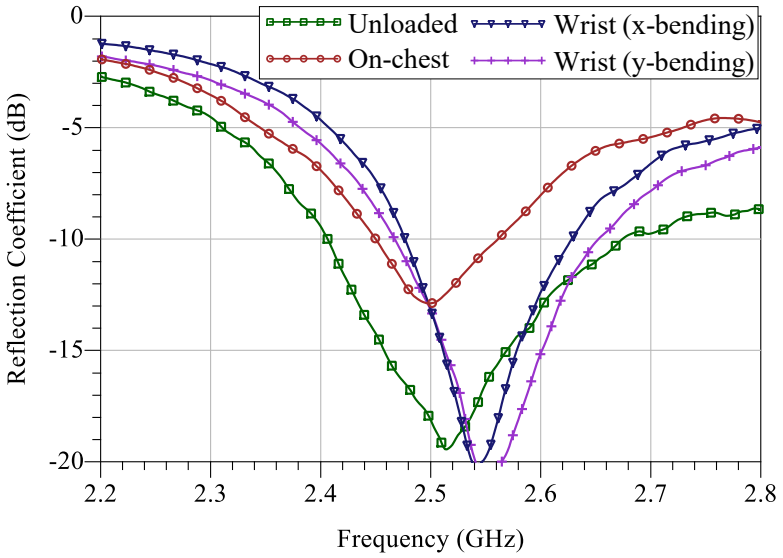

FIGURE 5.16: Measured reflection coefficient of the antenna for different body parts.

To further investigate the port coupling, the DC output of the rectifier was measured while injecting power into port-1, to mimic active wireless transmission. The measurements were performed at 830 MHz (the rectenna's peak resonance), and 2.4 GHz (the resonance of port-1). For 10 dBm of power going into port-1, the DC voltage across an open load was below 510 and 550 mV, respectively. Based on the rectifier's simulation, this corresponds to less than -15 dBm of power being accepted by the rectifier. Therefore, the mutual coupling between the information transmission port (port-1) and the rectenna (port-2) is over 25 dB, further verifying the high isolation between the communications and RFEH ports observed in Fig. 5.14.

5.6.3 Antenna Radiation Properties Measurements

The antenna's 3D polarimetric radiation patterns were measured on a body shadowing phantom in an anechoic chamber. The measurements were carried at the University of Bristol Communication Systems & Networks lab by G. S. Hilton [301, 302], following the standard setup used by the author in [244], presented in Chapter 7. The total efficiency $\eta_{\text{Tot.}}$ of the antenna (inclusive of mismatch) was calculated with respect to a reference monopole based on the total radiated power as in [156]. Fig. 5.17 shows the antenna measurement setup on the phantom's body. The antenna's $\eta_{\text{Tot.}}$ at 2.4 GHz is 66% and 63%, before and after the rectifier is connected, respectively. The 0.2 dB difference between the measured gain, with and without the rectifier, highlights the minimal interaction between the rectifier and the 2.4 GHz antenna. Fig. 5.18 shows the normalized gain patterns on the YZ and XZ broadside E- and H-planes. The directivity D of the antenna is 9.2 and 9.3 dBi, with and without the rectifier, respectively. This confirms that the rectifier does not affect the antenna's radiation properties. From the measured efficiency and directivity, the measured realized gain of the antenna is 7.2 and 7.5 dBi, with and without the rectifier, respectively.

From the measured patterns, the antenna is predominantly vertically-polarized, with 25 dB measured co-/cross-polarization isolation on the E-plane. On the H-plane, despite an increase in the cross polarization over the simulated values, the antenna still maintains over 15 dB polarization purity in the main broadside beam. However, this increase in the cross-polarized component has previously been reported for textile antennas measured on a body phantom [11, 175], and is not regarded as a disadvantage in off-body wearable communications [175].

The antenna's co-polarized patterns were measured on the phantom's arm as well as body, to show the additional off-body diffraction and shadowing effects. Fig. 5.17-b shows the on-arm test setup of the antenna. In addition, the antenna's patterns were measured on two prototypes, with and without the energy harvesting rectifier, to demonstrate that the rectifier does not affect the 2.4 GHz antenna's patterns. Fig.

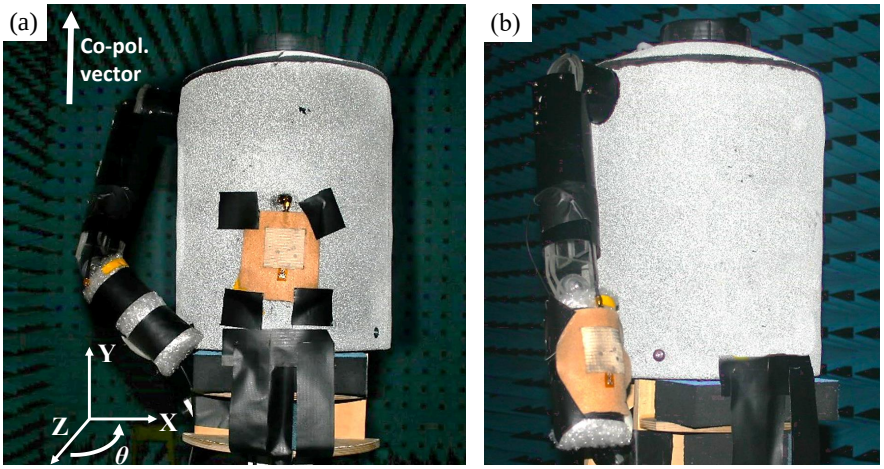

FIGURE 5.17: Photographs of the measurement setup of the antenna on a body phantom in an anechoic chamber, performed at the University of Bristol: (a) on-body setup; (b) on-arm setup.

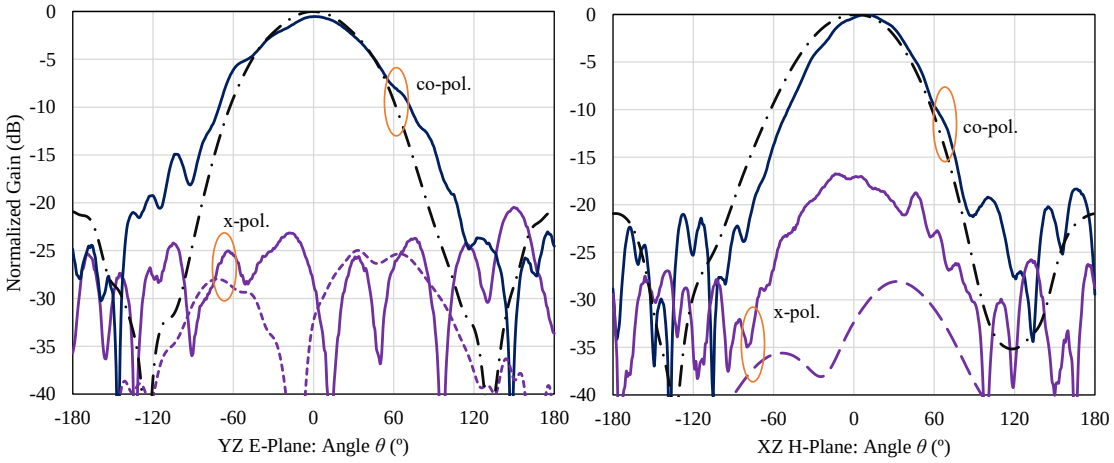

FIGURE 5.18: Simulated (dashed) and measured (solid) patterns (normalized to D=9.2 dBi) of the proposed SWIPT antenna, with a connected rectifier, at 2.4 GHz, on a phantom body (Fig. 5.17-a).

5.19 shows the measured E-plane co-polarized radiation patterns with and without the rectifier, as well as on-arm/body.

From Fig. 5.19, it can be confirmed that the inclusion of the rectifier not only has a minimal influence on the radiation efficiency, but also does not affect the main beam of the antenna. When the antenna is placed on-arm, additional diffraction and off-body reflection is expected, which results in an increase in the patterns behind the antenna. This however, does not affect the main beam significantly, and implies improved angular coverage behind the user when the patch is used on-arm. Multiple on-wrist positions and angular alignments can vary the off-body radiation pattern [156].

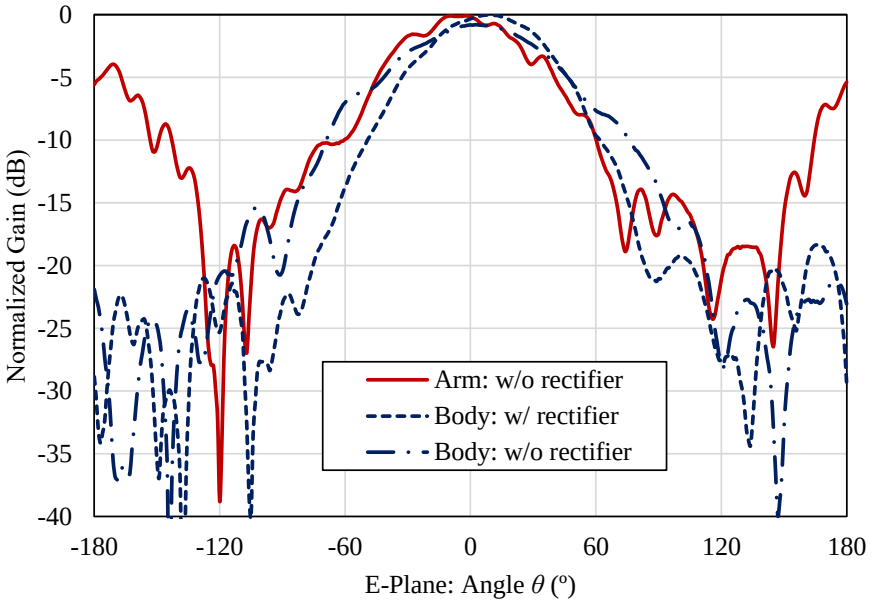

FIGURE 5.19: Measured co-polarized normalized E-plane patterns of the antenna with (w/) and without (w/o) the rectifier on the phantom's body (Fig. 5.17-a) and arm (Fig. 5.17-b).

5.7 SWIPT Rectenna Measurements and Evaluation

To characterize the rectenna, a wireless power source is used. As the rectenna's input impedance is not 50 Ω, signal generators cannot be used to directly power the rectifier using a coaxial feed. A 10 dBi log periodic antenna was connected to a VNA set to transmit a CW. The antenna was placed at 1.2 m from the source with the DC output connected to a variable resistive load and an oscilloscope (×10 probe). The distance between the transmitter and the receiver exceeds the minimum Fraunhofer far-field of 0.89 m, for the log periodic antenna's length of 40 cm. Fig. 5.20 shows the test setup of the proposed antenna, similar to that used in Chapter 4.5 [289]. The communications port was terminated using a 50 Ω SMA termination while measuring the DC output.

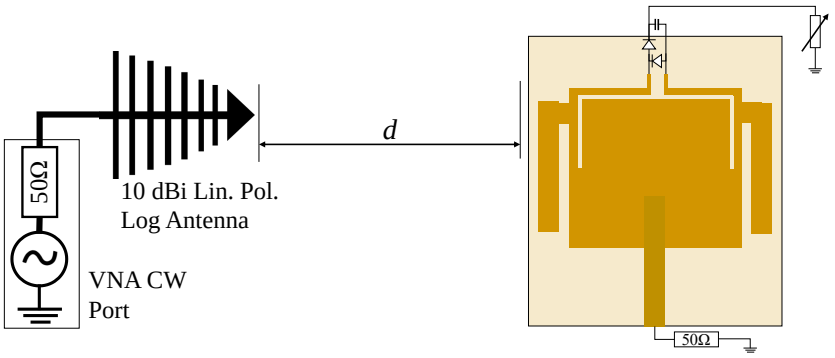

FIGURE 5.20: Measurement setup of the rectenna using an incident plane wave.

The power available at the rectenna was calculated using the power density S of the incident plane-wave and the antenna's effective area $A_{\text{eff.}}$, using the simulated 1.7 dBi

gain at port-2 [289]. The PCE of the rectenna was calculated using (3.9). Firstly, a frequency sweep is carried out at multiple S. From the measured Z_{Antenna} at port-2 (Fig. 5.15), the antenna is expected to match the rectifier around the 868 MHz license-free band. Furthermore, due to operating further away from resonance, the antenna's response will be more broadband due to having a flatter impedance curve over frequency. Fig. 5.21 shows the measured broadband DC output of the rectenna across a 20 kΩ load. A high-impedance load is used to improve the voltage sensitivity of the rectenna while performing the broadband measurements to improve the accuracy for low S.

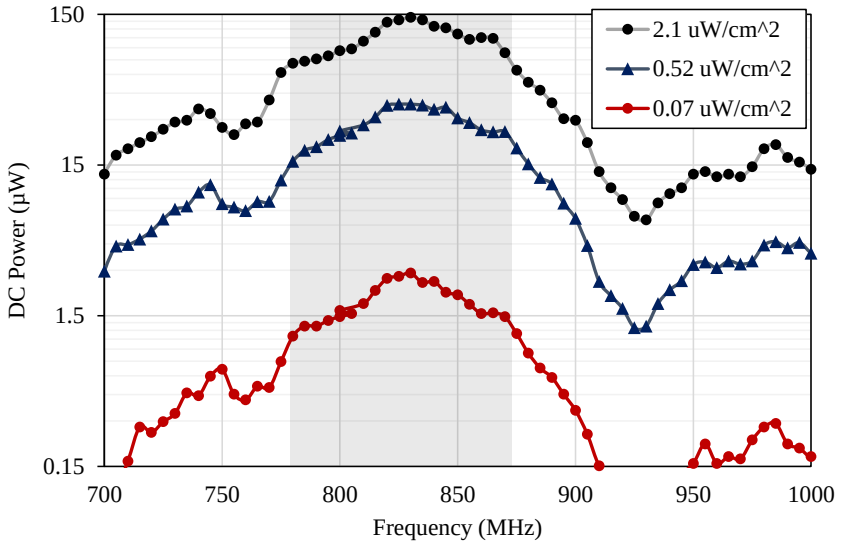

FIGURE 5.21: Measured DC power harvested by the rectenna at varying frequencies for a 20 kΩ load; the shaded region indicates the half-power bandwidth.

From Fig. 5.21, the rectenna achieves a half-power fractional bandwidth of 11.5% from 780 to 875 MHz covering the 868 MHz EU license-free band. The broader bandwidth than the compact FDA presented earlier is due to the more stable input impedance of the antenna shown in Fig. 5.15. The measured PCE for −20 dBm received power, calculated from the incident power density, is 37% showing that the textile implementation does not degrade the high PCE achievable through antenna-rectifier co-design. Moreover, it is observed that for the 30× dynamic range of S investigated, the rectenna's response is highly linear showing a very stable relative DC output for a wide dynamic range.

To maximize the harvested power, it is essential to identify the maximum power transfer point of the rectenna. A load sweep was performed at two fixed power densities at 830 MHz. Fig. 5.22 shows the measured DC voltage and PCE of the rectenna at various loads from 1 to 100 kΩ. For S as low as 0.8 μW/cm^2, the rectenna achieves a peak PCE of 67% with a 5 kΩ load, with over 0.65 V DC output. As with frequency, the optimum load of the rectenna is linear and does not vary for a lower S, showing that the proposed rectenna will maintain its maximum PCE when connected to a boost converter of a fixed input impedance, such as [11], without requiring MPPT capabilities.

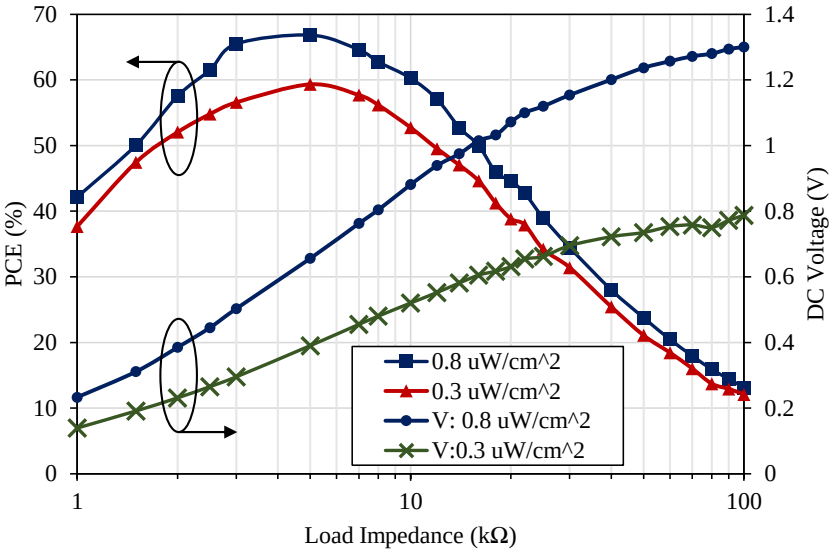

FIGURE 5.22: Measured DC output of the rectenna, at 830 MHz, for varying resistive loads.

After identifying the optimum frequency and Z_L, a power sweep is performed to investigate the rectenna's performance for varying S. Fig. 5.23 shows the measured DC output of the rectenna for $0.01<S<2$ μW/cm^2. The power sweep is carried out with a high-impedance (20 kΩ) and the optimal (8 kΩ) load. This shows the rectenna's performance for use cases where a high DC voltage sensitivity or a PCE are preferred, respectively.

It is observed that in the non-linear region of the rectenna (Fig. 5.23-b), the PCE exceeds 40% from less than 0.1 μW/cm^2. The peak PCE of the rectenna is reached below 1 μW/cm^2 showing a high sensitivity and suitability for low-power RFEH. For a 20 kΩ load (16.5 μA current draw), a typical average current draw for a duty-cycled low-power wireless sensor node [308], the rectenna produces 330 mV, the voltage required to start a commercial BQ25504 boost converter [39], from S=0.1 μW/cm^2. This presents 6× sensitivity improvement over [39], for a non-textile rectenna requiring S=0.6 μW/cm^2 to produce the required 330 mV.

Table 5.3 compares the proposed antenna/rectenna to SoA wearable and textile antennas and rectennas. This work presents the only antenna designed specifically for SWIPT. Compared to other textile rectennas, [178, 181, 289], the proposed rectenna achieves the highest peak PCE with at least 5× sensitivity improvements compared to [178], operating in the same band, by requiring a significantly lower S to reach the maximum PCE. While [11] achieves a high peak PCE, the rectifier uses a matching network implemented on a low-loss rigid substrate. While in Chapter 4, [289], the rectenna achieves a better sensitivity, its peak PCE is 20% lower than that of the co-designed SWIPT rectenna, due to being specifically matched to a low power level using a lossy lumped inductor. Finally, considering the sub-1 GHz frequency of operation, the SWIPT rectenna's electrical area

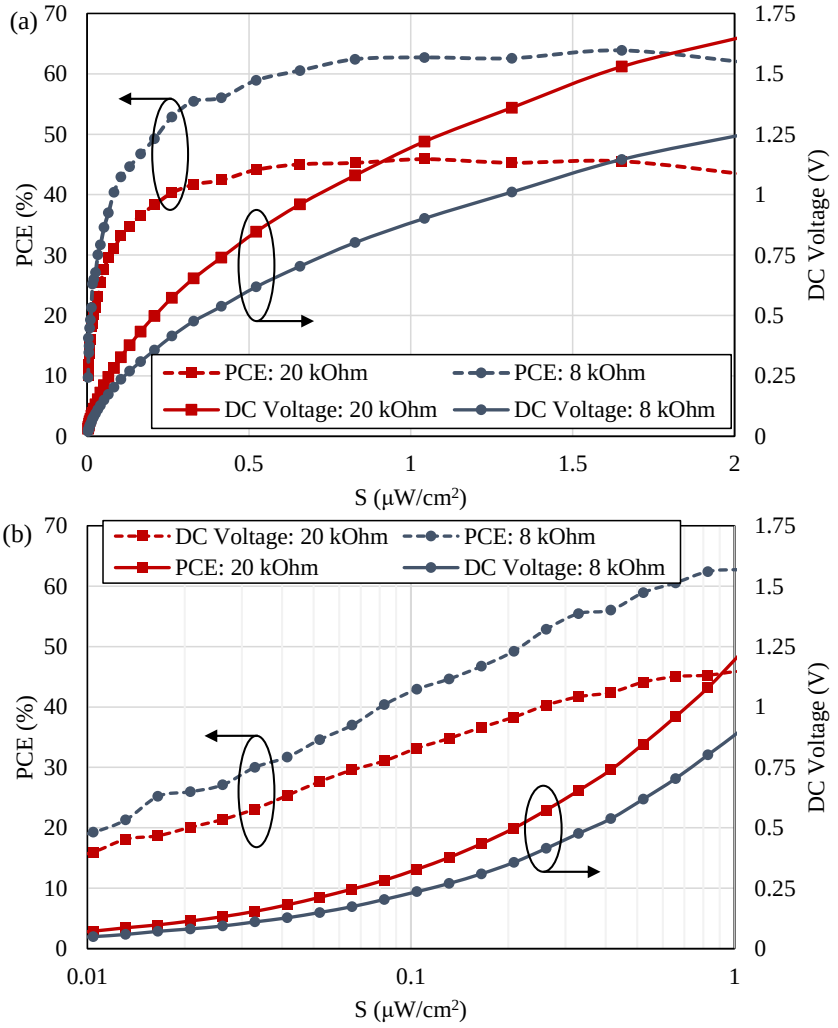

FIGURE 5.23: Measured PCE and DC voltage output of the rectenna for a varying S at an optimal (8 kΩ) and a high impedance (20 kΩ) load for a wide S range (a) and low S (b).

is very small compared to SoA textile rectennas, owing to the meandered dipole-like radiating arms and the built-in inductive tuning loop.

Not included in the comparison table is the dual-port 5.8 GHz SWIPT rectenna in [305], due to being implemented on a low-loss rigid substrate. Nevertheless, the proposed rectenna achieves a higher peak PCE of 63.9% compared to 51.1% in [305]. In addition, this work presents over 10 dB rectenna sensitivity improvement over [305] by reaching 60% PCE from −10 dBm received power, calculated using (3.9), compared to approximately 32% by [305], while not requiring a stand-alone rectifier matching network.

TABLE 5.3: Comparison of the proposed textile SWIPT antenna with reported textile antennas.

Study	**Application**	**Substrate**	**Frequency**	**Comm. Gain**	**Rectenna Gain**	**Total Efficiency**	**Sensitivity (min. S for peak PCE)**	**Peak PCE**	**Electrical size (λ_0)**
This work	**SWIPT**	**felt, tanδ=0.02**	**2.4 GHz; 830 MHz**	**7.2 dBi**	**1.7 dBi**	**63%***	**0.8 μW/cm^2**	**63.9%**	**0.213 × 0.190 × 0.009**
TAP'20 [289] (Chapter 4)	WPT	felt, tanδ=0.02	830 MHz	NA	0.6 dBi	NR	0.5	53.3%	0.330 × 0.330 × 0.00027
TAP'20 [175]	Communication	felt, tanδ=0.01	2.45 GHz	7.5 dBi	NA	83%†‡	NA	NA	0.544 × 0.544 × 0.016
TMTT'20 [181]	WPT	polycotton, tanδ: NR ≈0.02	2-5 GHz	NA	−20 dBi**	NR	100 μW/cm^2	32%	>1.00 × 1.00 × 0.0006
TMTT'18 [11]	WPT	felt, tanδ=0.023◇	2.45 GHz	NA	6.8 dBi	66%	NR	64.6%	0.740 × 0.390 × 0.028
TAP'13 [178]	WPT	pile, jeans tanδ=0.018	830 MHz	NA	4.6 dBi	NR	3	53.3%	0.702 × 0.556 × 0.0088

NA: not applicable; NR: not reported; *on-body efficiency; **evaluated from the graphs; †unloaded efficiency; ‡ exclusive of mismatch; ◇Antenna substrate, rectifier on low-loss Rogers substrate

5.8 Summary and Conclusions

In this chapter, antenna-rectifier co-design was investigated along with the design of a parametrically-tunable dipole antenna. Antenna-rectifier co-design was then proposed as an antenna-based solution for SWIPT, presenting the first SWIPT antenna with matching network elimination and implemented on textiles for wearable communications. Both antennas, the flexible dipole rectenna and the textile SWIPT antenna/rectenna, achieve the highest reported PCE compared to their counterparts in literature, as compared in Tables 5.1 and 5.3, respectively. The key findings in this chapter can be summarized as

- Based on iterative source and load impedance tuning, which considers the rectifier's layout, at a low power level (-20 dBm), the highest PCE of a rectifier can be achieved.
- The use of a high-Z dipole enables a higher PCE, over a wider dynamic range, compared to 50 Ω lumped matching, such as that proposed in Chapter 4.
- High port-isolation, combined with a Z_{in}-tunable inductive feed, enables a dual-port antenna to act simultaneously as a communications antenna and a rectenna.
- Utilizing compact dipole-like radiators enables highly-miniaturized rectenna elements to integrate within convectional antenna designs, such as a microstrip patch, operating at a higher frequency.

Based on the performance of the antennas presented in this chapter, the proposed dual-band/mode SWIPT antenna is a prime candidate for battery-less BANs due to its high antenna and rectenna efficiency and gain, stable wearable performance, and small form-factor.

Chapter 6

Wearable mmWave Energy Harvesting

Despite showing the potential for an improved end-to-end efficiency in the mmWave spectrum, based on directional transmitters and receivers, several key challenges exist before mmWave rectennas can be used to power flexible and textile-based systems. In particular, the following challenges are more significant at mmWave frequencies compared to the sub-6 GHz spectrum:

1. The increased dielectric losses in low-cost substrate with tanδ >0.01, resulting in reduced $\eta_{\text{Rad.}}$;
2. Antenna fabrication accuracy, where the small feature size requires low fabrication tolerances, with a feature size down to 150 μm;
3. Human body absorption, where mmWaves are heavily attenuated by human tissue, and do not penetrate past the skin layer;
4. A need for broadband antennas and rectifiers, to fully utilize the wide bandwidth available at mmWave bands.

While textile antennas have been implemented at 60 GHz for body-centric communications [159, 164], and 77 GHz for sensing [309], all reported implementations are based on conventional antenna designs, resulting in a low $\eta_{\text{Rad.}}$, due to the lossy nature of textiles.

In this chapter, textile-based antenna design for mmWave wearable energy harvesting is presented. In addition, theoretical and practical analysis are presented to demonstrate the benefits of mmWave energy harvesting compared to sub-6 GHz bands.

A broadband microstrip antenna is designed based on dual-TM modes, achieving a 23% fractional bandwidth from 25 to 31.8 GHz with stable patterns and over 25 dB polarization purity. To the best of our knowledge, this is the first microstrip patch antenna

to be investigated on textiles for the 24-30 GHz mmWave K and Ka bands. The proposed antenna has a wider bandwidth compared to other rigid and flexible microstrip patches while maintaining stable radiation patterns. The textile substrate is characterized based on a simple new method using single-port measurements only.

The proposed antenna for mmWave WPT is evaluated using two approaches:

1. Compact WPT receiver: similar-sized transmitter and receiver antennas evaluated at 2.4 GHz and 26 GHz, showing 11 dB higher S_{21} by operating at 26 GHz due to the improved aperture efficiency.
2. Large-area rectenna: a scalable rectenna array with individual rectifiers (i.e. DC combining) is evaluated analytically based on commercially-available Schottky diodes, showing the potential for 6.3× higher power reception in LOS compared to a UHF patch, at d=2 m, while occupying the same area.

This demonstrates the advantages of mmWave WPT, delivering an order of magnitude performance improvements over UHF WPT.

The antenna fabrication method and ϵ_r measurement technique are presented in Section 6.1. The design and simulation of the multi-mode textile antenna is presented in Section 6.2 with the experimental validation in Section 6.3. The experimental and theoretical evaluation of the antenna as a wireless power receiver is presented in Section 6.4.

6.1 Antenna Fabrication Method and Substrate Characterization

6.1.1 Antenna Fabrication

Flexible RF circuits and antennas have previously been fabricated using photolithography on polyimide copper laminates [42, 183, 185]. In this work, photolithography is utilized to etch the antenna's traces, resolving small features down to 100 μm, on 25 μm-thick copper-clad Kapton. The first fabrication step shown in Fig. 6.1-a and -b, the photoresist deposition, is usually based on spin-coating on a silicon wafer [183, 293], or using additive manufacturing such as inkjet printing [42]. In this work, the photoresistive ink has been roll-coated, using a smooth ink roller, onto the substrate which has been adhered to a flat surface. Whilst we have used a 150 mm diameter silicon wafer in this work as the supporting substrate, this roll-coating approach means the size of the antenna is not limited to a silicon wafer or an FR4 tile, allowing the fabrication of large-area antenna arrays using a straightforward process. As in Fig. 6.1-c, this allows prototyping multiple antenna designs with lower costs due to using a large-area UV mask. The

antennas are then cut and adhered to the textile substrate (Fig. 6.1-d and e) Fig. 6.1-f, g, and h show photographs of the multi-antenna wafer, before and after etching. This technique allows rapid prototyping of multiple designs or low-volume manufacturing.

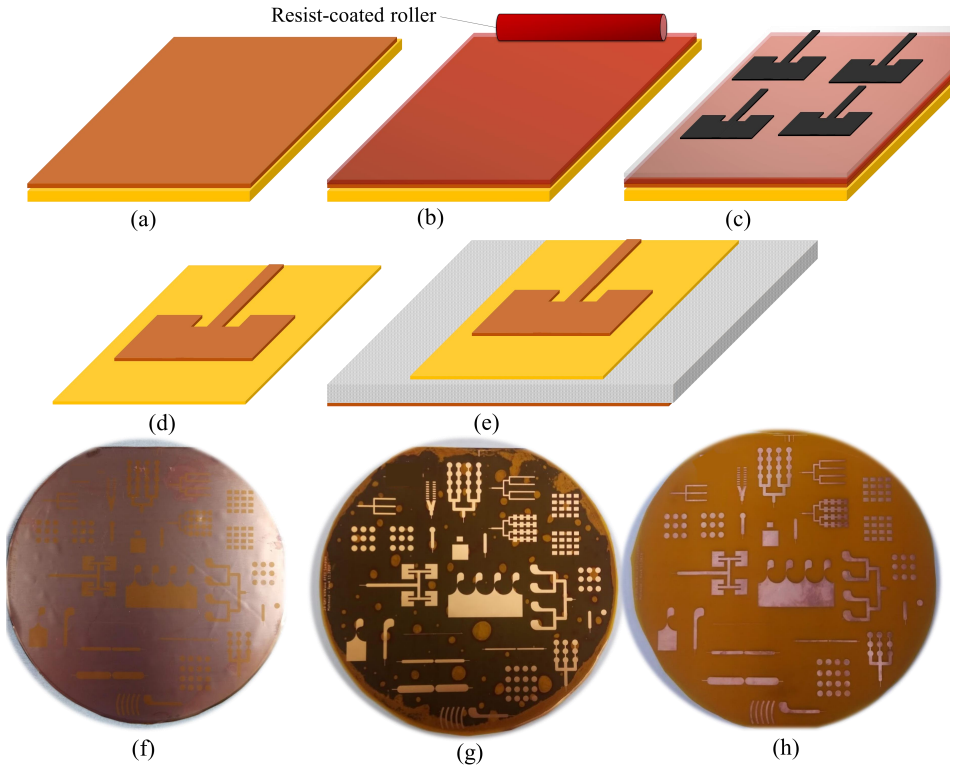

FIGURE 6.1: Fabrication steps of the textile-based mmWave antennas: (copper-on-Kapton laminate) (b) resist-coating of the planar polyimide copper laminates, (c) UV exposure using a dark mask, (d) individual antennas after cutting, (e) adhesion to the fabric, (f) photograph of the multi-antenna wafer before etching, (g) after etching, (h) after exposing the copper traces.

The fabricated flexible circuit is adhered to the textile (330 μm woven polyester+90 μm Kapton and adhesive interface) using a spray-mount adhesive or a heat-activated adhesive film. The thickness of the sprayed adhesive layer has been measured using a micrometer to be consistently under 10 μm. A similar process is used to attach the ground plane; the ground plane does not require any photolithography and can be cut directly prior to adhesion on the opposite side of the textile. The fabricated antenna prototypes can be seen in Fig. 6.2 showing high fabrication accuracy. The array elements shown in Fig. 6.2-b demonstrate that this process can be utilized to fabricate textile-based antennas for mmWave BANs beyond 60 GHz, where the antennas have sub-mm sized features such as the inset feed. The assembled prototype, with a solder-terminated connector, is shown in Fig. 6.2-c.

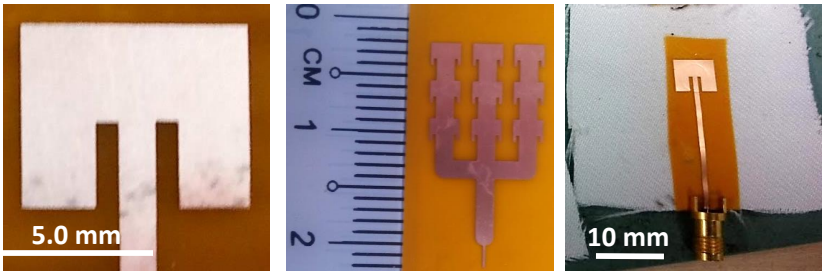

FIGURE 6.2: Photographs of the patch antenna prototypes: (a) the proposed patch antenna on Kapton before integration with the textile, (b) a 3×3 60 GHz patch array, (c) the assembled textile antenna with a coaxial connector for VNA measurements.

6.1.2 Single-Port Real Permittivity Measurements

Accurate knowledge of the substrate's dielectric properties is required prior to designing an antenna. The substrate used in this work is composed of polyimide-on-polyester as well as the inter-layer adhesive. Textile-based antennas have been previously designed based on dielectric properties measured using the two-line method [11], stub-loaded lines [159], or based on the resonance of patch antennas [201]. For methods involving microstrip lines, two-port measurements of two-lines are often required [199]. This subsection presents a new method for broadband dielectric characterization of substrates using one-port reflection measurements of an open-terminated (reflect) line. The method has been used to characterize the sandwich polyimide-woven polyester-polyimide substrate used in this work, up to 55 GHz, limited by the cut-off frequency of the first higher order modes of the microstrip lines.

Connector integration is a key challenge in mmWave textile-based circuits testing. In [66], it was observed that the standard 1.85 mm connector designed for boards of 1.6 mm thickness resulted in additional reflection and acted as a filter around 28 GHz. Therefore, relative permittivity extraction based on forward transmission will posses a de-embedding challenge. The use of an open-terminated line, shown in Fig. 6.3, is proposed for measuring the real relative permittivity ($\Re\{\epsilon_r\}$) based on the reflected phase.

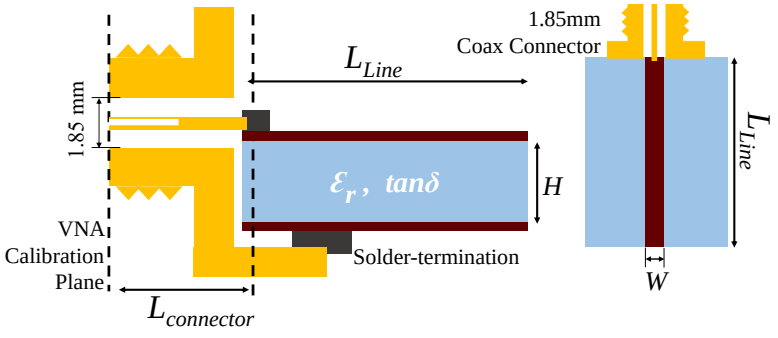

FIGURE 6.3: The microstrip line used in the relative permittivity measurements.

For an open-terminated line, maximum reflection is expected as in

$$\lim_{Z_L \to \infty} \Gamma = 1. \tag{6.1}$$

Therefore, the phase delay of the reflected signal will correspond to a line of twice the mechanical length,

$$L_{\text{reflected}} = 2 \times L_{\text{Line}}. \tag{6.2}$$

The phase delay can then be used to calculate ϵ_r based on the knowledge of L_{Line}. While the wrapped phase will experience distortion due to impedance mismatch at the coax-microstrip transition plane, the unwrapped phase will have minimal distortion. It is expected that an open-ended microstrip line may cause non-uniformities due to the parasitic capacitance. Therefore, it is essential to model the transmission line structure to understand the impact of the parasitics on the phase measurements. When simulated in CST, an open microstrip line did not exhibit any discontinuities in the reflected phase up to 60 GHz, for lines of $40<Z_0<60$ Ω.

Two textile-based microstrip lines of W=1.7 mm, H=0.42 mm, and 50 and 30 mm length were used in ϵ_r measurements. Fig. 6.4 shows the textile-based microstrip lines and the measurement setup. A 67 GHz Agilent E8361a PNA VNA is used to measure the microstrip lines. A 2-port calibration has been performed using a standard 1.85 mm e-cal kit up to 67 GHz, the cables are 1.85 mm "economy" test cables with 6 dB insertion loss. Although the calibration moves the measurement plane to the end of the test cable, the length of the calibration kit's metrology grade connector is not identical to the connector on the device-under-test. This is particularly relevant when using different connector series and lower-grade connectors, to those on the calibration kit. A production-grade 1.85 mm edge-launch connector is used to connect the microstrip lines to the VNA's coaxial cables.

Instead of using the VNA's automated port-extension, the S_{11} of the open-ended connector, (a) in Fig. 6.4, was measured. The connector's S_{11} was used to de-embed the additional phase delay ϕ, introduced by the connector, from the microstrip lines' S_{11} as in

$$\phi_{\text{Line}} = \phi_{\text{Meas.}} - \phi_{\text{Connector}}. \tag{6.3}$$

Fig. 6.5-a shows the measured unwrapped reflected phase delay of the connector $\phi_{\text{Connector}}$ and the microstrip lines ϕ_{Line}. In order to extract ϵ_r, two microstrip lines, of the same dimensions, were simulated in Keysight ADS using the closed-form microstrip models. ϵ_r was modeled as a an exponential function of frequency and an optimizer was used to evaluate ϵ_r based on the measured S_{11} unwrapped phase. Fig. 6.5-a shows the estimated ϵ_r and the simulated phase delay of the microstrip lines. A very close agreement is observed up to 50 GHz between the simulated and measured phase delay showing the accuracy of the extracted ϵ_r. In Fig. 6.5-b, the variation between the simulated phase, using the extracted $\Re\{\epsilon_r\}$, and ϕ_{Line} of the 50 mm microstrip line. As observed in the

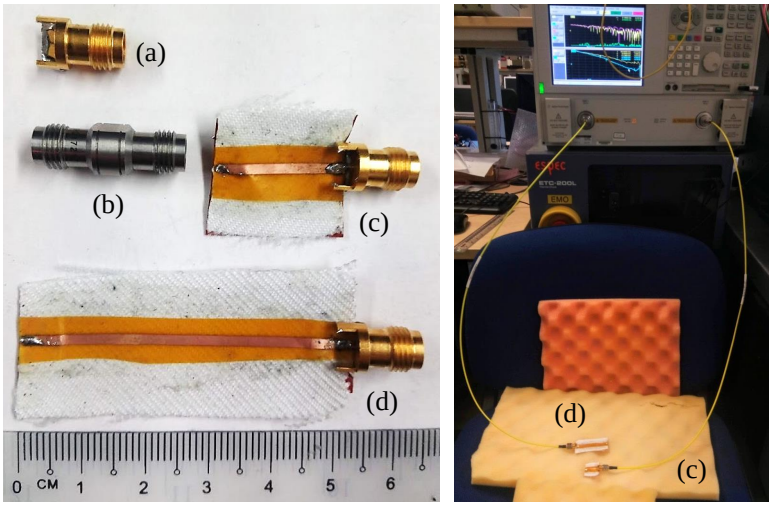

FIGURE 6.4: Samples used in the permittivity measurements (left) and the VNA test setup (right); (a) open-ended 1.85 mm connector, (b) precision 1.85 mm adapter, (c) 20 mm microstrip, (d) 50 mm microstrip.

shaded region of Fig. 6.5-b, the phase error based on the extracted ϵ_r is less than $\pm 1\%$ in the antenna design bandwidth.

For additional validation, a precision jack-to-jack 1.85 mm through adapter (Fig. 6.4-b) from Johnson-Cinch was used to validate the proposed method. The adapter has an air dielectric and hence the measured ϵ_r should be very close to 1. A coaxial line with a 16.3 mm length, 1.85 mm and 0.8 mm outer and inner diameter, respectively, was simulated in ADS to match the measured S_{11} phase of the 1.85 mm adapter. The extracted ϵ_r of the adapter is 1.05, which represents a $<5\%$ error compared to the ϵ_r of air. The error between the simulated and measured reflected phase is 3.6% for the air-dielectric precision adapter. This error arises from not knowing the exact length of the adapter after factoring in the length of the connector on the e-cal kit. This error was de-embedded in the microstrip measurements using the measured phase delay of $L_{\text{connector}}$. Fig. 6.5 shows the simulated and measured reflected phase of the 1.85 mm adapter, showing a close agreement up to 67 GHz. Therefore, the proposed method can be used to extract $\Re\{\epsilon_r\}$ of materials with less than 5% error, without the need for micro machined parts, bespoke TRL calibration kits, or precisely mounted connectors, which is particularly suitable for antenna design on non-uniform and inhomogeneous substrates such as textiles. $\tan\delta$ was measured using the same method using the reflected S_{11} magnitude to be 0.026.

On the other hand, due to the parasitic capacitance of the open-ended microstrip line, the discontinuity implies that this method cannot be used beyond a certain frequency. In this case, the phase response is distorted beyond 50 GHz. However, for the open-ended precision coax (shown in Fig. 6.4-b) the measured phase response is very stable up to 67 GHz, due to being matched to 50 Ω, its improved shielding, and the high-precision

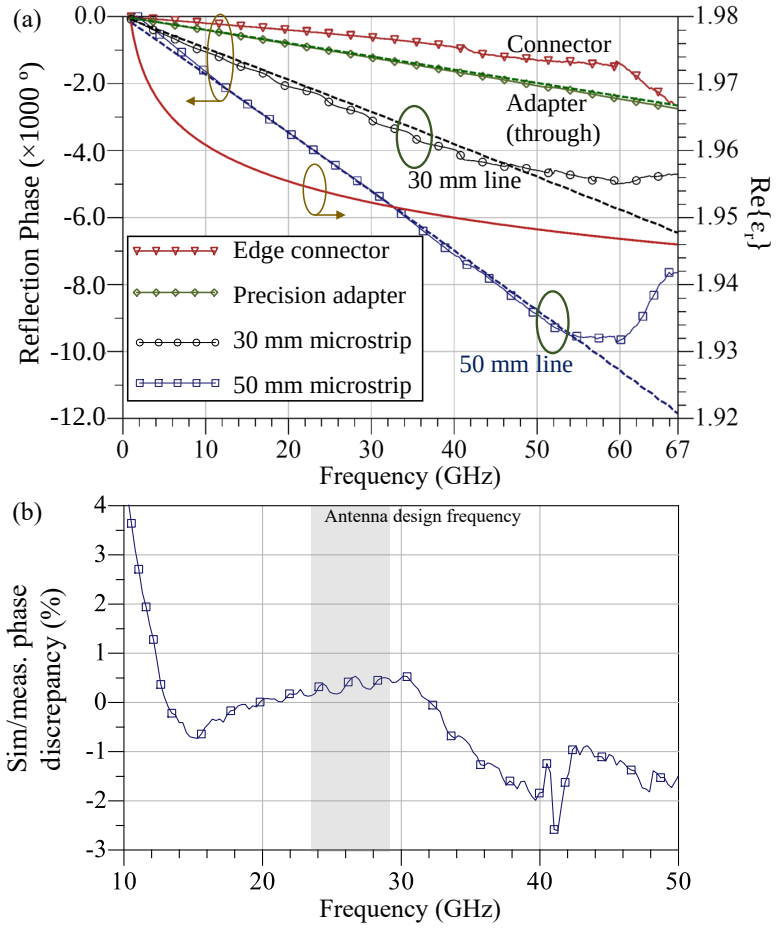

FIGURE 6.5: Extraction of the real real permittivity of the textile microstrip: (a) the simulated and measured reflection phase ($\phi[S_{11}]$) of the textile microstrip in simulation (dashed) and measurements (solid), as well as the extracted $\Re\{\epsilon_r\}$; (b) variation between the modeled and measured ϕ_{Line} of the 50 mm microstrip based on the extracted $\Re\{\epsilon_r\}$ (b).

manufacturing compared to textile-based microstrip lines. Therefore, the frequency limit of this method will be predominantly determined by the transmission line dimensions.

6.2 Textile Patch Antenna Design and Simulation

6.2.1 Broadband Microstrip Antenna Design

To design an antenna for wearable energy harvesting at mmWave bands the antenna needs to maintain a wide input bandwidth (S_{11}). As mmWaves have very poor tissue penetration capabilities beyond the skin [310], the antenna's patterns needs to be predominantly off-body. In addition, due to the wide variation in the angle of incidence of power,

the antenna needs to cover a wide beamwidth. Previously, microstrip antennas with multiple radiative modes were used to obtain several resonances at nearby frequencies, improving the bandwidth compared to a TM_{10} patch [281]. Nevertheless, to excite multiple modes simultaneously, a complex antenna structure is often needed [281, 311, 312].

The dimensions of a rectangular microstrip patch antenna can be calculated analytically for a given TM resonant mode based on the length and width [306]. For a planar (i.e. $t<<\lambda$) microstrip cavity, the resonance frequency f_{mn} of a TM_{mn} mode is given by

$$f_{mn} = \frac{k_{mn}c}{\sqrt{\epsilon_r}} \tag{6.4}$$

$$k_{mn} = \sqrt{(\frac{m\pi}{a})^2 + (\frac{n\pi}{b})^2} \tag{6.5}$$

where c is the speed of light, and f_{mn} and k_{mn} are the resonant frequency and wavenumber for the mn mode, respectively [306]. a and b are the patch dimensions on the m and n respective axes. While this calculation does not account for the fringing fields, it represents a coarse estimate which can be used to guide the full-wave design and simulation.

To achieve a wide S_{11} bandwidth covering the mmWave 5G bands (24.25-29.50 GHz [313]), the proposed antenna is based on dual resonant modes. Both modes operate at close frequencies in order to widen the patch's bandwidth. Single mode patch antennas of various structures are first simulated and analyzed, to understand their matching and radiation properties, prior to optimizing the broadband patch. Firstly, a TM_{02} patch is designed with a=9 mm as shown in Fig. 6.6-a. Given ϵ_r=1.95 ($1.9<\epsilon_r<2$ due to the non-uniform gaps between the fabric and the polyimide), the TM_{02} patch has a calculated theoretical resonance at 24.4 GHz using (6.4). Fig. 6.6-a shows the layout of the first TM_{02} patch iteration. The simulated S_{11} is shown in Fig. 6.6.

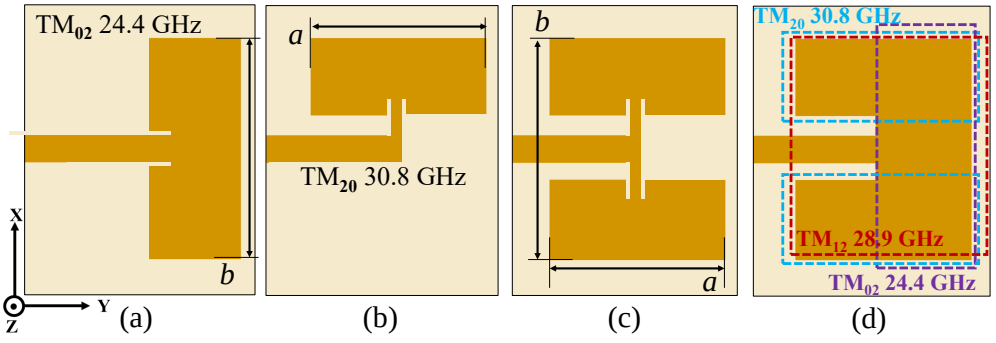

FIGURE 6.6: Broadband antenna design steps: (a) TM_{20} patch at f_1; (b) TM_{02} patch at f_2; (c) symmetric array configuration of f_2 TM_{02} patch; (d) the proposed dual-mode patch antenna.

The next step is designing a higher frequency patch. For b=7.125 mm, the analytical TM_{02} resonance, f_2, is 30.5 GHz. Fig. 6.6-b shows the layout of the TM_{02} patch. To achieve a symmetric design TM_{02} is used in a 1×2 array configuration (Fig. 6.6-c),

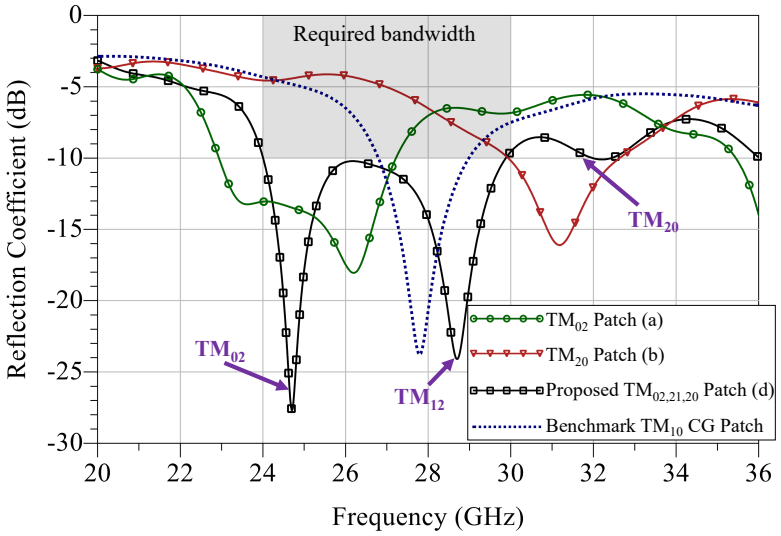

FIGURE 6.7: Simulated S_{11} of the single-mode patch cells and the proposed dual-mode broadband antenna; a TM_{10} CG patch is included for bench-marking.

which does not detriment the S_{11} matching, based on the CST simulations. Finally, the dual-mode patches is designed as shown in Fig. 6.6-d, covering the required bandwidth between 24 and 30 GHz, as shown in Fig. 6.7, with the optimal dimensions a=9.0 and b=7.13 mm. The modes and the active radiating regions shown in Fig. 6.6-d were based on the resonant modes calculated using (6.4), and the CST simulated E-fields. For benchmarking, a common geometry (CG) TM_{10} patch with a $\lambda/4$ impedance transformer has been simulated, showing a narrower bandwidth in Fig. 6.6 than the individual patch cells resonating at the second TM mode, and a significantly narrower bandwidth than the proposed antenna. When simulated on a low-loss substrate ($\tan\delta$<0.0007), the antenna maintains a $S_{11}<-6$ dB from 22.5 to 26.7 GHz.

The electric (E-field) distribution of the individual TM_{20}/TM_{02} single-mode patches are shown in Fig. 6.8-a and 6.8-b, respectively. By observing the E-field, both antennas are expected to have broadside far-field patterns with a wide -3 dB beamwidth. From CST, the single patch cells (Fig. 6.6-a and b) achieve a 95° and 102° half-power beamwidth of at 24.5 and 30.5 GHz, respectively. The peak simulated directivity is 8.5 and 7.5 dBi at 24.5 and 30.5 GHz. Due to the 1×2 array configuration of the 30.5 GHz region (Fig. 6.6-c), shown in Fig. 6.6-c, the proposed patch (Fig. 6.6-d) achieves a simulated broadside peak directivity of 10 dBi.

A prolonged microstrip feed was introduced to minimize any distortion from the feed to the antenna's radiation properties [159]. However, the coaxial connector and the microstrip feed may cause additional reflection and spurious radiation which might distort the antenna's radiation pattern. The coaxial to microstrip feed was simulated in CST and it was observed that the spurious radiation is less than -19 dBi, under 30 GHz, showing minimal influence on the antenna's patterns. The additional losses in the microstrip feed will be representative of the insertion losses in a distributed microstrip matching

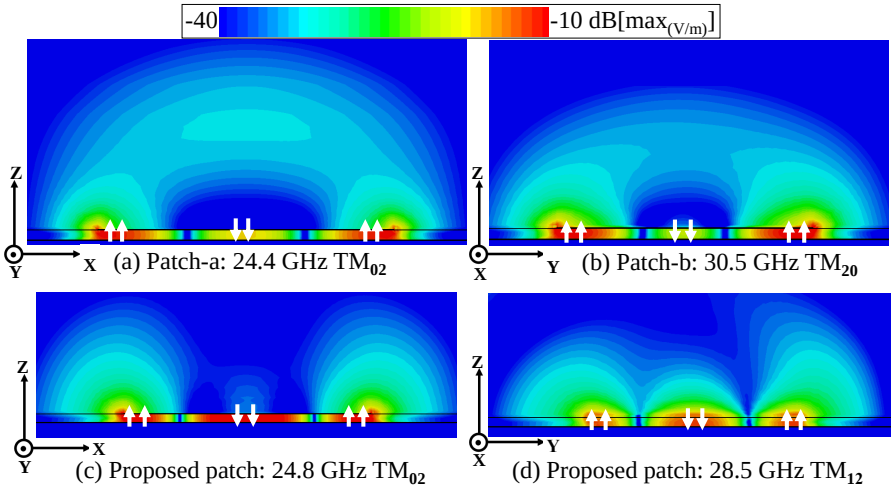

FIGURE 6.8: Simulated E-fields across the antenna: (a) TM_{20} patch; (b) TM_{02} patch; (c) proposed patch TM_{20} mode at 24.8 GHz; (d) proposed patch TM_{21} mode at 28.5 GHz.

network, should the antenna be matched to a rectifier, or in an array feed network. Fig. 6.9-a shows the layout and dimesnions of the antenna.

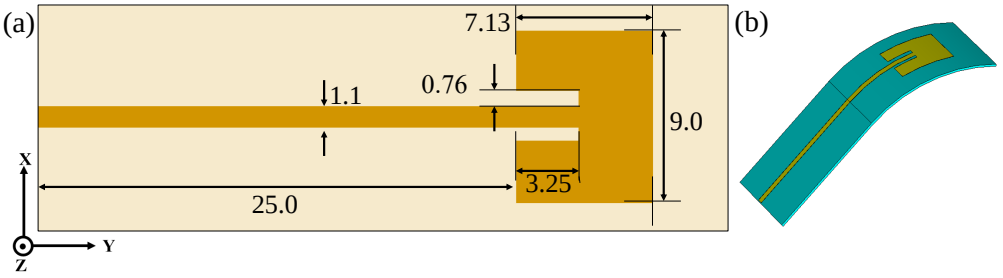

FIGURE 6.9: The proposed dual-radiative region microstrip antenna: (a) layout and dimensions (in mm) of the fabricated prototype, (b) simulation model of the bent antenna.

6.2.2 Bending and Wearable Operation

For wearable operation, the antenna was simulated in proximity with a tissue model. A simplified layered model is used [185]. The skin layer, shown in Fig. 6.11, is based on the measured skin properties above 26.5 GHz from [310]. It was previously shown that mmWaves do not penetrate deeper than the skin layer [314]. Fig. 6.11-a shows the antenna at 3 mm separation from the tissue model, as well as the dielectric properties and thickness of each layer. The simulated reflection coefficient on the tissue model shows less than 2% shift in the antenna's resonance when placed on the body, this is attributed to the additional capacitance introduced by the higher ϵ_r of the tissue compared to air. The impact of bending has been investigated by bending the antenna across a 15 mm radius, as shown in Fig. 6.9-b, which results in 4% shift in the resonance, as shown in Fig. 6.10, and does not alter the $S_{11} < -10$ dB bandwidth from 25 to 28.5 GHz.

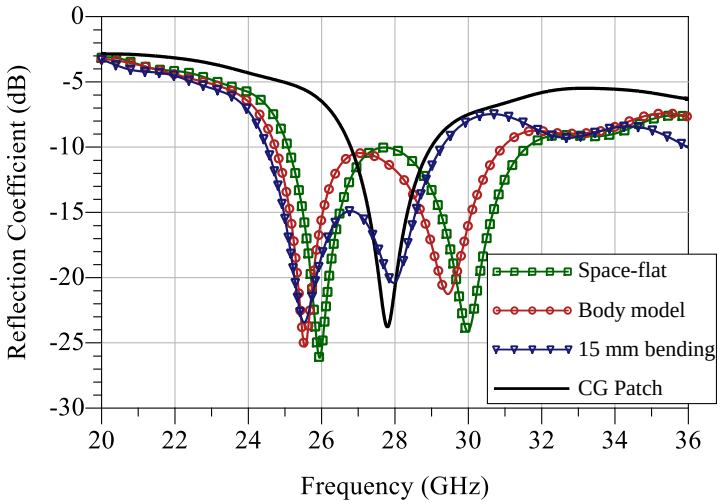

FIGURE 6.10: Simulated reflection coefficient of the proposed dual-radiative region textile patch antenna in space, during bending, and at 3 mm from the human body model and a common geometry patch (CG Patch).

The tissue model has been used to calculate the antenna's SAR at 28 GHz, shown in Fig. 6.11-b. The highest absorption is observed in the skin layer, as most of the mmWave power does not penetrate deeper than the skin layer [314]. The maximum SAR of 0.461 W/kg, when normalized to 10 g tissue mass, is compliant with the IEEE C95.1 regulatory limit of 2.0 W/kg. The SAR was calculated for a 0.5 W (≈27 dBm) input power, which is higher than the maximum power level a textile mmWave rectenna may be exposed to, as shown in the experimental rectenna development in Chapter 7.4.

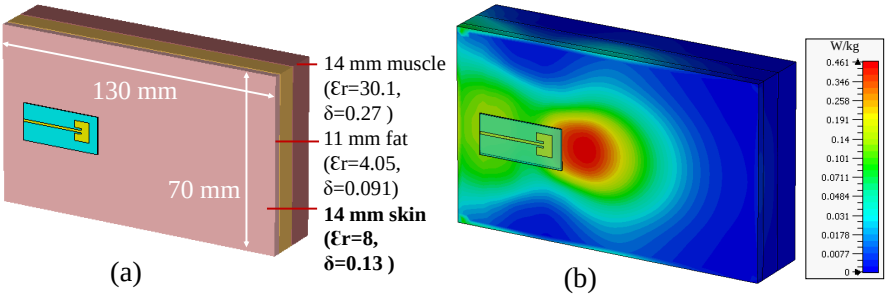

FIGURE 6.11: Simulation of the patch antenna on the body model: (a) body phantom structure, (b) simulated SAR at 28 GHz for a 0.5 W input.

6.3 Antenna Measurements

6.3.1 Antenna Bandwidth

Two antenna prototypes have been used to measure the antenna's reflection coefficient. By using two prototypes, the uncertainty introduced by the connector's soldered interface can be observed and minimized. Due to the thin textile substrate compared to

conventional circuit boards, the 1.6 mm-thick connector and pin are expected to introduce additional discontinuities at the coax/microstrip interface, altering the S_{11} response. The connector-fed antenna has been simulated in CST, Fig. 6.12 shows the simulated and measured reflection coefficient of the connector-fed antenna.

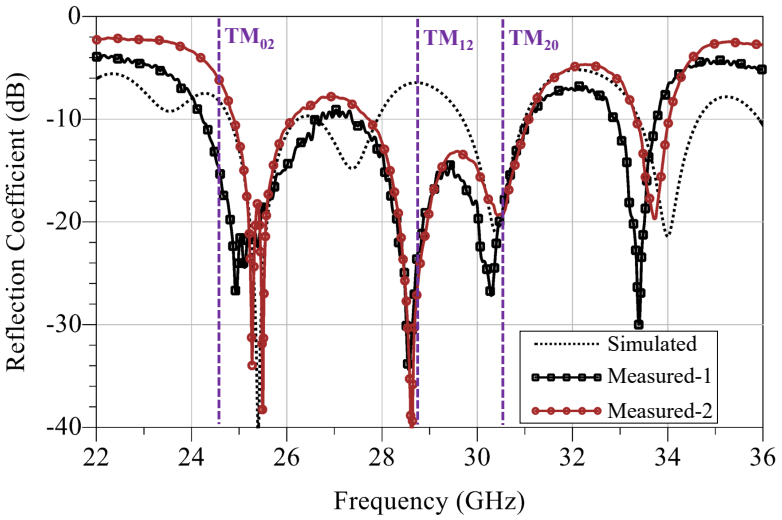

FIGURE 6.12: Measured reflection coefficient of two antenna prototypes (solid) and the CST simulation with a soldered connector (dashed).

Fig. 6.12 demonstrates that the simulated (with the connector) and measured S_{11} exhibit a good agreement. The analytically calculated resonant frequencies of each mode using (6.4) closely agree with the measured resonances observed on both measured prototypes. From 26 to 28 GHz, a discrepancy can be observed between the prototypes. This can be attributed to the length of the connector's unshielded pin, approximately $\lambda/4$ at 27 GHz, which acts as an impedance transformer around 27 GHz causing additional reflection, as observed in the S_{11} of prototype-2 in Fig. 6.12. For both measured prototypes, the antenna maintains an impedance bandwidth between 24.9 and 31.1 GHz, with an S_{11} under -8 and -10 dB on prototype 1 and 2, respectively.

The antenna's S_{11} was measured on-hand and under bending. The antenna was bent both in space and on-hand, as shown in the inset in Fig. 6.13, while measuring the S_{11}. As observed in Fig. 6.13, the antenna's S_{11} response remains mostly unaffected in human proximity and under bending.

6.3.2 Antenna Radiation Patterns

The 3D polarimetric radiation patterns of the proposed antenna were measured in an anechoic chamber at 24 and 26 GHz. The measurements were carried at the University of Bristol Communication Systems & Networks lab, by G. S. Hilton [315], following the standard setup previously used by the author in [244], presented in the next chapter. The measurement frequency was limited by the PA's frequency and the WR-42 horn

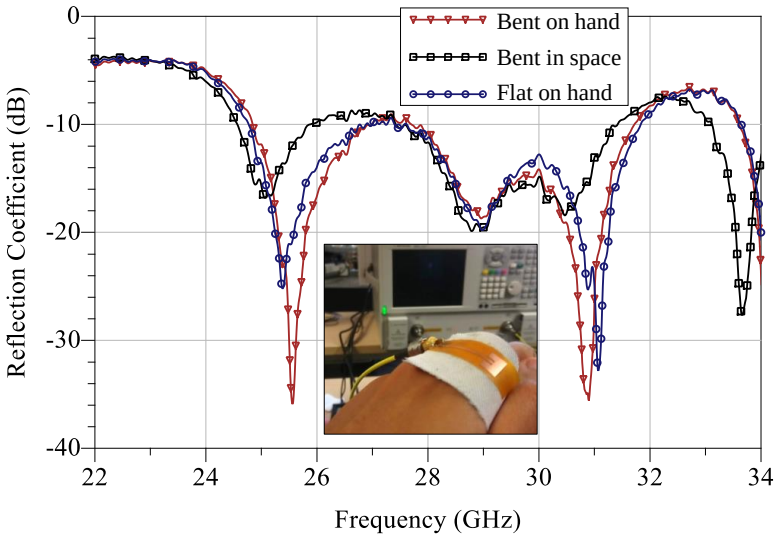

FIGURE 6.13: Measured reflection coefficient of the microstrip antenna under bending and near the body; inset shows the on-hand bending.

$f_{\text{cut-off}}$. To improve the repeatability of the measurements, the antenna was mounted on a large (radius>$5\lambda_0$) circular ground plane, as in [244]. Fig. 6.14 shows the 3D measured directivity D, normalized to 10 dBi, and the polarization of the measured D. The polarization of the textile antenna has been normalized using a gain-standard 20 dBi WR-42 horn.

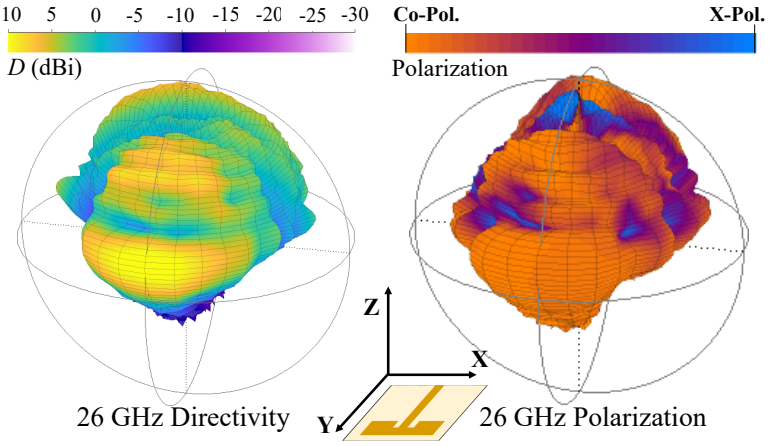

FIGURE 6.14: Measured 3D directivity D and polarization of the proposed antenna, on a large ground plane, at 26 GHz.

The peak measured D is 13.2 and 11.2 dBi, at 24 and 26 GHz respectively. The measured results are indicative of the antenna's performance over a continuous ground plane, such as a fully-textile shielding between the antenna and the human body, which was shown to reduce the SAR of mmWave wearable antennas [244]. The simulated and measured radiation patterns of the antenna, with the 1.85 mm connector and the large ground plane, are shown in Fig. 6.15. It can be observed that the simulated and measured co-polarized D agree in the main off-body forward beam direction ($-90°<\theta<90°$), and

that the antenna's main lobe on the Z-axis is broad, enabling a more position-tolerant energy harvesting performance.

On the principal plane, the antenna achieves 13 and 25 dB simulated co/cross-polarization at 24 and 26 GHz respectively. Polarization purity is often regarded as a FoM in antenna design for communications. In the context of energy harvesting, a high co/cross-polarization isolation does not translate to better energy harvesting performance. It was previously shown that both directivity and polarization can almost be irrelevant when the receiver is far from the base-station, and that dual-polarization using orthogonal antennas in a large-area implementation are needed for polarization-insensitive harvesting [53]. On the other hand, while circular polarization can be preferred in directional WPT [76], it is still prone to mismatch between right and left-hand circularly polarized incident radiation [15]. Finally, in the more general wearable BAN antenna case, a high polarization purity is not required due to the mobility and rotation of the antenna, for example when the antenna is used on the wrist or arm [156, 290].

The 3D total radiated power was used to measure the efficiency (inclusive of mismatch) of the proposed antenna, with respect to a reference WR-42 horn [156]. The radiated power of the textile antenna and the reference horn were measured at 24 and 26 GHz. 3 measurements of both the antenna-under-test and the reference horn were performed; a 1.3% standard deviation was observed. The measured S_{11} of the connectorized antenna was used to calculate the radiation efficiency excluding mismatch. The antenna's measured $\eta_{\text{Rad.}}$ is 60% and 59.4%, ±5%, at 24 and 26 GHz respectively. The simulated efficiency is 55% and 53%, at 24 and 26 GHz, agreeing within 5% with the measured efficiency. Using the measured efficiency, the antenna's measured gain is 8.2 dBi at 26 GHz.

Table 6.1 compares the proposed textile-based antenna design to reported mmWave microstrip antennas. It can be seen that the proposed antenna achieves the widest fractional bandwidth of 26% compared to other single-layer antennas, owing to its dual-resonant structures. To compare the radiation efficiency vs. reported textile mmWave antennas, the measured radiation efficiency was normalized to the antenna's electrical thickness using

$$\eta_{\text{norm.}} = \eta_{\text{rad.}} \times \frac{\lambda}{t}, \tag{6.6}$$

where t is the antenna's thickness and $\eta_{\text{rad.}}$ is the measured antenna efficiency.

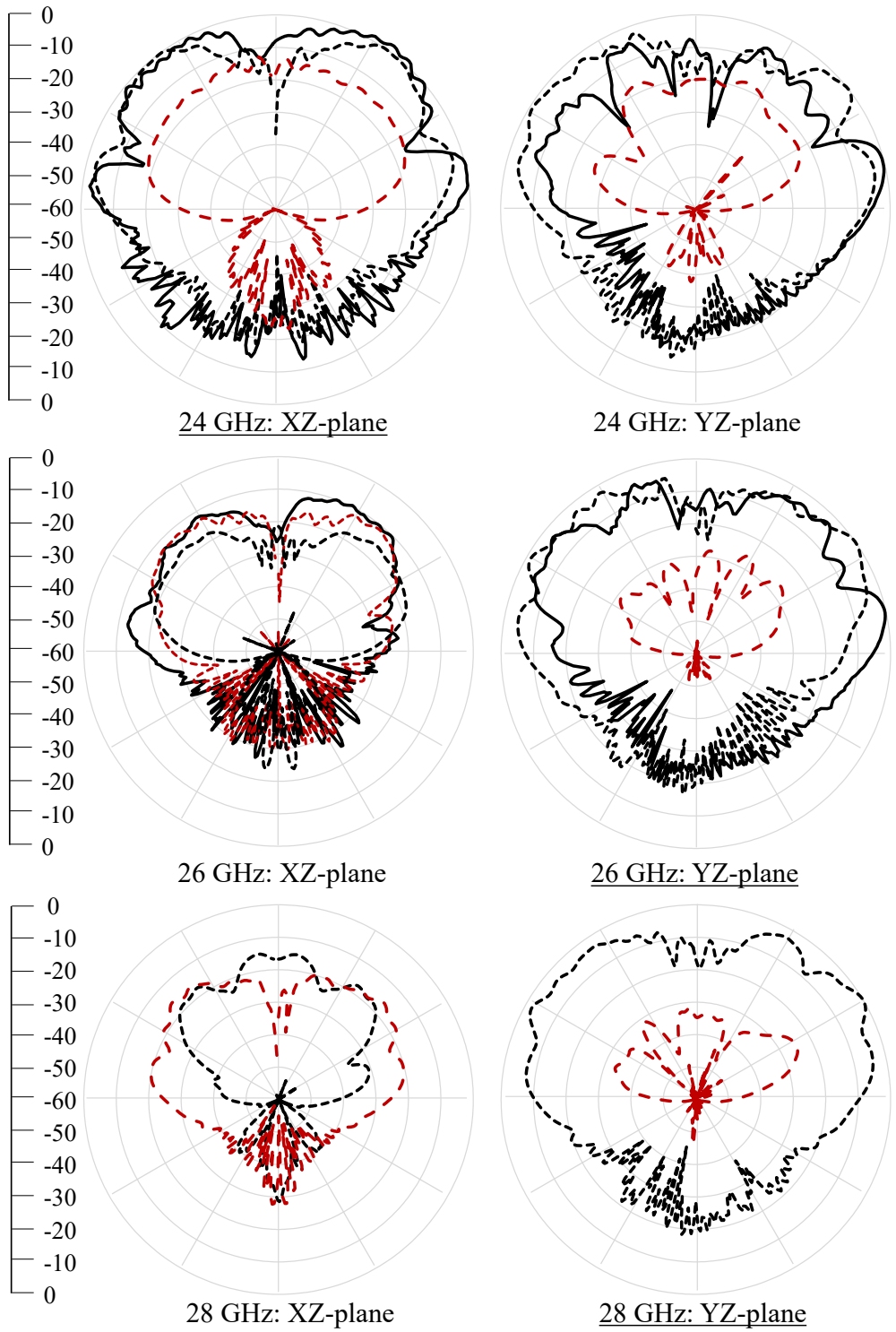

FIGURE 6.15: Measured (solid) and simulated (dashed) co-polarized (black) and cross-polarized (red) normalized radiation patterns of the proposed antenna.

TABLE 6.1: Comparison of the proposed textile antenna with reported planar mmWave microstrip antennas.

Study	**Antenna**	**Substrate**	**Bandwidth (GHz)**	**Fractional BW**	**Antenna efficiency**	$\eta_{\text{norm.}}$	**Gain (dBi)**	**Co/x-pol. isolation (dB)**	**Electrical vol. (λ_0^3)**
This work	**TM_{20}/TM_{21} Patch**	**Kapton on woven polyester (tanδ= 0.026)**	**24.9-31.1**	**22%**	**50-60%**	**15.2**	**7.7 at 24 GHz; 8.9 at 26 GHz**	**13 at 24 GHz*; 25 at 26 GHz***	**0.59× 0.75× 0.034**
AWPL'12 [164]	End-fire quasi-Yagi	Woven cotton (tanδ= 0.016)	57-65	13%	48%	12.6	11.9	13	3× 0.76× 0.04
TAP'13 [159]	2×2 TM_{10} patch array	Woven cotton (tanδ= 0.02)	56-65	14.9%	41%	11.0	9	15 (meas.); >20 (sim.)	1.10× 0.96 × 0.037
TAP'19 [312]	TM_{10}/TM_{10} slotted patch	Taconic + Rogers (tanδ < 0.001)	30-50	45.4%	85%*	7.7	5-8.5	16 (meas.); 25 (sim.)	1.25× 1.25× 0.110
AWPL'19 [316]	Archimedean spiral	Duroid 5880 (tanδ < 0.001)	21.1 - 34.1	46.4%	96%*	53.7	6.5	≈7†	1.06 × 1.06 × 0.013

NR: not reported; *Simulated result; †right/left-hand circular polarization isolation estimated from the patterns).

Compared to the textile antennas in [317] and [159], operating at 60 GHz, the proposed antenna achieves a higher radiation efficiency while having a lower profile (compared to λ_0). Compared to the multi-mode patch in [312], the proposed antenna compares favorably when the antenna efficiency is normalized to the thickness, despite being implemented on textiles and not RF laminates. In addition, the wider bandwidth in [312] was achieved using a SIW cavity and a very thick ($0.11\lambda_0$) substrate. While broadband "wire-type" antennas such as [316] achieve higher efficiency and bandwidth on low-loss substrates, the antenna requires double-sided etching and the efficiency is only achievable with tanδ<0.001 substrates. Other printed TM_{10} patches, [75, 272], implemented on low-cost substrates or using printed conductors achieve a narrower bandwidth and a lower radiation efficiency than the proposed antenna.

6.4 mmWave Wireless-Powered BAN Evaluation

The textile patch antenna's radiation properties are utilized to analytically evaluate the performance of a mmWave-powered BAN. In this section, we compare the WPT efficiency based on the proposed patch to a similar sized off-body antenna based on the same area, in Section 6.4.1, demonstrating that a higher-efficiency WPT link can be achieved at mmWave bands compared to UHF, when the antennas' area is restricted. In section 6.4.2, the wireless power harvesting capabilities of a large-area rectenna system based on the proposed antenna is evaluated and compared to a UHF off-body rectenna.

6.4.1 Compact Single-Receiver

Higher power can be delivered to a compact receiver in mmWave bands due to the comparable physical aperture size of the antenna to the wavelength. This section demonstrates the benefits of using the proposed antenna for WPT to and from an area-constrained transmitter and receiver. Two symmetric textile patch antennas were connected to a VNA's ports to measure the forward transmission between them in space, as shown in Fig. 6.16. As the proposed antenna is only matched for mmWave bands and will have a very high reflection coefficient for UHF bands, the measured forward transmission has been corrected post-measurement to exclude the impedance mismatch losses at 2.4 GHz. By positioning the antennas at d=50 cm, d is equal to $4_{2.4\text{GHz}}$ ensuring the antennas are in their far-field regions.

Fig. 6.17 shows the measured forward S_{21} from 0.5 to 4 GHz and from 22 to 34 GHz. It can be seen that due to the antenna's improved radiation efficiency in mmWave bands, it is possible to achieve around 11 dB S_{21} improvement at 26.5 GHz compared to 2.4 GHz, despite the increased path loss, even after excluding the mismatch losses at 2.4 GHz. The additional advantage of using patch antennas for WPT in mmWave bands is the

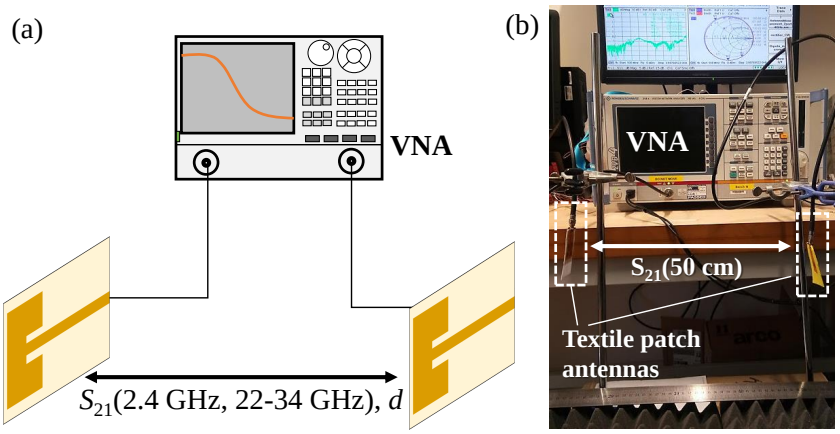

FIGURE 6.16: Measured forward transmission between two symmetric 7.13×9×0.5 mm^3 antennas at 50 cm at UHF and mmWave: (a) schematic; (b) photograph of the UHF setup.

ability to implement the off-body patch on a low-profile substrate. Moreover, while the impedance mismatch losses were excluded at 2.4 GHz for a fair comparison, achieving a low S_{11} at 2.4 GHz with such a compact antenna ($0.06\times0.07\lambda^2_{2.4\text{GHz}}$), a matching network is required, adding to the insertion losses and the overall cost and complexity of the WPT solution.

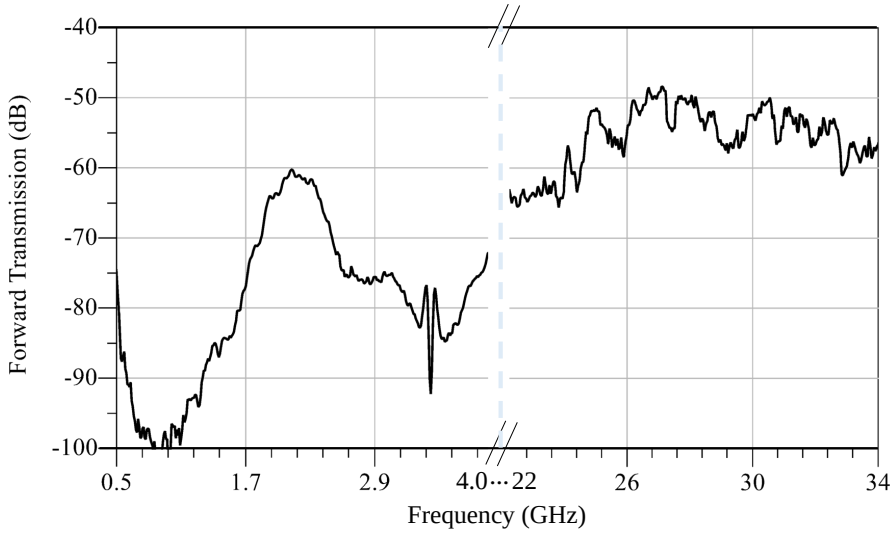

FIGURE 6.17: Measured forward transmission between two symmetric antennas at 50 cm at UHF and mmWave.

6.4.2 Large-Area Implementation

Where area is not a constraint, an alternative method to improve the power reception by a wearable mmWave rectenna is a large-area implementation [179]. An array of rectennas based on the proposed antenna is considered. Each rectenna is formed of a single element rectifier. Loss-less DC combining of the output of the rectifiers is assumed.

As the power is combined at DC, the large area rectenna does not result in a more directional radiation pattern, thus does not reduce the antennas' harvesting beamwidth. DC combining has been demonstrated with less than 1% losses [318], therefore, loss-less DC combining is assumed. Fig. 6.18-a shows the architecture of the large-area mmWave rectenna array, and the rectenna's structure in Fig. 6.18-b.

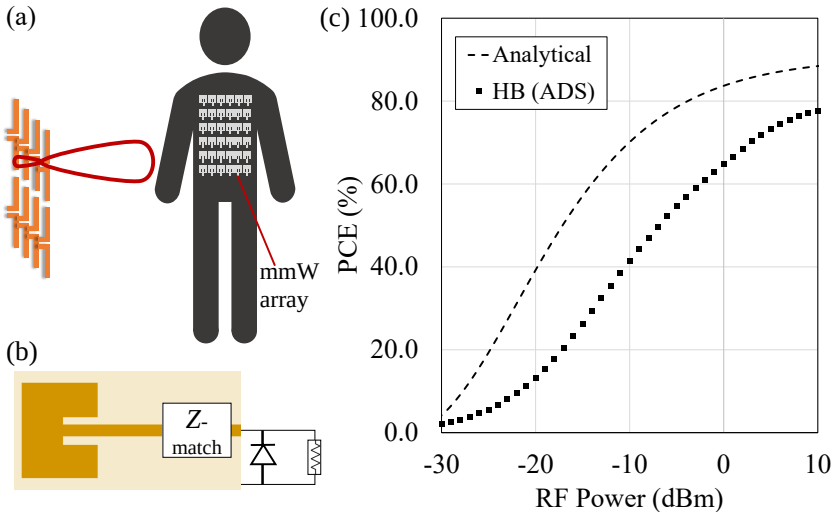

FIGURE 6.18: The large-area mmWave power receiver: (a) textile-based rectenna array with directional transmitter and ideal DC combining, (b) a single rectenna cell, (c) analytically calculated and simulated PCE of the rectifier at 28 GHz.

In previous work evaluating the performance of mmWave energy harvesting networks, an analytical model for the PCE is used [235]. Both the linear [235] and non-linear models [319] previously used were not based on actual rectifier devices. In addition, a quadratic PCE formula may not accurately model all the physical loss contributors such as diode losses and harmonic generation [204]. The analytical diode PCE formulas proposed in [204] are used as a starting point for the PCE evaluation. However, as discussed in [283], such analytical closed form approximations do not accurately reflect the losses due to harmonics generation at very low power levels, and HB simulation is more suited. Therefore, in our comparison between mmWave and UHF WPT performance, HB results are used for a more conservative estimate.

The diode considered in this work is the VDI W-ZBD GaAs Schottky diode, used for low-power rectification up to 100 GHz for its low forward voltage and parasitic capacitance [238, 320]. Fig. 6.18-c shows the calculated PCE for the rectifier using the analytical formulas from [204] and HB simulation. The peak PCE of 77% observed in the HB model is within 10% of the reported PCE at 36 GHz in [243], based on commercial Schottky diodes [12]. Moreover, -12 dBm rectification with over 12% PCE was previously demonstrated up to 90 GHz [321].

Two transmitters are considered: a 28 GHz 53 dBm EIRP and an 892 MHz (the center resonant frequency of [178]) 36 dBm EIRP. These are the maximum permissible EIRP levels for both bands. In mmWave bands, the maximum EIRP is higher than sub-5 GHz

bands. For example, an EIRP of 75 dBm is permitted for a 5G base-station, where the higher EIRP is achieved using high-gain phased arrays [230]. The 53 dBm EIRP could be realized using a 1 W transmitter and a 23 dB antenna, which is permissible for license-free bands above 5 GHz [322]. Below 5 GHz, the EIRP limit is capped at 4 W (approximately 36 dBm). From a practical implementation perspective, the antenna's theoretical minimum physical aperture area $A_{\text{Phys.}}$ can be calculated from the aperture efficiency $\eta_{\text{App.}}$. For a fixed $\eta_{\text{App.}}$ and a target antenna gain G (dimensionless) [117]. Assuming a 90% aperture efficiency, typical for radiating aperture antennas [117], a 23 dB antenna at 28 GHz would occupy an area of 2000 mm^2. This represents 95% less area than a 6 dB antenna operating at 900 MHz. Therefore, utilizing mmWave wireless charging base-stations promises reduced base-station antenna size allowing more pervasive deployment. Multiple array sizes based on the proposed antenna are considered, with a 5.4 mm ($\lambda/2$ at 28 GHz) spacing between the array elements. The power harvested by the rectennas is calculated using an empirical propagation model.

The UHF textile patch antenna presented in [178] for sub-1 GHz WPT is considered as a reference to evaluate the performance of mmWave powering of BANs. For both mmWave and UHF, the maximum PCE obtained from the non-linear HB simulation is used.

Fig. 6.19 shows the received power by the UHF and mmWave antennas. Although free-space propagation at 28 GHz are significantly higher compared to 892 MHz, the increased array size allows recovering higher amounts of power than the UHF patch for arrays of 6×6 elements or larger.

The area consumed by the UHF patch is 190×240 mm^2 [178], considering a single mmWave array element size of 9×14 mm^2 and a 5.4 mm separation between the elements, a 13×13 array could be realized in approximately the same area as the UHF patch. The 13×13 mmWave array is considered for further evaluation of the 28 GHz-powered BAN case. To provide more accurate modeling of the propagation losses, an empirical path loss exponent is used to calculate the power received by the antennas at 28 GHz. The received DC power P_{RX} has been calculated using

$$P_{\text{RX}} = P_{\text{EIRP}} G_{RX} \left(\frac{c}{4\pi\lambda}\right)^2 \frac{1}{d^{\alpha}} \times \text{PCE}, \tag{6.7}$$

where α is the path loss exponent for the distance d, and the PCE is the HB-simulated PCE shown in Fig. 6.18-c. $\alpha = 2.0$ and $\alpha = 2.9$, for LOS and N-LOS respectively. α values are based on the empirical channel models of 28 GHz propagation in [323]. Only free-space LOS propagation is considered for the UHF antenna. The DC power Fig. 6.20 shows the calculated P_{RX} by the mmWave patch array and the single UHF patch. As the analysis in this section is based on the measured off-body gain of the patch, it is an accurate representation of the antenna's performance as a wearable wireless power receiver.

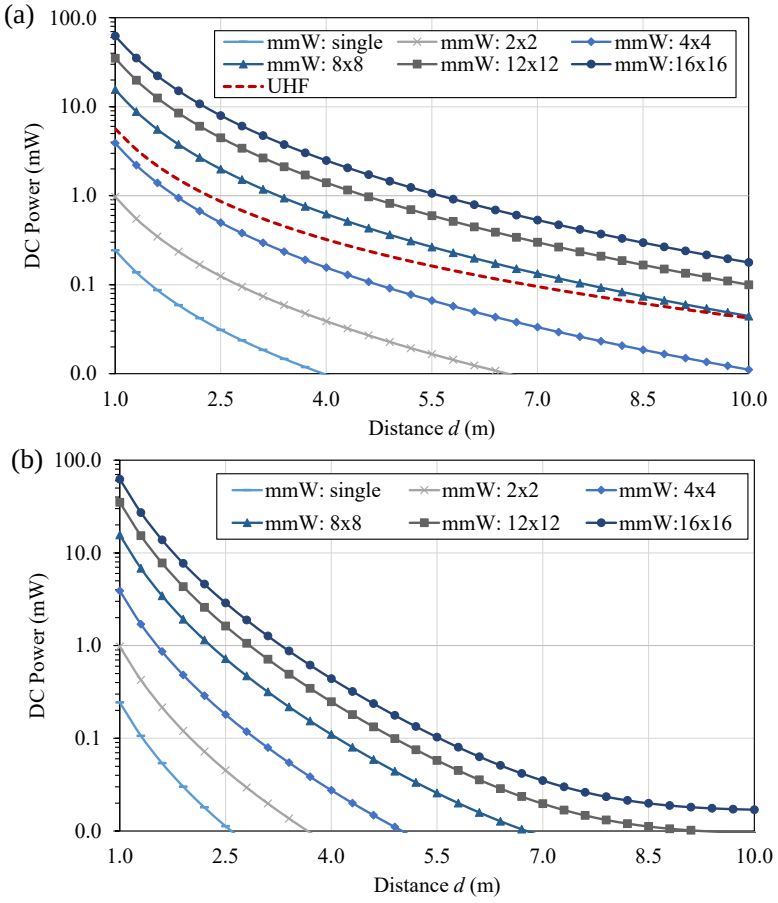

FIGURE 6.19: DC power harvested by different-sized arrays, based on the measured antenna gain and empirical path loss model, at 28 GHz: (a) LoS, (b) N-LoS.

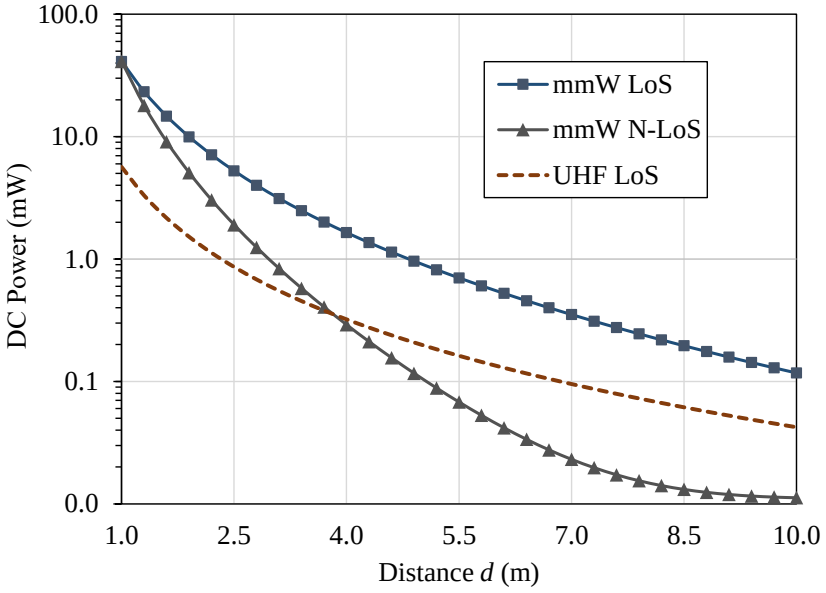

FIGURE 6.20: Calculated received power by the 892 MHz UHF patch and 13×13 28 GHz array, occupying the same area, based on empirical propagation losses.

Despite the increased path losses, and the empirical path loss exponent, for both the LOS and N-LOS cases, more power can be delivered to the wearable receivers at 28 GHz compared to 892 MHz, when using textile microstrip patch antennas. This demonstrates that body-centric WPT and RFEH from an off-body source can achieve improved end-to-end efficiency due to the smaller size of the antennas. Table 6.2 compares the power received by the mmWave and UHF antennas calculated using (6.7). The received DC power density is calculated using $P_{\mathrm{RX}}/A_{\mathrm{Phys.}}$. Owing to the higher permissive EIRP and the compactness of the mmWave patch, the received power density is higher than that at UHF. Therefore, the large-area implementation can harvest up to 6.3× higher power compared to the UHF solution occupying the same area. The array calculation does assume ideal DC power combining which represents a challenge for sub-mW power levels. However, DC combining circuitry for rectennas have been previously developed with less than 1% power ripple for balanced and imbalanced inputs [318].

Table 6.2: Textile-based LoS mmWave and UHF WPT summary.

	mmW single	13×13 mmW array	UHF single [178]
Patch area (mm^2)	9.0×14	187×247	190×240
G (dBi)	6.0	-	4.6
P_{RX} at 2 m (mW)	0.1	10.9	1.74
P_{RX} density ($\mathrm{mW/m}^2$)	574	311	38.2

6.5 Summary and Conclusions

This chapter presented a new textile-based microstrip patch antenna design based on multiple radiative modes for improving the antenna's bandwidth. With at least 50% radiation efficiency, the proposed antenna is a candidate for mmWave-powered BANs. The key findings can be summarized as:

- Based on multiple radiative regions, a higher-order mode patch antenna can be demonstrated with a wide bandwidth on a thin substrate, for mmWave WPT.
- For compact transmitting and receiving antennas, operating at the mmWave bands enables over 10 dB forward transmission improvement over a short (50 cm) LoS range, compared to 2.4 GHz.
- For large-area implementations, an array of rectennas operating at 28 GHz can improve the harvested power by up to a factor of 6, over a similar sized sub-1 GHz microstrip patch, assuming the maximum PCE of a rectifier is achieved and the DC output can be combined with minimal losses.

This chapter highlights the significance of mmWave WPT and the need for high-efficiency low-cost rectennas operating in mmWave bands, to allow BANs to become energy-neutral using off-body mmWave WPT. High-efficiency rectifiers as well as DC power combining mechanisms are essential to allow mmWave antenna and rectenna arrays to surpass their UHF counterparts' energy harvesting performance.

Chapter 7

Textile-Based Broadband mmWave Rectenna

In this chapter, rectenna development for the 5G mmWave bands is presented. A novel broadband textile antenna is proposed for wearable applications, the first textile-based antenna covering the 5G spectrum with radiation efficiency improvements over conventional antenna designs such as a microstrip patch and a disc monopole. The rectenna is integrated with a fully-distributed microstrip voltage doubler rectifier based on a commercial Schottky diode demonstrating a 1.3-V DC output from less than 12 dBm of mmWave power across the full bandwidth between 20 and 26.5 GHz, and more than 1 V from under 10 dBm from 23 to 24.5 GHz.

This chapter is based on the content published in [244] and [66]. This chapter presents novel contributions to mmWave antenna design presenting the widest bandwidth antenna implemented on a flexible substrate based on a novel design, as well as achieving the highest radiation efficiency among reported textile-based mmWave antennas. Furthermore, this chapter presents the design and implementation of a broadband mmWave rectifier using a fully-distributed elements microstrip matching network, for compatibility with a standard 50 Ω antenna, presented in section 7.3. This work demonstrates the first textile-based, flexible mmWave rectenna for wearable RFEH applications in future 5G mmWave bands (section 7.4), and the first rectenna with broadband (28% fractional bandwidth) 1.3 V DC sensitivity from 12 dBm of wireless power above 20 GHz.

7.1 Antenna Design and Fabrication

7.1.1 High-Efficiency, Broadband Antenna Design

5G mmWave bands are motivated by the wider available spectrum. In Europe, China, Africa and Brazil, 26 GHz is chosen as a center frequency while in the US, Japan, South Korea and India the legislated frequency is 28 GHz [313]. In addition, 1 GHz bandwidth will be allocated to individual mobile service providers in the so-called mmWave 5G bands [313]. Collectively, the 26 and 28 GHz bands cover a bandwidth of 5.25 GHz, approximately 20% fractional bandwidth. Such wide bandwidth motivates research into broadband antenna design both for communication and wireless power harvesting applications.

To realize a rectenna capable of harvesting energy at 5G bands, along with the 24 GHz license-free band, the antenna needs a wide impedance bandwidth. Moreover, as a textile or flexible rectenna may be used in proximity with human tissue, a frequency-independent antenna is preferred to minimize any detuning impact. The proposed monopole antenna is inspire by the broadband Antipodal Vivaldi Antenna (AVA) [324]. Although the proposed antenna's geometry is not self-complementary or symmetric due the 50 Ω microstrip line width being comparable to the radiator, resulting in a narrower bandwidth, the radiator's shape and size have been tuned in simulation to achieve a bandwidth covering the 24, 28 and 36 GHz bands.

The main aim of the antenna design process has been to prioritize maximizing the radiation efficiency. Given the high tanδ of textile substrates [11], this has been achieved by choosing an antenna design where a minimum part of the radiator is parallel to the ground-plane (e.g. a monopole) to minimize the electric field dissipation in the substrate. This is explored in comparison to a standard patch antenna in Section 7.1.2. The AVA's layout and dimensions are shown in Fig. 7.1.

7.1.2 Comparison with a Microstrip Patch Antenna

For benchmarking the radiation efficiency, bandwidth, and gain, a microstrip patch antenna has been simulated to validate the assumptions on the influence of the radiator's area on the antenna's efficiency, and to demonstrate the improvement of the proposed design over a standard design on the same substrate. Patch antennas have been widely reported in wearable mmWave antennas [159] and in low-cost additively manufactured rectennas [75,135,234]. Both antennas have been simulated using CST Microwave Studio using the measured substrate properties ($\epsilon_r = 1.56$ and tan$\delta = 0.027$). Fig. 7.2 shows the simulated reflection coefficient of the antennas. The gain and radiation efficiency are shown in Fig. 7.3.

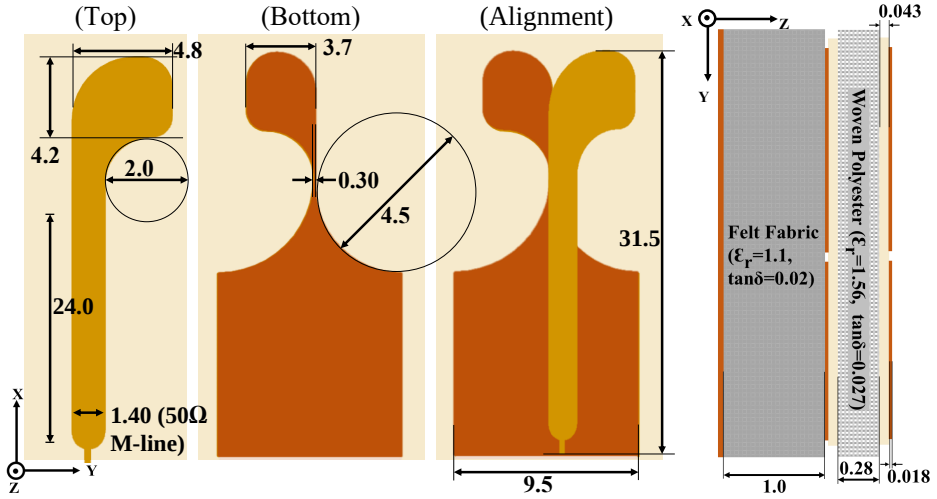

FIGURE 7.1: The proposed antenna layout and dimensions (in mm), showing the double-sided AVA and the substrate composition

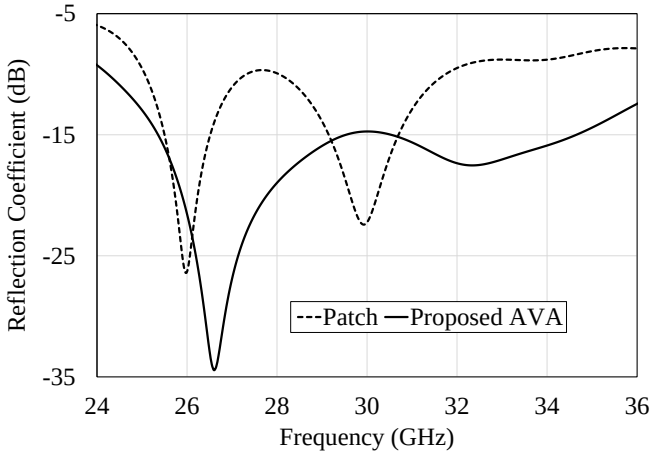

FIGURE 7.2: Simulated reflection coefficient of the two antenna designs considered, a common-geometry patch and the proposed novel AVA.

Overall, a more broadband behavior is expected from the proposed AVA, as demonstrated by the lower S_{11} in Fig. 7.2 and more stable gain in Fig. 7.3. However, at 26 GHz, where both antennas achieve $S_{11} < -20$ dB, the proposed AVA achieves over 67% higher radiation efficiency relative to the patch antenna, demonstrating more than 3 dB gain improvement. This is explained by the patch antenna's higher dielectric losses discussed earlier; over 53.7% of the accepted power is dissipated in the patch's textile substrate as opposed to only 32.4% of the power accepted by the proposed AVA.

7.1.3 Comparison with a Broadband Disc Monopole

While the proposed AVA-inspired monopole outperforms the microstrip patch in bandwidth and efficiency, other broadband monopole antenna designs, such as the disc monopole explored in Chapter 4 [279], may be able to achieve similar performance. In

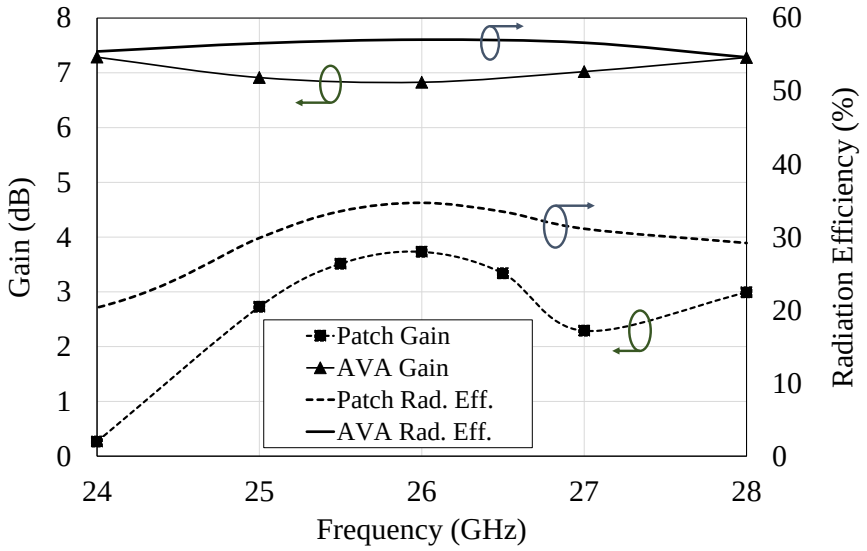

FIGURE 7.3: Simulated gain and radiation efficiency of the patch antenna and the proposed AVA at the frequencies of interest.

this sub-section, the performance of the proposed antenna is compared to a standard disc monopole, on the same substrate, based on 3D CST simulation, in order to justify the antenna choice in this chapter. The microstrip-fed disc has a radius of 8 mm, and is fed using a 50 Ω microstrip line. The diameter of the disc was chosen to maintain an $S_{11} < -10$ dB bandwidth from 24 to 40 GHz. Both antennas have 10 mm feeds to ensure a fair comparison. Both antennas were backed by a conductive reflector at 1 mm felt clearance for off-body isolation, as detailed in the next section. Fig. 7.4 shows the simulated $\eta_{\text{Rad.}}$ of both antennas. The higher $\eta_{\text{Rad.}}$ of the AVA in Fig. 7.4 compared to Fig. 7.3 is due to the shorter feed length (10 mm vs. 20 mm), resulting in lower insertion losses.

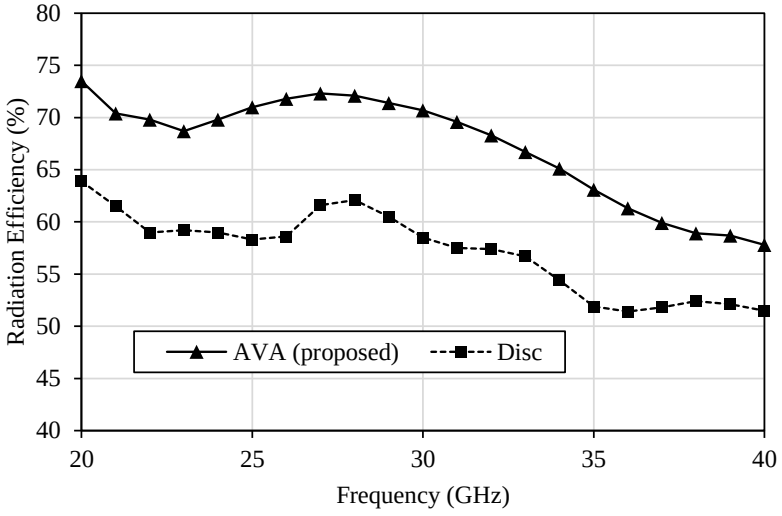

FIGURE 7.4: Simulated radiation efficiency ($\eta_{\text{Rad.}}$) of the proposed AVA and a standard disc monopole over the same textile substrate.

From Fig. 7.4, it is evident that the proposed patch achieves over 16% relative $\eta_{\text{Rad.}}$ improvement over a standard disc monopole. This is attributed to the smaller area of the radiating aperture of the AVA-inspired monopole compared to the disc, which results in lower E-field dissipation in the substrate. While a small disc could be utilized to overcome this effect, discs with radius<8 mm were found to have an $S_{11} > -8$ dB, showing that the bandwidth requirement will not be met by a conventional disc monopole.

In addition to $\eta_{\text{Rad.}}$, the simulated gain patterns of both antennas have been simulated and compared. As both antennas were backed by a conductive reflector, it is expected that both antennas will achieve an off-body radiation pattern. However, as observed in Fig.7.5, only the proposed AVA-inspired monopole achieves a stable broadside beam resembling that of a patch antenna. Therefore, the proposed antenna will maintain a better angular coverage in wearable off-body mmWave EH applications. In addition, the proposed reflector-backed AVA achieves a higher front-to-back ratio, evident over both principal planes, demonstrating the antenna's suitability for off-body applications. Therefore, should a monopole antenna be used for broadband off-body applications based on reflector backing, it is essential to design the antenna to (a) achieve the desired bandwidth, (b) achieve a high radiation efficiency on the lossy textile substrate, and (c) maintain a broadside radiation pattern with a high front-to-back ratio, for optimal off-body performance.

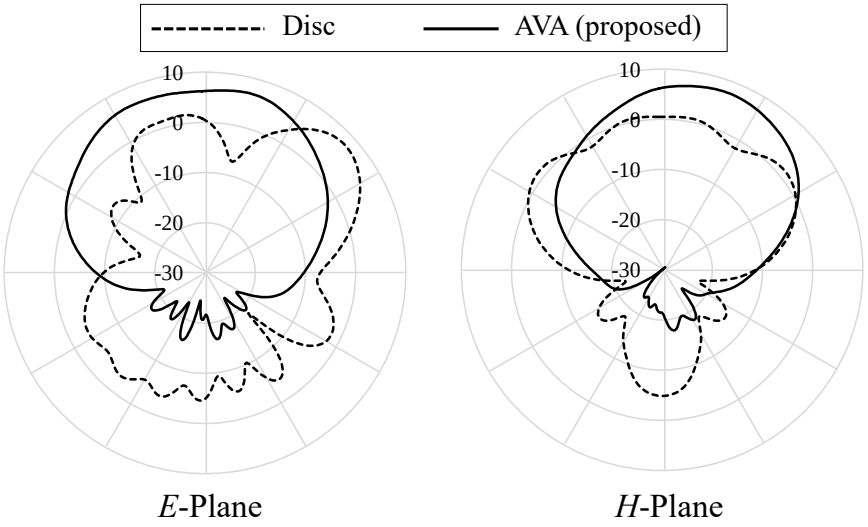

FIGURE 7.5: Simulated gain patterns at 24 GHz of the proposed AVA-inspired monopole and the standard disc, over a 1 mm-spaced textile reflector.

7.1.4 Wearable Antenna Isolation

Obtaining stable off-body broadside radiation patterns is essential for efficient wearable rectenna operation. In [66], a novel approach of employing the human body as a reflector has been devised to improve the antenna's efficiency, bandwidth, and gain at the frequencies of interest. This has been achieved using asymmetric alignment of the

radiator arms to allow the far-fields to reflect off the human body, hence improving the gain. However, this approach is only valid when the antenna is separated from the human body by more than 4 mm, which cannot be guaranteed in all modes of operation.

In order to ensure the antenna maintains stable radiation patterns and bandwidth in the presence and absence of the human body, an additional metal reflector layer is proposed. Thus, broadside radiation patterns can be achieved by the monopole at its fundamental frequency. A microwave shielding fabric (copper and nickel coated) has been used for the reflector plane, as metalized fabrics are breathable, more user-friendly compared to copper sheets and, in this case, do not need to be patterned to produce small features.

The minimum separation between the antenna and the reflector has been set to 1 mm ($0.08\times\lambda_0$/ at 24 GHz). A 1 mm felt fabric (of lower tanδ compared to woven polyester) has been inserted between the antenna and the reflector as shown in Fig. 7.1 to support the reflector. While the additional fabric layer will degrade the antenna's radiation efficiency (due to the additional dielectric losses), the effect is expected to be minimal compared to degradation in the efficiency due to absorption by the human body.

7.1.5 Antenna Fabrication

Ultra-thin polyimide copper laminates exhibit improved flexibility compared to copper foils, and lower thickness compared to printed interface layers, minimizing dielectric losses. The antenna is fabricated on the polyimide laminates using photolithography. A minimum feature size of 150 μm is achieved using standard PCB manufacturing equipment. After the adhesion of the flexible circuit onto the textile substrate, the via holes are drilled and conductive thread is inserted to form the conductor. The antenna has been fabricated using the standard photolithography process described in [66,185]. However, to realize the double-sided voltage doubler rectifier, conductive threads are utilized to create DC vias, solder paste has been used to connect the via (thread) to the copper traces on the top and bottom layers. Fig. 7.6 shows a cross-section of the structure. The fabricated antenna and rectenna prototypes are shown in Fig. 7.7. The measured dielectric properties of the polyimide-woven polyester sandwich substrate utilized is $\epsilon_r = 1.67$ and tanδ = 0.027 using the method proposed in Chapter 6.1.2 and two-port two-line measurements.

7.2 Antenna Simulation and Measurement

The 3D model of the antenna has been simulated using full-wave electromagnetic simulation in CST Microwave Studio. The 1.85 mm connector used to measure the fabricated antenna has been included in the antenna's model to observe its effect both

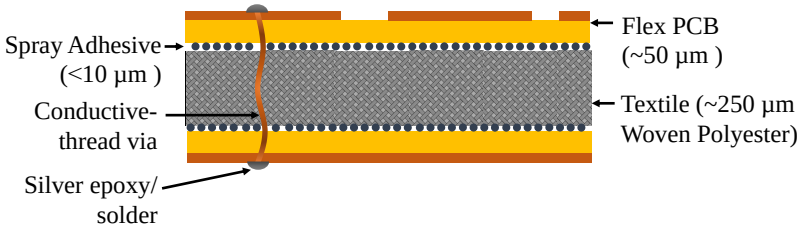

FIGURE 7.6: Cross-section of the antenna showing the multi-layer substrate and the through-textile via.

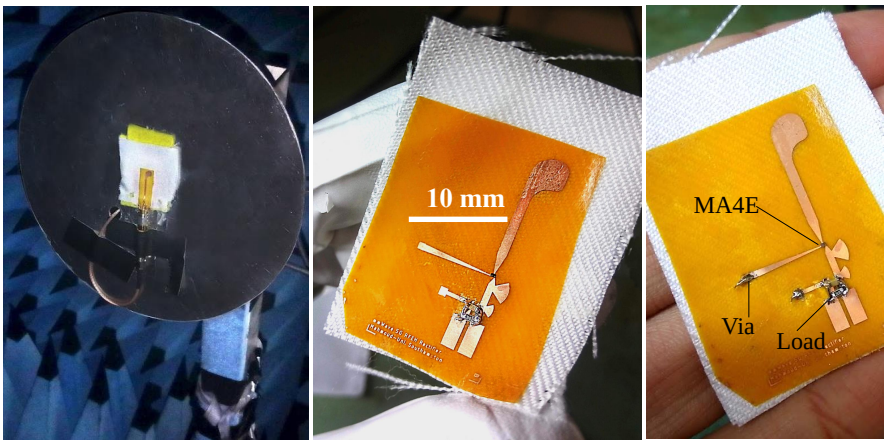

FIGURE 7.7: Photograph of the connectorized antenna (left), used for the S_{11} and radiation properties measurements, and the integrated rectenna (right).

on the antenna's impedance bandwidth and on the radiation patterns, in addition to obtaining a closer match with the measured results for validating the simulation model. A human skin layer, based on CST's Voxel library has been added to investigate the effect of human proximity on the antenna. As a significant portion mmWaves do not penetrate deeper than skin layers due to absorption [314], only the skin layer has been included in the model. Furthermore, as the antenna utilizes a solid reflector plane, minimal power from the antenna's power would be absorbed by the body. 1% of the accepted power by the antenna has been absorbed by the skin layer positioned 0.1 mm beneath the reflector.

The fabricated antenna has been measured using an E8361A 67 GHz PNA VNA with a Short Open Load Through (SOLT) calibration. The 1.85 mm connector has been soldered to the bottom ground plane using a uniform solder layer to avoid impedance mismatch at the coax-microstrip transition. Fig. 7.8 shows the simulated and measured reflection coefficient of the antenna, showing a bandwidth covering the full 5G spectrum up to 40 GHz. The simulation and measurements agree in covering the required bandwidth of 24 GHz and 5G RFEH. The level of agreement at the frequency bands of interest is consistent with similar designs such as the 24 GHz antenna array in [76]. The measurements have been performed with the antenna placed on a human hand and no change has been observed on the measured S_{11}, this has also been previously presented in [66] despite the reduced isolation over the proposed reflector-backed AVA.

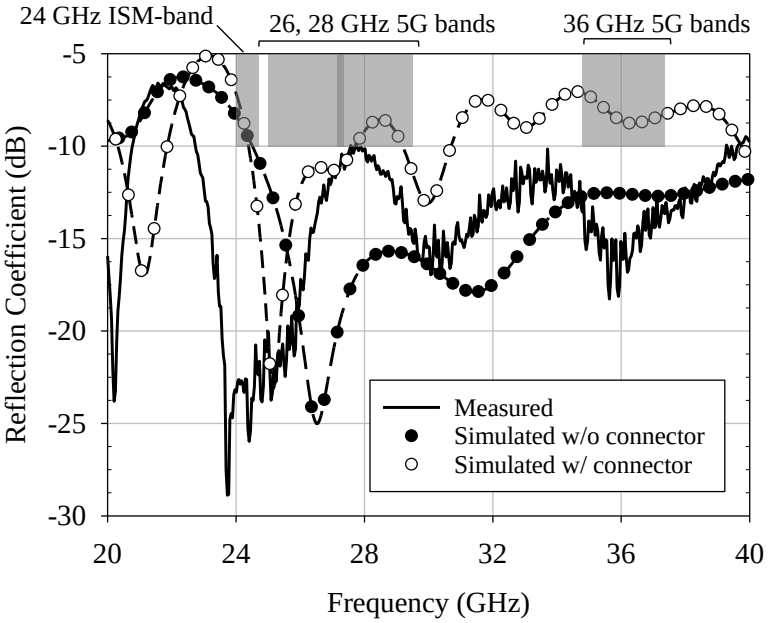

FIGURE 7.8: Simulated (dashed) with (w/) and without (w/o) the connector, and measured (solid) reflection coefficient of the proposed textile mmWave antenna.

For evaluating the far-field properties of the AVA, two designs have been considered: the 25-mm microstrip-fed AVA in Fig. 7.1 (simulated and measured), and the same antenna with a short 5-mm feed to match the antenna integrated in the final rectenna (simulated). The longer feed sample has been used for model-validation through 3D far-field measurements, to avoid distortion to the measurements due to the connector size.

The 3D far-field radiation patterns of the antenna have been measured in an anechoic chamber (Fig. 7.7), at 24 GHz, and simulated using CST's field monitors. A WR-42 horn antenna has been used as a reference for the radiation efficiency (η) measurements . An extended microstrip feed-line of 25 mm has been included to mitigate distortion from the connector to the radiation patterns [159]. However, the insertion losses in the microstrip line are expected to reduce the measured $\eta_{\text{Rad.}}$. With respect to the horn antenna, η=67%, including the -1.5 dB (simulated) losses in the prolonged microstrip feed. Compared to the 60% measured $\eta_{\text{Rad.}}$ of the microstrip patch proposed in Chapter 6, the $\eta_{\text{Rad.}}$ improvement owing to the optimized design for lossy substrates is evident. The normalized gain patterns of the antenna at 24, 28 and 36 GHz are shown in Fig. 7.9, the measured 3D pattern at 24 GHz is shown in Fig. 7.10.

Both the simulated and measured radiation patterns show over 20 dB front-to-back ratio, implying minimal interaction between the antenna's broadside radiation and the human body shielded by the reflector. The computed radiation efficiency and gain (validated by the de-embedded measured radiation patterns and efficiency agreement with the simulated results) are shown in Fig. 7.11. The only discrepancy observed between

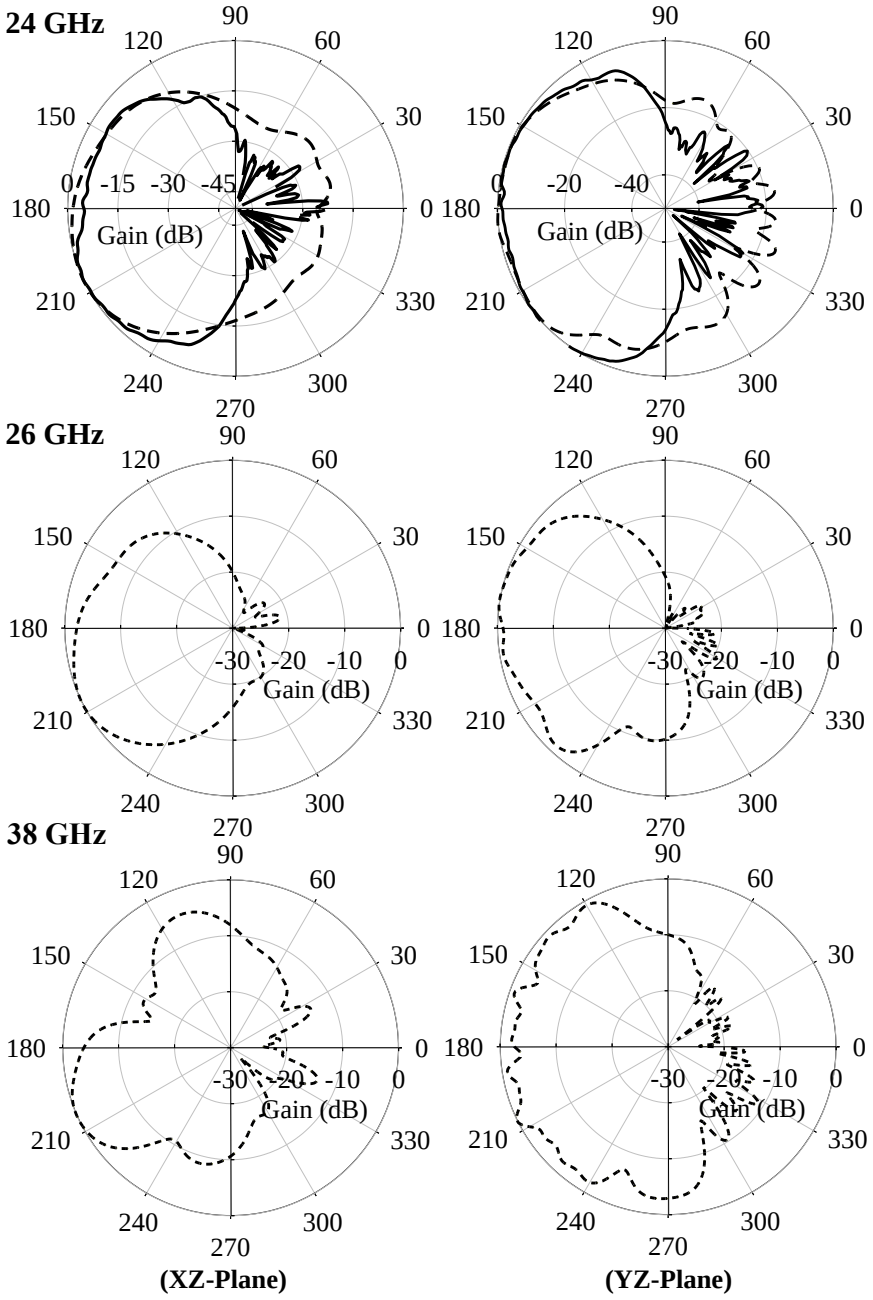

FIGURE 7.9: Normalized simulated (dashed) and measured (solid) gain of the proposed AVA at: (a) 24, (b) 26 and (c) 36 GHz, on the XZ and YZ planes of the antenna.

the simulated and measured radiation properties is the higher back-radiation in the simulated model, due to the smaller size of the reflector in the model to reduce the problem's mesh size. However, in real-life operation and in the measured prototype, the textile reflector could be electrically large minimizing the back-lobe radiation as observed in the measured plots.

From the rectenna's radiation properties shown in Fig. 7.11 (excluding the simulated insertion losses in the long feed-line), the antenna achieves a radiation efficiency of more than 70% up to 30 GHz, peaking at 73.4% at 26 GHz. The decay in efficiency at higher

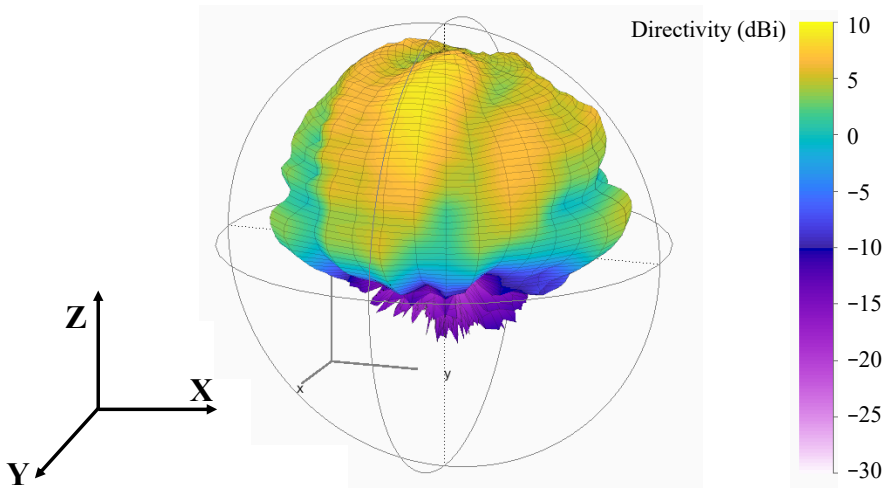

FIGURE 7.10: Measured 3D radiation patterns of the proposed antenna at 24 GHz.

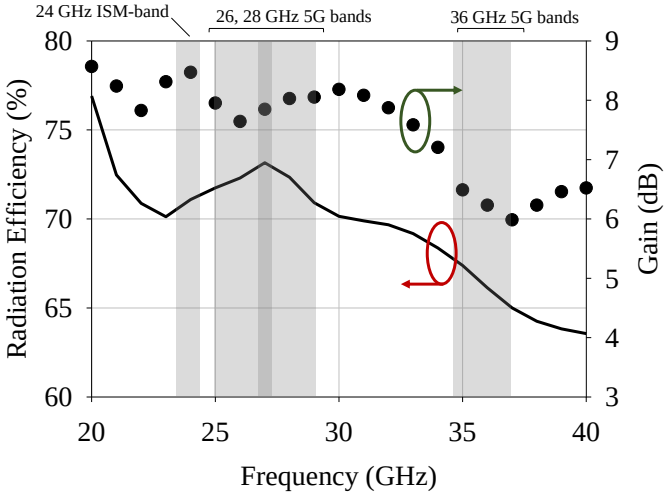

FIGURE 7.11: De-embedded radiation efficiency and gain of the proposed AVA, on-body, with a 5 mm microstrip feed matching the rectifier's feed length.

frequencies is due to the increase in the dielectric losses in the substrate. The proposed antenna with the reflector plane achieves slightly lower efficiency than the previously simulated 77% without the reflector in [66]. However, the solid reflector results in more stable radiation properties over the full bandwidth, as observed in Fig. 7.11, in addition to guaranteeing that the achieved efficiency does not degrade in human proximity.

Table 7.1 compares the performance of the proposed AVA against reported textile-based and additively manufactured low-cost mmWave antennas. It can be seen that the proposed antenna achieves the highest radiation efficiency compared to the reported antennas implemented on low-cost substrates. The antenna in [232] is able to achieve efficiencies higher than 90% due to the low loss substrate and its CPW geometry. To add, the smaller length of [232] does not include a sufficiently large ground plane due to the coax connector acting as a ground plane for the antenna in simulation and measurement.

TABLE 7.1: Comparison of the proposed antenna measured properties with state-of-the-art printed and textile antennas

	This work	2019 [232]	2013 [159]	2012 [317]
BW (GHz)	23-40 (54.0%)	26-40 (42.4%)	55-65 (16.7%)	57-64 (11.6%)
Antenna	AVA	CPW monopole	2×2 patch	Yagi-Uda
Substrate	Textile (tanδ=0.027)	LCP (tanδ=0.002)	Textile (tanδ=0.02)	Textile (tanδ=0.016)
Gain (dB)	7.41*, 8.47†	8.76	7.8	11.9
Radiation pattern	Broadside single-beam	Broadside two-beams	Broadside single-beam	End-fire
Efficiency	67%*, 73%†	90% (simulated)	41%	48%
Electric dimensions (λ_0)	$3.0\lambda_0 \times 0.94\lambda_0$	$1.12\lambda_0 \times 1.02\lambda_0$‡	$4.26\lambda_0 \times 1.03\lambda_0$	$5.2\lambda_0 \times 1.6\lambda_0$

*Measured: antenna+25 mm microstrip, †Simulated antenna+5 mm microstrip ‡Small length due to the miniaturized CPW feed and connector's ground.

7.3 Textile mmWave Rectifier

7.3.1 Diode Selection and Modeling

The main criteria when choosing a diode at mmWave bands is a high $f_{\text{cut}-\text{off}}$, otherwise the diode will not act as a rectifying element and the harmonics will propagate to the output through the diode and package parasitics. The diode's PCE will be adversely reduced at frequencies approaching $f_{cut-off}$. Moreover, a significant portion of the energy at the output will always exist at the 1st and 2nd harmonics and not at DC [207], implying that proper harmonic termination is implemented at the output [75, 76, 234]. The cut-off frequency is defined in this work as the frequency where the resistance and the reactance of the diode are equal. This can be calculated using (2.4) [205, 206]. While in [206] only the junction capacitance is considered due to the devices being measured on-wafer, when the diodes are packaged the total (junction+packaging) capacitance needs to be considered.

Two diodes have been considered: a Si Skyworks SMS7630 and a GaAs Macom MA4E-1319, recommended by the manufacturers for detector applications above 26 and 80 GHz, respectively. The diodes have been simulated in ADS using HB. To achieve the highest accuracy between 20 and 30 GHz, the simulation was based on the datasheet SPICE parameters, and optimized models using the available measured s-parameters (for the SMS7630) and the IV-curves in [75] (for the MA4E). Fig. 7.12 shows the simulated input impedance of the SMS7630 and the MA4E, based on the 0 dBm s-parameters and the IV-curve, respectively, when terminated with an ideal 50 Ω load. The Smith chart in Fig. 7.12 shows the cut-off region of the diodes' impedance (striped shading) and the rectification region (solid-green shading). The diode parameters used in the non-linear

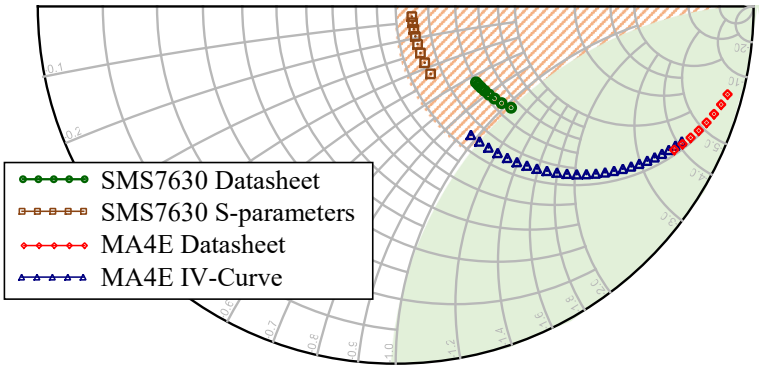

FIGURE 7.12: Simulated (LSSP) input impedance of the SMS7630 and MA4E diodes from 20 to 40 GHz, using diode parameters from the datasheet as well as the optimized models based on experimental characterization.

simulations in this work are C_j=0.02 pF R_S=9 Ω for the junction capacitance and series resistance, and C_P=0.035 pF L_P=0.3 nH for the packaging capacitance and inductance.

It can be observed that although the SMS7630 junction (datasheet parameters) is capable of rectification at 24 GHz (impedance falling in the solid-green shaded region), when the packaged diode's parasitics are considered, the diode acts as a short-circuit allowing f_0 to propagate to the output. The MA4E1319 on the other hand is usable up to 40 GHz (based on the Large-Signal S-Parameters LSSP-simulation using the parameters from [75]), yet the packaging parasitics show significant discrepancy with the datasheet model of the junction which can be used through 90 GHz. The discrepancies could be attributed to the diode's mounting imperfections while the manufacturer's parameters are likely measured using de-embedded probes.

7.3.2 Rectifier Design

The MA4E1319 GaAs Schottky diode pair has been chosen as the rectifying element. With two diode's integrated in the same package, it is expected that the external parasitics will be lower improving the cut-off frequency of the diode. The voltage doubler's impedance, seen on the Smith chart in Fig. 7.13, is predominantly capacitive. Therefore, a high-impedance inductive matching network is required. Moreover, the 1 pF input capacitance can be achieved using the microstrip feed's own distributed capacitance. A tapered microstrip line could be used to match the impedance of the rectifier as in Fig. 7.13-b, stepping-up the impedance of the rectifier to match the 50 Ω source, as well as conjugating the capacitive diode impedance using the microstrip line's own inductance.

A key challenge in broadband impedance matching is the trade-off between bandwidth and Quality factor, where a sufficiently low S_{11} may not be achievable over a wide range of frequencies. The theoretical limit on the minimum achievable reflection coefficient of

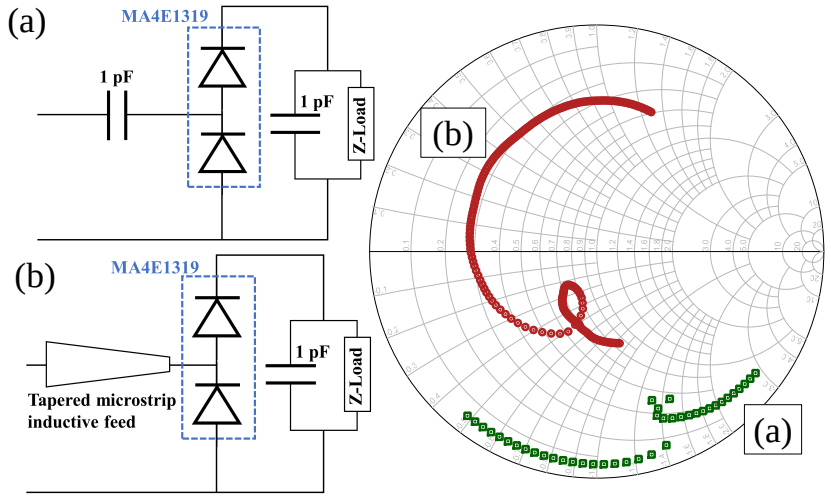

FIGURE 7.13: Schematic of the voltage doubler and Smith charts showing the impedance matching approach of. (a): conventional voltage doubler, (b): rectifier with the tapered matching line and distributed microstrip input capacitance.

a load is given by

$$|\Gamma_m| \geq= e^{\frac{-1}{2BRC}} \tag{7.1}$$

$$S_{11} \geq 20\log(\Gamma_m), \tag{7.2}$$

the Bode-Fano return-loss limit, a function of the bandwidth B, and the equivalent RC circuit of the load, in this case the rectifier and the DC load.

Harmonic balance simulation was used to extract the rectifier's impedance (Fig. 7.13-a), the bandwidth B has been set to 4 GHz (24-28 GHz). The equivalent RC circuit of the rectifier in Fig. 7.13-a has been extracted using optimization of an RC load with tunable resistance and capacitance, to match the simulated LSSP; the extracted values are R=904 Ω and C=0.161 pF. The calculated minimum achievable Fano S_{11} is −7.5 dB ($\Gamma_m \geq 0.42$). While in [298] the increase in the number of diodes has been studied in order to increase the return loss of a rectifier through reducing R, this approach is not possible at mmWave frequencies due to the higher losses incurred in the additional rectifier stages.

In order to step up the input impedance of the 50 Ω source and achieve an inductive feed-line, the microstrip line feeding the diode is tapered to gradually increase the inductance of the source. A tapered line is also used at the ground connection of the voltage doubler, the length of the tapered lines has been optimized in simulation to match the 50 Ω antenna to the rectifier at the frequencies of interest. While an L-matching network could be used to achieve a high Q-factor matching, improving the PCE at low P_{RF} levels as in [76] and [248], a wide bandwidth rectifier is prioritized in order to demonstrate the feasibility of harvesting from a broad bandwidth to meet 5G RFEH requirements.

To prevent the high-frequency component of the input from propagating to the output, significantly reducing the net DC output, radial stubs ($\lambda/4$ at 26 and 52 GHz) are utilized for harmonic rejection at the output. The DC test pads included at the output, to allow measuring the voltage across the load, were found to not have any effect on the rectifier's performance in simulation. Fig. 7.14 shows the layout of the rectifier, and the modified antenna ground plane to accommodate the rectifier. As the ground via is for the DC return current, the impedance matching of the vias is not critical. Furthermore, different thicknesses, resistances, and inductances of the vias have been studied in ADS and were found to have minimal impact on the rectifier's performance.

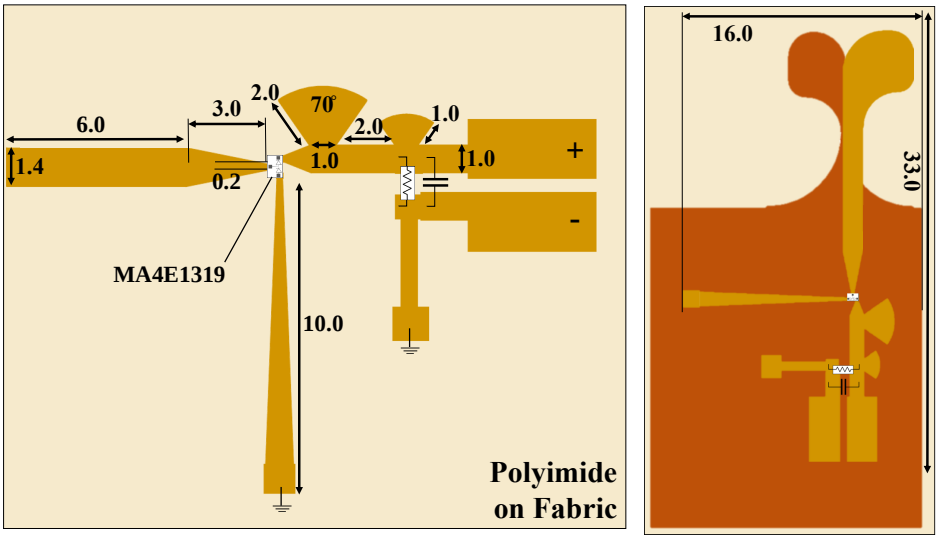

FIGURE 7.14: The dimensions, in mm, of the proposed textile-based 5G rectifier (left) and the integrated rectenna layout (right).

In terms of textile coverage and breathability, the proposed rectenna occupies a small area of 16×33 mm^2. Thus, should the rectenna be used in a large-area array configuration, a $\lambda_0/2$ (6.25 mm at 24 GHz) would imply a coverage of less than 60% of the total area of the garment. Furthermore, [293] has shown scalable integration of polyimide-circuit filaments in standard textile weaves for improved integration, user-comfort and reliability.

7.3.3 Rectifier Simulation and Measurement

The reflection coefficient of the 1.85-mm connector-fed textile rectifier prototype has been measured using a VNA. Due to cabling losses at 28 GHz and the VNA's power limit, the maximum power deliverable by the VNA is −5 dBm. Fig. 7.15 shows the simulated and measured S_{11} of the rectifier. The connector has been modeled as a tapered microstrip line of 5 mm length. While the observed reflection is higher than 3 dB, this is attributed to the wide variation in the input impedance of the rectifier due to its large electric length, impeding a sufficiently low S_{11}, in addition to the Bode-Fano theoretical limit on the minimum reflection calculated to be above −7.45 dB.

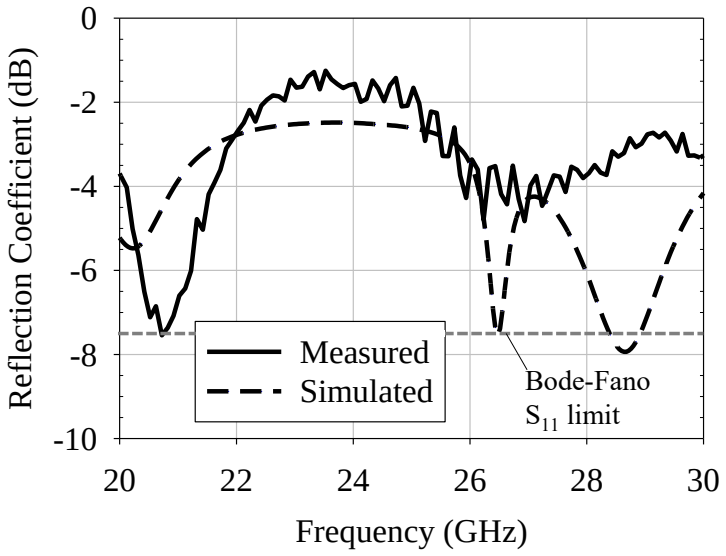

FIGURE 7.15: Measured and simulated reflection coefficient of the rectifier at −5 dBm.

In order to measure the PCE of the rectifier, the DC voltage across the load has been measured using an oscilloscope. A Wiltron 68069B CW signal generator (providing up to 13 dBm) has been used to provide sufficient power to investigate the performance of the connectorized rectifier. A Keysight N8485A 33 GHz power meter has been used for power-calibration and for measuring the net power available at the rectifier's input after factoring in cabling and unleveled output losses, reducing the uncertainty in the mmWave power level to ±0.1 dB. The power has been swept from 0 dBm to the setup's maximum output of 13 dBm. Fig. 7.16 shows the measured DC output, across a 10 kΩ resistor, at 24 GHz.

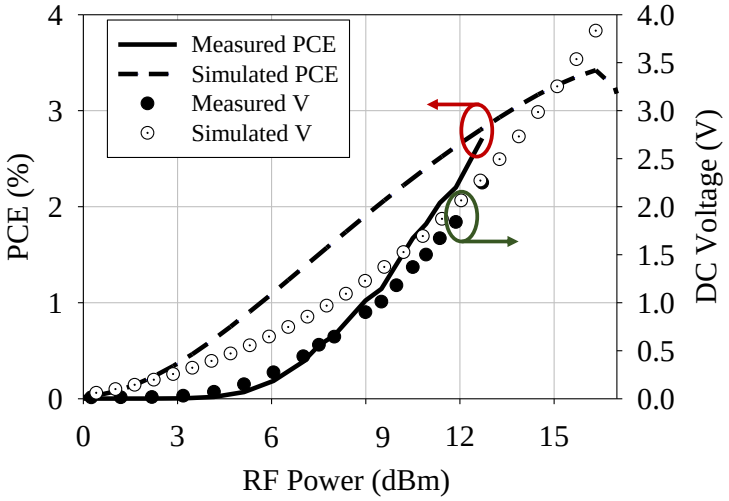

FIGURE 7.16: Measured and simulated PCE of the rectifier and the DC voltage across a 10 kΩ load at 24 GHz.

Above 10 dBm, the simulated output voltage matches, within 10%, the measured values. The agreement between simulation and measurement shown in Fig. 7.16 at 10 dBm is higher than that in [76] and [224], where approximately 25% discrepancy has

been reported in the measured voltage output compared to simulation, despite them being implemented on rigid low-loss substrates with a well-defined ϵ_r. This validates the proposed rectifier's performance and design approach for flexible lossy textile substrates. The discrepancy between the simulation and measurement at lower power levels can be attributed to:

1. Inaccuracy in modeling the connector in the Harmonic Balance simulation altering the rectifier's input impedance.
2. Inaccuracy of the MA4E junction resistance at low mmWave power levels reducing the PCE.
3. The imperfect connection between the rectifier's pads and the traces resulting in additional series resistance.

When considering the theoretical limit on the received power, the PCE can be calculated using

$$PCE_{Fano} = \frac{P_{DC}}{(1 - |\Gamma_m|^2)P_{RF}}, \tag{7.3}$$

referenced to the theoretical maximum for the power received after factoring out Fano's reflection, instead of the power available from the generator. The maximum PCE_{Fano} achieved by the rectifier at 24 GHz is 14% at 12.7 dBm, with a net DC output of 0.5 mW, sufficient for low-power nodes and transceivers in [325–327].

The output of the rectifier has been investigated at different load impedances. Fig. 7.17 shows the PCE of the rectifier at 24 GHz for different load impedances at 10 dBm. The higher optimal load impedance of the proposed rectifier compared to the reported mmWave rectifiers (Table 7.2), due to the voltage doubler, configuration results in the improved 1 V sensitivity.

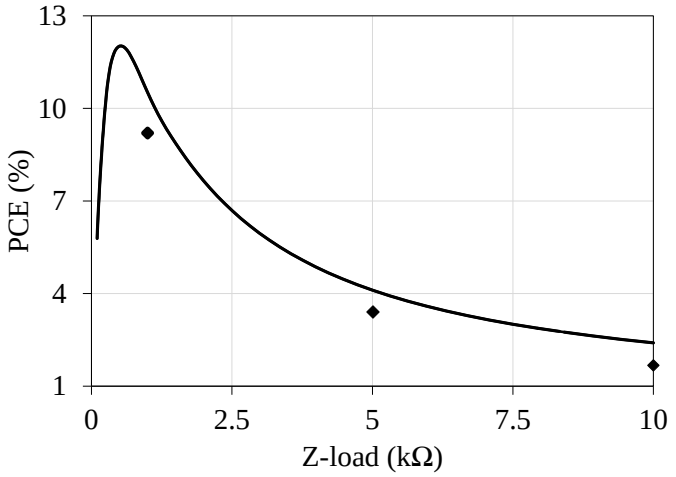

FIGURE 7.17: Simulated (solid line) and measured (discrete points) PCE for variable load impedance at 10 dBm.

In order to evaluate the rectifier's capability of harvesting energy across a broad bandwidth for 5G applications, the frequency of the CW single-tone input to the rectifier has been varied. The load impedance of the broadband rectifier has been set to 10 kΩ, despite the reduced PCE, for improved voltage sensitivity. Fig. 7.18 shows the output voltage of the rectifier from 22 to 26 GHz.

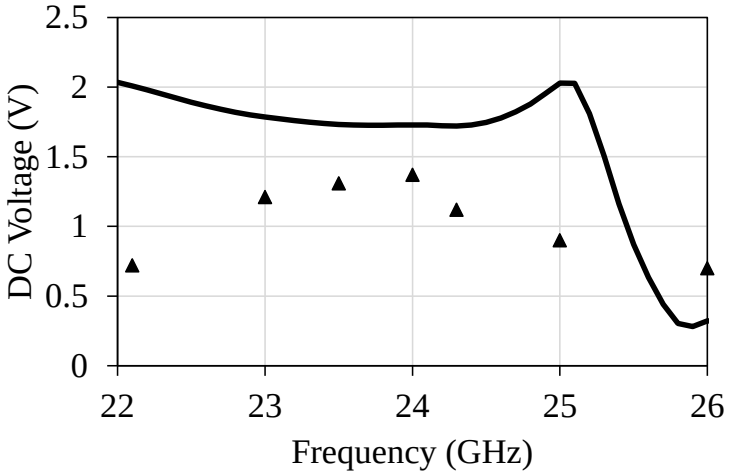

FIGURE 7.18: Simulated (solid line) and measured (discrete points) DC voltage output of the connector-fed textile rectifier at 10 dBm with a 10 kΩ load.

While the measured output voltage at 24 GHz approaches the simulated value, the rectifier's DC output is cut-off at frequencies higher than 24.5 GHz even though its input impedance matching is expected to be maintained based on the small-signal S_{11} in Fig. 7.15. This is attributed to the coax-microstrip connector interface resulting in lower output voltage at frequencies above 24 GHz. Therefore, the broadband wireless testing in the next section has been performed to overcome the additional measurement uncertainties introduced by the coax connector.

7.4 Rectenna Wireless Testing and Evaluation

The integrated rectenna has been tested using the CW generator, connected to a Keysight 83020A PA, capable of producing up to 25 dBm at 26.5 GHz, and a standard 20 dBi horn antenna. While this setup should have an EIRP of more than 44 dBm, due to the PA's gain compression, additional attenuators were introduced between the CW and the PA to minimize the unleveling of the output and suppress the gain compression effect. Finally, due to the non-linear behavior of the PA and the CW generator at higher power levels, a calibrated RF power meter has been connected to the connectorized textile antenna to estimate the power levels at the receiver. The mmWave power levels reported in this section are based on the power calibration using the textile AVA connected to the power meter. Fig. 7.19 shows the rectenna test setup. The 10 cm separation, between the horn's radiating aperture and the rectenna, shown in Fig. 7.19 represents $8\times\lambda$ at 24

GH. This is consistent with the separation reported in the wireless testing of the 17 GHz rectenna in [224] with 8.8 λ separation between the horn transmitting antenna and the rectenna.

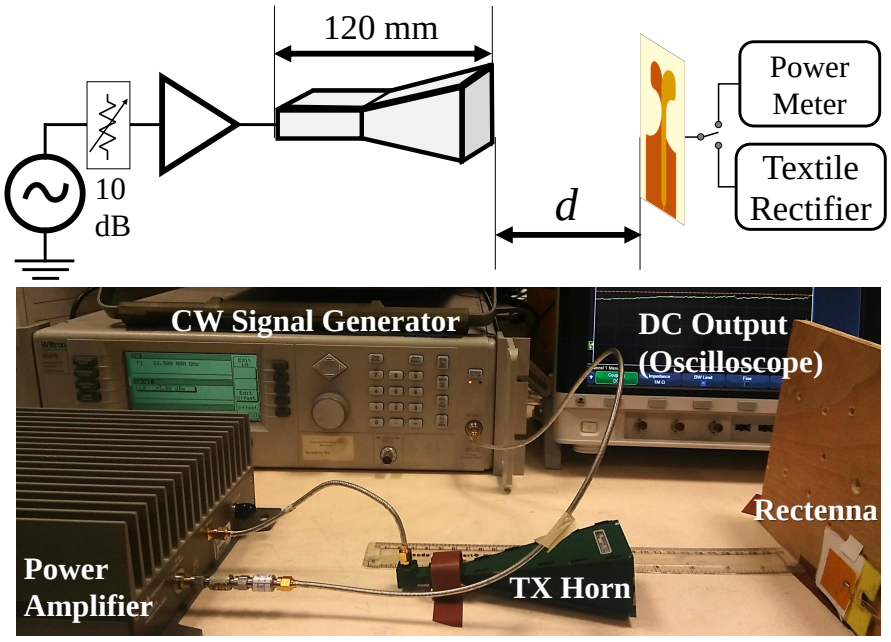

FIGURE 7.19: The wireless test setup schematic and photograph of the textile rectenna.

The distance d has been varied to vary the power level at the rectenna. The distance between the horn's radiating aperture and the coax-waveguide transition is 120 mm. Therefore, the total separation between the rectenna and the CW signal from the PA is d+120 mm. While the power is typically proportional to $1/d^2$, due to the measurements being carried with d being comparable to the horn's dimensions, the far-field gain and path loss models are not accurate. The input power to the PA in this setup has been kept below −15 dBm. Fig. 7.20 shows the measured DC output of the rectenna at varying separation, as well as the measured incident mmWave power, at 24 GHz, using the power meter. The distance sweep shows improved voltage-sensitivity over the mmWave rectenna in [327], tested using a 42 dBm EIRP with a 25 dB horn, by more than 1 V at 20-mm separation from the horn's radiating aperture. CW excitations have been previously utilized to test the performance of broadband rectifiers in [224, 298].

To evaluate the rectenna's performance at higher power levels, the CW output has been increased until a 20 dBm is observed on the power meter. At 24 GHz, from an incident power of 20 dBm, the rectenna achieves more than 6.5 V with a 10 kΩ load. This is the highest reported output voltage of a low-power rectenna operating between 20 and 30 GHz. The measured DC output of the 10 kΩ-loaded rectenna is 6.5, 5.7, 4.6 and 4.2 volts from 20, 19, 18, and 16 dBm, respectively. These results have been measured using the test setup in Fig. 7.19 with the power levels based on the measurement using the power meter.

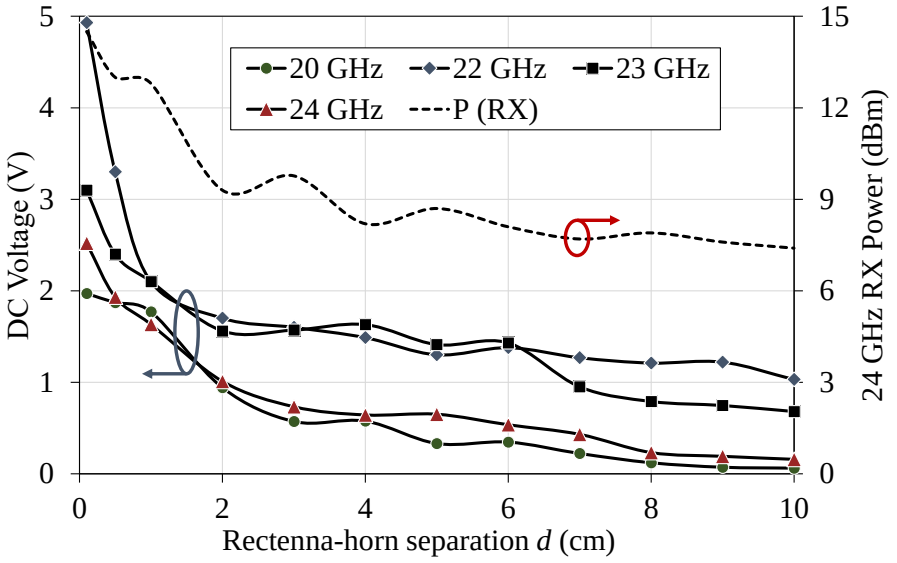

FIGURE 7.20: Measured DC output of the rectenna at variable separation from the horn antenna.

In order to demonstrate the rectenna's capability of broadband harvesting across the full mmWave 5G spectrum. A broadband frequency sweep has been performed using the wireless setup in Fig. 7.19. The rectenna has been placed at 1 cm from the horn antenna. To estimate the mmWave power level at the input, the calibrated power meter has been connected to the 50 Ω textile AVA and positioned in the same place as the rectenna. The power from the CW has been configured at individual measurement points, to overcome the variation in the path loss and the antennas' coupling, to ensure approximately 12 dBm of power is available at the rectenna. Through this power calibration, the gain-compression and PA's non-linearities could be overcome. Fig. 7.21 shows the measured DC voltage the PCE, the error bars reflect the ±1 dB uncertainty in the incident power level. This demonstrates the rectenna's ability to produce over 1.3 V DC across the 10 kΩ load resistor, from 12 dBm of power with PCE varying between 1 and 6.3% validating its broadband performance.

The simulated values in Fig. 7.21 were obtained from the ADS model of the rectifier excluding the antenna. However, as the textile AVA is 50 Ω and the wireless power has been measured using the power meter, the results are expected to agree within the ±1 dB wireless power uncertainty. The main discrepancy between the simulation and measurements shows up below 23 GHz, this is attributed to the proposed antenna, which was only designed and characterized for operation from 24 GHz. Thus, the PCE in this case is bottle-necked by the antenna. The rectifier design can be integrated with a different antenna should it be used below 24 GHz. Above 25.5 GHz, the measured output is observed to exceed the simulated output of the rectifier. This could be attributed to the shorter feed-length of rectifier, when considering the antenna's 50 Ω feed, and the inaccuracies from the resistive and capacitive load mounting.

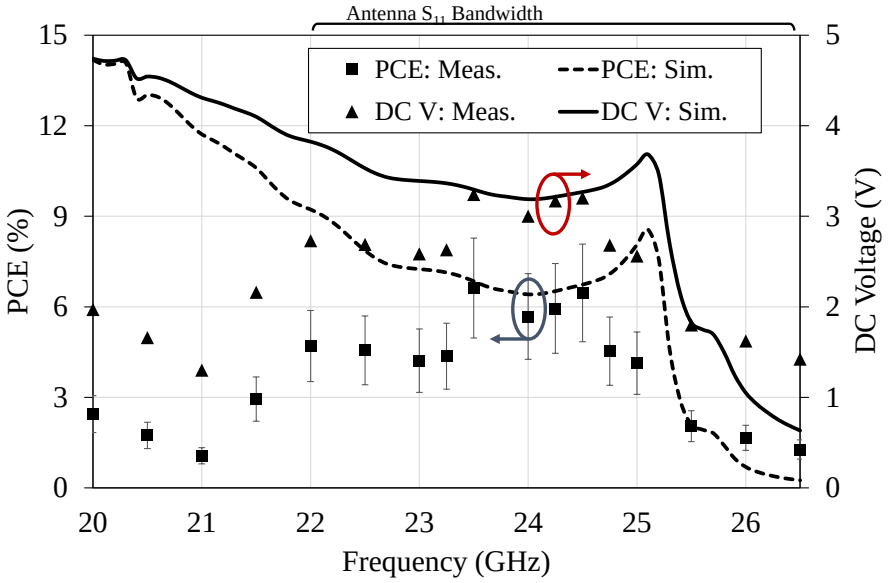

FIGURE 7.21: Measured PCE and DC voltage output of the rectenna from 12 dBm of wireless power, showing more than 1 V output from 20 to 26.5 GHz.

The measurements were limited to 26.5 GHz due to the PA's and the waveguide horn antenna's maximum frequency. However, as the rectenna achieves more than 1.4 V at 26.5 GHz, it is predicted that the rectenna's cut-off frequency is beyond 26.5 GHz, demonstrating its capability of harvesting across the full 5G spectrum. Moreover, the fabricated rectifier's performance above 26 GHz (being significantly better than the simulated due to higher cut-off frequency), could be attributed to over-estimation of the parasitic packaging capacitance reproduced from [75], where the utilized dual-diode package results in less parasitics and hence improves the rectifier's usable frequency range. While [224] demonstrates a broadband 1 V sensitivity from 12 dBm between 14 and 23 GHz, this work is the first demonstration of a broadband 1 V sensitivity above 20 GHz, with more than 6.5 GHz of 1.2-V bandwidth from less than 12 dBm of incident power.

In the context of harvesting energy from 5G cellular networks, the 28 GHz EIRP available from a base-station and a mobile device is 75 and 43 dBm/100 MHz, respectively [230]. Thus, given the rectenna's 7.41 dB measured realized gain, a mobile phone transmitting at 26 GHz and placed at 10 cm from the textile rectenna will result in 10 dBm received power at the rectenna yielding over 1 V of DC output. Furthermore, a 1 V DC output can be achieved with more than 5 m separation between the rectenna and a mmWave base-station; the size of a 10 Gbit/s 5G urban micro-cell is typically r=10 m [230]. This work has only evaluated the rectenna's performance under CW excitation, the impact of multi-tone modulated signals on a rectifier's performance have been previously investigated in [328].

Table 7.2 shows a comparison of the proposed rectenna with state-of-the-art mmWave and 5G rectennas. While it can be seen that the rectennas in [76] and [248] achieve higher efficiency due to the improved single-tone impedance matching, they both have lower

load impedance (reducing the voltage sensitivity) in addition to being implemented on dedicated low-loss RF substrates allowing the implementation of large-area distributed elements matching networks. On the other hand, despite the high voltage sensitivity achieved by the 3D printed rectenna in [234], implemented on a lossy flexible 3D-printed substrate, the PCE is expected to be very low due to the high load impedance utilized to guarantee a 1 V DC output. Finally, to the best of the authors' knowledge, this is the first rectenna with a broadband 1 V sensitivity aimed at broadband mmWave 5G energy harvesting, in addition to being fabricated on textiles with a high-efficiency broadband antenna shielded for operation near the human body.

TABLE 7.2: Comparison of the proposed textile rectenna with state-of-the-art mmWave Energy Harvesters above 20 GHz.

	This Work	TCAS 2014 [76]	AWPL 2014 [248]	WPTC 2017 [75]	IMS 2019 [234]
Antenna Design	Broadband AVA (single element)	Cavity-backed 2×2 patch array	4×4 patch array	2×2 patch array	2×1 patch array
Substrate	Textile (ϵ_r = 1.67, tanδ = 0.027)	Rogers Duroid (tanδ=0.001)	Rogers Duroid (tanδ=0.001)	LCP (tanδ=0.003)	3D printed FLGR02 (ϵ_r=2.83, tanδ=0.03)
Diode	MA4E-1319	MA4E-1317	MA4E-1317	MA4E-2038	MA4E-2038
Frequency Bands (GHz)	Antenna: 22.6-40, rectifier: 20-26.5	24	35	24	28
1 V Sensitivity	9.5 dBm (24 GHz)	11.9 dBm	2.8 mW	11 dBm	12.5 dBm
Maximum DC Voltage	6.5V (20 dBm)	1.2V (13 dBm)	2.2 V (8.45 dBm)	2.58V (18 dBm)	2.1V (17 dBm)
Load (kΩ)	10, 0.63	0.16	1	0.739	750
10 dBm PCE	12% (24 GHz, 630Ω)	24%	67% (7 mW)	7.6%*	<0.1%*
Rectenna 1 V Bandwidth	6.5 GHz (20-26.5 GHz)	Single-tone	1 GHz	Single-tone	Single-tone
Electrical Size (relative to free-space λ)	2.6λ×1.3λ	4.4λ×4λ	2.56λ×4.9	2.96λ×0.89λ	Not reported
Area (L×W, mm^2)	32.6×16	55×50	22×42	37×11.1	Not reported

*Calculated from the DC voltage curve

7.5 Summary and Conclusions

In this chapter, a textile-based broadband rectenna for 5G RFEH and WPT has been presented based on a novel wearable antenna design and a broadband high-sensitivity rectifier. The textile antenna achieves the highest radiation efficiency of reported textile-based mmWave antennas at more than 70% with a stable gain over 8 dB. The proposed rectenna is capable of generating a 1 V DC output from 21.5 to 25 GHz from power levels as low as 9.5 dBm, more than 1.3-V from 20 to 26.5 GHz from 12 dBm of wireless power, and up to 6.5 V from 20 dBm at 24 GHz. This work represents the first demonstration of a textile-based rectenna operating beyond 20 GHz and the first broadband rectenna for 20-26.5 GHz (K-band) RFEH. The key findings can be summarized as:

- Broadband antenna design based on a miniaturized radiator enables higher $\eta_{\text{Rad.}}$ on lossy substrates, by reducing the E-field dissipation in the substrate.
- Reflector-backed textile antennas can be implemented with a low-profile ($\approx$1 mm), a broad, 57% fractional bandwidth, and high (>67%) radiation efficiency in the Ka/K-bands.
- Despite the high microstrip insertion losses at mmWave bands on a high-tanδ substrate, a textile-based rectenna can be demonstrated with a 15% half-power fractional bandwidth based on tapered-line matching and harmonic termination
- Based on the mmWave 5G EIRP limits, the proposed rectenna can potentially produce a 1 V output across a 10 kΩ load at 10 cm and 5 m, away from a mobile device and a base-station, respectively.

The broadband high radiation efficiency achieved by the proposed antenna, and the high DC output of the rectenna, demonstrate that mmWave wireless systems, for power or information transfer, will not be limited to high-end applications, and that a mmWave-powered and -connected IoE is feasible.

Chapter 8

Fully-Textile RFEH Module: CPW Rectenna Filament Design and Textile Supercapacitor Integration

For RFEH to be adopted in wearable e-textile systems, there is a need for a wearable-friendly RF-powered energy supply, incorporating a flexible energy storage device such as a textile supercapacitor (TSC). On one end, mechanical ferroelectric and triboelectric energy harvesters were demonstrated directly charging TSCs for wearable applications [329,330]. Nevertheless, the end-to-end efficiency of such systems does not exceed 1% due to the high impedance of the harvesters. On the other end, conventional rectennas were integrated with commercially-available capacitors and supercapacitors based on complex DC power management interface circuitry [14, 39, 331, 332]. Based on the capacitive-loaded rectifier characterization, in Chapter 4.4.3 and published in [289], an electrolytic capacitor could be charged to a voltage level sufficient for modern CMOS electronics to operate. Therefore, a high-efficiency high-power rectifier can be designed and optimized specifically for a textile-based energy storage device, i.e. a TSC, presenting a highly-integrated wearable-friendly RFEH solution.

In this chapter, an e-textile RFEH and energy storage module is proposed for wearable applications, capable of harvesting 8.4 mJ in under 4 minutes, at 4.2 meters from a 915 MHz 34.77 dBm source. The integrated module has a calculated end-to-end efficiency of 38% at 1.8 m from the transmitter. On-body, the rectenna's efficiency is 4.8%, inclusive of in-body losses and transient shadowing, harvesting 4 mJ in 32 seconds from 16.6 μW/cm^2. Compared to textile energy harvesters, and other rectennas based on DC power management circuitry, it is concluded that the proposed e-textile rectenna is the most efficient method for charging a wearable energy storage device from μW/cm^2 power densities.

In Section 8.1, the design methodology for an e-textile RFEH module is introduced and contrasted to existing rectennas integrated with energy storage devices. The design and characterization of a wearable CPW rectenna filament is presented in Section 8.2. The implementation and characterization of the TSC is then presented in Section 8.3. The rectifier's performance when integrated with the TSC is analyzed experimentally using DC and RF techniques in Section 8.4. Finally, the wireless performance of the rectenna is evaluated in a license-free ISM-band WPT application in Section 8.5, and compared to similar work showing the highest reported end-to-end efficiency. The contents of this chapter have been submitted for publication in [333], and published in [334] and [335].

8.1 Concealed E-Textile RF Energy Harvesting and Storage Module

The requirements for compact e-textile filaments include being implemented on a thin and flexible substrate, maintaining a narrow width (<1 cm), and containing a small number of miniaturized lumped components, not to reduce the flexibility and user-friendliness of the textile [293]. The circuit filaments can then be encapsulated for improved reliability and woven into the fabric for concealed integration [183]. Examples of previously reported e-textile systems are washable UHF RFID tags based on narrow dipole antennas [183], and accelerometers [336].

The techniques reported in [14, 39, 331, 332, 337, 338] to realize rectennas integrated with energy storage devices, based on an intermediate supercapacitor/battery-charging PMICs, are not well-suited to wearable e-textiles. To explain, a PMIC such as the TI BQ25504, used in [14, 39, 331, 332] or the Linear LTC3588 [338], require over 10 lumped components, along with a complex PCB layout to function correctly. Such designs are not wearable-friendly and cannot be integrated in compact and unobtrusive e-textiles. In Table 8.1, recent rectenna implementations charging an energy storage device are summarized based on the complexity of their implementation, in terms of components count, and the maximum end-to-end RFEH efficiency η.

A photograph of the proposed system is shown in Fig. 8.1. The rectenna is fabricated using photolithography, [183], on a single-sided polyimide copper-laminate with less than 50 μm-thickness. The rectenna's DC output is directly connected to the TSC and concealed in fabric pockets as in Fig. 8.1-b. This integration technique improves the circuit's resilience to bending [293], as shown in Fig. 4.16, and washing [183], in addition to not affecting the user's comfort. As in Table 8.1, the proposed rectenna contains only five lumped components, making it suitable for seamless integration in fabrics, as shown in Fig. 8.1-b and c. The entire system is compact and occupies an area of 11.5×1.5 cm, i.e. $0.016\lambda_0^2$ when normalized to λ_0 at 915 MHz.

TABLE 8.1: Comparison of rectennas integrated with energy storage.

	Implementation	**Components count**	**Peak η**
[39]	Planar and 3D rectenna with a commercial PMIC and SC	>20*	1.7%‡
[332]	PCB rectenna with a commercial PMIC and SC	>20*	1.8%‡
[14]	3D-printed rectenna with a commercial PMIC and Capacitor	>20*	1.2%‡
[337]	PCB rectenna + custom CMOS boost converter and flexible battery	≈23**	12%†
[338]	PCB rectenna + whip antenna with a commercial PMIC and SC	≈45**	25%†
This work	**Textile-integrated rectenna and supercapacitor with no PMIC**	**5**	**38%†**

*Based on the PMIC datasheet; **estimated from circuit photograph; † >1μW/cm^2 rectenna; ‡ <1μW/cm^2 rectenna; SC: supercapacitor.

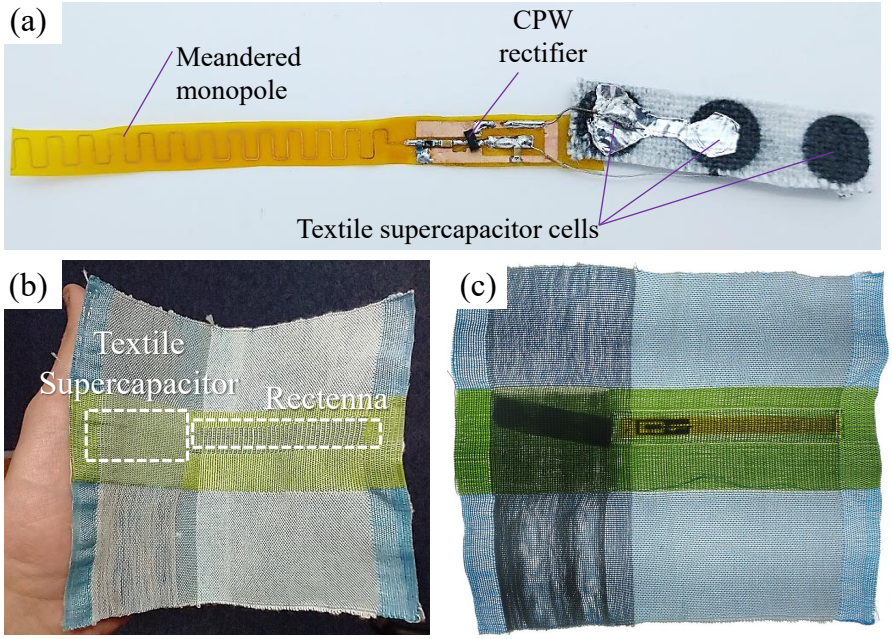

FIGURE 8.1: Photographs of the proposed integrated e-textile RF energy harvester and storage module: (a) the rectenna filament and encapsulated textile supercapacitor (dimensions in mm); (b) the concealed system in fabric; (c) components of the system visible under high exposure.

8.2 Rectenna Filament Design and Characterization

8.2.1 E-Textile CPW Antenna Design

In EH, a small footprint is essential to enable large-area implementations. "Wire" monopole antennas occupy a significantly smaller physical area compared to their effective radiating aperture [117]. Therefore, the rectenna is designed based on a CPW monopole with a miniaturized ground plane. To further reduce the area of the harvester, the length of the monopole was reduced through meandering.

For unisolated monopoles, it is expected that the resonance of the antenna shifts to a lower frequency, due to the high permittivity of tissue compared to air [185]. While a broadband textile antenna was previously used to overcome detuning in the sub-1 GHz rectenna in Chapter 4, sub-1 GHz broadband antennas require large area and cannot be integrated within flexible e-textile filaments which have a width under 10 mm.

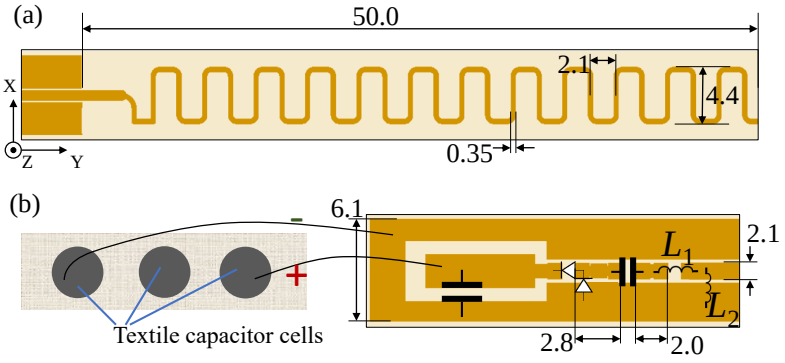

FIGURE 8.2: Layout and dimensions (in mm) of the meandered CPW antenna filament (a) and the compact voltage doubler rectifier (b).

The CPW antenna was simulated in CST Microwave Studio to evaluate its impedance bandwidth and radiation properties. A prototype, with a soldered SMA connector, was measured using a VNA for experimental validation. The proposed antenna is tuned using length reduction, a technique used where shielding is impossible, such as in implanted and insole antennas [185, 339]. Reducing the length of the radiator shifts the free-space resonance to a higher frequency. Subsequently, when the antenna is used in human proximity, the resonance will shift to the lower, desired, frequency. The simulated and measured S_{11} of the antenna are shown in Fig. 8.3. The shaded region in Fig. 8.3 shows the cross-over between the antenna's -6 dB (VSWR<3) bandwidth in space and when measured on-body, with an approximately 1 mm air gap between the antenna (in-fabric) and the body. Compared to [185] which achieves an S_{11} around -3 dB at its design frequency in space, the proposed antenna is able to maintain an $S_{11} < -6$ dB at 915 MHz both in presence and absence of the human body, under flat and bent conditions.

The radiation patterns of the CPW antenna were simulated and measured experimentally. Fig. 8.4 shows the co-polarized (vertically on the Y-plane) gain patterns of the

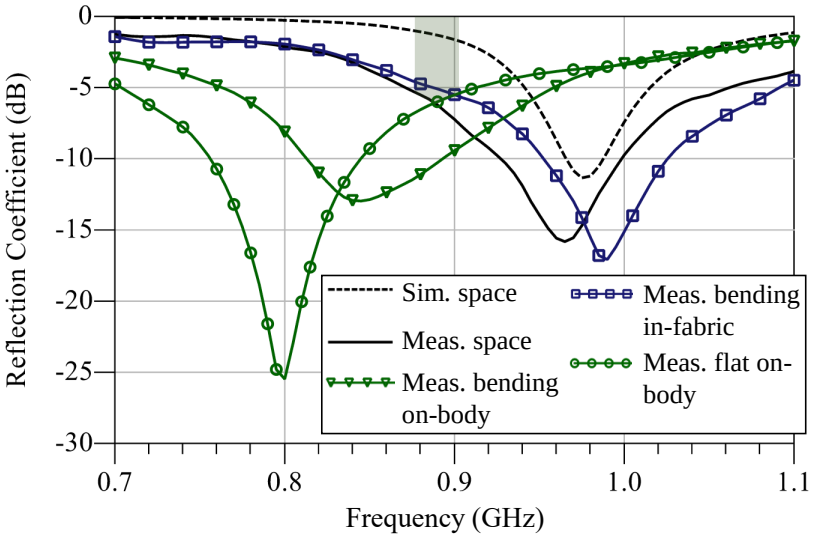

FIGURE 8.3: Simulated and measured 50 Ω S_{11} of the CPW antenna filament.

antenna on the XZ and XY planes. The measured gain was calculated using the free space path loss model at 1.1 m from a 10 dBi log-periodic antenna. The discrepancy between the simulations and measurements is attributed to additional reflection off the SMA connector, which is comparable in size to the CPW feed and the antenna's ground. Nevertheless, it can still be verified that the antenna is predominantly omnidirectional across both the XY and XZ planes. In Appendix A [288], it was shown that using omnidirectional rectennas improves the power harvested in wearable operation.

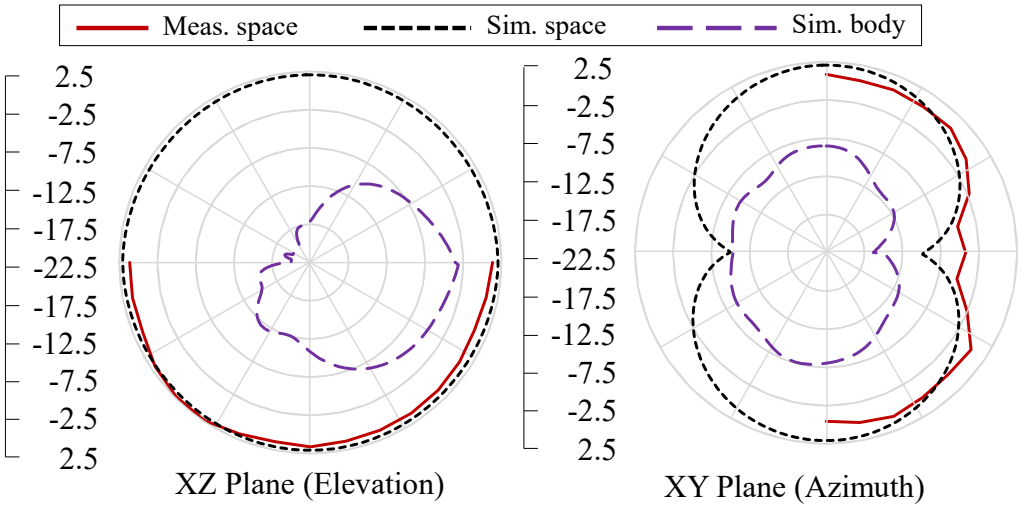

FIGURE 8.4: Simulated (dashed) and measured (solid) gain patterns of the antenna at 915 MHz, in free space and and on the Austinman CST phantom.

The antenna has also been simulated on the Austinman phantom in CST, in order to investigate the impact of in-body losses on the radiation patterns. As predicted, the body shadows radiation behind the user, resulting in a broadside pattern as observed on the elevation *E*-plane in Fig. 8.4. On the azimuth plane, the antenna maintains an omnidirectional on-body pattern, showing its ability to harvest arbitrarily directed

radiation, as discussed extensively in appendix A [288]. The simulated 3D gain patterns of the antenna in space and on the Austinman phantom are shown in Fig. 8.5

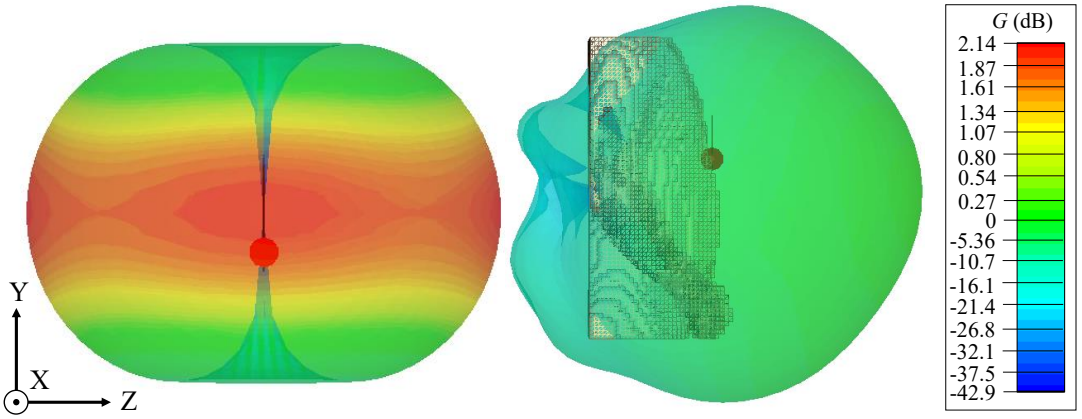

FIGURE 8.5: Simulated 3D gain patterns of the antenna in free space (left) and on the Austinman phantom (right).

8.2.2 Rectifier Design and Impedance Matching

The proposed rectifier is based on a voltage doubler topology, producing a higher DC potential which enables faster charging of the supercapactior. The selected diode is the Infineon BAT15-04R, based on its low forward voltage (0.25 V) and high breakdown voltage (4 V). With two diodes in the same package, the overall component count is reduced. In addition, the mechanical reliability of the system is improved and the electrical packaging parasitics (inductance and capacitance) are reduced.

As the antenna was designed with Z_0=50 Ω, the rectifier needs matching to 50 Ω. Given the predominantly-capacitive input impedance of rectifiers [80, 289], a series inductor is used for impedance matching. The rectifier's input impedance, before matching, is shown in Fig. 8.6. By adopting a voltage doubler topology, the equivalent RC circuit of the rectifier has a smaller R and C components, which subsequently enables achieving more broadband performance according to the Bode-Fano bandwidth limit [244, 298]. In addition, as the imaginary component of the rectifier's input impedance is significantly higher than the real component, a higher RF potential will be present at the diode's junction enabling more efficient rectification [111]. The simulated rectifier's optimal input impedance of 20+j230 Ω can also be achieved using a co-designed antenna as in Chapter 5.

The rectifier matching was optimized using HB simulation, including the CPW layout and the diode's packaging parasitics. Fig. 8.2-b shows the layout of the CPW rectifier. The selected matching inductor L_1 is a 22 nH wirewound inductor. By opting for a smaller value inductor, the parasitic resistance and capacitance of the commercially-available inductor will be lower, enabling a higher PCE. A shunt inductor, L_2=47 nH, is

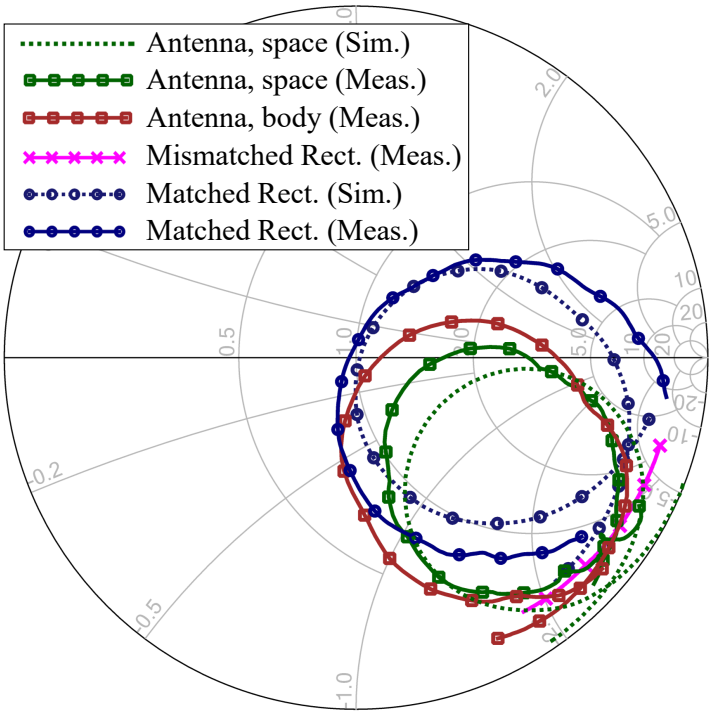

FIGURE 8.6: Smith chart plot showing the antenna and the rectifier's simulated and measured input impedances, showing the 50 Ω matching.

added to create a return path for the DC currents [296]. The value of L_2 was chosen A 0603 footprint is chosen for the inductors and the voltage doubler charge pumping 100 pF capacitors, to enable a reliable interconnect between the rectifier and the flexible e-textile filament [293]. Fig. 8.6 shows a close agreement between the simulated and measured input impedance of the matched rectifier, normalized to 50 Ω. The antenna's input impedance is also included in the Smith chart to show that the 50 Ω nominal impedance is maintained throughout both the antenna and the rectifier matching planes.

8.2.3 Rectifier Experimental Characterization

The matched rectifier was characterized using a VNA in CW mode to investigate its performance for varying power levels, frequencies, and load impedances. Due to its CPW structure, the rectifier's performance is expected to be textile-independent, enabling it to be used for various fabrics with no limits on the thickness or the dielectric properties. In addition, the performance is expected to be maintained in human proximity. The DC output of the flexible rectifier filament was measured in space, in fabric, and on-hand, as shown in Fig. 8.7.

The frequency of the RF input power was swept at 0 and 10 dBm. Fig. 8.8 shows the measured PCE from 600 to 1400 MHz. It can be observed that the rectifier achieves a half-power fractional bandwidth of 57%. In addition, the rectifier achieves an approximately stable PCE above 75% from 980 to 1120 MHz at 10 dBm. The wide bandwidth

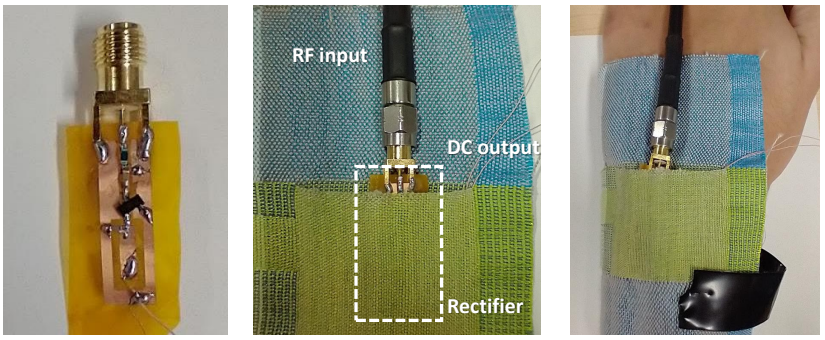

FIGURE 8.7: Photographs of the connectorized rectifier test setup: (a) rectifier in space; (b) in-fabric "e-textile" rectifier; (c) body-worn rectifier.

demonstrates that due to the low Z_{in} of the voltage doubler, a first-order matching network based on a single lumped inductor is able to result in a half-power fractional bandwidth over 50%, at the rectifier's optimal resistive load for 4.5 kΩ.

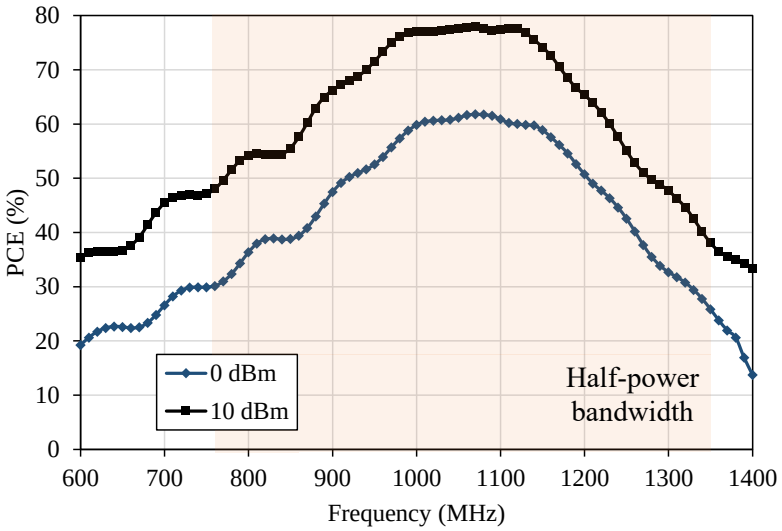

FIGURE 8.8: Measured PCE of the rectifier over a frequency sweep showing a 57% half-power −3 dB fractional bandwidth.

The DC output as well as the input reflection coefficient were measured to characterize the performance of the rectifier for varying load impedances. Fig. 8.9 shows the rectifier's measured PCE and S_{11} for varying load impedances, at 0 and 10 dBm. From the measured PCE, it can be observed that the rectifier maintains over 50% of its maximum PCE for load impedances as low as 600 Ω. A high PCE across a low-impedance load is particularly important when directly charging a capacitor without a DC-DC converter, where the equivalent series resistance of a capacitor is typically under 100 Ω.

To characterize the rectifier's large-signal PCE, the RF power was swept from −20 to 15 dBm, translating to approximately 0.1 to 10 m from a sub-1 GHz 33 dBm EIRP source. The PCE was measured in the three test setups shown in Fig. 8.7, for the optimal load of 4.5 kΩ. The DC voltage was measured across both the optimal load and a 10 MΩ

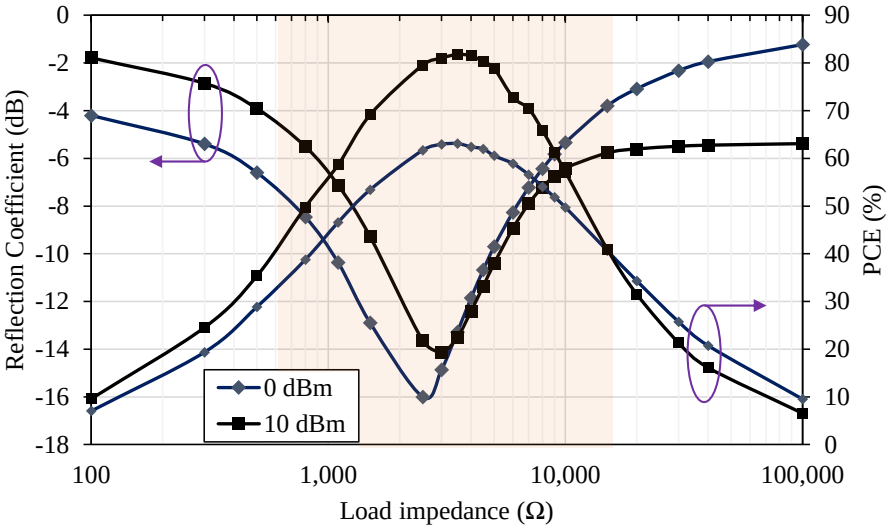

FIGURE 8.9: Measured reflection coefficient of the rectifier for varying load impedances at 1 GHz; the shaded region indicates the half-power load range.

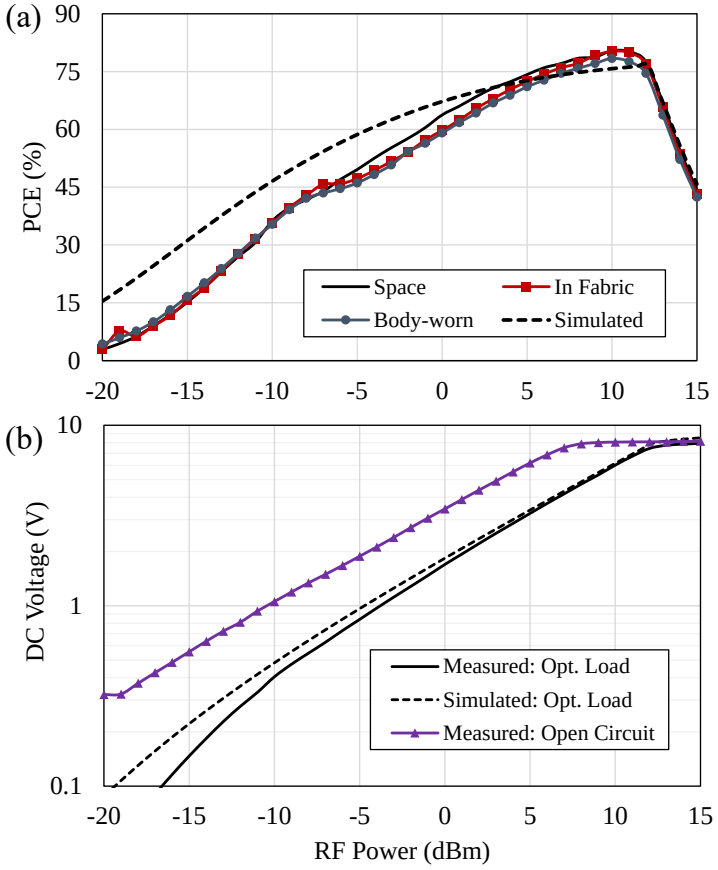

FIGURE 8.10: Measured (solid) and simulated (dashed) DC output of the proposed rectifier for varying power levels: (a) RF-DC PCE; (b) DC voltage.

"open" load. Fig. 8.10-a and b show the simulated and measured PCE and DC voltage, respectively, at 1 GHz.

From Fig. 8.10-a, it can be observed that the proposed rectifier achieves over 60% PCE from 0 to 13 dBm, with a DC voltage over 1.8 V across the 4.5 kΩ optimum load. Therefore, it is expected that the rectifier can charge the TSC efficiently from under 0 dBm. Compared to recent flexible, printed, and textile-based rectifiers operating between 820 MHz and 2.4 GHz [179, 289, 340, 341], the proposed rectifier achieves the highest peak-PCE of 80%. This is attributed to the careful impedance matching, for a higher power input, using a low-value and high-Q lumped inductor and the distributed CPW traces. In addition, the diode selection with a relatively high V_{Br} of 4 V and a low forward voltage of 0.25 V enables the peak-PCE improvement over [179, 289, 340, 341], which were all based on a diode with a lower V_{Br} of 2 V.

8.3 Textile Supercapacitor (TSC)

The TSC is composed of an aqueous electrolyte and spray-coated carbon electrodes on a conventional cotton fabric substrate. The TSC was designed and fabricated by S. Yong and N. H. Hillier [333], as desribed in [329]. Fig. 8.11-a and b show the structure of the TSC sprayed on the cotton substrate. The cross-section of the TSC is shown in Fig. 8.11-c using scanning electron microscopy (SEM), showing the polymer encapsulation, the carbon electrodes, and electrolyte-wetted cotton substrate. After the supercapacitors are fabricated on the textile substrate, each individual TSC cell is housed in a Swagelok test cell. This allows more reproducable measurements and guarantees a time-invariant device performance during both the DC and RF characterization.

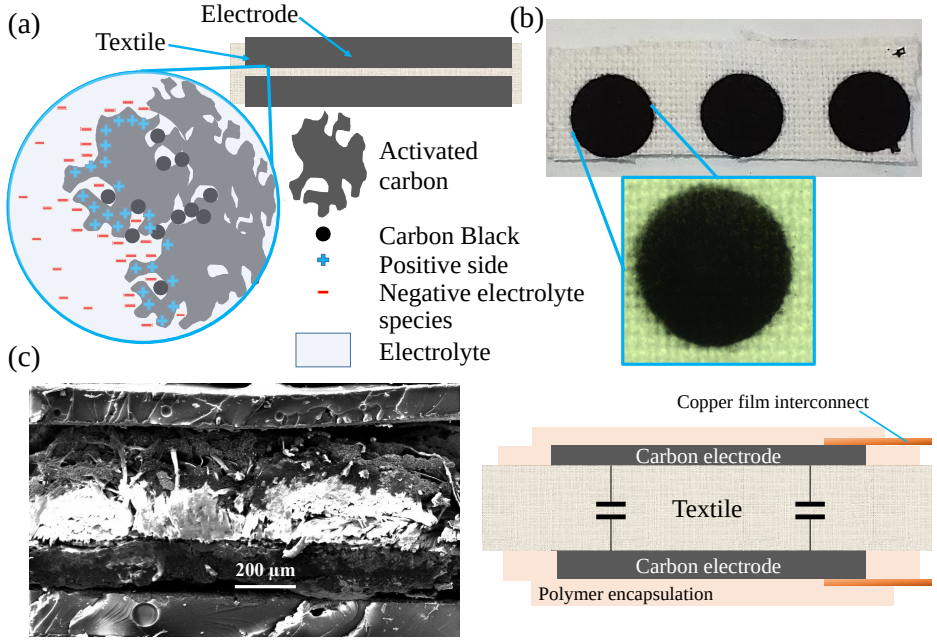

FIGURE 8.11: The proposed three-cell TSC: (a) 2D layout; (b) phorograph and optical micrograph of the TSC cells; (c) SEM image and layout showing the TSC's cross-section.

The TSC was characterized using galvanostatic cycling (GC), i.e. charging using a fixed DC current, and electrochemical impedance spectroscopy (EIS), to extract it equivalent circuit model. Fig. 8.11 shows the measured real and imaginary impedance of the TSC from 0.1 Hz to 250 kHz, as well as the extracted equivalent circuit. The inset in Fig. 8.11-a shows the close agreement between the extracted circuit model of the TSC and the measurement. For DC charging currents between 0.25 and 3 mA/cm^2, the TSC maintains a stable aerial capacitance with less than 5% reduction in the capacitance for charging currents above 2 mA, which are unlikely to be encountered in RF-charging up to 15 dBm.

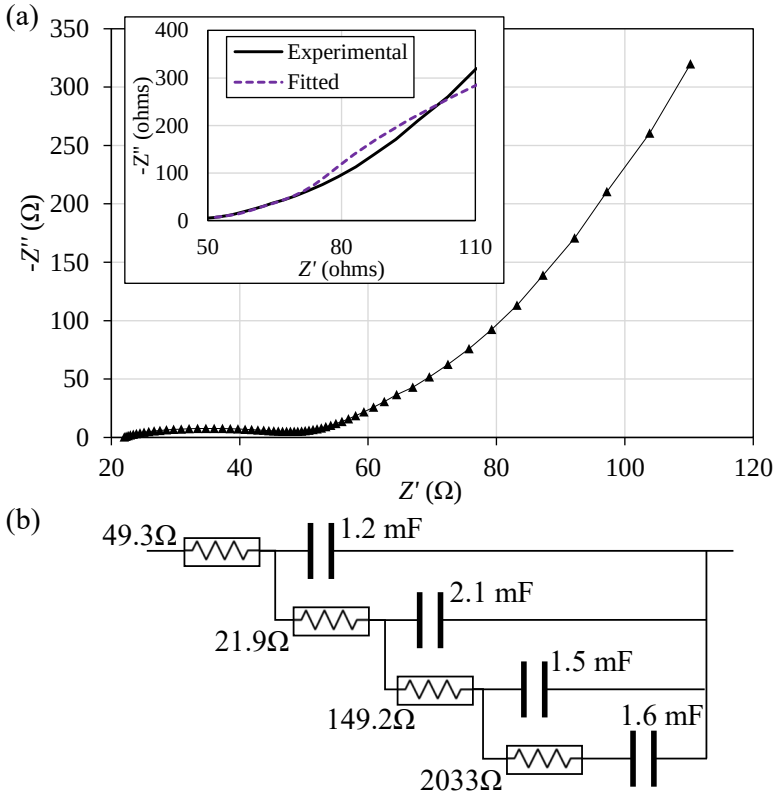

FIGURE 8.12: EIS equivalent model of the TSC: (a) measured and fitted real and imaginary impedance; (b) the equivalent circuit model of the three-cell TSC.

The TSC was subjected to 5 symmetric charging and discharging cycles. Due to the breakdown voltage of water, a single TSC cell is limited to 1.2 V. Nevertheless, the TSC needs to withstand the output of the rectifier, and to be able to drive electronic circuits within the supply range of low-power ICs (3.3 V to 1.2 V). Therefore, three cells are connected in series. This increases the TSC's ideal maximum voltage to 3.6 V. However, due to the purposeful simplicity of the power unit no balancing circuits were utilised, therefore, the TSC is not charged beyond 3.2 V in this work. Fig. 8.13-a shows the charging and discharging curve of the single-cell and three-cells TSC from a DC current density of 1 mA/cm^2. In Fig. 8.13-b, the charging and discharging voltage curves are shown for DC currents between 0.20 and 1.6 mA. These values correspond

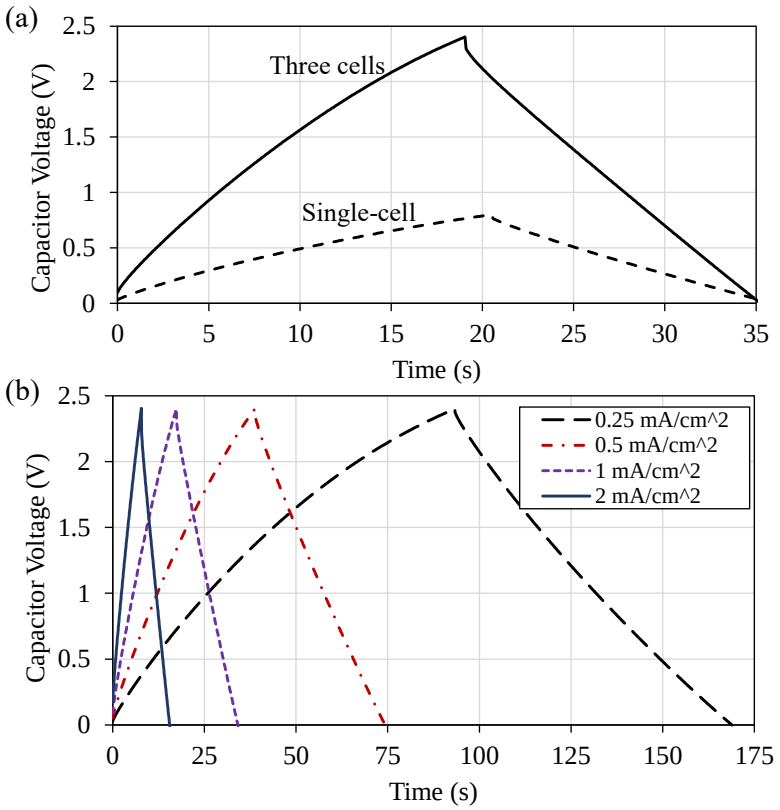

FIGURE 8.13: GC measurements of the TSC: (a) the single and three-cells TSC at for 1 mA/cm^2 charging current; (b) the three-cell TSC under varying current densities.

to the anticipated DC output of the rectenna, for various RF power levels from 15 to 0 dBm.

The measured voltages across the capacitor during GC measurements indicate that the TSC is well-suited for integration with a rectenna. For instance, the input current of 0.2 mA (0.25 mA/cm^2) corresponds to the current driven by the proposed rectifier for P_{RF} >2 dBm, for 4.5 kΩ load. From the instantaneous voltage drop (during the current reversal) and the known measurement currents, the equivalent series resistance of the TSC (ESR) was calculated using ESR $= \Delta V/\Delta I$ as 71.9 Ω.

8.4 Integrated Rectifier and Supercapacitor Evaluation

8.4.1 RF Charging and Time-Variant S-Parameters

In Section 8.2, the rectifier was characterized with a resistive load in its steady state. By using a 50 Ω RF power source, it is possible to characterize the performance of the rectifier while charging the TSC with less than 0.1 dB uncertainty in the RF power level [11]. In addition, using a VNA, it is possible to measure the single-tone time-variant s-parameters (S_{11}) of the rectifier while the capacitor is being charged.

The designed rectifier has been directly connected to the TSC to characterize the combined rectifier-supercapacitor performance. The TSC was charged for up to 180 seconds, or until the capacitor reaches 2.9 V, below its voltage limit of 3.6 V. The VNA power output was swept from −4 dBm to 14 dBm, with an intermediate frequency of 10 Hz, i.e. the rectified signal resembles a 10 Hz square wave, to enable simultaneous S_{11} measurements while charging the TSC. Fig. 8.10 shows the voltage across the capacitor for varying RF power inputs to the rectifier.

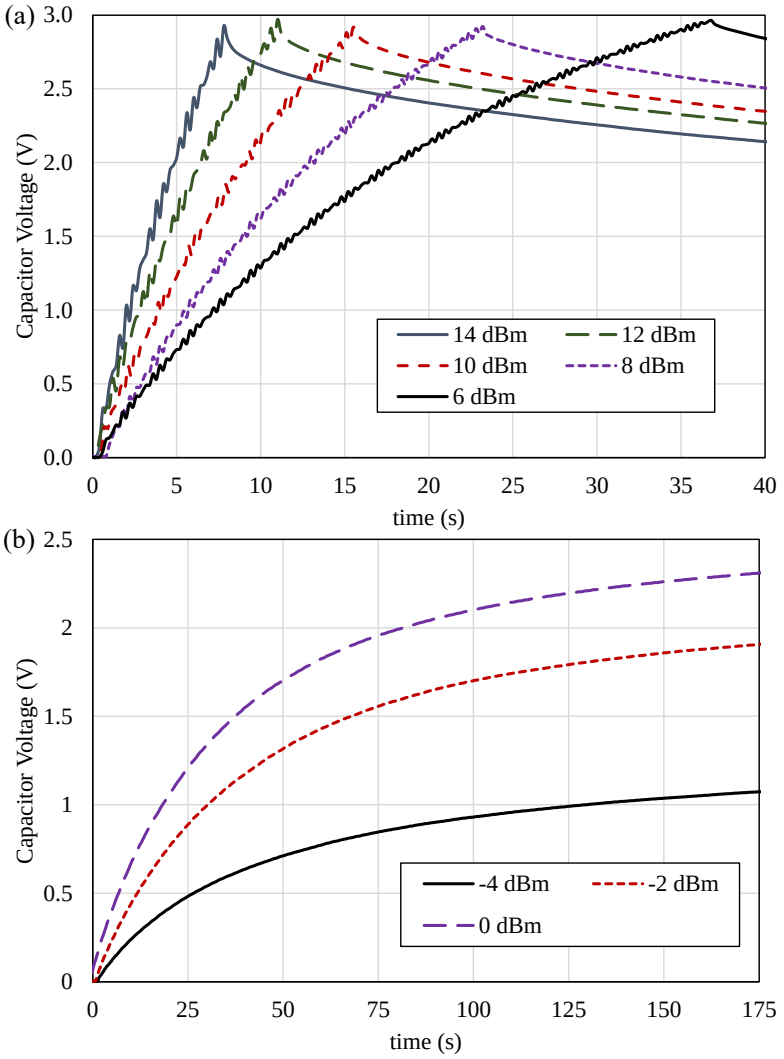

FIGURE 8.14: Measured voltage across the 7.5 mF textile supercapacitor for varying RF power levels: (a) >1 mW available power; (b) sub-mW power levels.

From Fig. 8.14-a, it can be seen that for power levels over 0 dBm, the rectifier can fully-charge the TSC to 31.5 mJ in under 37 seconds. Below 0 dBm (Fig. 8.14-b), while it takes over a 100 seconds to charge the capacitor to 1 V from −4 dBm, the energy stored in the capacitor is still in excess of 3 mJ, enabling various low-power intermittent sensing and computing tasks [342]. After the maximum voltage is reached, in Fig. 8.14-a, the TSC is allowed to discharge freely across a 1 MΩ load. This results in a ≈2 μA current

draw, the equivalent of a low-power micro-controller (e.g. TI CC2640) in sleep mode with full memory retention.

As the rectifier charges the TSC, the current drawn by the TSC varies depending on its charge level. The time-variant S_{11} of the rectifier, measured by the VNA while providing RF power to the system, enables understanding the impact of the TSC on the rectifier's impedance matching. Fig. 8.15 shows the measured S_{11} of the rectifier during charging, as well as the calculated equivalent DC load impedance based on the TSC charging current. The charging current was calculated using $I = C \times dV/dt$, from the measured voltage in Fig. 8.14-b. In this impedance calculation, it is assumed that the leakage of the TSC is negligible and that all the current drawn by the TSC induces a change in the voltage across the TSC.

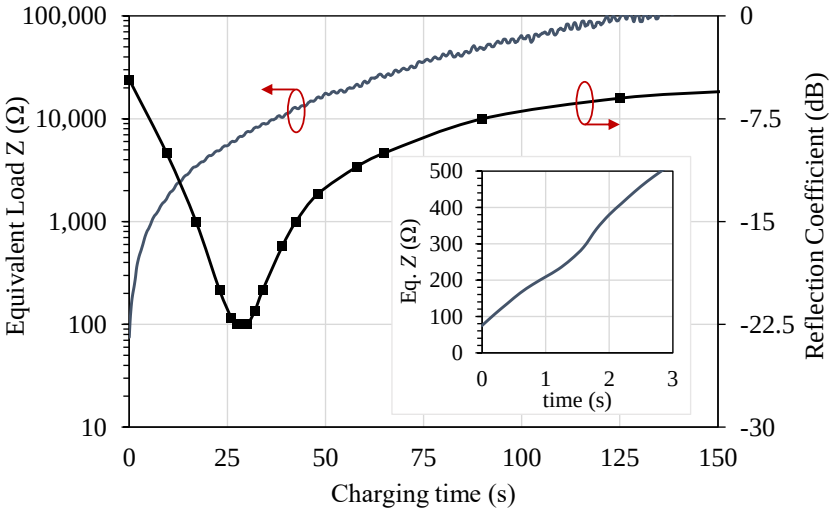

FIGURE 8.15: Measured S_{11} of the rectifier while charging the TSC, at 0 dBm, and the calculated equivalent load Z of the TSC; inset shows Z of the first 3 seconds.

At the start of the charging process, the only limit to the current drawn by the rectifier is the capacitor's ESR (71.9 Ω from the EIS measurements). In the inset in Fig. 8.15, it can be seen that the equivalent load Z of the TSC, observed by the rectifier, is 74 Ω at t=0, closely agreeing with the measured ESR. Recalling Fig. 8.9, a resistive load of 100 Ω corresponded to an S_{11}=−4 dB, where the measured S_{11} rectifier when charging the capacitor starts from around −5 dB. As charge builds on the capacitor, the charging current reduces and the equivalent Z lies within the optimal load impedance range of the rectifier, demonstrated by the measured S_{11} below −10 dB from 5 to 60 seconds in the charging curve in Fig. 8.15. While a PMIC such as TI's BQ25504 (used in [14,39,331,332]) would mask the variations in the load current through MPPT, it is demonstrated that the overall charging efficiency of the proposed system surpasses that of a rectifier with an MPPT boost converter PMIC, in the next subsection.

8.4.2 Rectifier-TSC Average Charging PCE Analysis

The average charging power for a fixed time period t is used to evaluate the holistic PCE of the of the RF rectifier and TSC, based on the DC energy stored in the TSC at time t, instead of the fixed τ in (4.3). The charging PCE was calculated using (4.3) using the 7.5 mF capacitance of the three TSC cells. The RF power available P_{RF} is the RF power provided by the VNA. Instead of τ, due to the limited maximum rated voltage of the TSC, for $P_{\mathrm{RF}} \leq -6$ dBm, 30 seconds is chosen for the time period t, to stay within the linear charging region of the TSC charging curve, as observed in Fig. 8.14. For 8 dBm and above, t is the time taken to reach 2.9 V, before the RF generator is stopped.

Fig. 8.16 shows the calculated $\mathrm{PCE}_{\mathrm{Charging}}$ and capacitor voltage at the end of the time period t. It can be observed that from -2 to 9 dBm, the $\mathrm{PCE}_{\mathrm{Charging}}$ is maintained above 20%, limited by the impedance mismatch between the rectifier and the TSC, the leakage of the TSC, and the rectifier approaching the breakdown voltage of the diodes beyond 8 dBm, as previously shown in Fig. 8.10-b. Furthermore, in 30 seconds of charging, the TSC can be charged to 1 V (3.75 mJ) from an RF input as low as -2 dBm.

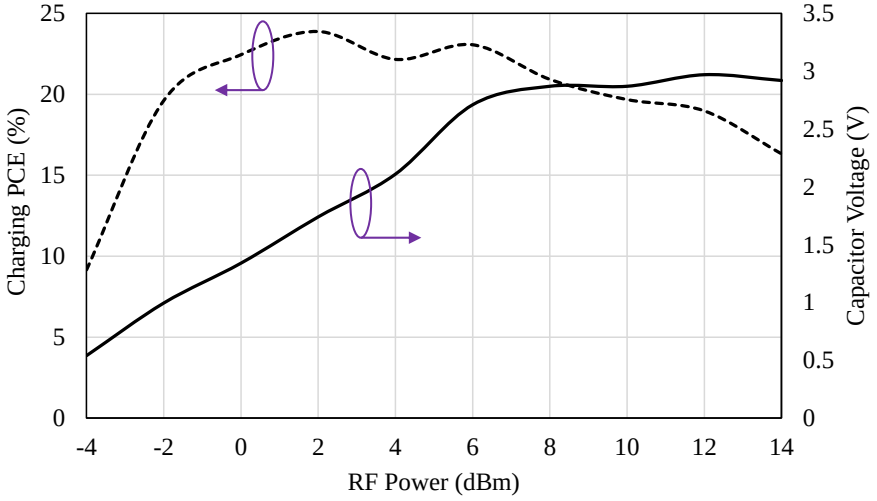

FIGURE 8.16: Measured voltage and average charging PCE of the capacitor for varying RF power levels, from an RF signal generator.

The reduction in the PCE of the rectifier compared to Fig. 8.10-a, where an optimum resistive load was used, was previously observed with electrolytic capacitors in Section 4.4.3, and [338]. In Section 4.4.3, the capacitive-loaded rectifier had an average charging PCE 62% lower compared to when it was terminated with an optimum resistive load. At 0 dBm, the proposed rectifier achieves an average charging PCE 60% lower than the steady-state PCE observed in Fig. 8.10. Despite the different rectifier topologies and diode models between this CPW voltage doubler rectifier and the microstrip single-series rectifier in Chapter 4, the consistent loss in the PCE shows that the impedance mismatch effects between the storage capacitor and the rectifier are mostly consistent across different rectifiers and energy storage devices.

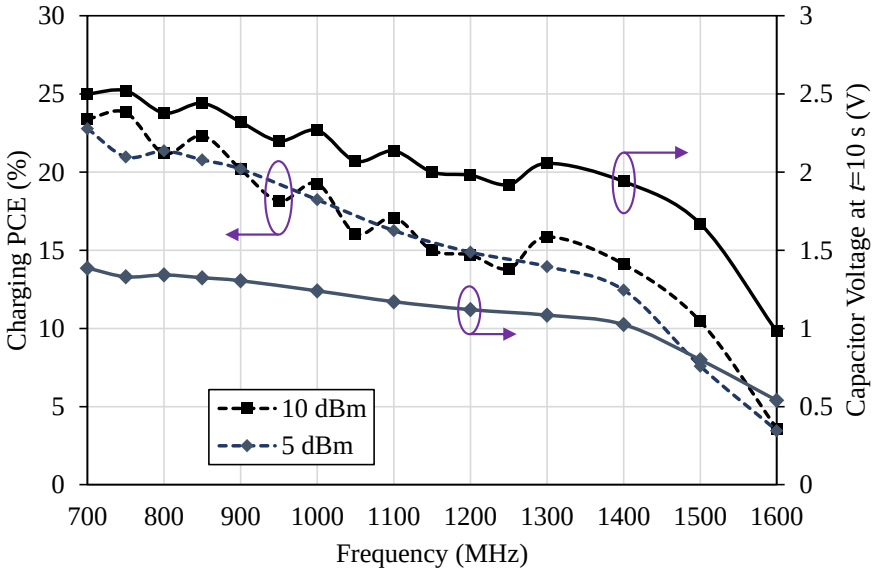

FIGURE 8.17: Measured charging PCE (dashed) and voltage across the capacitor (solid) for 10 s of charging.

The TSC-loaded rectifier is then investigated for an input frequency sweep. Around 1 GHz, several frequency bands such as the 868/915 MHz ISM, 940-960 MHz GSM, and LTE/4G/5G bands down to 700 MHz are considered potential candidates for RFEH. As the resistor-loaded rectifier achieves a half-power fractional bandwidth of 57% (Fig. 8.8), the frequency of the RF source was swept from 700 MHz. Fig. 8.17 shows the capacitor voltage after 10 seconds of charging from 700 to 1600 MHz, for a 5 and 10 dBm input.

In Fig. 8.17, it can be observed that the TSC-loaded rectifier achieves a half-power fractional bandwidth of 72.7% from 700 to 1450 MHz, for the rectifier's center frequency of 1050 MHz in Fig. 8.8, during the first 10 seconds of charging. This represents a 27.5% half-power bandwidth improvement over the resistive-loaded rectifier. It can also be seen that the broadband high charging PCE is maintained at both 5 and 10 dBm. Therefore, the wider bandwidth achieved by the capacitive-loaded rectifier compared to resistive-loading (in Fig. 8.8) can be identified as a key benefit of directly connecting an RF rectifier to a supercapacitor.

8.5 Wireless Rectenna Testing

8.5.1 Distance Sweep

In order to demonstrate the integrated rectenna and supercapacitor wireless charging module in a real-world application, a 915 MHz 3 W (34.77 dBm) EIRP Powercast transmitter is positioned at varying separation from the rectenna. As observed in Fig. 8.17 the

TSC-loaded rectifier achieves over an octave half-power bandwidth and is therefore expected to charge efficiently from the 915 MHz source. The rectenna was concealed inside the bespoke fabric pocket and connected to the supercapacitor cells in their Swagelok test cases using conductive silk-coated Litz threads. Fig. 8.18 shows a photograph of the wireless test setup of the rectenna.

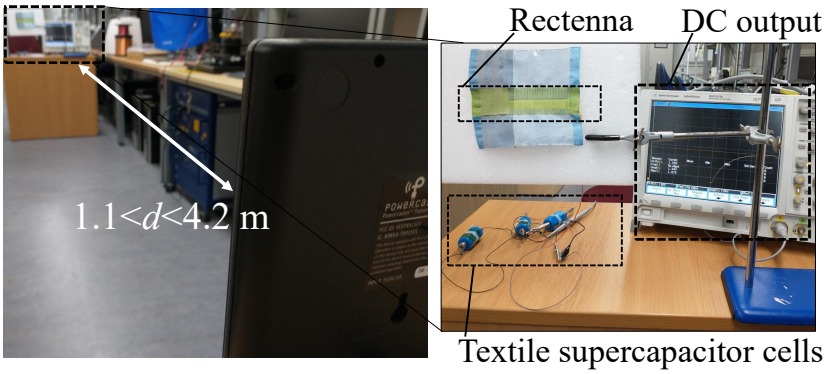

FIGURE 8.18: Wireless test setup of the rectenna using a 34.77 dBm 915 MHz Powercast transmitter.

Fig. 8.19 shows the measured DC voltage across the capacitors during wireless charging at varying distances from the Powercast transmitter. From the capacitance of 5.5 mF of the three cells used in this test, the energy stored in the capacitor is around 28 mJ in under 3 minutes at 2.2 meters from the source. This corresponds to an incident plane wave with a power density S of 4.4 μW/cm^2. At 4.2 m away from the source (S=1.2 μW/cm^2), the integrated module harvests 6.2 mJ of DC energy in 4 minutes of charging. For a high S of 19.7 μW/cm^2 (d=1.1 m), the TSC is fully charged to 3.2 V (28.2 mJ) in 45 seconds.

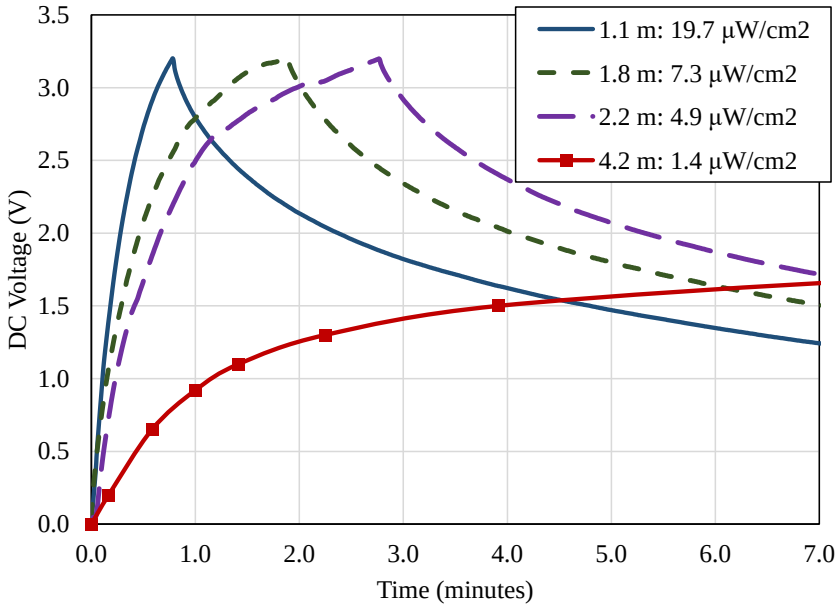

FIGURE 8.19: Measured voltage across the 5.5 mF capacitor during wireless charging at varying separation from the 915 MHz 34.77 dBm transmitter.

The RF power available at the rectenna was estimated using the calculated RF power density S of the plane wave available from the transmitter [39, 289]. The power received by the rectenna is calculated using the antenna's effective area based on the measured peak gain of the antenna (Fig. 8.4). The peak gain is chosen to obtain a conservative estimate of the rectenna's PCE [341]. The wireless charging efficiency was calculated using (4.3) based on the available RF power for a charging period t of 30 seconds. Fig. 8.20 shows the calculated end-to-end PCE of the rectenna while charging the TSC. Using this setup, the wireless charging PCE is inclusive of the mismatch losses between the antenna and the rectifier, the mismatch between the rectifier and the TSC, as well as the rectification losses and the self-leakage of the TSC. The rectenna achieves its maximum wireless charging PCE of 38% at d=1.8 m from the source. Below 1.8 m, the power available at the rectenna exceeds 10 dBm and subsequently the rectifier is operating in its breakdown region and therefore the PCE reduces. At 4.2 m from the source, the proposed module achieves an end-to-end efficiency of 17% from S=1.35 μW/cm^2, showing its suitability of RFEH from low power densities. The energy harvested in 7.1 minutes of charging from S=1.35 μW/cm^2 (d=4.2 m) is 10.8 mJ.

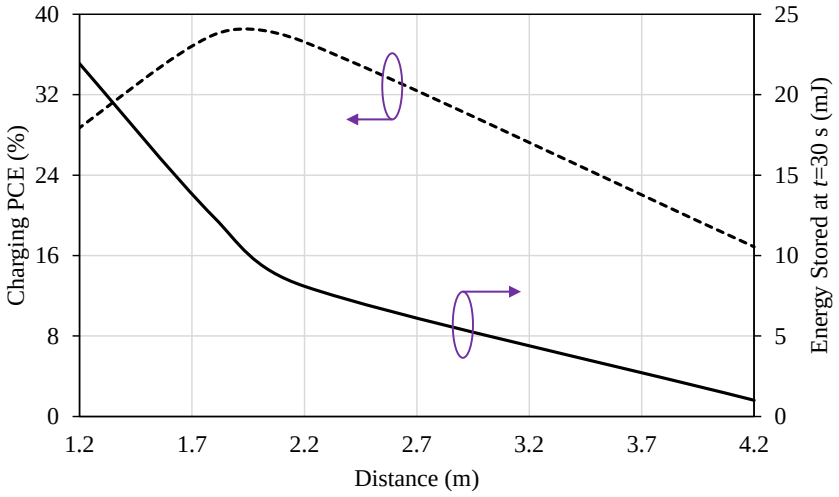

FIGURE 8.20: Measured energy stored in the capacitor and average charging PCE for the first 30 seconds of wireless charging for varying distance from the source.

8.5.2 Wearable Operation

To demonstrate the wearable operation of the integrated e-textile energy harvesting module, the textile-concealed rectenna was placed on a user's body and connected to the TSC. The TSC was encapsulated using a heat-pressed polymer film, shown in Fig. 8.11-c, for bonding the three cells and providing a reliable electrical interconnect to the rectenna's output leads. Fig. 8.21 shows the capacitor voltage during wireless charging on the body along with a photograph of the measurement setup. From Fig. 8.21, it can be seen that despite the decrease in the received power due to a degradation in the antenna's gain, which typically exceeds −4 dB, as shown in Fig. 4.7 for the broadband

monopole, and can be up to −20 dB as reported in [181] above 2 GHz, the TSC can still be charged to approximately 1.6 V in 65 seconds. While charging, the effects of body shadowing were investigated through various body movements which introduce additional shadowing. The shaded regions in Fig. 8.21 show the time where the rectenna was covered by hand which significantly reduces the received RF power.

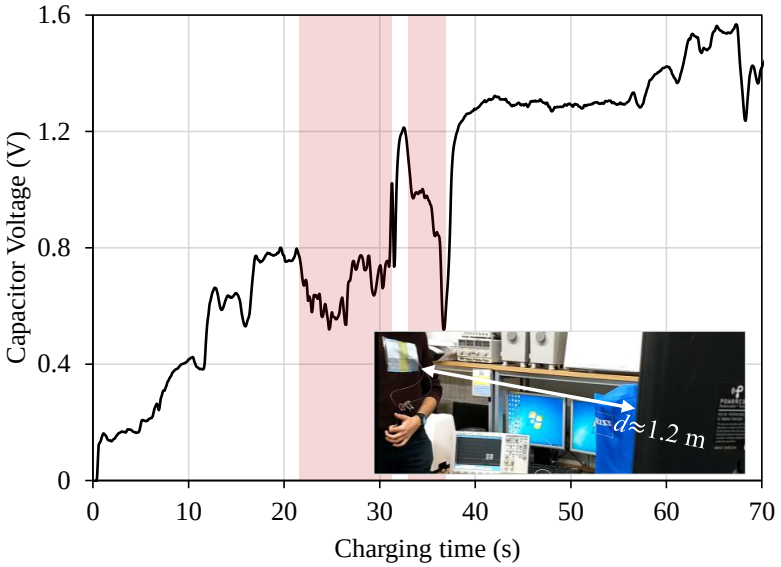

FIGURE 8.21: Wireless charging of the body-worn rectenna and TSC at 1.2 m from the transmitter; inset shows a photograph of the wearable test setup.

Despite the introduced body shadowing for about 8 seconds, from t=22 to t=30 s, and the lack of shielding of the proposed rectenna, the rectenna charges the TSC to 1.2 V in the first 32 seconds. This demonstrates a wearable charging efficiency of 4.8%, inclusive of the antenna losses due to human proximity, from an incident power density of ≈16.6 μW/cm^2. Therefore, the proposed rectenna and TSC integrated module can be used both in presence and absence of the human body. While a power density of 16.6 μW/cm^2 is relatively high and may not be available from ambient sources, recent low-profile (sub-1 mm-thick) unshielded textile rectenna implementations were only able to yield over 1 V DC (across a resistor in steady-state operation), from S >40 μW/cm^2 at 2.9 GHz, and using as many as 81 individual rectenna cells [181].

8.5.3 Comparison with Previous Work

The proposed energy harvesting and storage unit is compared to related work in Table 8.2. The charging efficiency is calculated using (4.3) for the linear region of the charging curve, yielding the highest efficiency of the harvester in comparison.

Previously, PCB rectennas were used to charge a supercapacitor and a battery in [331] and [337], respectively. Nevertheless, in both cases, the rectifier was not designed specifically for directly charging the storage device. Therefore, their average charging

efficiency is lower than the proposed rectenna-supercapacitor module. In addition, the power consumption of the power management stage contributes to reducing the end-to-end efficiency with the harvested DC power being under 5 mW.

The rectenna in [14] achieves a high sensitivity enabling the BQ25504 PMIC to operate from -12.6 dBm ($0.8\ \mu W/cm^2$) in cold-start mode. Nevertheless, due to optimizing the system for low RF input, the end-to-end charging efficiency is very low and the complexity of the implementation makes it unsuitable for e-textiles. Where a boost converter was not needed due to a sufficient RF input, a charging efficiency up to 25% was achieved in [338] while charging a 15 μF capacitor with a maximum range of 2.3 m. The proposed rectenna achieves around 50% higher end-to-end PCE compared to [338] in addition to occupying significantly smaller area and to being implemented using all textile-based components for the antenna and the mF-range textile supercapacitors. Therefore, it can be seen compared to other high power rectennas: [338] and [337], the proposed textile module achieves the highest end-to-end efficiency.

TABLE 8.2: Comparison with reported energy harvesters integrated with energy storage devices

Study	**Energy Harvester**	**Energy Storage**	**Implementation**	**DC Power management**	S (μW/cm^2)	**DC Energy (mJ)**	**Charging Time (minutes)**	**Average efficiency**	**Dimensions (mm)**
This work	**Sub-1 GHz rectenna**	**Textile supercapacitor**	**Textile-based**	**None**	**6.6; 1.2**	**28.7; 8.1**	**1.8; 7**	**38%; 15%**	**115×15 (70×6.5$^\diamond$)**
[331]	Sub-1 GHz rectenna	Supercapacitor	PCB	BQ25504	12.6; 5.0	12.6; 12.6	6; 12	1.6%; 2%	110×60$^\diamond$
[338]	Sub-1 GHz rectenna	Electrolytic capacitor	PCB+whip antenna	LTC3588	23.8	0.043	0.02	25%	>100× 50 × 100‡
[14]	2.4 GHz rectenna	Electrolytic capacitor	3D-printed enclosure	BQ25504	0.8	0.12	3	1.2%	47×47×20
[337]	Sub-1 GHz rectenna	Flexible battery	PCB + 130 nm IC	boost converter	31.8*	105.9	50	11.6%	90×90$^\diamond$
[329]	Ferroelectret insole	TSC	Textile-based	None	31 μW†	0.176	60	0.16%	60×60$^\diamond$
[330]	Triboelectric yarn	TSC	Textile yarns	None	8.5 μW†	0.083	1.7	1%	30×30$^\diamond$

*Calculated from the reported distance and EIRP; †instantaneous DC power output; ‡approximated from the photographs; $^\diamond$harvester-only area

Compared to other textile-based energy harvesters such as mechanical ferroelectret insoles and triboelectric yarns [329, 330], the efficiency of the capacitor charging was calculated relative to the optimum DC output, due to the difficulty in estimating the mechanical power density available at the harvesters. However, it can still be seen that RFEH provides at least an order of magnitude efficiency improvement due to rectennas' low impedance. To explain, a rectenna enables charging currents in the order of 100 μA to few mA, from a power density as low as 1.2 μW/cm^2, translating to a significantly shorter charging time and a higher end-to-end efficiency. Therefore, the proposed rectenna and TSC is the only e-textile solution capable of harvesting millijoules of energy in less than 4 minutes of charging from power densities down to 1 μW/cm^2, while maintaining an overall compact and low-complexity structure.

8.6 Summary and Conclusions

In this chapter, an RF-powered e-textile energy harvesting and storage module was presented based on a flexible antenna filament and a textile supercapacitor. By designing a high-voltage RF rectifier with a high PCE in the 100 μW-10 mW RF power range, the proposed energy harvesting and storage module achieves the highest reported end-to-end efficiency exceeding 30%, at over 2 m from a license-free power transmitter, and over 4% wearable PCE inclusive of body absorption and shadowing effects. The key findings in this chapter can be summarized as:

- A flexible CPW rectenna filament is well-suited to e-textile applications, owing to its high miniaturization, a very low-profile (<50 μm), and maintaining its antenna and rectifier performance inside a textile substrate/superstrate and near the body.
- For rectennas targeting S >1 μW/cm^2, directly connecting the rectifier to an energy storage device achieves a higher average charging PCE compared to rectennas utilizing a DC-DC converter PMIC.
- An improvement of over 27% in the half-power bandwidth of a rectifier can be achieved by directly connecting the rectifier to a supercapacitor, compared to its bandwidth with a fixed resistive load.
- The proposed rectenna, having a relatively low equivalent impedance, is capable of charging e-textile energy storage devices with over an order of magnitude efficiency improvement compared to other mechanical wearable energy harvesters integrated with TSCs.

Chapter 9

Antenna-Rectifier Co-Design for Additively-Manufactured Rectennas

While a few rectenna implementations have been reported based on screen printing [343] and inkjet printing [42, 340], antenna-rectifier co-design has not been widely demonstrated using additively-manufactured rectennas. This can be explained by observing the recent reported implementations of electrically-small rectennas, such as [344] and [345], containing critical features under 0.5 mm which cannot be resolved using direct-write or screen printing. Furthermore, the dipole design proposed in Chapter 5, while maintaining compactness and conformability, still contains fine features which cannot be implemented using a low-resolution commercial dispenser or screen printer.

In this chapter, a high-impedance dipole antenna design is proposed for low-resolution additive manufacturing, enabling the realization of high-efficiency rectennas utilizing antenna-rectifier co-design without the need for fine features. In addition, meshed conductors are investigated, reducing the conductive ink used in the rectenna by 70% and enabling the realization of co-designed optically-transparent rectennas while maintaining high-PCE, in this context, optical transparency refers to the theoretical transparency of the mesh, calculated using (9.1). First of all, antenna fabrication by direct-write dispenser printing is presented in Section 9.1. The dipole antenna design and tuning are then discussed in Section 9.2, and measured experimentally in Section 9.3. Rectennas of varying mesh fill-factors are then evaluated experimentally in Section 9.4, achieving SoA PCE compared to reported printed rectennas, and finally demonstrated for ambient RFEH in Section 9.5. The contributions in this chapter have been published in [341].

9.1 Antenna Fabrication by Direct Writing

Direct-write dispenser printing represents a hybrid material printing technique that combines the benefits of screen and inkjet printing [346]. Conductive ink, commonly a silver paste, is deposited directly on the substrate to form the conductive traces. Unlike screen printing and subtractive photolithography of copper sheets, dispenser printing is a zero-waste process. Only the required ink is deposited on the substrate and no conductive material is wasted.

With direct-write dispenser printing, it is possible to fabricate thicker conductive layers than with inkjet printing [347]. This reduces the surface resistivity, without printing additional layers or using a more expensive ink such as silver nano-wires. Furthermore, dispenser printing is more suitable for prototyping and low-volume manufacturing compared to photolithography and screen printing. Since no dark Ultra-Violet (UV) mask or printing screen are required, the up-front cost and the lead time can be minimized [348].

On the other hand, dispenser printing can have a lower throughput than screen printing and is less-suited to mass production. Nevertheless, being a thick-film technique, dispener-printed antennas can be realized with screen printing. Compared to conventional PCBs, printing eliminates the need for photolithography equipment and photoresistive inks, and is compatible with a wider range of organic substrates. It was previously shown that by fabricating large-area systems on glass and other low-cost substrates, the material cost can reduce by up to 88%, compared to commercial RF laminates such as Rogers "low-cost" antenna-grade laminate [270].

The printer utilized in this work is a low-cost commercial Voltera V-One desktop printer, specified for prototyping circuit boards with minimal calibration of parameters such as the droplet size or the height of the dispensing nozzle. A silver ink of bulk resistivity 9.5×10^{-7} Ωm is used. This translates to about 0.012 Ω/square. However, at UHF bands, given the varying surface roughness of the ink, this can increase to 0.5 Ω/square due to skin depth effects. The fabrication steps shown in Fig. 9.1 are straightforward and can be summarized as:

a) Planarizing the flexible substrate by adhering (using a spray or tape adhesive) it to a rigid surface.

b) Dispensing the antenna's traces based on the CAD design.

c) Thermal curing on a hot plate at 170°C for 40 minutes.

d) Mounting the components using solder paste or low-temperature solder.

To evaluate the accuracy of dispenser printing and identify the minimum reproducable feature size, multiple conductive traces have been printed and examined. Fig. 9.2

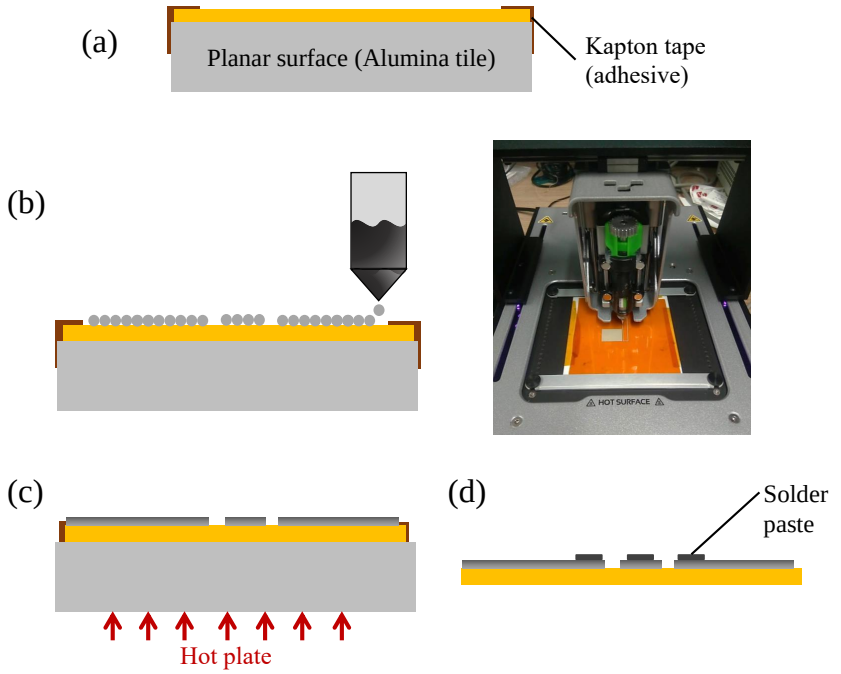

FIGURE 9.1: Flexible circuit fabrication steps using dispenser printing: (a) flexible substrate adhesion to a planar surface, (b) dispensing the conductive silver ink layer, (c) thermal curing of the ink, (d) mounting components and connectors using solder paste or low-temperature solder.

shows micrographs of a dispenser-printed trace on the flexible Kapton substrate (ϵ_r=3.2, tanδ=0.02) of 75 μm thickness. It is observed that around 15 μm non-uniformity can be observed on the edges of the printed line in Fig. 9.2-a. This represents an acceptable tolerance and will not affect the antenna's response. However, an open-ended trace (Fig. 9.2-b) may have variations in the width of up to 100 μm. Thus, critical features of less than 0.5 mm need be avoided when designing the antenna, which reduces the fabrication tolerance to less than 5% and minimizes any impact on the antennas' impedance.

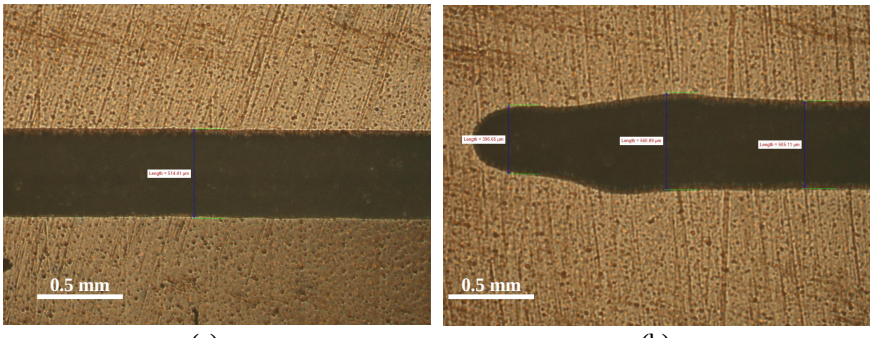

FIGURE 9.2: Micrograph of a 500 μm-wide trace printed using dispenser printed: (a) trace edge, (b) continuous section of the trace.

9.2 Antenna Design and Simulation

9.2.1 High Impedance Antenna Design and Tuning

The antenna needs to be based on a predominantly-inductive FDA or a compact loop to achieve the desired highly-inductive input impedance. The FDA proposed in Chapter 5, despite being parametrically-tunable, requires a fabrication process which can resolve features smaller than 200 μm. For a tunable high-impedance FDA to be realized using commercial dispenser or screen printing, a novel design with a minimum feature size of at least 0.5 mm is needed. While the proposed antenna is realized using dispenser printing for rapid prototyping, the design is compatible with screen printing, which is more suited to mass production [309].

The proposed FDA geometry shown in Fig. 9.3 maintains a minimum feature size of 1 mm. Therefore, the antenna will be more resilient to fabrication imperfections such as non-uniform edges. The large dipole folds, W_1 and W_2, along with the thick shorting terminals B are parametrically-tunable to achieve an input impedance matching that of a capacitive discrete rectifier or an RFID IC (i.e. a CMOS rectifier). Additionally the ratio of L_1 to L_2, controlled using X is used to control the resonant of the antenna and will therefore have the biggest influence on the real antenna impedance. Compared to a conventional dipole antenna, the proposed antenna contains a closed current return loop between the rectifier's terminals, eliminating the need for an additional shunt inductor [296]. The inductive slot enables simpler input impedance tuning to match rectifiers based on different diodes and for varying power levels.

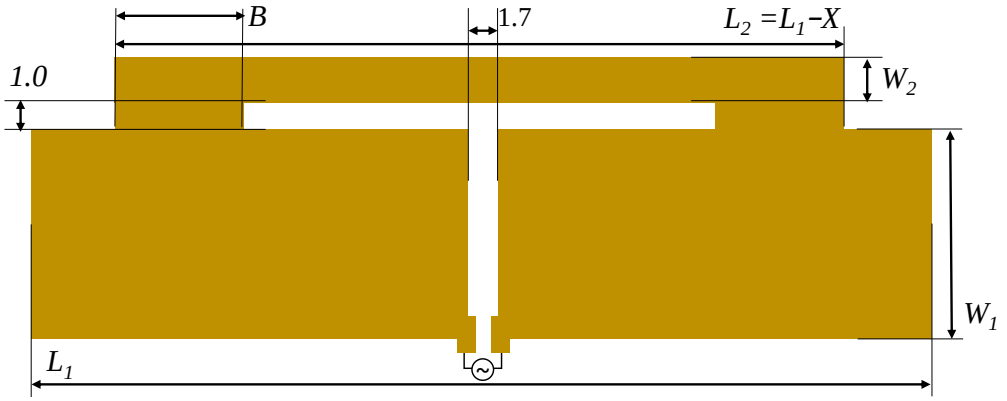

FIGURE 9.3: Layout and dimensions of the proposed high-impedance dispenser printed FDA.

The antenna has been simulated in CST Microwave Studio using a balanced feed to extract its impedance. The conductivity of the model has been adjusted based on the measurements reported in the next section to improve the simulation accuracy. As the antenna is designed for sub-1 GHz RFEH and WPT, the antenna needs to match the rectifier around 915 to 940 MHz, for it to be used for ISM-band WPT as well as GSM

900 ambient RFEH. Parametric studies of the antenna's impedance at 915 MHz have been performed to observe the variation based on scaling different antenna parameters. As explained in [300], increasing the width of the antenna's folds W_1 or the shorting strip W_2 would result in reducing the impedance of the antenna due to the increased fringing capacitance. Moreover the overall length of the antenna L_1, the length of the fold L_2 and the shorting folds width B can be adjusted to control the resonance frequency of the antenna, which would in turn have the maximum impact on the impedance at any given frequency. Fig. 9.4 shows the antenna's input impedance at 915 MHz for variable L_1, X, B, W_1, and W_2. The starting parameters, in mm, for each sweep are $L_1 = 70$, $X = 10$, $B = 10$, $W_1 = 15$, and $W_2 = 5$. For the desired input impedance of Z_{Antenna}=20+j280Ω at 930 MHz, the chosen parameter values (in mm) are $L_1 = 58$, $X = 2.5$, $B = 10$, $W_1 = 15$, and $W_2 = 5$. Meshing of the proposed antenna is investigated in the next subsection. Z_{Antenna} was selected based on the harmonic balance simulation of the rectifier, to maximize the PCE under −10 dBm.

9.2.2 Meshed Antenna Design

As the antenna incorporates a large metal plane, this will increase the printing time and consume more ink, increasing the cost of the antenna. Furthermore, the antenna cannot be integrated in a transparent system such as solar cell-integrated antennas or display antennas [349]. Meshing the conductor, by perforating the antenna using variable fill-factors, can be introduced without significantly altering the antenna's performance [350]. The mesh density or fill factor represents the ratio of the mesh lines to the grid-spacing. Fig. 9.5 shows the layout of the proposed solid antenna and for different mesh densities. The layout also shows the traces for a voltage doubler based on the SMS7630-079LF Schottky diode. The line width has been set to 0.3 mm, the smallest reproducible line using the Voltera V-One printer.

By reducing the mesh fill-factor, antennas of varying optical transparency can be realized. The theoretical optical transparency T_{Mesh} of a meshed antenna is defined

$$T_{\text{Mesh}} = (1 - \frac{W_t}{W_t + W_G})^2, \tag{9.1}$$

where W_t is the trace width and W_G is the size (length and width) of the gaps. This definition of an antenna's transparency is widely used and represents the ratio of metal-to-gaps [229, 349–353]. Therefore, the transparency of the antenna (mesh density) can also be regarded as the percentage of material reduction compared to a solid antenna. This is highly desirable for additive manufacturing to reduce the printing costs. After meshing, the printing time of the rectenna was reduced by over 80% to under 10 minutes for T_{Mesh}=70%, down from 55 minutes for the non-transparent antenna.

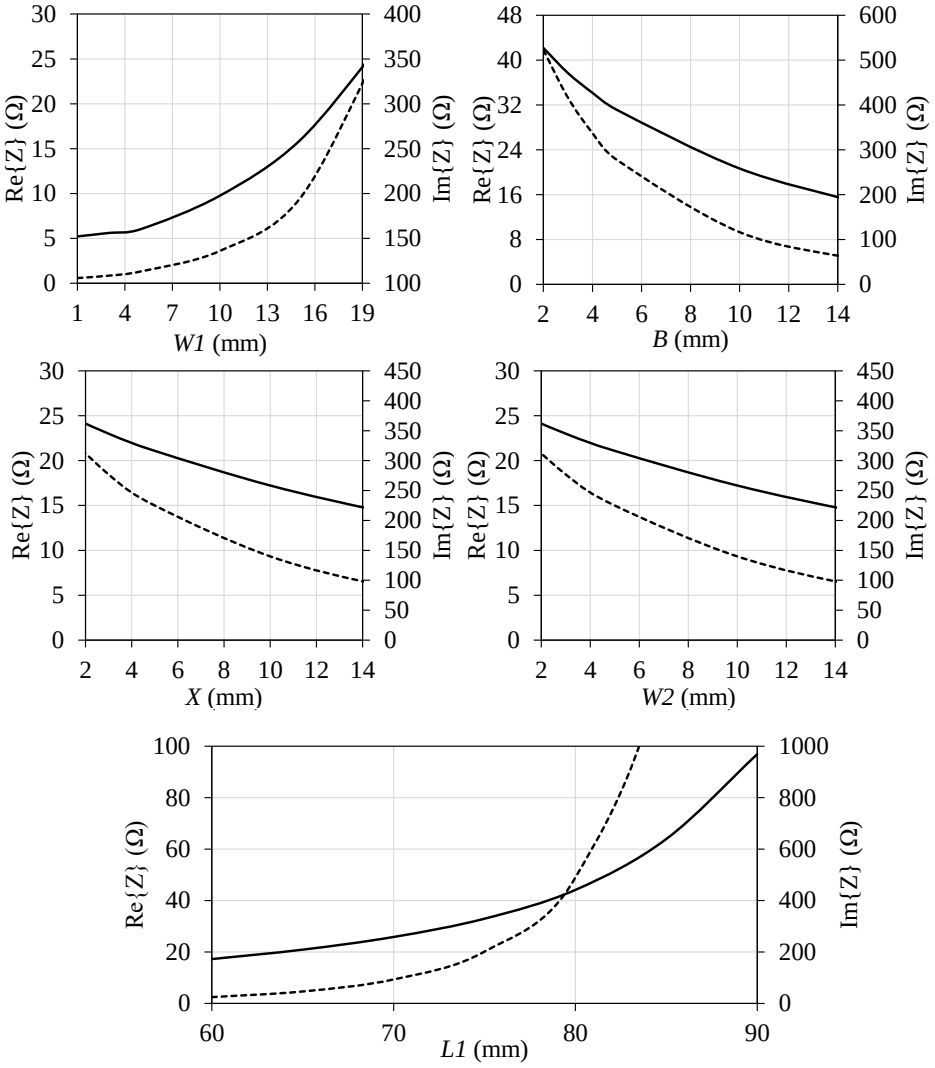

FIGURE 9.4: Real (dashed) and imaginary (solid) input impedance of the FDA as a function of the tuning parameters at 915 MHz; baseline parameters are $L = 70$, $X = 10$, $B = 10$, $W_1 = 15$, and $W_2 = 5$.

While the substrate used is Kapton, which is only optically-translucent rather than transparent, transparent variants of polyimide have been presented with similar dielectric properties to Kapton [354]. Kapton polyimide was used due to being commercially available widely from various vendors. In addition to transparent polyimide [354], optically-transparent flexible substrates can be used without altering the antenna's response. For example, the PET substrate used for a microstrip antenna array in [355] has similar dielectric properties (ϵ_r=3.25, tanδ=0.02 [355]) to the Kapton film used in this work. Thus, the proposed antenna's impedance and efficiency would not change if it was printed on PET. PDMS, a flexible but usually mm-thick substrate, has a tanδ=0.021 at 2.5 GHz [356]. Therefore, printing this antenna on PDMS will also not result in performance degradation.

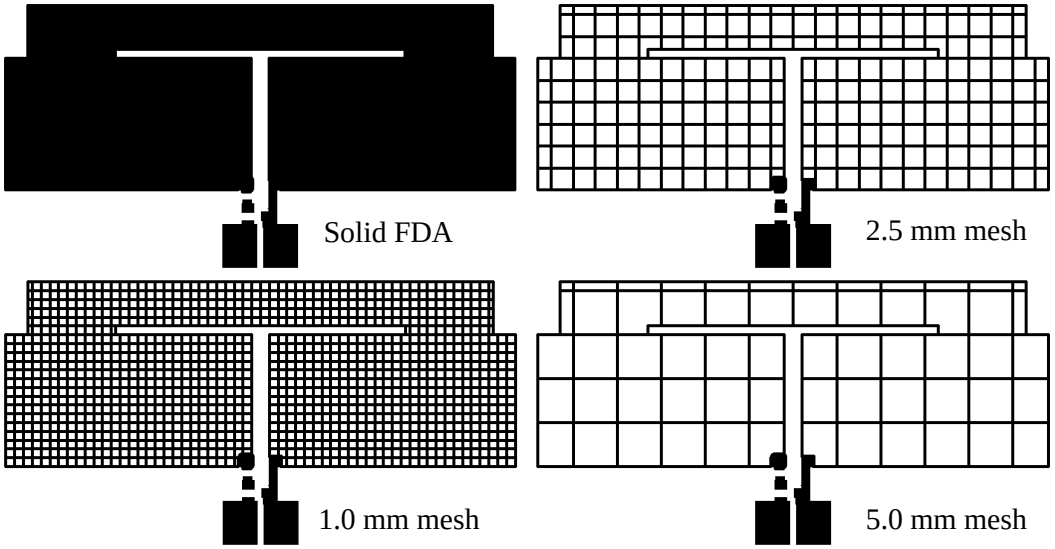

FIGURE 9.5: Layout of the FDA with different mesh spacing.

The antenna prototypes are shown in Fig. 9.6 during (a) and after (b) printing, and after curing (c). In Fig. 9.6-d and e, the rectenna/antenna are shown with highly-translucent traces. In Fig. 9.6-f, the antenna is shown while producing over 1.7 V DC output required to light the LED at varying distances, $0.1<d<1$ m, from a Powercast transmitter (3 W, 915 MHz) with various bending and crumpling radii, a video demonstration is included in the supplementary material of [341].

9.2.3 Antenna Radiation Properties

The proposed antenna, being a small dipole, is expected to have omnidirectional radiation properties. The radiation patterns of the antenna were simulated in CST Microwave Studio. Fig. 9.7 shows the normalized simulated patterns over the azimuth and elevation planes, where peak directivity of the antenna is 1.85 dBi. The radiation patterns were only analyzed numerically in CST due to the unavailability of an antenna measurement setup with three ports (i.e. a four-port VNA), to differentially excite the antenna under test in a balanced way. This is in line with recent implementations of complex-conjugate antennas for RFEH where the radiation patterns were presented based on numerical (CST) simulation [34, 83].

To investigate the impact of meshing on the antenna's performance, the gap width W_G was swept from 1 to 10 mm. It is expected that with a lower fill factor the antenna's (Ohmic) loss resistance will increase, which can reduce the radiation efficiency and gain. Fig. 9.8 shows the simulated radiation efficiency and gain as a function of W_G. Therefore, it is expected that antennas with a higher theoretical transparency will have a lower PCE.

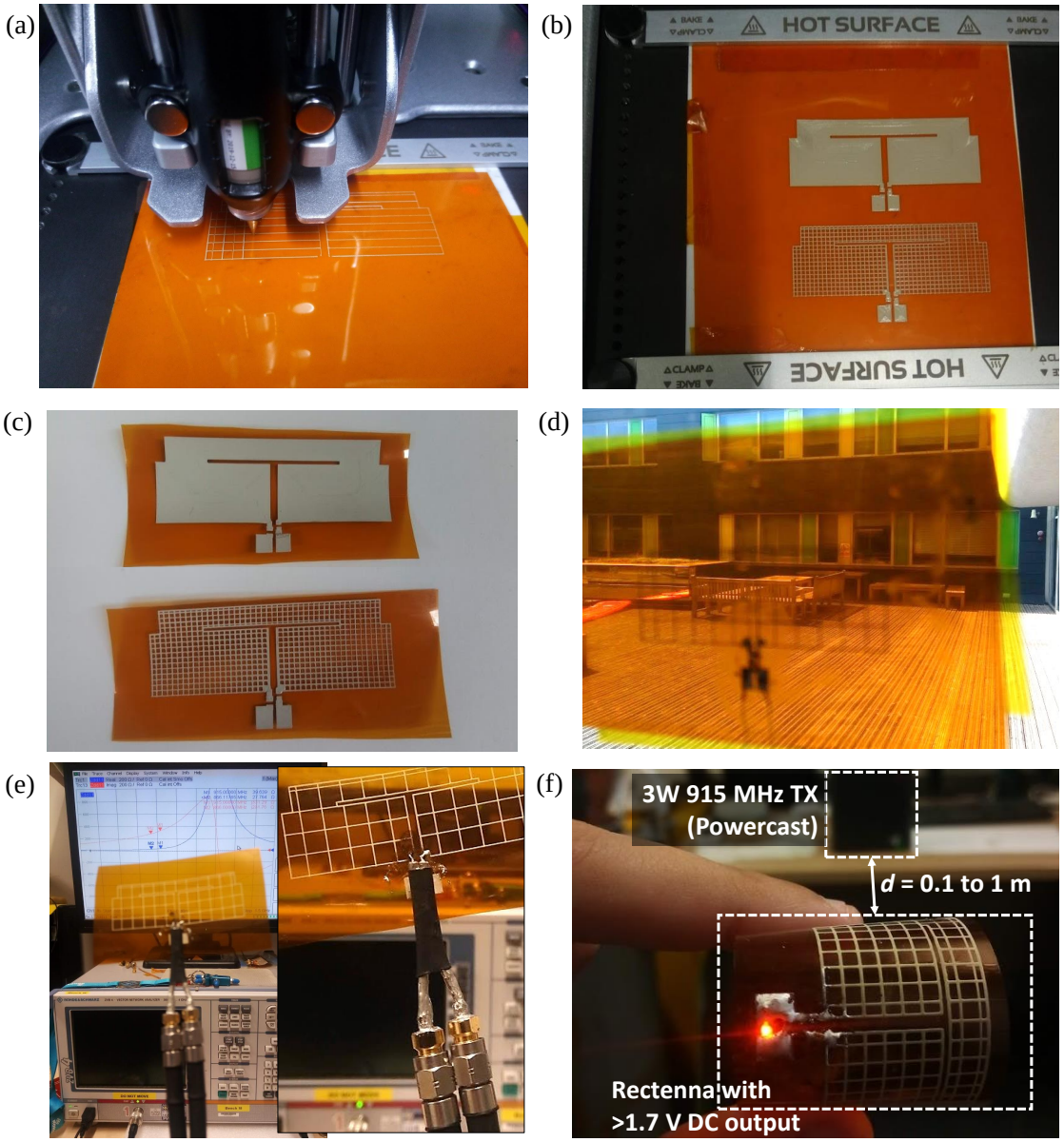

FIGURE 9.6: Dispenser-printed FDA prototypes photographs: (b) printed uncured ink on the polyimide substrate; (c) the cured solid and meshed FDAs; (d) demonstration of the assembled meshed rectenna's translucency; (e) differential impedance measurement with a coaxial jig and two-port VNA; (f) the assembled rectenna showing a >1.7 V DC output lighting an LED.

9.3 Antenna Measurements

9.3.1 Solid Antenna Measurements

A meshed FDA prototype, with 1 mm mesh spacing and 0.3 mm trace width has been fabricated to experimentally characterize its input impedance. The balanced Z_{in} of the FDA has been measured using a two-port VNA and a common-ground co-axial jig [307]. Fig. 9.6-e shows the balanced impedance measurement setup of the antenna.

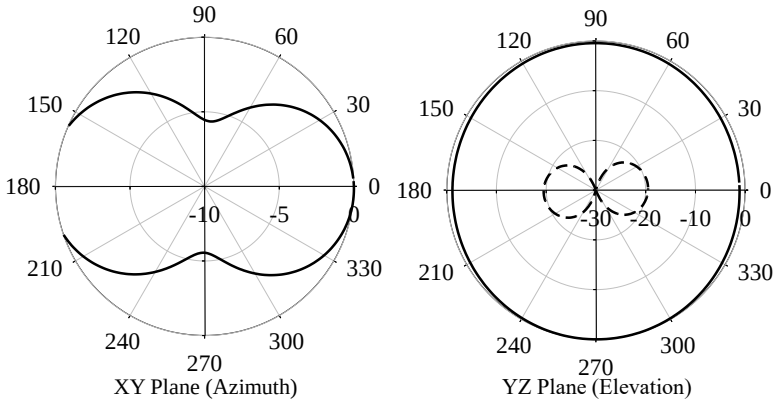

FIGURE 9.7: Simulated normalized radiation patterns of the proposed antenna: co-polarized (solid) and cross-polarized (dashed).

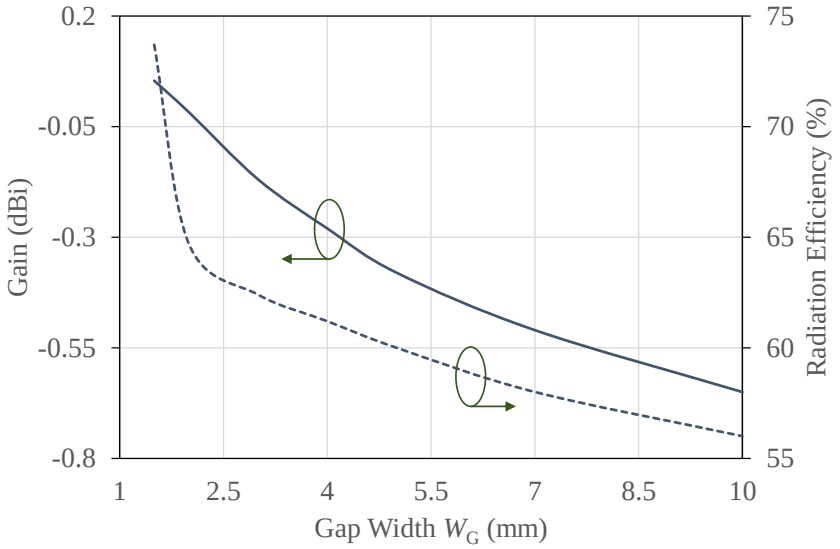

FIGURE 9.8: Simulated gain (solid) and radiation efficiency (dashed) of the antenna for varying W_G.

The feed point of the antenna resembles the position of the connection to the rectifier. Fig. 9.9 shows the simulated and measured Z_{in} up to 3 GHz. The frequency response of the fabricated antenna is observed to closely match the simulation model. However, around resonance, the fabricated antenna demonstrates lower imaginary and higher real impedance components compared to the simulation model. This indicates that the fabricated antenna has a lower quality factor compared to the model due to additional resistive losses. The loss-discrepancy can be attributed to the conductivity of the simulation model, and the surface roughness of the conductive ink, as the polyimide model utilized is material-accurate at the simulation frequency. Nevertheless, at the frequencies of interest, around 900 MHz, it is observed that the discrepancy in the imaginary impedance is less significant.

To achieve higher accuracy in the simulation model for optimizing the antenna, the surface resistance of the conductors in simulation has been varied to match the measured

antenna impedance. The closest match between the simulation and measurements was obtained using a conductivity of $2\times10^5\sigma$/m and a surface roughness of 10 μm, this translates to about 0.1 Ω/square sheet resistance at 900 MHz.

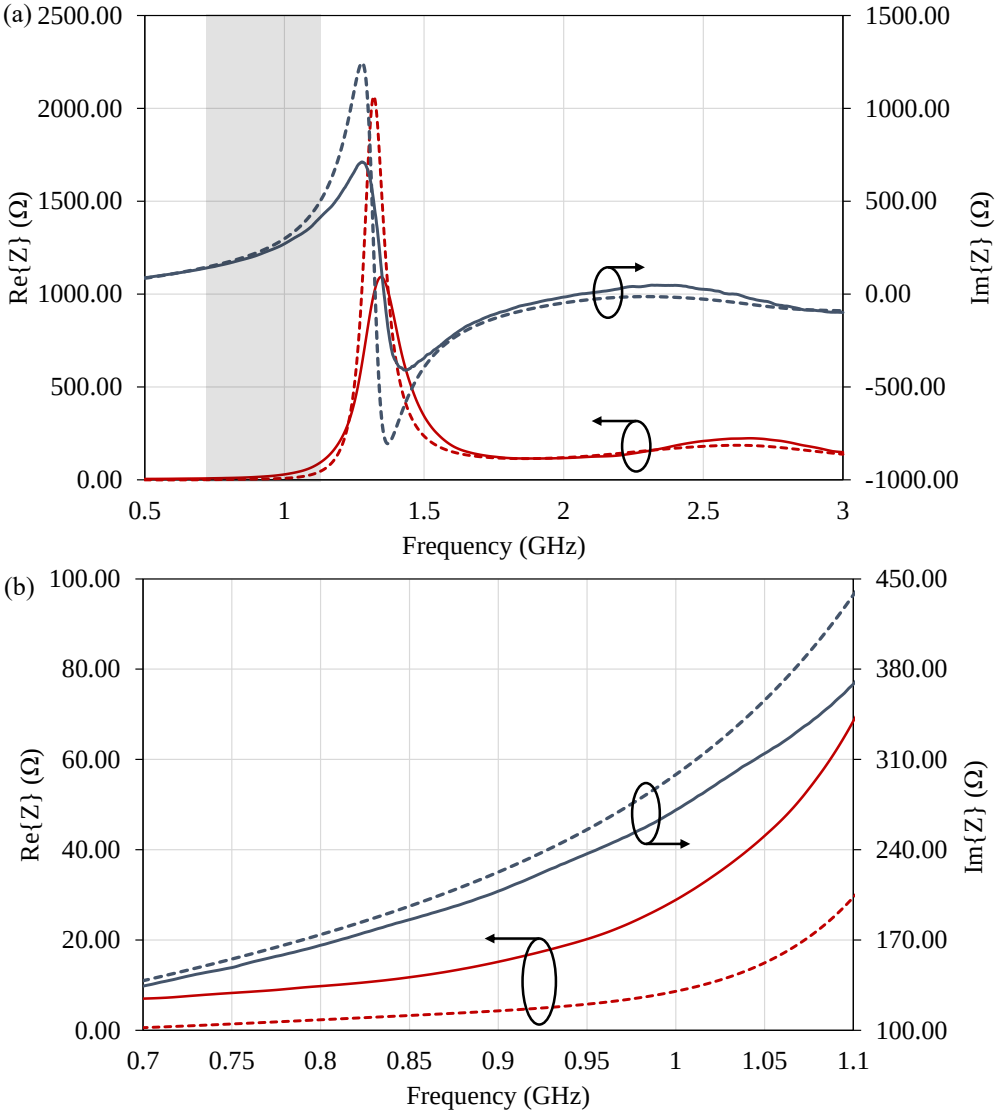

FIGURE 9.9: Simulated (dashed) and measured (solid) input impedance of the FDA with a 1 mm mesh spacing from 0.5 to 3 GHz (a) and around the 868/915 MHz ISM-bands (b).

9.3.2 Varying Transparency Input Impedance Measurements

The three meshed and the solid FDAs have been fabricated to experimentally quantify the impact of the mesh density on the antenna's Z_{in}. Through this process, the mesh density could be utilized as an additional tuning parameter of the FDA's impedance. The input impedance of the FDAs has been measured using the same balanced-feed coaxial jig. Fig. 9.10 shows the measured input impedance of the FDAs shown in Fig. 9.5. It is evident that the antenna's impedance is directly linked to the mesh density, where a

lower mesh density results in higher input impedance. However, for up to 2.5 mm mesh-spacing, the variation in the reactance is less than 10% compared to the solid antenna. Therefore, the antennas with a mesh gap equal to or smaller than 2.5 mm are used in the rectenna evaluation without further tuning. The effect of a higher real input impedance on the rectifier's PCE is minimal, as discussed in the next section.

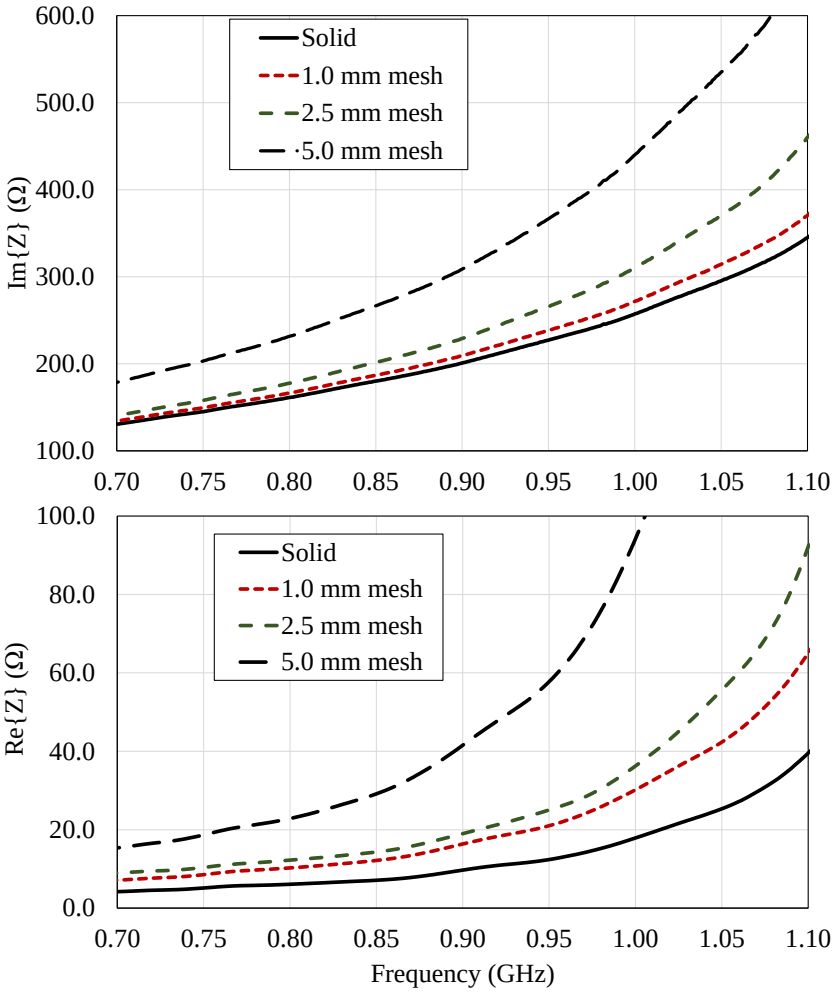

FIGURE 9.10: Measured real and imaginary input impedance of the proposed antenna based on varying mesh spacing (i.e. theoretical transparency) for the same dimensions.

9.4 Rectenna Measurements

9.4.1 Rectifier Design and Simulations

The rectifier is based on the voltage doubler designed in Chapter 5. The rectifier has been simulated using HB and An optimum input impedance of $Z_{\text{rect.}}$=20+j280 Ω has been extracted from harmonic balance simulation to achieve maximum PCE below −10 dBm. While the rectifier's input impedance is expected to vary with frequency, optimizing the impedance at power levels below −15 dBm results in maximizing the

PCE for sub-μW/cm^2 power densities. The rectifier is tuned for 930 MHz to be able to harvest ambient RF power from GSM signals as well as CW power at 915 MHz from a dedicated transmitter (e.g. Powercast/RFID reader).

Fig. 9.11 shows the rectifier's simulated PCE at 930 MHz for varying real antenna impedances, at different RF power levels. The solid lines represent the PCE calculated as $P_{\mathrm{DC}}/P_{\mathrm{RF}}$, inclusive of impedance mismatch losses. On the other hand, the dashed lines represent the maximum achievable PCE exclusive of mismatch, calculated as $P_{\mathrm{DC}}/P_{\mathrm{accpeted}}$. As observed in Fig.9.10, the real impedance of the antenna can vary significantly based on the mesh fill-factor (i.e. the transparency). Therefore, the rectifier's PCE has been simulated as a function of $\Re\{Z_{Ant}\}$. In Fig. 9.11, it can be seen that for up to 5 mm W_G, the PCE, inclusive of impedance mismatch, stays within 10% of the peak PCE of the rectifier.

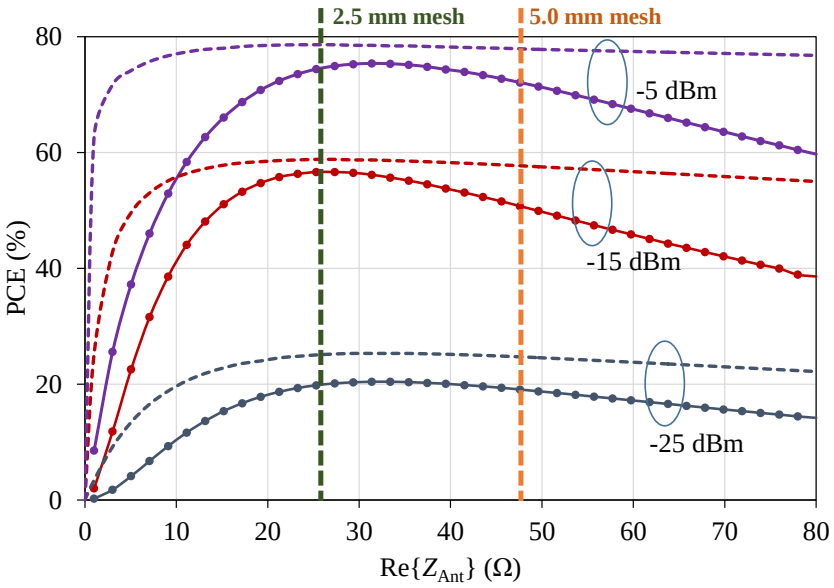

FIGURE 9.11: Simulated PCE of the rectifier including (solid) and excluding (dashed) mismatch, at 930 MHz with a 20 kΩ load, for varying $\Re\{Z_{Ant}\}$

9.4.2 Rectenna DC Measurements

To characterize the rectennas' DC output and PCE, a 10 dBi directional antenna with a CW input are used to wirelessly-power the rectenna with varying power densities S. The rectenna is placed at 1.1 m from the source, which satisfies the minimum Fraunhofer far-field distance of 0.88 m based on the transmitting antenna's length of 40 cm. Fig. 9.12 shows the schematic and photograph of the rectennas' test setup.

The PCE has been calculated using the available power density S and the power across the load Z_L using (3.9). As discussed in Section 3.1.1, (3.9) includes the rectification as well as impedance mismatch losses, between the antenna and the rectifier. By using the antenna's lossless directivity as G, in the effective area calculation (3.6), the antenna

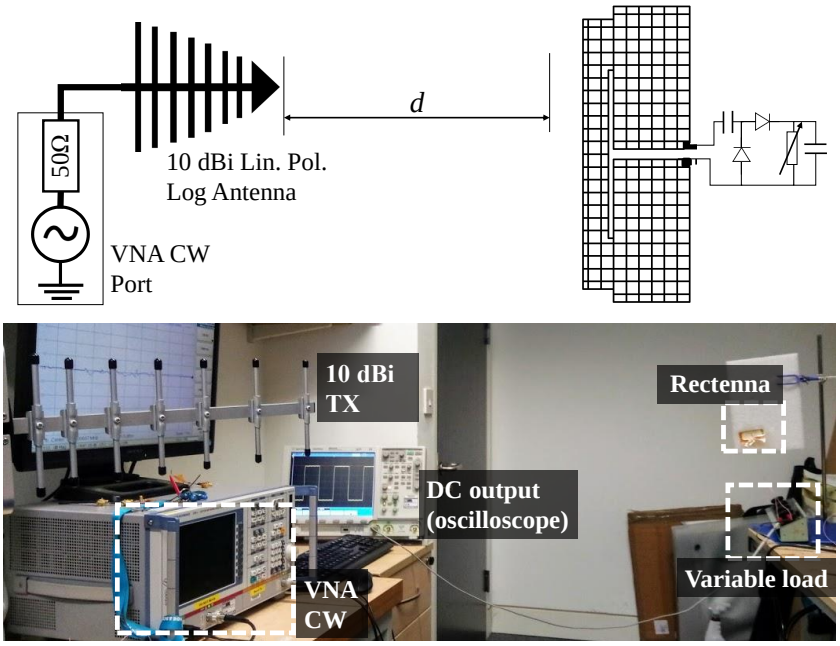

FIGURE 9.12: Wireless measurement setup of the meshed high-impedance rectenna using a directional transmitter.

losses are factored in the PCE which enables holistic evaluation of the rectenna. This prevents overestimation of the PCE due to any inaccuracies in the gain or radiation efficiency figures obtained from the CST antenna simulations, due to variations in the material properties.

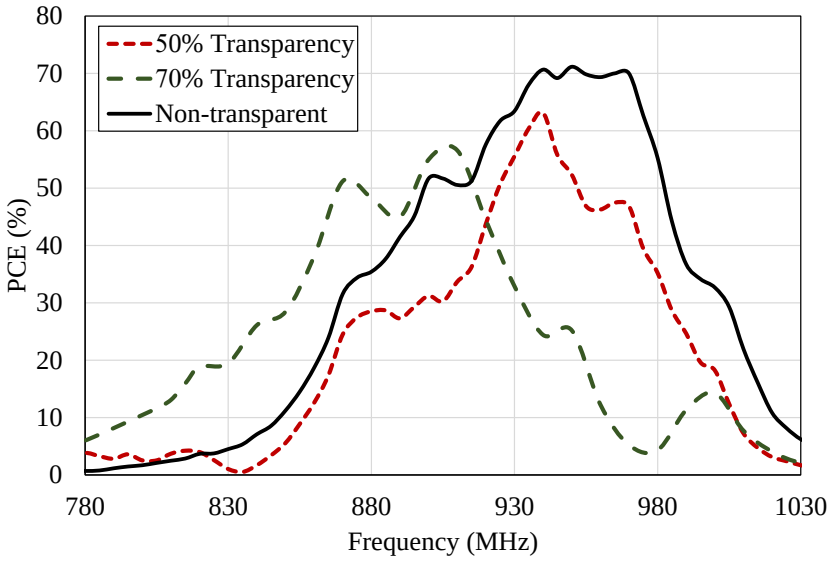

FIGURE 9.13: Measured PCE of the proposed non transparent, 50% and 77% transparent rectennas from S=0.88 μW/cm^2 for a 7 kΩ load at variable frequencies.

A frequency sweep was carried out for a fixed transmitted power (12 dBm−0.5 dB cable loss) corresponding to 0.88 μW/cm^2. Fig. 9.13 shows the rectennas' PCE across the sub-1 GHz license free 868/915 MHz and GSM900 bands. It can be seen that with

increasing transparency the rectennas' resonance shifts to a lower frequency. This is attributed to the increasing $\Re\{Z_{Ant}\}$ and $\Im\{Z_{Ant}\}$ with reducing fill-factor previously measured in Fig. 9.10. The results in Fig. 9.13 were measured across a 7 kΩ load.

A resistive load sweep was carried out to identify the maximum power transfer point of the rectennas. Fig. 9.14 shows the simulated and measured PCE as a function of the load impedance. It is observed that the antennas' varying transparency does not affect the optimal load despite having different $\Re\{Z_{Ant.}\}$. The rectennas' optimal measured load of 7 kΩ is suitable for integration with commercial and custom boost converters such as [39] and [11], respectively.

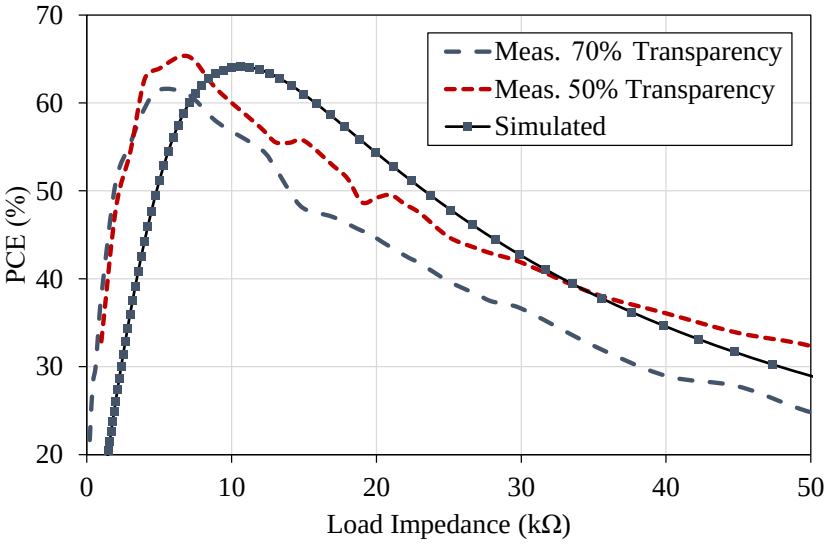

FIGURE 9.14: Simulated rectifier PCE for a varying load and rectenna measurements for 77% and 50%-transparency from S=1 μW/cm^2.

Three rectennas were characterized under varying S: a non-transparent solid rectenna, a 70%-transparent (2.5 mm mesh-spacing) rectenna, and a 50%-transparent (1 mm mesh-spacing) rectenna. To demonstrate the rectenna's high PCE at low power levels, the CW input was varied from −11 to 15.5 dBm, to present the rectenna with $0.005<S<2$ μW/cm^2. Fig. 9.15 and 9.16 show the PCE and the DC voltage output of the rectennas.

As observed in Fig. 9.15, the solid rectenna has an improved PCE and sensitivity, achieving PCE=50% at approximately 50% lower power than its transparent counterpart. The PCE of the 70%-transparent rectenna reaches 60% for S=0.66 μW/cm^2. Additionally, the DC voltage output of all three prototypes of varying transparency exceeds 325 mV from S=0.25 μW/cm^2. This represents over 2× sensitivity improvement over SoA compact rectennas designed for ultra-low power transmission [39], where a minimum of S=0.62 μW/cm^2 was required to achieve the 330 mV required for starting-up a commercial DC-DC boost converter.

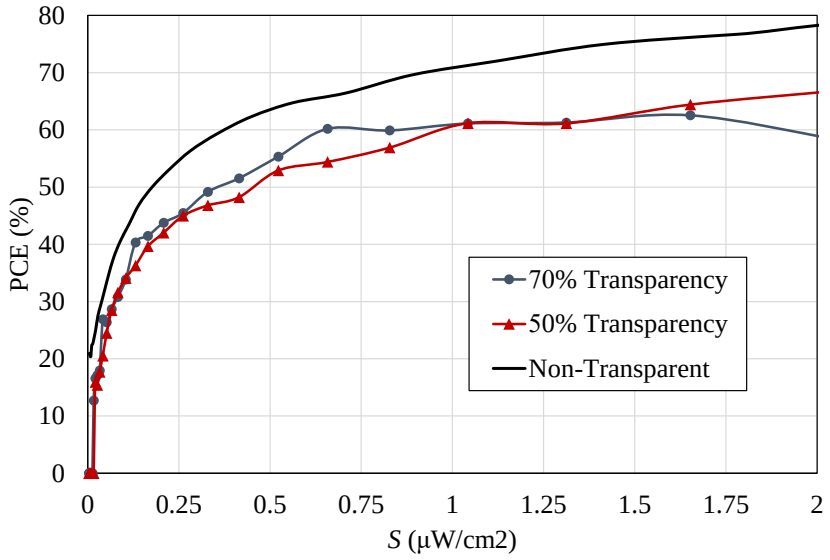

FIGURE 9.15: Measured PCE of the proposed non transparent, 50% and 70% transparent rectennas from an incident plane wave S, for a 7 kΩ load.

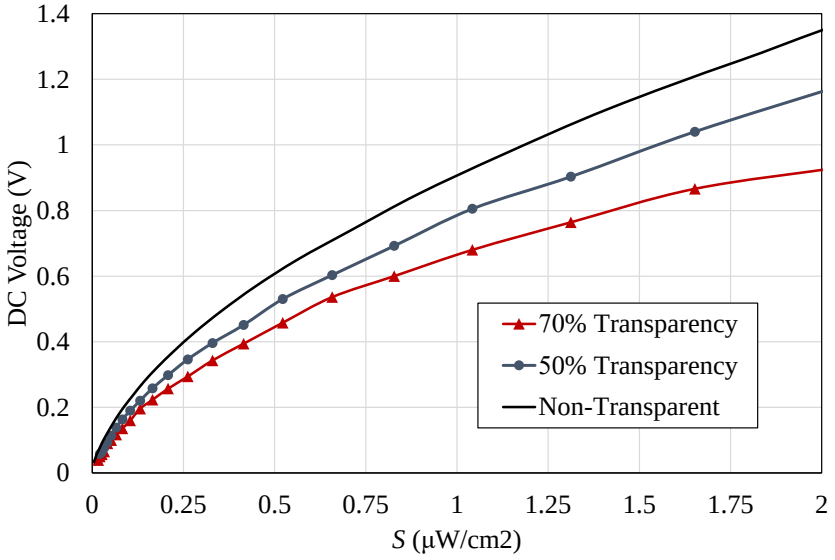

FIGURE 9.16: Measured DC voltage of the non-transparent, 50%-, and 70%-transparent rectennas from an incident plane wave S, across a 7 kΩ load.

9.4.3 Rectenna Radiation Efficiency Calculation

From the calculated PCE in Fig. 9.15, it is possible to estimate the antennas' radiation efficiency. At −15 dBm, the rectifier has a simulated PCE of 57% with the optimum source impedance of 20+j280 Ω. Using the non-transparent antenna's simulated directivity of 1.6, −15 dBm can be received from a power density S=0.18 μW/cm^2. At S=0.18 μW/cm^2, the proposed rectennas achieve 50%, 42%, and 43%, PCE, for 0%, 50% and 70% transparency, respectively. Therefore, the radiation efficiency of the antennas can be estimated, relative to the PCE achievable by a loss-less source. The calculated

radiation efficiency is 88%, 74%, 75% for the non-transparent, 50%-transparent and 70%-transparent antennas.

The drop in the radiation efficiency between the non-transparent and transparent rectennas correlates with the simulated results in Fig. 9.8, and with the previously reported observations in [229]. Between the 50%- and 70%-transparent rectennas, the variation in the calculated radiation efficiency could be attributed to fabrication tolerances and uncertainties in the test setup, resulting in minimal impact of the antenna's transparency on its effective PCE. It was previously noted that wireless testing of rectennas can incur ±1 dB error in the incident power [11].

9.4.4 Evaluation and comparison with Previous Work

The proposed rectenna is compared, in Table 9.1, to SoA printed, flexible, or textile-based RF energy harvesters, as well as a complex 3D transparent rectenna. It can be observed that despite the overall low complexity of the design, and its implementation using silver inks with relatively low conductivity on lossy ($\tan\delta$=0.02) substrate, the proposed rectenna achieves the highest PCE for S<1 μW/cm^2, compared to rectennas operating at similar frequencies such as [43, 178] and the rectenna proposed in Chapter 4, owing to the precise antenna co-design with the rectifier achieving minimal reflection and a high voltage input at the rectifier's terminal. It can also be seen that despite being electrically smaller than other implementations (at similar and higher frequencies), the proposed rectenna achieves a surpassing DC voltage showing improved RFEH performance. Finally, the proposed rectenna is the only transparent 2D rectenna built entirely using low-cost materials on a flexible substrate while maintaining a high PCE from sub-μW/cm^2 power densities.

Compared to the high-efficiency and sensitivity textile rectenna in Chapter 4, the miniaturized CPW rectenna proposed in this chapter achieves over 20% higher peak PCE, at the same S, due to the improved impedance matching and due to avoiding lumped components. While [229] achieves a very high DC voltage from ultra-low power densities, this is only achieved when the output of eight antenna elements, each having an individual rectifier, is combined; the output from a single port does not exceed 0.5 V for S as high as 5.5 μW/cm^2. In addition, the size of the proposed rectenna is more compact, when compared to the wavelength, than the individual patch elements in [229]. This would results in a higher DC output from a large-area rectenna array implementation based on the proposed antenna. The complexity of the proposed rectenna is the lowest compared to other rectennas in Table 9.1 due to:

1. the ability to be directly printed on any conformable thin and light substrate;
2. not utilizing a standalone matching network;

3. having the smallest electrical size (area and volume) with the ability to be meshed for optical transparency and material-reduction.

Other conformable rectennas on low-cost substrates (textiles and paper) such as [43,178] utilize lumped components, namely inductors, for impedance matching. Such inductors not only occupy additional space but also significantly increase the cost of the rectenna in mass production, compared to passive low-cost printed antenna traces. Finally, the proposed rectenna (70%-transparent and non-transparent) achieves the highest PCE compared to the rectennas in Table 9.1, showing its suitability for low power RFEH applications.

In the context of flexible, wearable, and printed rectennas, future implementations can be realized using stretchable conductors [357]. In a recent implementation, dipole antennas were found to maintain their bandwidth for up to 15% strain. While the radiation patterns of the antenna may be distorted, with a higher cross-polarized component in the same frequency band due to the size increase. However, changes in the polarization are less significant, as discussed in Chapter 4.1.2. Nevertheless, the flexible conductive ink and the polymer substrate utilized in this work are not stretchable and will undergo irreversible damage should the rectenna be stretched beyond the printed conductor's tensile strength.

TABLE 9.1: Comparison of the proposed rectenna with flexible, transparent and printed harvesters.

Study	**Conductor**	**Substrate**	**Optical transparency**	**Frequency (GHz)**	**Peak PCE at S**	**PCE at S=0.5 μW/cm^2 (%)**	**DC V at S=1 μW/cm^2**	**Electrical size (λ_0^3)**	**Complexity**
This work	**Silver ink, $2\times10^5\sigma$/m**	**Kapton, tanδ=0.02**	**NTA**	0.94	**78.5% at S=2**	**64.8%**	**0.9**	**0.212 × 0.212 × 0.0003**	**Very simple (2D)**
This work	**Silver ink, $2\times10^5\sigma$/m**	**Kapton, tanδ=0.02**	**70%**	0.92	**62.5% at S=1.7**	**55%**	**0.65**	**0.212 × 0.212 × 0.0003**	**Very simple (2D)**
TAP'13 [178]	Conductive fabric	pile+jeans, tanδ_1=0.009, tanδ_2=0.023	NTA	0.876	50%	NR	NR, <0.5 V*	0.702 × 0.556 × 0.0088	Simple (2D)
TMTT'18 [43]	Copper taper	paper (tanδ=0.05)	NTA	0.9	57% at S=6	36%‡	0.25‡	0.337 × 0.337 × 0.028	Simple (2D)
TMTT'19 [229]	μmesh conductor	Glass + RO5880	92.4%	2.45	≈49%‡ at S=5	45%‡	1.5‡	1.23 × 1.23 × 0.3†	Complex (3D)
TAP'20 [340]	Silver ink	LCP	NTA	2.45	40% at 0 dBm	NR	NR	0.37 × 0.205 × 0.0015	Simple (2D)
TAP'20 [289] (Chapter 4)	Conductive fabric	Felt, tanδ=0.02	NTA	0.83	53%	53%	0.67	0.33 × 0.33 × 0.003	Simple (2D)

NTA: non-transparent antenna; †thickness estimated from photograph based on length of SMA joints; *estimated from the output at S=3 μW/cm^2; ‡estimated from the graphs

9.5 Indoor Up-Link Ambient Energy Harvesting

As reviewed in Chapter 2.3, the GSM 900 band typically has the highest ambient PSD. RFEH from the up-link (i.e. from a phone) has previously been investigated showing up to 17× higher mean RF PSD in busy indoor environments, such as a train, compared to down-link [44]. By observing the transient DC output of the rectenna in time-domain, for a variety of real cellular emissions, it is possible to assess the validity of RFEH from the up-link. In addition, by calculating the transient harvested DC power, it is possible to predict and model the behavior of low-power intermittent systems such as [342], when powered using rectennas.

The proposed rectenna, with a 70% transparency, was used to harvest the ambient radiation from a smartphone in an office environment. The down-link PSD was measured, using a spectrum analyzer and a simple dipole, to be under −40 dBm in the room where the test was carried. Hence, in this environment, the down-link RF power level is too low to be harvested using any of the rectifiers reported in literature [17]. The phone was placed at 7 cm from the rectenna adhered to a wooden desk demonstrating a potential use-case in an office. The DC output of the rectenna was measured using an oscilloscope (×10 probe) across a 20 kΩ load. The inset in Fig. 9.17-a shows the indoor ambient RFEH test setup.

The measured DC output of the rectenna was recorded for various phone activities. First of all, the DC output was measured when the phone was idle, before and after receiving a text message (SMS), shown in Fig. 9.17-a. The peak DC power generated from the idle phone is 1.2 μW with 155 mV. While such output can supply a commercial power management circuit such as the Analog ADP5090 (minimum operational voltage=80 mV) with sufficient DC voltage and current, the output is highly varying and comes in <50 ms bursts. However, when the idle phone is receiving an SMS, the DC power harvested peaks at 3.8 μW with >250 mV over a longer stable 4 s period. This represents a 15 μJ DC energy yield which can enable intermittent computation on a commercial low-power micro-controller, while the power is being generated [342].

The second case considered is voice-calls. Before the phone rings, the "idle" DC power harvested increases to 4.5 μW (300 mV), in 30 ms periods. While ringing, the DC output stabilizes at 12.5 μW (500 mV) for the entire duration, as shown in Fig. 9.17-b. To demonstrate the variations that could arise from movements of the phone, the phone was moved in the 20×20×15 cm space surrounding the rectenna. The phone was also rotated by 90° while moving to demonstrate potential polarization misalignment between the phone and the rectenna. Fig. 9.17-b, from 16 s, shows the effects of moving the phone on the DC output. The sharp drop observed around 17 s is caused by the phone's linear polarization being cross-polarized with respect to the rectenna, resulting in a very low polarized gain. When aligned, it is shown that the variations in distance can reduce the DC voltage by around 50%. The incoming call is declined at 49 s showing a drop in

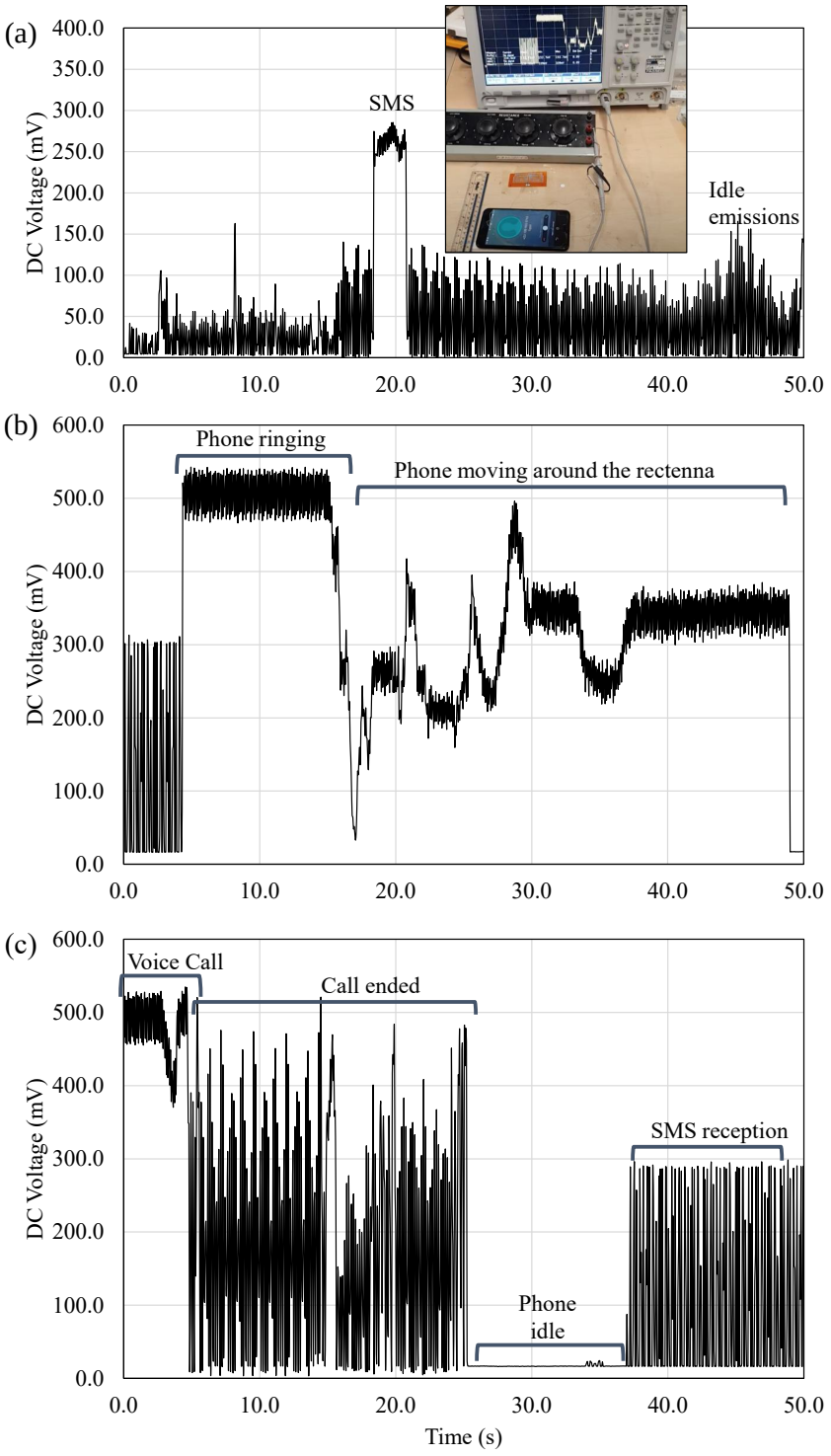

FIGURE 9.17: The rectenna's DC output when harvesting ambient RF power from a GSM-connected phone: (a) idle phone emissions and short message reception, inset shows the measurement setup; (b) voice call while moving the phone around the rectenna; (c) end of a voice call.

the DC output to <20 mV. Video 2 in the supplementary multi-media file shows the movement of the phone while measuring the output in Fig. 9.17-b. The same process is repeated for a voice-call which is accepted. It can be seen in Fig. 9.17-c that as soon as

the call is accepted, at 4.5 s, the stable RF transmission is interrupted and the harvested voltage shows up in 30 ms bursts instead.

A previous demonstration of a flexible rectenna harvesting from a ringing phone at GSM frequency was reported in [43]. The output of the paper rectenna in [43] (previously compared in Table 9.1), when put in contact (<1 cm clearance) with the phone, was 360 mV. The proposed rectenna on the other hand has a 500 mV output at over 7 cm from the phone, and 300-500 mV DC output with the phone moving up to 20 cm away from the rectenna. This is due to the improved voltage sensitivity at lower power levels, as well as improved PCE, as characterized with a power-calibrated CW source in the previous section.

9.6 Summary and Conclusions

In this chapter, a direct-write high impedance printed antenna is proposed for RFEH. The antenna's geometry, designed with >1 mm features to accommodate all low-cost printing processes, can be tuned to match rectifiers' Z_{in}. The proposed antenna has been meshed using various fill factors to demonstrate the feasibility of optically-transparent RFEH. The rectenna achieves a state-of-art PCE of 70% and 60%, for the non-transparent and 70%-transparent rectennas, respectively, for power densities below 1 μW/cm^2. The key findings can be summarized as:

- Despite its miniaturization, a printed antenna can be designed with a scalable Z_{in} using only low-resolution (>1 mm) features, for matching network-free rectennas.
- Meshed antennas, enabling optical transparency and reducing the time and cost of additive manufacturing, can be utilized in rectennas surpassing SoA PCEs, while using up to 70% less conductors.
- Owing to the sub-μW/cm^2 sensitivity, the proposed 70%-transparent rectenna can harvest over 330 mV across an optimal load, from a mobile phone with various positions and alignments, which can power various low-power sensor nodes reported in literature.

Chapter 10

Conclusion

RFEH and WPT are of increasing relevance to the exponentially growing IoT and IoE markets. Rectennas, scalable to different RF power levels and frequency bands, are the key component in an RFEH or WPT system that determines the system's performance and can significantly affect its end-to-end efficiency. The ability to realize rectennas using low-cost, flexible and printed materials has been demonstrated showing that material-induced losses can be overcome through antenna design and impedance matching techniques. This has been demonstrated using different architectures and for multiple fabrication methods up to mmWave bands. The key findings and contributions in this thesis, along with a critical reflection on the work carried, are summarized, suggested future work based on the findings is also discussed.

10.1 Key Findings

Rectennas have been demonstrated with SoA performance using lossy materials based on both novel and conventional antenna designs. When implementing the rectifier, and subsequently other microwave circuits on textiles or lossy materials, lumped components can enable SoA efficiencies and optimal matching, when combined with careful layout design, taking parasitics into account. The wire-type antenna, despite being prone to detuning in proximity with human tissue, was found to be a suitable topology for wearable RFEH, enabling more compact harvesters than aperture antennas and a high PCE for sub-μW/cm^2 RFEH. Furthermore, scalable impedance matching can be integrated within the antenna overcoming the transmission lines lumped component losses. Finally, despite their omnipresence in EH systems, DC power management circuits can be omitted in S>1 μW/cm^2 UHF RFEH, improving the system's end-to-end efficiency and reducing its complexity.

The challenge of efficient SWIPT can be tackled with an antenna-based solution, enabled by antenna-rectifier co-design. While complex transceiver topologies with switching

mechanisms are typically studied for SWIPT, a textile antenna with a high port isolation and small form-factor demonstrated SoA RFEH performance with uncompromised off-body communications performance, bringing antenna-based solutions closer to SWIPT. Antenna-rectifier co-design is not limited to fine-featured antennas with high fabrication accuracy, and can be implemented using additive manufacturing, it can also leverage emerging antenna design techniques such as meshed antennas with a minimal impact on the PCE.

Despite the consensus that mmWave bands equal higher losses, compact systems as well as large-area rectennas can benefit from mmWave EH. Designing antennas specifically to overcome the dielectric losses at mmWave bands enables high radiation efficiency and a wide bandwidth, enabling a mmWave-powered IoT. Nevertheless, the practical limitations of GaAs diodes, the packaging parasitics, and the challenges associated with designing and testing a mmWave rectenna still hinder progress in mmWave EH research and development, requiring both circuit and system-level optimizations to make mmWave rectennas more pervasive.

10.2 Summary of Contributions

Several component and system-level contributions to antenna and rectenna design for RFEH and WPT were presented in this thesis. The key contributions of this work are as follows:

- The highest reported PCE of sub-1 GHz rectennas - By identifying the loss sources in lumped and distributed matching elements, two rectennas achieving over 40% PCE at -20 dBm were proposed with and without a matching network. Demonstrated in a low-profile omnidirectional and dual-polarized rectenna, the all-textile rectenna achieves over 45% PCE from S<0.5 μW/cm^2, in presence and absence of the human body, showing the suitability of wire-type antennas for wearable RFEH.
- SWIPT enabled by antenna-rectifier co-design - Achieving over 25 dB port isolation, a two-port dual-band dual-mode textile antenna/rectenna was proposed for SWIPT. Despite occupying an area under $0.05\lambda_0^2$, the rectenna achieves a 62% peak PCE at S=0.8 μW/cm^2. The off-body communications antenna achieves 66% and 63% radiation efficiency with and without the rectifier, respectively, showing minimal influence of the rectifier on communications.
- E-textile rectenna and energy storage integration - a CPW e-textile rectenna was proposed for integration with a TSC, and studied in time-domain using RF and DC measurements. The end-to-end charging efficiency of the TSC surpasses all reported rectennas integrated with capacitors and batteries. With a high PCE in

presence and absence of the body, RFEH is the most efficient method of charging wearables from μW/cm^2 power densities.

- Scalable antenna design for additively manufactured rectennas - a compact dipole antenna with low-resolution features was proposed for printed electronics. The scalable impedance of the antenna enables it to match the proposed rectifier, achieving over 70% PCE for S<1 μW/cm^2. Meshed rectennas, without a matching network, were investigated for the first time showing less than 14% reduction in the PCE while using 70% less materials and maintaining optical translucency.

- Broadband mmWave rectenna and high-η antennas on lossy substrates - a textile-based antenna was proposed improving the radiation efficiency based on radiator miniaturization for reducing the dielectric losses. For the first time, a mmWave rectenna was demonstrated on textiles and achieving a 1.3 V output from 12 dBm, from 20 to 26.5 GHz, with a higher PCE than reported >20 GHz rectennas on lossy substrates, representing the first broadband mmWave rectenna in the K-band.

- Review of rectenna topologies and mmWave EH - A quantitative and qualitative classification of reported rectennas based on their impedance matching, directivity, and polarization. A comprehensive review of mmWave rectennas was also presented and the outstanding challenges in integrating CMOS rectifiers with low-cost antennas were discussed.

10.3 Critical Evaluation and Suggested Extensions

As discussed in Sections 10.1 and 10.2, this thesis has presented several contributions enabling low-power and unobtrusive RFEH for IoT applications. In this section, the results achieved in this work are reviewed from a system perspective, and critically evaluated based on their applicability to real-world RFEH usecases, in addition to presenting the suggested extensions prior to the adoption of the proposed technology in real-world applications.

Throughout this work, rectennas have been optimized for maximum PCE from a low power density, mostly agnostic of the deployment environment, including for example, the channel. While antenna properties such as omnidirectionality and dual-polarization harvesting capability have been proposed, for increasing the rectenna's applicability to arbitrarily incident radiation, new antenna designs and metamaterial-antenna co-designs can be investigated specifically for the "worst-case" scenario, that is for instance body shadowing in N-LOS RFEH. Moreover, while the formulation of WPT as a random problem was presented in Appendix A, a suggested extension is an experimental study investigating the total power harvested by a mobile rectennas.

While mmWave EH was investigated showing the potential for improved performance over sub-6 GHz bands, a key future study is the large-area implementation of the mmWave rectenna array with DC combining. Such work is essential to identify future challenges in rectification, in addition to power combining and management, and to demonstrate the mmWave rectenna implementations can indeed achieve the projected end-to-end efficiency improvement over sub-6 GHz bands.

Ambient RFEH, its feasibility based on SoA rectennas, and its implications on a wireless network represent a key ongoing research challenge, partially addressed in this work. For instance, the rectenna proposed in Chapter 9 was demonstrated harvesting from the up-link, and the rectenna proposed in Chapter 5 was reviewed in [40] as one of the potential enablers of future RFEH based on a 2020/2021 ambient PSD survey. Nevertheless, the DC power output, especially after DC-to-DC step-up conversion needs to be characterized over prolonged time periods in a real ambient RFEH environment. More importantly, the impact of ambient RFEH on the coverage of cellular networks needs to be quantified and studied experimentally, to show that shadowing is not a major concern should ambient RFEH be adopted on a large scale.

Wearable and IoE rectennas need to be resilient both electrically, through immunity to detuning, and mechanically, through immunity to failure or degradation upon repetitive bending, stretching, or other external influences. For example, the robustness of the proposed rectennas has been investigated in terms of immunity to bending and to detuning in human proximity has been investigated in Chapter 4. However, the antennas in this work have been designed with the desired RF performance as the first objective, with the mechanical robustness achieved through post-fabrication encapsulation. An extensive study is however required on wearable and e-textile antenna design for reliability, where the antennas are not only designed to achieve the desired input impedance and radiation properties, but also to achieve a high mechanical reliability based on an improved geometry, which can withstand bending, stretching, and potentially metal cracking and fatigue without altering its electrical response.

10.4 Future Research Directions

In this thesis, novel contributions to rectenna design on textiles and flexible substrates were presented, in addition to contributions to antenna design for low-cost dielectrics and conductors. Suggestions for future extensions based on the findings in this work are outlined in this section.

10.4.1 Rectennas for WPT and RFEH

This work has demonstrated the potential of rectennas being a reliable power source for e-textiles. Future work includes integration of the developed e-textile energy conversion devices in complete systems demonstrating sensing and wireless communication functionality. One way to achieve this will be through self-powered textile-based transponders, utilizing a high-efficiency rectenna to power an RFID-compliant receiver and a low-power micro-controller. The same antenna can then be used for backscattered communications for an energy-neutral computational RFID sensor node, or for active transmission based on a high-isolation SWIPT antenna.

In this work, a SWIPT-specific antenna design was proposed based on port-isolation and studied under CW excitation. Future investigations of SWIPT could leverage the work done on power-optimized waveforms and RFEH-specific modulation techniques can be designed with multi-port SWIPT antennas in mind. Future work on SWIPT could include rectennas incorporated within antenna arrays, full-duplex SWIPT antennas/rectennas, and broadband SWIPT antennas with polarization diversity. For instance, re-configurable polarization transmitters can be used to selectively power certain rectennas or sensor nodes, based on full-duplex multi-port SWIPT rectennas. Outside antennas research, the extensive work done at system and network level could benefit from the proposed dual-port single and multi-band antennas, where the performance achieved by multiple antenna elements can be combined in a single structure, reducing the complexity of previous SWIPT architectures. Waveform design for SWIPT, based on the proposed rectennas, can lead to system-level improvements in the performance of wirelessly-powered networks.

The ability to design rectennas for efficient power conversion below -15 dBm, demonstrated in chapters 4 and 5, is well-suited for ambient RFEH, but is still constrained by the losses in commercially-available diodes. The integration of the proposed antenna-rectifier co-design techniques with novel highly-sensitive CMOS rectifiers can enable ambient RFEH in more locations and applications. In addition, owing to the large-scale integration of devices in CMOS, the cost of RF-powered systems can be significantly reduced to that of an RFID tag by eliminating all off-chip components, and integrating the CMOS rectifier with a co-designed low-cost rectenna. Moreover, the emergence of sub-threshold computing and low-voltage/power transceivers may allow certain applications to sustain operation using the freely available RF power. Moreover, the continuously-reducing power budget of duty-cycled computing could enable nodes to sustain operation using intermittent power bursts while harvesting from nearby devices such as mobile phones. As highlighted in the evaluation in Section 10.3, the impact of ambient RFEH on cellular networks needs to be clarified.

Beyond 5G, mmWave bands are approaching wide-scale commercial deployment for high-speed communications. The ambient power available in urban micro-cells may enable rectennas to yield enough DC power for ultra low-power compact devices. The textile-based broadband mmWave rectenna demonstrated in Chapter 7 shows that the low-cost fabrication methods and lossy substrates do not have a significant detrimental impact on the rectenna's performance, given careful rectifier design. Therefore, e-textiles can benefit from mmWave WPT using large-area rectenna arrays due to the reduced antenna size required to achieve a high gain and radiation efficiency. Furthermore, future regulations for WPT at mmWave bands may allow mmWave-powered networks using dedicated WPT transmitters, which have been numerically shown to have an improved efficiency over sub-6 GHz RFEH networks. As discussed in the author's review [12], integration of low-cost antenna designs with CMOS mmWave rectifiers is the most promising way to realize a mmWave-enabled, i.e. mmWave-powered and -connected, IoT.

10.4.2 Textile-Based, Printed and Wearable Antennas

Antenna design on low-cost substrates empowers a breadth of applications beyond WPT and RFEH. For example, scalable and tunable high-impedance design on compact flexible circuits, presented in Chapter 5 on textiles and using dispenser printing in Chapter 9, enables the design of antennas directly conjugating capacitive MOS RF front-ends such as PAs and LNAs, potentially eliminating CMOS inductors utilized in 50 Ω matching of low-cost IoT applications. This not only enables smaller CMOS dies, reducing the cost of an IoT node, but also enables improving the efficiency of RF front-ends due to the elimination of the on-chip inductors, which often have a low quality-factor due to their size limitations.

As for broadband 50 Ω antennas on textile substrates, such designs can be utilized for broadband applications beyond communications. For instance, microwave imaging and radar-based sensing can benefit from unobtrusive low-cost antennas integrated in clothing and other flexible surfaces. Moreover, the recent developments in breast-cancer detection using antenna arrays, through-body imaging through UWB signals, and proximity and gesture detection using compact low-power radars could reach a higher level of integration in every-day objects based on the proposed high-efficiency antenna designs, on materials that are typically deemed unsuitable as microwave and mmWave substrates. Finally, the ability to realize high-efficiency and broadband mmWave antennas on textile substrates demonstrates that mmWave bands will not be limited to high-end applications such as smartphones and automotive radars. Therefore, new applications including multi-band satellite communications and high data-rate point-to-point communications for wearable devices can be realized improving future BAN's security and throughput, and overcoming the ever-growing demand for more wireless channels.

Appendix A

Selected Publications and Data Access

In this appendix, the full text of the following publications, referenced in parts of this thesis, are included in the following order:

- Mahmoud Wagih, Oktay Cetinkaya, Bahareh Zaghari, Alex S. Weddell, Steve Beeby "Real-World Performance of Sub-1 GHz and 2.4 GHz Textile Antennas for RF-Powered Body Area Networks" *IEEE Access*, 2020.
- Mahmoud Wagih, Geoffrey S. Hilton, Alex S. Weddell, Steve Beeby "2.4 GHz Wearable Textile Antenna/Rectenna for Simultaneous Information and Power Transfer" *15^{th} European Conference on Antennas and Propagation*, Dusseldorf, Denmark, 2021.

The data-sets underpinning are accessible through the University of Southampton institutional repository, and referenced in the journal publications outlined in Section 1.4. The associated datasets are:

- Mahmoud Ashraf Hassan Wagih Mohamed, Geoffrey S. Hilton, Alexander Weddell and Stephen Beeby (2021) Data associated with the Dual-Band Dual-Mode Textile Antenna/Rectenna for Simultaneous Wireless Information and Power Transfer. University of Southampton doi: 10.5258/SOTON/D1777
- Mahmoud Ashraf Hassan Wagih Mohamed, Nicholas Hillier, Sheng Yong, Alexander Weddell and Stephen Beeby (2021) Data suppporting "RF-Powered Wearable Energy Harvesting and Storage Module based on E-Textile Coplanar Waveguide Rectenna and Supercapacitor. University of Southampton doi: 10.5258/SOTON/D1737

- Mahmoud Ashraf Hassan Wagih Mohamed, Geoffrey S. Hilton, Alexander Weddell and Stephen Beeby (2020) Data for Broadband Millimeter Wave Textile-Based Flexible Rectenna. University of Southampton doi: 10.5258/SOTON/D1493.

- Mahmoud Ashraf Hassan Wagih Mohamed (2020) Data for Meshed High-Impedance Matching Network-Free Rectenna Optimized for Additive Manufacturing. University of Southampton doi: 10.5258/SOTON/D1632

- Mahmoud Ashraf Hassan Wagih Mohamed, Alexander Weddell and Stephen Beeby (2020) Data for Omnidirectional Dual-Polarized Low-Profile Textile Rectenna with over 50% Efficiency for Sub-μW/cm^2 Wearable Power Harvesting. University of Southampton doi: 10.5258/SOTON/D1571

- Mahmoud Ashraf Hassan Wagih Mohamed, Oktay Cetinkaya, Bahareh Zaghari Alexander Weddell and Stephen Beeby (2020) Dataset for "Real-World Performance of Sub-1 GHz and 2.4 GHz Textile Antennas for RF-Powered Body Area Networks". University of Southampton doi: 10.5258/SOTON/D1479

- Mahmoud Ashraf Hassan Wagih Mohamed, Alexander Weddell and Stephen Beeby (2020) Dataset for: Millimeter-Wave Power Harvesting: A Review. University of Southampton doi: 10.5258/SOTON/D1568

IEEE Access
Multidisciplinary | Rapid Review | Open Access Journal

Date of publication xxxx 00, 0000, date of current version xxxx 00, 0000.

Digital Object Identifier 10.1109/ACCESS.2017.DOI

Real-World Performance of Sub-1 GHz and 2.4 GHz Textile Antennas for RF-Powered Body Area Networks

Mahmoud Wagih, (Graduate Student Member, IEEE), Oktay Cetinkaya, (Member, IEEE), Bahareh Zaghari, (Member, IEEE), Alex S. Weddell, (Member, IEEE), and Steve Beeby, (Senior Member, IEEE)

School of Electronics and Computer Science, University of Southampton, Southampton, SO17 1BJ UK (email. mahm1g15@ecs.soton.ac.uk)

Corresponding author: Mahmoud Wagih (e-mail: mahm1g15@ecs.soton.ac.uk).

This work was supported by the UK Engineering and Physical Sciences Research Council (EPSRC) under Grant EP/P010164/1 and the European Commission through the EnABLES Project funded under H2020-EU.1.4.1.2. Grant number 730957
Datasets supporting this article are available from the University of Southampton Repository at DOI: 10.5258/SOTON/D1479.

ABSTRACT In Radio Frequency (RF)-powered networks, peak antenna gains and path-loss models are often used to predict the power that can be received by a rectenna. However, this leads to significant over-estimation of the harvested power when using rectennas in a dynamic setting. This work proposes more realistic parameters for evaluating RF-powered Body Area Networks (BANs), and utilizes them to analyze and compare the performance of an RF-powered BAN based on 915 MHz and 2.4 GHz rectennas. Two fully-textile antennas: a 915 MHz monopole and a 2.4 GHz patch, are designed and fabricated for numerical radiation pattern analysis and practical forward transmission measurements. The antennas' radiation properties are used to calculate the power delivered to a wireless-powered BAN formed of four antennas at different body positions. The mean angular gain is proposed as a more insightful metric for evaluating RFEH networks with unknown transmitter-receiver alignment. It is concluded that, when considering the mean gain, an RF-powered BAN using an omnidirectional 915 MHz antenna outperforms a 2.4 GHz BAN with higher-gain antenna, despite lack of shielding, by 15.4× higher DC power. Furthermore, a transmitter located above the user can result in 1× and 9× higher DC power at 915 MHz and 2.4 GHz, respectively, compared to a horizontal transmitter. Finally, it is suggested that the mean and angular gain should be considered instead of the peak gain. This accounts for the antennas' angular misalignment resulting from the receiver's mobility, which can vary the received power by an order of magnitude.

INDEX TERMS Antennas, Body Area Networks (BAN), Electronic Textiles, Energy Harvesting, Internet of Things, ISM Bands, RF Energy Harvesting, Wearable Antenna, Wireless Power Transfer

I. INTRODUCTION

TEXTILE-BASED and wearable antennas [1], sensor nodes [2], energy harvesters [3] and Wireless Power Transfer (WPT) modules [4] have been proposed to enable reliable and autonomous Body Area Networks (BANs) on flexible and wearable materials for seamless integration in garments. BANs and body-centric passive sensing have various interesting applications in a smart city environment, such as tracking diabetic patients [5]. For active wearable sensing and communication nodes, power-autonomy is a fundamental need for the Internet of Things (IoT) [6], [7].

WPT and Radio Frequency Energy Harvesting (RFEH) are methods of enabling power-autonomous networking [8], and are considered as a controllable power harvesting and transfer technique for powering the IoT [9]. Antennas and coils for WPT on textile substrates using flexible materials have been widely-reported [4], [10]. Rectifying antennas (rectennas) are the main energy harvesting component, where the received power from the dedicated WPT or ambient RFEH source is dependent on the antenna's parameters such as gain, beamwidth, and polarization [11]. Such antenna parameters are highly angle-dependent and hence will vary with the source-rectenna alignment. While the peak gain is introduced as a figure of merit in link-budget calculations in WPT [12], in an ambient RFEH environment using a more directional antenna does not translate to higher energy reception [13],

where the direction of the incident power may not align with the narrower beam-width.

Wireless networks powered through RFEH or WPT from a dedicated wireless power base-station have been extensively studied [14]. In addition, Simultaneous Wireless Information and Power Transfer (SWIPT) has been proposed utilizing the same carrier frequency to power a battery-less receiver while decoding the information carried by the RF wave [15]. Power transfer using digitally-modulated wave-forms has been studied for SWIPT applications based on off-the-shelf energy harvesters [16]. SWIPT has previously been utilized in back-scattered RFID [17]. Moreover, wireless powering of implants has been demonstrated using radiative Ultra-High Frequency (UHF) WPT [18], [19].

To enable RF-powering of e-textiles and BANs, textile-based rectennas and antennas have been realized using various fabrication methods and frequency bands from sub-1 GHz UHF up to mmWave bands [10], [20]–[24]. Wearable rectenna designs have been focused on antenna designs shielded from the body and hence utilize patch antennas. Recently, an unshielded tee-shirt rectenna array has been proposed for broadband applications [25]. To overcome the efficiency degradation due to human proximity, a large array (9×9) is used to improve the power received by the rectenna.

The trade-offs in RF-powered network design include the choice of the carrier frequency, transmitter and receiver antenna designs and therefore the gain [11], and the nodes distribution [26]. For instance, it has been shown that the energy coverage is improved in the 28 GHz mmWave band compared to sub-6 GHz networks due to the highly-directional large antenna arrays at mmWave bands [27]. However, realizing high-efficiency rectifiers at such a high frequency is difficult due to the diodes' cut-off frequencies. On the other hand, a sub-1 GHz carrier allows the reduction of the propagation losses and the use of existing transmitters such as RFID readers [17]. RF-powering using drones [28], fixed energy harvesting base-stations [29], and ray-tracing [30] have been reported demonstrating the possibility of powering multiple nodes reliably using RF power. While a standard (non-textile) rectenna has been evaluated using the 3D voltage radiation patterns [31], most textile-based rectennas have been characterized using standard antenna parameters such as the peak gain and radiation efficiency. On the other hand, the layout of the rectifier and the feeding mechanism of the rectenna may distort the radiation patterns of the characterized antenna-only prototype

RF propagation in on- and off-body scenarios has been widely investigated for different frequency bands [32], [33]. Recent work has focused on maximizing the efficiency of an on-body link using fixed antennas, where the path loss could be minimized using beam-steering or directional antennas [32]. Wireless links for in-body wearable communications have been investigated for UWB implants [34]. However, most on-body propagation studies are concerned with fixed antennas, where the only variation may be introduced by the movement of certain body parts. When it comes to an RFEH or WPT scenario, the angle of incidence of the RF power may not be aligned with the rectenna's main-beam. Furthermore, while an antenna radiating off-body, such as a microstrip patch, has been favorable for wearable rectennas [10], [22], [23], it may significantly reduce the power received from a transmitter shadowed by the body. This is due to the antenna's high front-to-back ratio, requiring more rectennas with additional techniques for DC-combining, to achieve the same angular coverage which may reduce the efficiency compared to a single rectenna [23].

This work evaluates the performance of an RF-powered BAN at two different license-free Industrial Scientific Medical (ISM) bands, 915 MHz and 2.4 GHz, using fully-textile antennas, i.e. antennas with textile conductors such as Litz threads [4], and electroplated fabrics [10]. A 915 MHz monopole and a 2.4 GHz patch are designed, simulated on a human model, and fabricated. The antenna prototypes are utilized for off-body path loss measurements and compared to reference dipole antennas positioned in free space. A BAN powered using four rectennas based on the characterized textile antennas is evaluated to identify the frequency band and antenna design resulting in the highest DC power reception.

The contributions of this paper can be summarized in:

1) Proposing the mean (average) angular gain and angular gain probability as metrics for evaluating energy harvesting antennas for mobile receivers such as wearable rectennas.
2) Numerically and experimentally comparing the LOS and N-LOS off-body "effective gain" of 915 MHz omnidirectional and 2.4 GHz broadside textile antennas.
3) Evaluating the performance of a 915 MHz and 2.4 GHz BAN based on multiple wearable rectennas using the angular mean gain and the gain distribution function.
4) Demonstrating that a 915 MHz unshielded antenna is more suited for ISM-band WPT compared to a 2.4 GHz patch with a potential for up to $15\times$ higher DC power reception.

This paper is structured as follows: section II presents the architecture of the BAN studied in this work. The textile antennas used in this study are designed and characterized in section III, the antennas are then used in section IV to measure the off-body propagation losses. Finally, the power received by a BAN powered using the designed textile antennas is evaluated in section V.

II. BODY AREA NETWORK ARCHITECTURE

In a wearable RFEH-BAN, it is expected that multiple nodes integrated in the user's garment can be wireless-powered using an off-body source. In this context, "off-body" radiation is defined as incident electromagnetic (EM) radiation from an antenna placed off the body. "On-body" propagation between two wearable antennas integrated in the same user's clothing is not considered in this study, as the power is delivered from an off-body transmitter. Scalable integration of rectennas in textiles and garments have previously been reported in a double-sided wrist bands, [23], to overcome

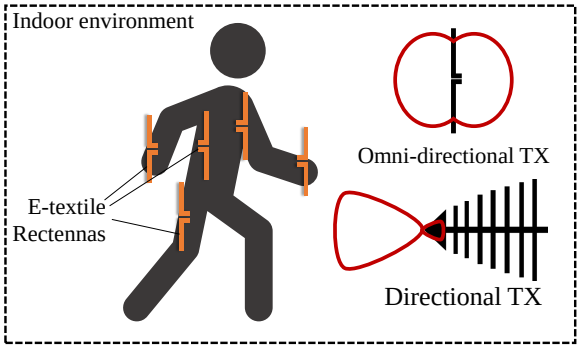

FIGURE 1. A wireless-powered BAN, powered using directional or omnidirectional dedicated license-free transmitters.

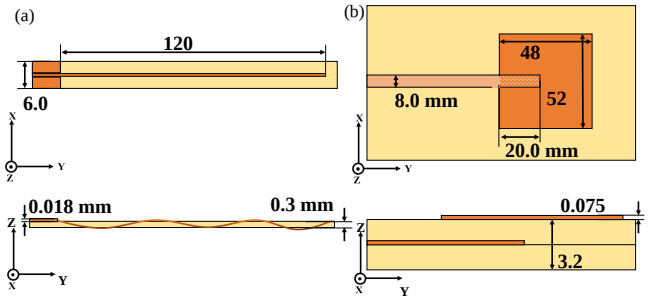

FIGURE 2. Layout and dimensions of the proposed textile AUTs: (a) 915 MHz monopole, (b) 2.4 GHz patch.

the directionality problem when the harvesting patch is not facing the transmitter. In addition, a 4×2 patch antenna array has been proposed to improve the DC power received from an incident plane-wave excitation [22].

In this paper, a BAN with multiple rectennas is considered; the power received by the rectennas is combined into a single DC output. The rectennas will be powered using a UHF license-free transmitter operating at either 915 MHz or 2.4 GHz. In an indoor environment, the rectenna's efficient harvesting range may not exceed 5 m due to the limits on the Equivalent Isotropically Radiated Power (EIRP) [35]. Therefore, the impact of the antenna's radiation properties, i.e. gain and angular beamwidth, will have significant impact on the received RF and subsequently DC power. Moreover, the position of the transmitter with respect to the user needs to be considered as an additional tuning parameter. For example, a transmitter at the same height as the user (horizontal), as opposed to a transmitter above the user (vertical) will affect the power received by the rectenna. The effects of the antennas' radiation properties for wearable RFEH need to be based on the radiation patterns of realistic fully-textile antennas in different RFEH scenarios, such as Line-of-Sight (LOS) and non-LOS operation. Fig. 1 shows a BAN powered using off-body transmitters at license-free bands.

III. WEARABLE ENERGY HARVESTING ANTENNA

A. ANTENNA DESIGN

To investigate the off-body propagation and radiation properties, and hence evaluate the harvesting capabilities of wearable rectennas, two antenna designs are proposed. The antennas are designed for a standard textile substrate and are fabricated using conductive threads and electroplated e-textiles. Thus, the measured performance of these antennas will be indicative of textile-based rectenna performance in wearable applications.

At sub-1 GHz bands, unshielded textile antennas may be used to maintain a low profile [36]. To explain, the relatively long wavelength (32.8 cm at 915 MHz) implies that a ground plane or an unconnected reflector will need to be placed over 1 cm behind the antenna to prevent detuning, which is unrealistic in a planar textile antenna. Therefore, textile antennas operating at sub-1 GHz have been considered with varying textile separation layers [37] as well as with variable separation from the human body [38], to investigate the impact on their radiation efficiency and gain.

The proposed antenna for sub-1 GHz WPT is a textile wire monopole, sewn using a conductive thread onto a standard (poly-cotton) textile substrate. Such a monopole antenna will have a lower gain than a dipole's theoretical directivity of 2.1 dBi [39]. This is due to the compact ground plane and the additional conductor losses in the textile Litz wire. Fig. 2-a shows the dimensions of the monopole microstrip antenna.

At 2.4 GHz, implementing a ground-backed patch antenna on textiles with reasonable (above 10%) radiation efficiency is more feasible. For example, the rectennas reported in [22] and [23] utilized patch antennas on textiles with up to 76% measured radiation efficiency in [23]. Fig. 2-b shows the dimensions of the patch antenna considered in this work. Fig. 3 shows the photographs of the textile antenna prototypes. Both antennas utilize highly conductive textiles (sheet resistance$<$10 mΩ/square) and therefore the fabrication techniques and materials will introduce minimum variation in the antennas' efficiency and gain compared to state-of-the-art textile antennas.

B. ANTENNA SIMULATION AND MEASUREMENTS

The antennas have been simulated using full-wave 3D EM simulation in CST Microwave Studio. The dielectric properties of the substrates used were based on the measured properties of felt and polyester cotton reported in [23]. The fabricated prototypes were connected to standard solder-terminated SMA connectors and their bandwidth was measured using a Vector Network Analyser (VNA).

The measured reflection coefficient (S_{11}) of the monopole and patch antennas in Fig. 4 shows a $S_{11} < -10$ dB bandwidth at 915 MHz and 2.45 GHz respectively. Thus, they can be used to measure the off-body propagation at these bands without any influence on the realized gain. The main discrepancy in the monopoles' S_{11} magnitude is due to the ground plane's size resulting in a more capacitive antenna in simulation. On the other hand, the SMA connector increases the actual ground plane size of the antenna during measurements resulting in the improved impedance match.

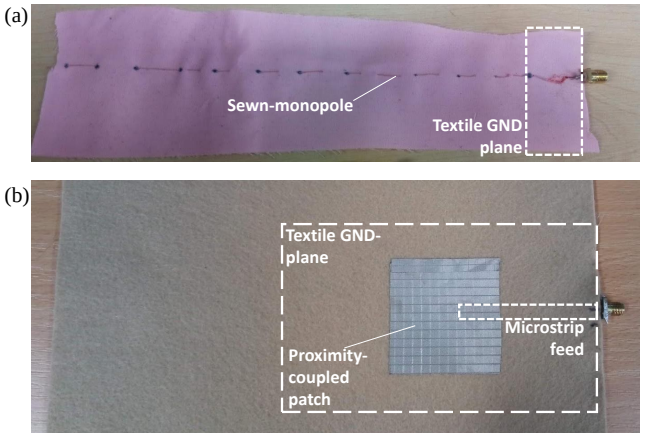

FIGURE 3. Photographs of the textile antennas used in the channel measurements: 915 MHz sewn monopole (a) and 2.4 GHz conductive fabric patch (b).

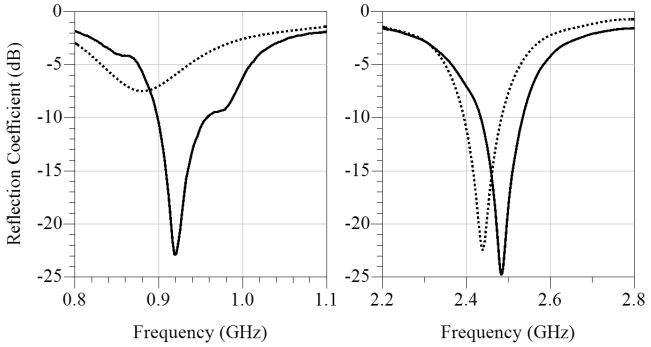

FIGURE 4. Simulated (dashed) and measured (solid) reflection coefficient of the textile monopole (left) and patch (right) antennas utilized in the off-body propagation measurements.

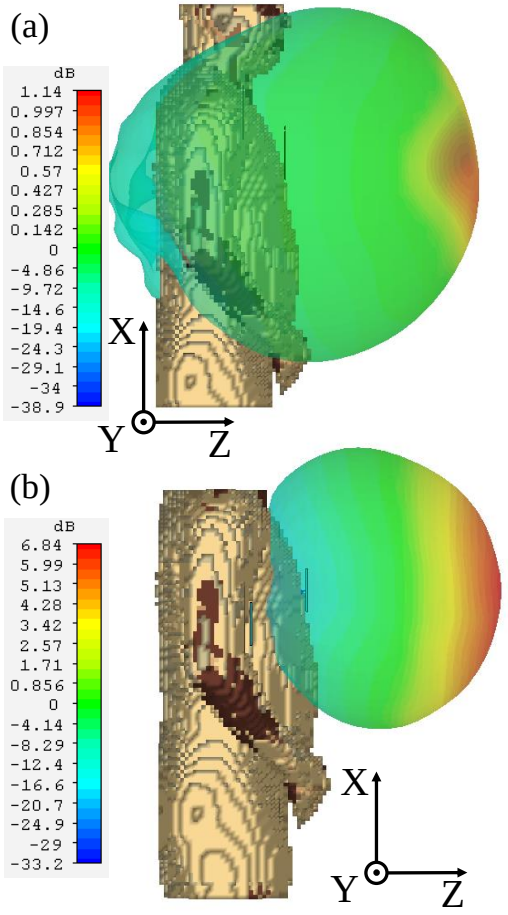

FIGURE 5. Simulated 3D farfield gain radiation patterns of the 915 MHz monopole (a) and the 2.4 GHz patch antenna (b).

C. OFF-BODY ANTENNA NEAR AND FAR-FIELDS

Field monitors in CST Microwave Studio have been used to investigate the near and far-field distributions around the human body. The EM-simulated radiation patterns will be utilized to analytically evaluate the performance of the network in Section V. The open-source human body EM simulation model AustinMan, [40], has been used to simulate the antenna's performance in proximity with the human body. The model utilized in this work is detailed to $8\times8\times8$ mm^3, as this work only considers off-body antenna and not implants in specific body positions, this resolution satisfies the accuracy requirement for a reasonable computation time and solver mesh size.

Two on-body antenna positions, on-chest and on-arm, have been considered to evaluate the radiation properties and mutual coupling between the antennas. To simplify the 3D modeling and reduce the time-domain solver mesh size, the antennas have been considered in a flat state, reducing the number of cells required to simulate the antenna. Textile-based patch antennas have previously been studied under bending and did not show variation around their resonant frequency [23]. The antennas have been placed at 5 mm clearance from the skin layer on the AustinMan phantom. The on-chest 915 MHz monopole antenna achieves a 1.1 dB gain with 3 dB beamwidth of 95°, while the 2.4 GHz patch achieves a gain of 6.84 dB with a narrower 63.7° 3 dB-beamwidth. The simulated 3D radiation patterns of the monopole and patch antennas are shown in Fig. 5-a and 5-b, respectively.

The near-field electric- (E-) field patterns around the antennas have been simulated to visualize the mutual-coupling between the wearable antennas. Fig. 6-a and -b show the E-field radiated from the 915 MHz textile monopole on-chest and on-shoulder. The e-field of the 2.4 GHz patches is shown in Fig. 7. It is observed that from both antennas, less than 1% of the radiated E-field is received by the other antenna. This has been validated by the S_{21} being less than -30 and -40 dB for the monopole and patch antennas, respectively, when placed on-chest and on-shoulder.

Near-field plots allow visualizing and understanding antennas' interaction with the human body [2]. This can be used to evaluate and understand the impact of different body positions on the power radiate by the antenna. Therefore, the E-field patterns of the the transmitting antenna can be used to understand the interaction of an incident wave on a receiver

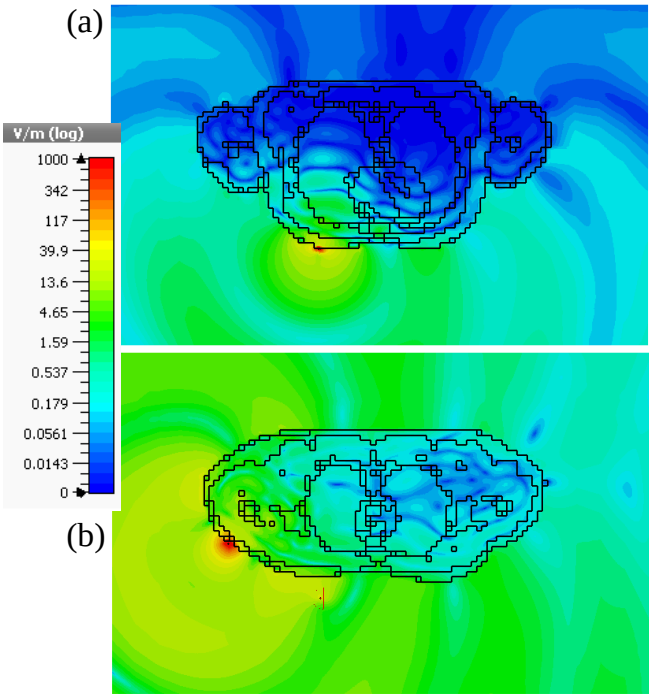

FIGURE 6. Simulated E-field distribution around the body at 915 MHz from: (a) antenna placed on the chest, (b) antenna placed on shoulder

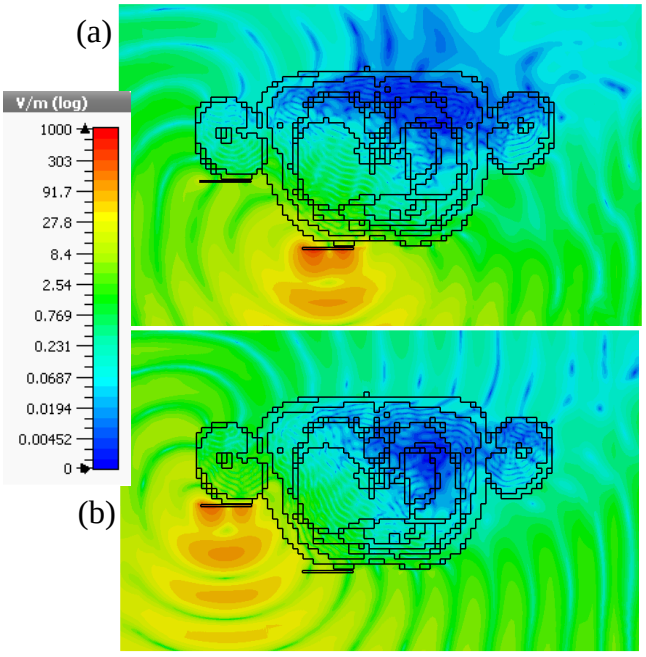

FIGURE 7. Simulated E-field distribution at 2.4 GHz from: (a) patch antenna on-chest, (b) patch antenna on shoulder.

with the body, due to reciprocity. For example, the on-shoulder antenna in Fig. 6-b shows the antenna's near-field surrounding the body with minimal body-shadowing effects. Hence, it is suggested to place off-body WPT antennas on the body's extremities to minimize shadowing. Furthermore, in Fig. 6-b, the E-field magnitude behind the user is higher than that of the patch in Fig. 7-b. This indicates the monopole antenna's ability to receive more power when not facing the transmitter compared to the patch, despite suffering from increased absorption and shielding by the body, due to its own lack of a metal plane or a reflector.

IV. OFF-BODY PROPAGATION MEASUREMENTS

To evaluate the performance of wearable RFEH antennas operating on the body, the textile antennas shown in Fig. 3 were used to measure the propagation losses between a directional transmitter and the wearable antenna. A reference wire-dipole antenna (of ideal 2.1 dB gain) has also been used at 915 MHz for benchmarking. A standard 10 dBi log-periodic antenna has been utilized as a fixed transmitter horizontal to the user. A VNA has been used to measure the Continuous Wave (CW) forward transmission (S_{21}) between the antenna-under-test (AUT) and the 10 dBi reference. The measurements were performed on a standing person, and do not include the effects of walking on the path loss. Fig. 8 shows the measurement setup.

The antennas were placed at a fixed distance D and the S_{21} between the source and the AUT has been measured. D has been set to 1 m from the radiating apertures of the transmitting and receiving antennas to ensure operation in the far-field region of the AUTs.

The antennas have been placed on multiple on-body positions, shown in Fig. 8-a, to accurately measure the impact of different body parts on the antenna's effective gain. The effective gain,

$$G_{\text{eff}} = S_{21\ \text{textile}} - S_{21\ \text{dipole}}, \tag{1}$$

is introduced to factor in the body shadowing effects compared to the S_{21} of an ideal 2.1 dBi $\lambda/2$ wire dipole measured in free space at the same D. This eliminates the errors due to multi-path effects and due to uncertainties in the path loss model or the transmitter gain. G_{eff} differs from standard gain measurements on a human body phantom by combining the off-body propagation effects in the gain figure. For instance, in the N-LOS case, the human body is a main contributor to the lower G_{eff}, due to shadowing. G_{eff} in the N-LOS case of a broadside patch antenna is reduced both by the body-shadowing effect as well as the antenna's own main beam misalignment with the transmitter. G_{eff} is relative to the dipole's gain.

The measured channel losses have been used to calculate the effective gain of the antennas shown in Table IV. By observation, the effects of LOS and N-LOS off-body propagation can be accounted for using the antenna's gain. Therefore, the propagation model can be simplified to free-space propagation. In addition, by performing the G_{eff} measurements on-body in an indoor environment, this factors in additional multi-path effects and the effects of clothing.

When comparing the unshielded 915 MHz omni-directional with the 2.4 GHz broad-side patch antenna, as predicted, the patch antenna maintains a higher effective gain

TABLE 1. Measured off-body effective gain (G_{eff}) of the AUTs

Body Pos.	3 cm from body: LOS			3 cm from body: N-LOS			Body contact: LOS			Body contact: N-LOS		
	Ref. dipole	Textile monopole	Textile patch	Ref. dipole	Textile monopole	Textile patch	Ref. dipole	Textile monopole	Textile patch	Ref. dipole	Textile monopole	Textile patch
	915 MHz		2.4 GHz	915 MHz		2.4 GHz	915 MHz		2.4 GHz	915 MHz		2.4 GHz
I	-2.6	-0.4	-0.8	-13.3	-13	-13.5	-11.3	-2	-2.4	-15.2	-14.7	-15.5
II	-3.9	-0.8	1.5	-13.1	-15	-11.5	-9.9	-6.1	-2.1	-12.8	-14	-16.5
III	-5	-1.9	-1.5	-10.1	-14.5	-17.5	-9.9	-15	-5.2	-19.9	-24.2	-16.5
IV	-4.1	-2.4	0.2	-11.9	-9	-12.5	-8.9	-9	-7.5	-13	-13	-12.5
V	-1.2	0.1	-0.4	-12.9	-10	-11.5	-8.7	-6	-5.5	-12	-15	-15.5
VI	-3.3	-2	-1.1	-12.2	-14.4	-12.5	-9.4	-9	-1.8	-14.2	-16	-13.5
FSPL*	-19.7	-22	-38.5	-19.7	-22	-38.5	-19.7	-22	-38.5	-19.7	-22	-38.5

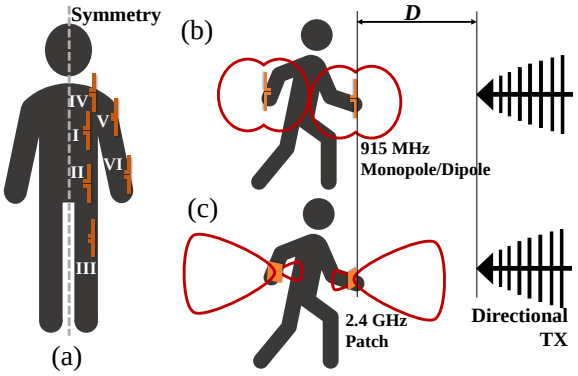

FIGURE 8. Measurement setup of indoor off-body propagation using the proposed antennas and a reference 915 MHz dipole antenna, horizontally-aligned, for distance D: (a) on-body antenna placement, (b) LOS and N-LOS scenarios for the omni-directional monopole, (c) LOS and N-LOS scenarios for the directional 2.4 GHz patch.

on the body. This is due to the improved isolation provided by the ground plane. However, it is still observed that the antenna's gain deteriorates by over 5 dB when measured at position VI at 3 cm clearance from the body. This shows significantly higher degradation compared to on-phantom measurements in an anechoic chamber reported in [23], where the radiation efficiency was reduced by less than 10% on the phantom.

On the other hand, when a N-LOS scenario is considered, the effective gain of the unshielded monopole is improved over a patch antenna. This is explained by the low back-radiation of the patch antenna, while this may be a figure of merit in directional WPT or communications, when the direction of incidence of the RF power is unknown, this implies that less energy will be received from the transmitter. The measured G_{eff} shows the same trend as the simulated off-body gain of the antennas, in Fig. 5, where the person (subject of measurements in Fig. 8) is different from the AustinMan model from [40]. Furthermore, when combining this with the overall lower propagation losses at 915 MHz, it can be concluded that WPT for BAN at sub-1 GHz bands enables a higher end-to-end efficiency. This will be validated through simulations of the RF-powered BAN in the next section.

V. WIRELESS POWER RECEPTION EVALUATION

As different on-body rectenna positions significantly affect the power received from an off-body source at the same distance, with up to 20 dB variation as shown in the empirical measurements using textile antennas on-body, multiple rectennas are to be placed on-body to improve the antennas' angular coverage. For both the 915 MHz monopole and the 2.4 GHz patch, four on-body antenna positions are considered. The antennas are positioned at points I, V from Fig. 8, on the model's chest and arm, at point IV (the model's shoulder) with the main beam directed above the user (X-direction in Fig. 5), and at point I on the model's back. The net radiation pattern of the four antennas, including mutual-coupling and body-shadowing effects, are combined in the 3D EM model to simplify the received power calculations. The textile rectennas are evaluated in two use-cases: a transmitter at the same height as the user (YZ plane), and a transmitter above the user (XY plane).

When simulating the network's performance using propagation models and the EIRP of a transmitter, the antenna's gain is often quoted as the main parameter [12], [26]. However, this neglects the impact of the 3D radiation patterns of the antenna. To illustrate, for non-stationary receivers, such as humans, the omni-directional gain of the antenna needs to be considered as alignment between the transmitter and receiver's main lobes is unlikely. This allows accurate prediction of the RFEH BAN's performance in LOS and N-LOS scenarios. The EM-simulated radiation properties of both antennas, and the measured textile antennas' effective gains are used to simulate the RF-powered BAN performance.

A. ANALYTICAL TRANSMITTER ANTENNA GAIN LIMIT

An additional parameter which can be utilized to optimize the RFEH BAN performance is the transmitter gain, where a higher gain antenna can be used to deliver the same EIRP output with a lower power output from the transmitter or the amplifier. Therefore, the end-to-end efficiency can be improved, due to transmitting at a lower power level. The transmitting antenna gain may then be utilized as a controllable parameter to improve the rectenna's power reception [12]. At 2.4 GHz and above, it is possible to increase the EIRP above 36 dBm by using a directional transmitter. However, for every 3 dB increase in the transmitter gain above 36 dBm the power input to the antenna needs to be reduced by 1 dB, up to 52 dBm.

By increasing the transmitting antenna's gain, the end-to-end efficiency in WPT can be improved at higher frequency bands such as the 5 GHz ISM-bands. Nevertheless, this is mostly limited to point-to-point WPT applications where the positions of the transmitter and receiver are fixed. In a wearable system, implementing directional narrow-beam WPT techniques will require complex control loops to ensure accurate beam-steering using a large transmitting phased array.

In practice, the physical size of the antenna limits the maximum achievable directivity and subsequently the gain. This can be estimated analytically using a simple loop antenna. A loop antenna is selected due to the availability of accurate closed-form expressions in literature to estimate the maximum gain based on the antenna's size [41].

Considering a simple loop antenna as an a example, the maximum directivity,

$$D = \frac{120\pi^2(ka)^2}{R}\max\{J^2[ka\sin(\theta)]\}, \qquad (2)$$

and subsequently the gain, is a direct function of the surface current J over the loop of radius a (2), where R is the radiation resistance, $k = 2\pi/\lambda$ is the wave constant, and θ is the angle at which the directivity is calculated [41]. A simple approximation to the solution of the integral has been proposed in [41] with a maximum error of 0.2 dB for both electrically small ($ka < \lambda/2$) and large ($ka > \lambda/2$) antennas.

Two loop antennas of radius a are considered to estimate the size requirements for a high gain transmitter for 915 MHz and 2.45 GHz WPT. The loops' peak gain has been calculated using the method in [41]. Fig. 9 shows the analytically-calculated directivity of the antennas as a function of their radius. It can be seen that to realize a transmitting antenna of high gain (over 9 dB) the antenna's radius becomes unrealistically-large for most IoT applications at 915 MHz. Thus, transmitters of higher gain than 10 dBi will not be considered in the RF-powered BAN simulations for practical antenna design considerations. It is important to note that although more innovative novel antenna designs and transmit-arrays can be employed to improve the transmitting gain without significantly increasing the size, high gain antennas typically require a large physical size (e.g. parabolic and horn antennas), even for aperture efficiencies exceeding 1 such as the textile patch in [23].

B. RF-POWERED BAN PERFORMANCE USING 3D ANTENNA GAIN

For a 3D space, the average gain of an ideal antenna is 0 dB regardless of the radiation pattern [39]. In [42], it was analytically demonstrated that a high-directivity antenna does not improve the received power from an ambient wave due to the variations in the propagation medium. However, [42] concludes that this may change for lower antenna efficiency. In this work, it is shown that a 915 MHz omnidirectional rectenna, with low radiation efficiency, can outperform its directional counterpart operating at 2.4 GHz when evaluated over meaningful 2D planes for body-worn energy harvesting.

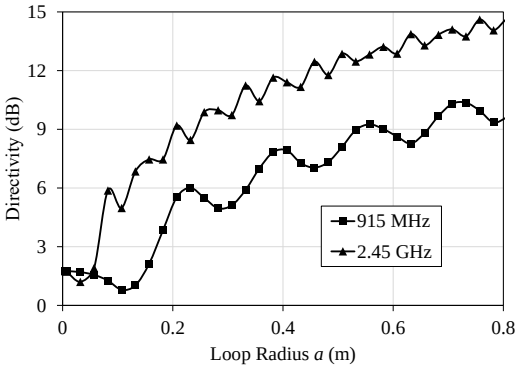

FIGURE 9. Loop antenna gain as a function of the radius at 915 MHz and 2.45 GHz.

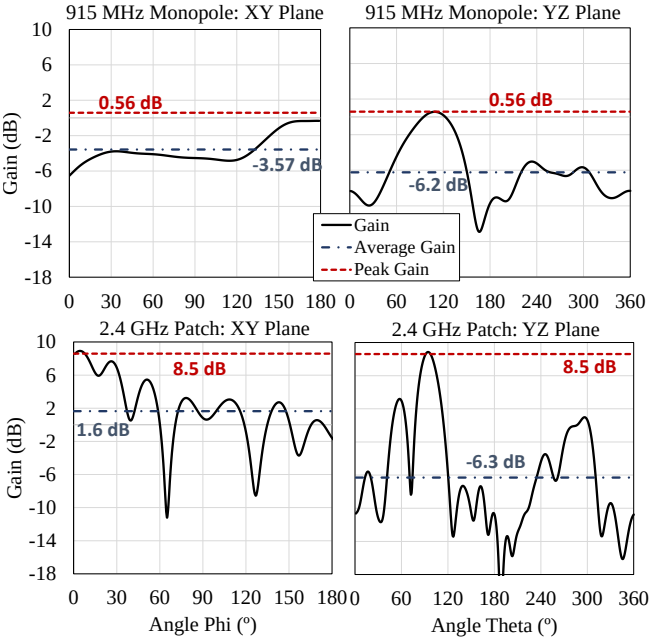

FIGURE 10. The patch and monopole antennas gain as a function of the angles theta (θ) and phi (ϕ), as well as the peak and average (mean) gains over each plane.

The angular gain of the entire receiving rectenna system, $G_{\mathrm{RX}}(\theta, \phi)$, is a function of the four rectennas placement in the 3D space around the body (x, y, z). The computed 3D patterns have been used to calculate the overall peak gain, the mean gains on the YZ and XY planes (planes defined in Fig. 5) as well as the angular gain to evaluate the performance of a randomly-aligned transmitter. Angles θ and ϕ are defined as the angular coordinates around the YZ and XY planes, defined in Fig. 5, respectively. Fig. 10 shows the Cartesian plot of the antennas' gain on the horizontal and vertical axis. The angular gain is directly influenced by the antennas' position on the body and can be used to evaluate the rectennas' performance in a 3D space (i.e. on the body)

$$G_{\mathrm{3D}}(x, y, z) \rightarrow G_{\mathrm{RX}}(\theta, \phi). \qquad (3)$$

Subsequently, the power received can be estimated using the angular-dependent gain to understand the performance of the BAN. Thus, the received RF power P_{RX} using free space propagation losses can be estimated including the angular dependency

$$P_{\mathrm{RX}}(x,y,z) = G_{\mathrm{RX}}(\theta,\phi)P_{\mathrm{TX}}\frac{1}{R^2}, \tag{4}$$

where R is the separation between the transmitter and the user and P_{TX} is the EIRP of the transmitter (4 W).

In order to demonstrate the variation in the simulated RFEH performance, three gain values are considered. The peak antenna gain $G_{\mathrm{Max.}} = \max\{G(\theta,\phi)\}$ is the most commonly utilized parameter in predicting the performance of RFEH and WPT networks [26]. The second metric is the average gain $G_{\mathrm{Avg.}}$, defined as the mean of the gain over the plane of interest, to account for the antenna's directionality. $G_{\mathrm{Avg.}}$ has been calculated independently for both θ and ϕ, and is shown in Fig. 10, using

$$G_{\mathrm{Avg:YZ}} = \frac{1}{360}\sum_{\theta=0}^{360^\circ} G(\theta), \tag{5}$$

$$G_{\mathrm{Avg:XY}} = \frac{1}{180}\sum_{\phi=0}^{180^\circ} G(\phi). \tag{6}$$

By considering the average gain rather than the peak gain, the performance of the rectenna when the receiving antenna's main lobe is not aligned with the transmitter can be accounted for, offering a more realistic insight on the antennas' performance. This work does not consider polarization mismatch; energy harvesting and WPT rectennas with dual-polarization reception capabilities have been widely presented based on dual-RF ports and dual-rectifiers with DC combining [43]. An extensive review of rectennas' polarization in RF energy harvesting and WPT applications has been presented in [11].

The average RF power received by the rectennas has been calculated using the free space propagation model and the antenna mean gains. A distance sweep has been carried out to show the spatial coverage range of an RF-powered BAN. The DC power is then calculated using the RF to DC Power Conversion Efficiency (PCE) of reported high-efficiency rectennas. The rectenna in [35] reports the highest sub-1 GHz PCE and is implemented on a flexible substrate using a dipole antenna, resulting in similar radiation properties to the textile monopole investigated in this work. At 2.4 GHz, the textile-based patch antenna coupled to a high efficiency rectifier in [23] achieves the highest PCE at power levels below -15 dBm. The measured and simulated PCEs from [35] and [23] are fitted to calculate the DC power output of the rectennas based on the textile antennas. Fig. 11 shows the measured and curve-fitted PCEs of the rectennas.

An EIRP of 4 W has been used when calculating the power delivered to the textile rectennas. The distance R between the transmitter and the rectenna has been swept from 2 m to 4 m. This ensures the rectenna is operating in the far-field, hence the path-loss model is valid. The rectenna's gain has been calculated using both the peak and mean gain obtained from the four antennas positioned on the body phantom, which is inclusive of the body shadowing effects, on-body propagation effects, and the mutual-coupling between the rectennas. Fig. 12 shows the calculated DC power received by the textile rectennas at 915 MHz and 2.4 GHz.

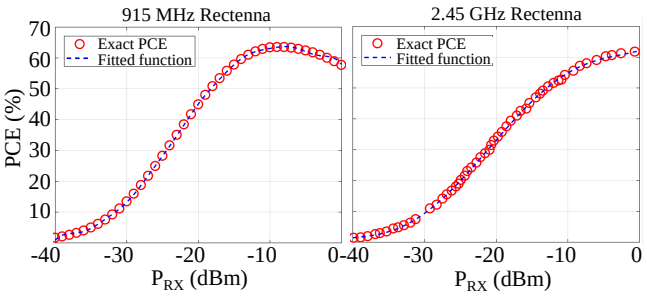

FIGURE 11. The flexible and wearable PCEs used at 915 MHz, [35], and 2.45 GHz, [23], to calculate the received DC power.

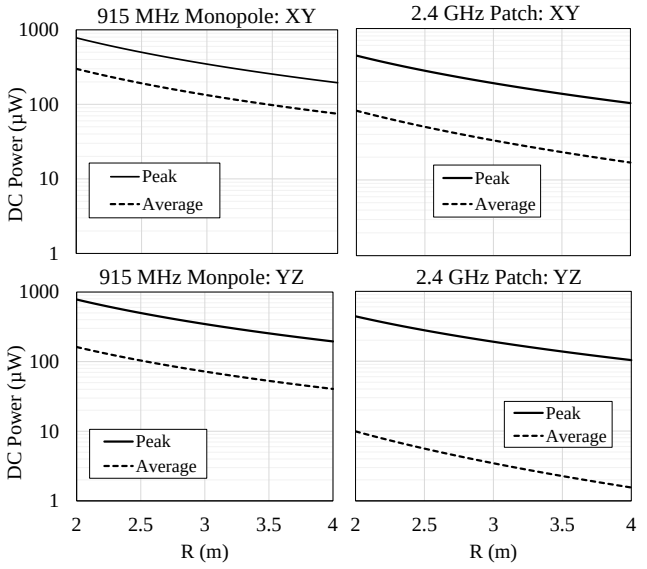

FIGURE 12. DC power received by the wearable 915 MHz and 2.4 GHz textile rectennas, on the XY and YZ planes, based on the antenna's peak and average (mean) gain.

One of the main aims of calculating the DC power delivered in a wireless-powered network is to evaluate the impact of certain antenna designs, based on the gain, on the power received by the rectennas. A higher DC power reception indicates a better BAN performance and a more suitable antenna design. The need to define multiple gain terms is clearly highlighted in Fig. 12, where the power delivered when considering the mean and maximum gains result in contradicting conclusions. When considering the antennas' peak gain, which is often quoted as the main figure-of-merit and assumes full angular alignment, the power received at 915 MHz is 0.77× higher than the power received at 2.4 GHz, on the XY plane. However, when considering the mean gainson the YZ and XY planes, the 915 MHz rectenna receives 15.4× and 2.6× higher DC power, respectively. This is

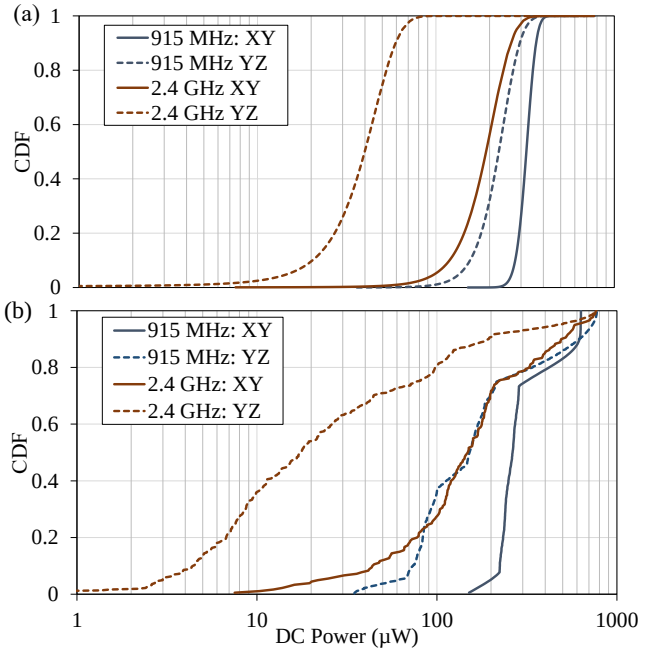

FIGURE 13. Theoretical (a) and empirical (b) CDF of the received DC power by the 915 MHz and 2.45 GHz rectennas.

despite the monopole having its efficiency and gain reduced due to the proximity with the human body model. Therefore, when delivering power to wearable rectennas, operating at a sub-1 GHz frequency using omnidirectional antennas yields higher DC power reception despite being more prone to body-shadowing and absorption. The difference in the received power ratio at both bands between the mean and peak gain is due to the significantly higher gain of the patch (6.84 dB) compared to the monopole (1.1 dB).

An additional optimization parameter for improving power reception in a BAN is the position of the transmitter with respect to the human. For both the 2.4 GHz and 915 MHz antennas, WPT from a source positioned above the user (on the XY plane of Fig. 5) results in improved energy reception. For a source above the user, such as mounted on the ceiling, the variation in the angular alignment of the antenna is limited to the 180° above the user. Subsequently, the average gain for both the broadside patch and the omnidirectional monopole on the XY plane is higher than on the YZ plane. In Fig. 12, at R=2 m on the YZ plane, the monopole antenna receives over eleven times higher DC power compared to the patch. The difference between the power received by both antennas is greater on the YZ plane due to the case where the transmitter is behind the user and not facing the radiating aperture of the patch antenna (the N-LOS scenario). This result agrees with the path loss measurements in table IV where the patch's effective gain is at its lowest in the N-LOS case and is lower than the monopole.

In real-life operation, the alignment of the rectenna with the power transmitter is random on the 360° YZ and 180° XY planes. Such random alignment is more prevalent when operating in the far fields of both the transmitter and the rectenna. Therefore, the probability of the received power needs to considered for both the XY and YZ axes. Fig. 13 shows the cumulative distribution function (CDF) of the received power at 2 m separation from the transmitter. From the CDF plots in Fig. 13, it is evident that the harvested power is higher when harvesting from the XY plane, for both the 915 MHz monopole and the 2.45 GHz patch. However, the effect us more prominent with the patch antenna, due to the more directional radiation patterns. Based on the empirical CDF in Fig. 13-b, the patch antenna's power reception CDF on the XY plane is comparable to the monopole. As a result, using a broadside patch antenna, positioned on the shoulder for instance, for harvesting from a source on the XY axis may result in improved energy reception compared to omnidirectional sub-1 GHz WPT. Nevertheless, it is concluded that on average and assuming a random position of the user, omnidirectional antennas combined with a source above the user (on the XY plane) result in the highest average received power, as in Fig. 12, as well as the highest power receiving probability, as in Fig. 13.

VI. CONCLUSION

In this paper, an RF-powered BAN with multiple power receivers, based on fully-textile antennas is studied, using realistic metrics for LOS and N-LOS dynamic WPT as opposed to peak gains. The effects of the frequency band, antenna design, and the antennas' position on the body have been investigated numerically and measured experimentally using textile antenna prototypes. Furthermore, more insightful real-world performance metrics are proposed improved RF-powered BAN evaluation.

Although omnidirectional sub-1 GHz textile antennas lack shielding from the body, the received DC power can be enhanced by over ten times compared to a 2.4 GHz high-gain patch antenna, when considering the average gain from a transmitter horizontally aligned with the body. The need for using the full 3D angular gain as well as the average gain when evaluating RF-powered networks is demonstrated, due to the random angular position of the user with respect to the power transmitter. The DC power reception improvement when using a 915 MHz monopole antenna has been quantified to vary between 0.7× and 15.4× higher DC power, depending on the plane of the incident RF power. It is concluded that omnidirectional sub-1 GHz antennas are the most suited for receiving power from an off-body source, when alignment between the user and the transmitter is unlikely and not controllable.

REFERENCES

[1] S. M. Salleh et al., "Textile Antenna With Simultaneous Frequency and Polarization Reconfiguration for WBAN," IEEE Access, vol. 6, pp. 2169–3536, 2018.

[2] M. Wagih, Y. Wei, and S. Beeby, "Flexible 2.4 GHz Sensor Node for Body Area Networks with a Compact High-Gain Planar Antenna," IEEE Antennas Wireless Propag. Lett., vol. 17, 12, pp. 49 – 53, 2018.

[3] S. Lemey, F. Declercq, and H. Rogier, "Textile Antennas as Hybrid Energy-Harvesting Platforms," Proceedings of the IEEE, vol. 102, no. 11, pp. 1833 – 1857, 2014.
[4] M. Wagih, A. Komolafe, and B. Zaghari, "Dual-Receiver Wearable 6.78 MHz Resonant Inductive Wireless Power Transfer Glove Using Embroidered Textile Coils," IEEE Access, vol. 8, pp. 24 630 – 24 642, 2020.
[5] X. Yang et al., "5G-Based User-Centric Sensing at C-Band," IEEE Trans. Ind. Informatics, vol. 15 no. 5, pp. 3040 – 3047, 2019.
[6] M. H. Rehmani et al., "IEEE Access special section editorial: Body area networks for interdisciplinary research," IEEE Access, vol. 4, pp. 2989–2992, 2016.
[7] D. Balsamo et al., "Wearable and autonomous computing for future smart cities: open challenges," in 25th International Conference on Software, Telecommunications and Computer Networks (SoftCOM). IEEE, 2017, pp. 1–5.
[8] H. J. Visser and R. J. M. Vullers, "RF Energy Harvesting and Transport for Wireless Sensor Network Applications: Principles and Requirements," Proceedings of the IEEE, vol. 101, 6, pp. 1410 – 1423, 2013.
[9] O. B. Akan et al., "Internet of hybrid energy harvesting things," IEEE J. Internet of Things, vol. 5 no. 2, pp. 736 – 746, 2018.
[10] G. Monti, L. Corchia, and L. Tarricone, "UHF Wearable Rectenna on Textile Materials," IEEE Trans. Antennas. Propag., vol. 61, 7, pp. 3869 – 3873, 2013.
[11] M. Wagih, A. S. Weddell, and S. Beeby, "Rectennas for RF Energy Harvesting and Wireless Power Transfer: a Review of Antenna Design," IEEE Antennas and Propagation Magazine, vol. Accepted: In Press, 2019.
[12] O. Cetinkaya and G. Merrett, "Efficient deployment of UAV-powered sensors for optimal coverage and connectivity," in EEE Wireless Communications and Networking Conference, 2020.
[13] S. Shen, C.-Y. Chiu, and R. D. Murch, "Multiport Pixel Rectenna for Ambient RF Energy Harvesting," IEEE Trans. Antennas Propag., vol. 66, 2, pp. 644 –656, 2018.
[14] X. Lu et al., "Wireless networks with rf energy harvesting: A contemporary survey," IEEE Communications Surveys & Tutorials, vol. 17, 2, pp. 757 – 789, 2015.
[15] T. D. P. Perera et al., "Simultaneous Wireless Information and Power Transfer (SWIPT): Recent Advances and Future Challenges," IEEE Communication Surveys and Tutorials, vol. 20, 1, pp. 264 – 302, 2018.
[16] F. Bolos et al., "RF Energy Harvesting From Multi-Tone and Digitally Modulated Signals," IEEE Trans. Microw. Theory Techn., vol. 64, no. 6, pp. 1918 – 1927, 2016.
[17] A. P. Sample et al., "Design of an RFID-Based Battery-Free Programmable Sensing Platform," IEEE Trans. on Instrumentation and Measurement, vol. 57 no. 11, pp. 2608 – 2615, 2008.
[18] A. N. Abdulfattah et al., "Performance analysis of mics-based rf wireless power transfer system for implantable medical devices," IEEE Access, vol. 7, pp. 11 775 – 11 784, 2019.
[19] S. M. Asif et al., "A wide-band tissue numerical model for deeply implantable antennas for rf-powered leadless pacemakers," IEEE Access, vol. 7, pp. 31 031 – 31 042, 2019.
[20] K. N. Paracha et al., "Wearable Antennas: A Review of Materials, Structures, and Innovative Features for Autonomous Communication and Sensing," IEEE Access, vol. 7, 2019.
[21] M. Wagih, A. S. Weddell, and S. Beeby, "Millimeter-Wave Textile Antenna for On-Body RF Energy Harvesting in Future 5G Networks," in 2019 IEEE Wireless Power Transfer Conference (WPTC), 2019.
[22] D. Vital, S. Bhardwaj, and J. L. Volakis, "Textile Based Large Area RF-Power Harvesting System for Wearable Applications," IEEE Trans. Antennas Propag., vol. Early Access, 2019.
[23] S.-E. Adami et al., "A Flexible 2.45-GHz Power Harvesting Wristband With Net System Output From -24.3 dBm of RF Power," IEEE Trans. Microw. Theory Techn., 2018.
[24] M. Wagih, A. S. Weddell, and S. Beeby, "Sub-1 GHz Flexible Concealed Rectenna Yarn for High-Efficiency Wireless-Powered Electronic Textiles," in 2020 European Conference on Antennas and Propagation (EuCAP), 2020.
[25] J. A. E. and, "An RF-Harvesting Tightly-Coupled Rectenna Array Tee-Shirt with Greater than Octave Bandwidth," IEEE Trans. Microw. Theory Techniq., vol. Early Access, pp. 1 – 1, 2020.
[26] O. Cetinkaya et al., "Energy-Neutral Wireless-Powered Networks," IEEE Wireless Communications Letters, vol. 8 no. 5, pp. 1373 – 1376, 2019.
[27] T. A. Khan, A. Alkhateeb, and R. W. Heath, "Millimeter wave energy harvesting," IEEE Transactions on Wireless Communications, vol. 15, 9, pp. 6048 – 6062, 2016.
[28] M. Mozaffari et al., "Efficient Deployment of Multiple Unmanned Aerial Vehicles for Optimal Wireless Coverage," IEEE Communications Letters, vol. 20 no. 8, pp. 1647 – 1650, 2016.
[29] S. He et al., "Energy Provisioning in Wireless Rechargeable Sensor Networks," IEEE Transactions on Mobile Computing, vol. 12 no. 10, pp. 1931 – 1942, 2013.
[30] Y.-S. Chen, F.-P. Lai, and J.-W. You, "Analysis of Antenna Radiation Characteristics Using a Hybrid Ray Tracing Algorithm for Indoor WiFi Energy-Harvesting Rectennas," IEEE Access, vol. 7, pp. 38 833 – 38 846, 2019.
[31] T. Q. V. Hoang et al., "3D Voltage Pattern Measurement of a 2.45 GHz Rectenna," IEEE Trans. Antennas Propag., vol. 61, 6, pp. 3354 – 3356, 2013.
[32] A. Thielens et al., "A Comparative Study of On-Body Radio-Frequency Links in the 420 MHz–2.4 GHz Range," Sensors, vol. 18, 2018.
[33] A. R. Guraliuc et al., "Effect of textile on the propagation along the body at 60 ghz," IEEE Trans. Antennas Propag., vol. 62, 3, pp. 1489 – 1494, 2014.
[34] C. Kissi et al., "Directive Low-Band UWB Antenna for In-body Medical Communications," IEEE Access, vol. 7, pp. 149 026 – 149 038, 2019.
[35] M. Wagih, A. S. Weddell, and S. Beeby, "High-Efficiency Sub-1 GHz Flexible Compact Rectenna based on Parametric Antenna-Rectifier Co-Design," in 2020 IEEE MTT-S International Microwave Symposium, 2020.
[36] P. Nepa and H. Rogier, "Wearable Antennas for Off-Body Radio Links at VHF and UHF Bands: Challenges, the state of the art, and future trends below 1 GHz," IEEE Antennas and Propagation Magazine, vol. 57 no. 5, pp. 30 – 52, 2015.
[37] D. L. Paul et al., "Impact of Body and Clothing on a Wearable Textile Dual Band Antenna at Digital Television and Wireless Communications Bands," IEEE Trans. Antennas Propag., vol. 61 no. 4, pp. 2188 – 2194, 2013.
[38] K. W. Lui, O. H. Murphy, and C. Toumazou, "A Wearable Wideband Circularly Polarized Textile Antenna for Effective Power Transmission on a Wirelessly-Powered Sensor Platform," IEEE Trans. Antennas Propag., vol. 61 no. 7, pp. 3873 – 3876, 2013.
[39] C. A. Balanis, Antenna Theory: Analysis and Design.
[40] J. W. Massey and A. E. Yilmaz, "AustinMan and AustinWoman: High-fidelity, anatomical voxel models developed from the VHP color images," in 2016 38th Annual International Conference of the IEEE Engineering in Medicine and Biology Society (EMBC), 2016.
[41] H. Schrank and J. Mahony, "Approximations to the radiation resistance and directivity of circular-loop antennas," IEEE Antennas and Propagation Magazine, vol. 36 no 4, pp. 52 – 55, 1994.
[42] S. Shen et al., "An ambient rf energy harvesting system where the number of antenna ports is dependent on frequency," IEEE Trans. Microw. Theory Techn., vol. Early Access, pp. 1 – 12, 2019.
[43] H. Sun and W. Geyi, "A new rectenna with all-polarization-receiving capability for wireless power transmission," IEEE Antennas Wireless Propag. Lett., vol. 15, pp. 814 – 817, 2015.

2.4 GHz Wearable Textile Antenna/Rectenna for Simultaneous Information and Power Transfer

Mahmoud Wagih*, *Graduate Student Member, IEEE*, Geoffrey S. Hilton†,
Alex S. Weddell*, *Member, IEEE*, and Steve Beeby*, *Senior Member, IEEE*
*School of Electronics and Computer Science, University of Southampton, U.K.
†Department of Electrical and Electronic Engineering, University of Bristol, U.K.
*{mahm1g15, asw, spb}@ecs.soton.ac.uk; †geoff.hilton@bristol.ac.uk

***Abstract*—Antennas and rectennas for self-powered body area networks (BANs) have attracted significant interest, in an effort to improve the sustainability of e-textiles. This paper presents a novel dual-port fully-textile antenna, based on a simple microstrip patch, for simultaneous wireless information and power transfer (SWIPT) at 2.4 GHz, presenting the first antenna-rectifier co-design implementation for SWIPT. The proposed antenna's input bandwidth covers the license-free band achieving 8.9 dBi measured directivity and 41% efficiency at 2.4 GHz, with a simple proximity-coupled microstrip feed. For power harvesting, port 2 is designed to achieve a scalable complex impedance to directly match the rectifier without a separate matching network, and achieves 6.3 dBi off-body gain. The proposed rectenna feed improves the antenna's isolation by at least 15 dB compared to a microstrip feed similar to port 1. The rectenna achieves over 40% power conversion efficiency (PCE) from −10 dBm, when placed directly on-body, with a 71% peak PCE.**

***Index Terms*—Antennas, Electronic Textile, RF Energy Harvesting, Rectifiers, Microstrip Antennas, Wireless Power Transfer**

I. Introduction

Textile-based antennas for body-centric communications have been widely investigated for wireless sensing, healthcare, and Internet of Things (IoT) applications [1], [2]. Wearable textile rectennas for Radio Frequency Energy Harvesting (RFEH)-powered Body Area Networks (BAN), from sub-1 GHz [3], [4], 2.4 GHz [5], and up to 26.5 GHz [6], have been developed using antennas with broadside radiation patterns, where the power would typically be received from a source off the body. Likewise, Industrial Scientific Medical (ISM)-band communication, using Bluetooth or Wi-Fi for example, will often take place between a wearable device and an off-body base-station [7]. Nevertheless, antennas for wearable systems performing both off-body communications and energy harvesting simultaneously have not been investigated or reported.

Simultaneous Wireless Information and Power Transfer (SWIPT) is an interesting application of RFEH [8], [9]. SWIPT topologies often involve switching mechanisms to divide the incident power using either time-based or power-based splitting between the rectenna and the information receiver [8]. However, such switches may require additional control hardware and will reduce the net harvested power from an incident plane-wave [9]. Therefore, SWIPT-specific antenna designs are needed to be able to simultaneously deliver power to the rectifier and information to the receiver without compromising on the rectenna's DC output. Recently, an antenna based on a hybrid coupler was proposed for SWIPT [10], as well as a dual-port antenna with 50Ω-matched rectifiers [11]. However, the designs are complex and cannot be integrated in wearables. Additionally, both designs required a matching network to connect the antenna to the rectifier and, for [11], the antenna is fundamentally no different from standard dual-port antennas or arrays with improved isolation.

Multi-port textile antennas have recently attracted significant interest for BAN. Applications such as full duplex wireless networks [12], and dual-polarization energy harvesting [3] have driven advances in wearable antenna design and fabrication. Nevertheless, a wearable antenna for SWIPT has not previously been demonstrated. Furthermore, realizing a rectenna based on existing multi-port textile antennas will require a matching network similar to [3]–[5]. On the other hand, co-designed rectennas without a matching network have several advantages over their counterparts with stand-alone matching [13]. This includes improving the Power Conversion Efficiency (PCE) as well as reducing the system's overall design complexity [14]. Yet, textile rectennas have not, thus far, been designed based on matching network elimination with antenna-rectifier co-design.

This work presents a fully-textile microstrip antenna for simultaneous wearable communications and energy harvesting from an off-body source. The antenna, occupying the same area as a conventional patch and using a miniaturized ground plane, achieves high gain (>5.7 dB) and radiation efficiency (>40%) across both ports. The energy harvesting port has been designed with an inductive feed to achieve a complex impedance chosen to directly match a rectifier. From an incident power −10 dBm, the rectenna port delivers 480 mV DC output, across an optimum load of 7 kΩ, with a 40% PCE, while simultaneously receiving (communicating) on port 1. This antenna is the only implementation demonstrating the feasibility of antenna-rectifier co-design integrated within a standard antenna design for communications, such as a patch,

This work was supported by the European Commission through the EnABLES Project: European Infrastructure Powering the Internet of Things, funded under H2020-EU.1.4.1.2. grant number: 730957.

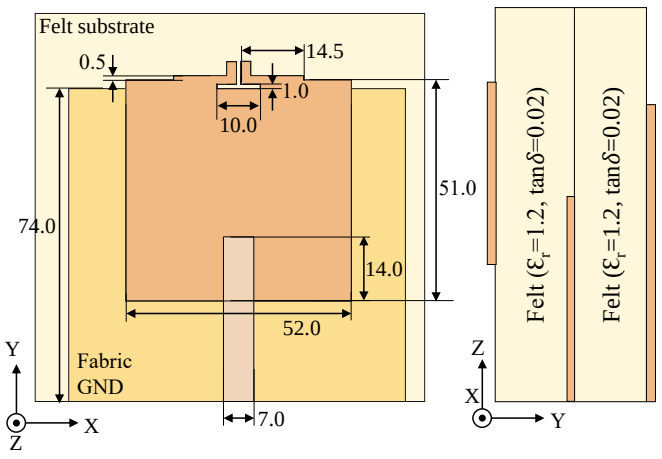

Fig. 1. Layout and dimensions (in mm) of the proposed SWIPT antenna.

showing high RFEH efficiency and improved ports' isolation for SWIPT applications.

II. Dual-Port Antenna Design, Simulation, and Fabrication

A. Antenna Design and Simulation

Microstrip patch antennas are the most common antenna design for off-body BAN applications due to their broadside radiation patterns and simple geometry. To design a microstrip patch for SWIPT applications without splitting power, a dual-port antenna is required with high isolation between the rectenna's RFEH and the communication ports.

First of all, a proximity-coupled microstrip patch is designed for a 3.2 mm-thick felt textile substrate (ϵ_r=1.2, tanδ=0.02). Electroplated conductive fabrics are selected for the antenna traces. The microstrip feed is sandwiched at 1.6 mm height from the ground-plane, Fig. 1 shows a cross section of the proposed antenna. The antenna is modelled and simulated in CST Microwave Studio. Initially, a symmetric microstrip feed to that on port 1 is added at port 2, as in Fig. 2 (a) and (b). This microstrip feed has a matched input impedance but also results in very high mutual-coupling, S_{21}=−4.5 dB, with port 1 reducing the antenna's realized gain by over 3.5 dB. Fig. 2-c shows the simulated port coupling (S_{21}) of the antenna with a conventional symmetric microstrip feed.

To reduce the mutual port coupling and adapt port 2 to RFEH applications, a novel differential feeding mechanism with an inductive loop is proposed. To explain, achieving a 50Ω impedance on port 2 is not significant for RFEH as a matching network will be needed to connect to a rectifier. However, the proposed inductive feed will result in a tunable complex impedance which can be used to directly match a rectifier [13]. Additionally, the proposed balanced feed at port 2 will reduce the coupling between the ports resulting in high gain across both ports.

It can be observed from the simulated s-parameters that the port isolation improves by over 40 dB with the new port structure. Owing to the new balanced feeding point of the antenna

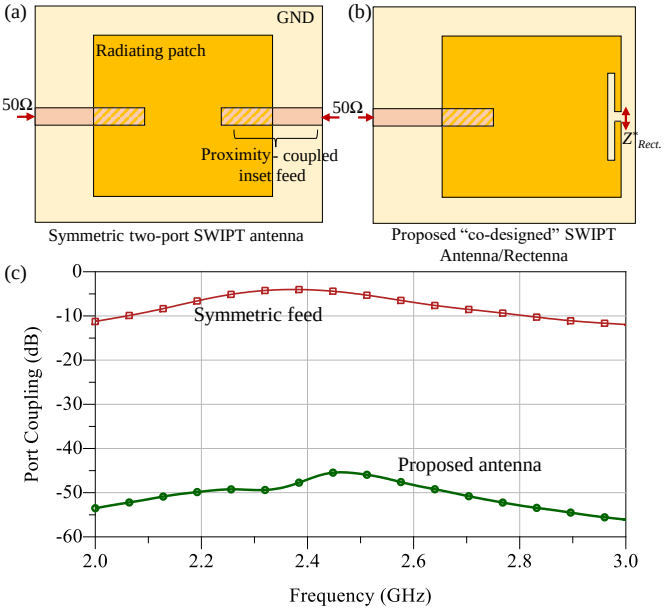

Fig. 2. The symmetric microstrip-fed antenna and proposed co-designed antenna: (a) layout of symmetric antenna; (b) layout of proposed antenna; (c) simulated S_{21} of both implementations.

with a built-in tuning loop, an inductive input impedance can be achieved to directly match a rectifier without the need for a matching network. However, a very low real input impedance will be observed due to the ground plane backing the loop. Therefore, the ground plane is miniaturized and the dimensions of the patch were tuned to achieve the desired input impedance to match the rectifier, by adding an additional dipole-like step shown in Fig. 1. At 2.4 GHz and −10 dBm, a voltage doubler rectifier based on the Skyworks SMS7630 Schottky diode, simulated using harmonic balance, achieves its maximum PCE with $Z_{\mathrm{Ant.}}$=15+j110Ω. The dimensions of the patch shown in Fig. 2 (the loop length and port-2 slots) were tuned to achieve $Z_{\mathrm{Ant.}}$ matching the rectifier.

B. Antenna Fabrication

The antenna is fabricated using laser-cut conductive fabric (P&P MW Weave). Conductive fabrics are more breathable and user-friendly compared to flexible circuits on polymer substrates, and can be patterned using simple methods such as die-cutting or laser-cutting. Fig. 3-a shows the rectenna prototype with the 50Ω communications port and the energy harvesting co-designed rectenna.

For the rectifier, the low-footprint Schottky diodes will require a more fine-featured fabrication process for the soldering pads. A thin and flexible circuit is fabricated to accommodate the voltage doubler using polyimide copper laminates [3]. While polyimide is not a textile material, it occupies less than 2% of the antenna's total area. In addition, due to its light weight and lower thickness than conductive fabrics, it does not reduce the user's comfort [6]. A rectifier fabricated on a polyimide flexible circuit adhered to a felt fabric substrate,

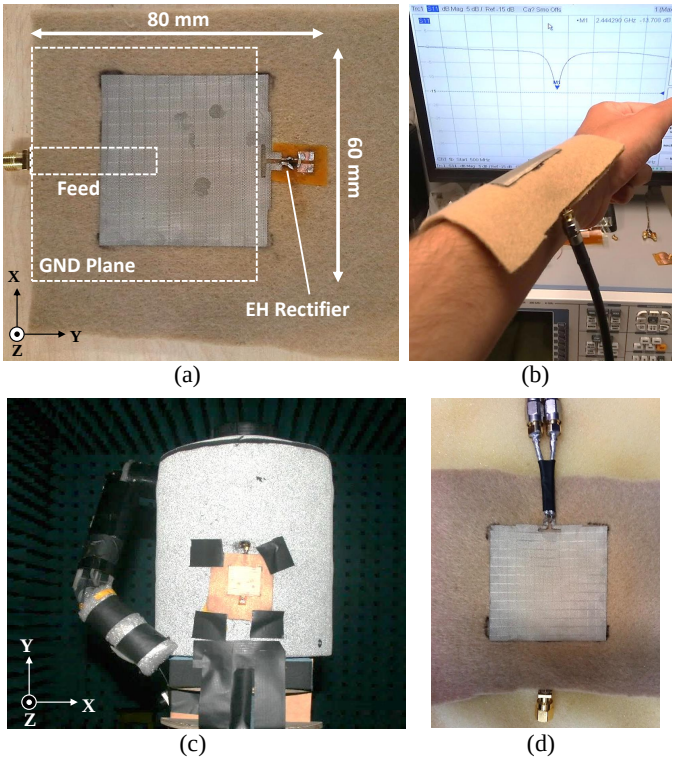

Fig. 3. Photographs of the proposed antenna: (a) The fabricated rectenna/antenna prototype; (b) antenna measurements while bending on-wrist; (c) antenna on body phantom in an anechoic chamber for radiation pattern measurements; (d) impedance measurement using a balanced jig.

using a similar technique to this work, was shown to withstand over 250 sharp bending cycles (<1 cm bending radius) with no degradation in the voltage output [3].

III. Antenna and Rectenna Measurements

A. Off-Body Communication Antenna Measurements

The fabricated antenna prototype, shown in Fig. 3-a, has been measured using a Rohde & Schwarz ZVB4 Vector Network Analyser (VNA) to characterize the antenna's impedance bandwidth. The antenna's reflection coefficient was measured before and after the rectifier was connected to the antenna. Fig. 4 shows that the measured S_{11} of the antenna covers the full 2.4 GHz ISM-band (2.4-2.5 GHz) with and without the rectifier, showing a maximum fractional bandwidth of ≈5%.

While port 2 adopts a balanced feed, a single-ended SMA was used to measure the mutual coupling between the ports with the two-port VNA. While this results in higher coupling than simulated (Fig. 2-c), it validates the improved isolation over a conventional microstrip feed at port 2. The measured mutual coupling between the ports (S_{21}) shows over 19 dB isolation at 2.4 GHz.

As the textile antenna is targeted at wearable applications, the S_{11} was characterized while conforming to different body parts. Fig. 5 shows the measured S_{11} of the antenna under bending on the body, as shown in Fig. 3-b. It can be seen that despite having a compact ground plane of 74×100 mm^2

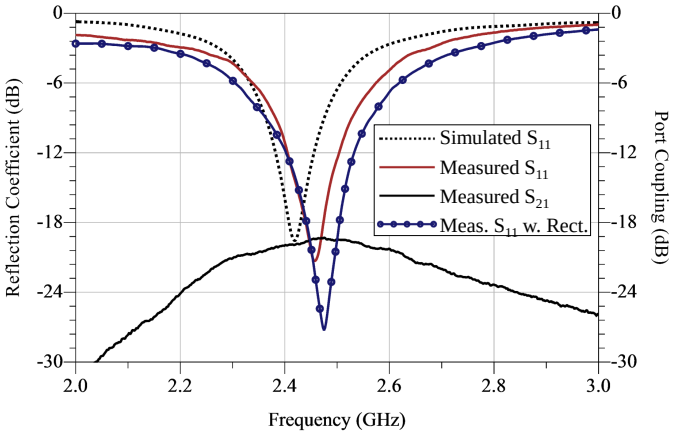

Fig. 4. Simulated and measured s-parameters of the proposed antenna, in space, before and after connecting the rectifier.

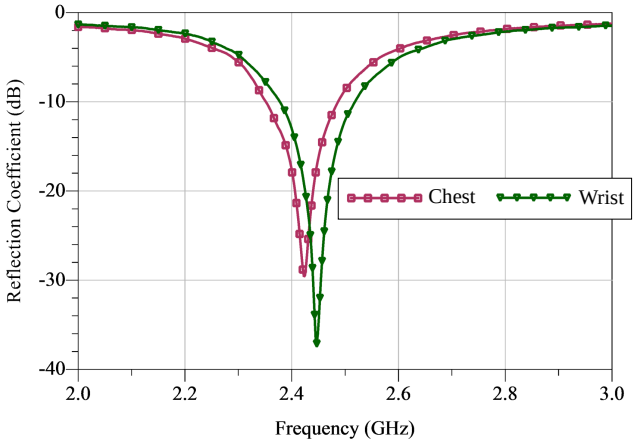

Fig. 5. Measured reflection coefficient of the antenna on a user's chest and while bending over a 3 cm radius around the wrist.

(0.47λ^2), the antenna still maintains high isolation from the body with minimal influence on its impedance bandwidth.

The antenna's 3D polarimetric radiation patterns were measured in an anechoic chamber on a body-shadow phantom, as shown in Fig. 3-c. The phantom uses radiation absorber to minimise the signal through the body while including the diffraction around the body that would be experienced in reality. This phantom is more suitable for 3D pattern measurements than liquid-filled phantoms [15]. The total efficiency of the textile antenna on the body phantom, inclusive of mismatch and rectifier-coupling losses, was then calculated with respect to a reference monopole as described in [15]. Fig. 6 shows the 3D measured directivity patterns and the polarization of the antenna.

The antenna achieves a peak measured directivity of 8.9 dBi. This agrees with the simulated 9.2 dBi directivity of the antenna placed on a large skin layer. Based on the measured total efficiency of −3.9 dB (41%), the measured realized gain of the antenna is 5.0 dBi. The measured co-/cross-polarization isolation is over 13 dB in the 3D half-power beamwidth. As

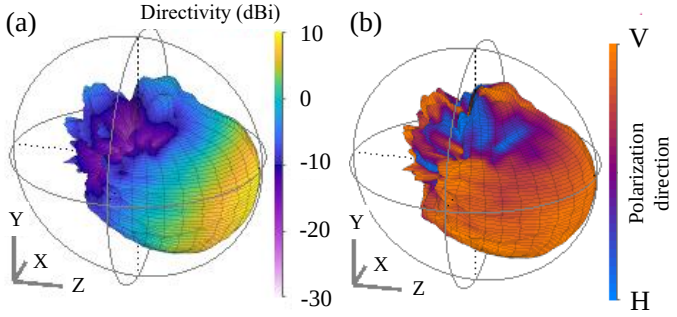

Fig. 6. Measured 3D radiation patterns of the antenna on a human phantom chest: (a) directivity and (b) polarization.

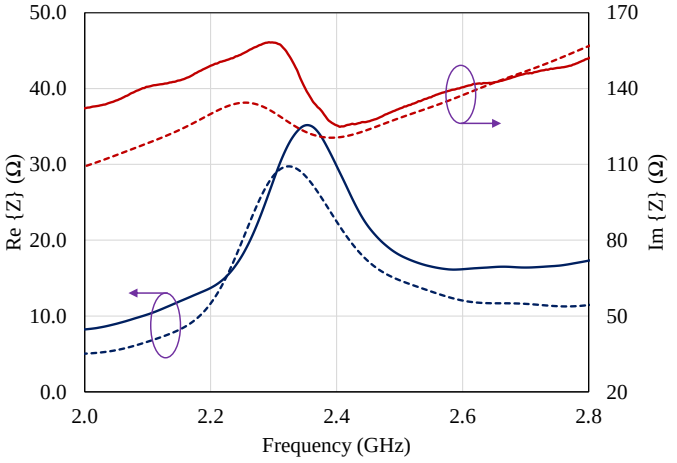

Fig. 7. Simulated (dashed) and measured (solid) differential input impedance of port 2 which directly conjugates the rectifier's reactance at 2.4 GHz.

shown in Fig. 6, the antenna's main broadside off-body lobe achieves maintains high polarization purity.

B. Wearable Rectenna Measurements

The first step in characterizing the rectenna's performance is measuring the antenna's input impedance on port 2. As port 2 utilizes a balanced feed, a differential test setup is required to accurately measure the antenna's impedance. A coaxial jig, shown in Fig. 3-c, was used to measure the impedance with a two-port VNA [16]. The simulated and measured input impedances at port 2 are shown in Fig. 7.

The measured input impedance of the antenna of 28.5+j125Ω has been used to re-simulate the rectifier's DC output for varying input powers at 2.41 GHz. The rectifier's large-signal PCE was simulated using harmonic balance in Keysight ADS based on the same model used to extract the optimum input impedance. Fig. 8 shows the simulated PCE of the rectifier based on the measured antenna's impedance.

In order to measure the rectifier's output, a wireless power source is required as the rectifier cannot be connected directly to 50Ω Continuous Wave (CW) generators. The VNA, set to transmit in CW mode at 2.41 GHz, was connected to a simple wire dipole antenna positioned at 60 cm from the rectenna. The rectenna was placed on a user's arm while performing

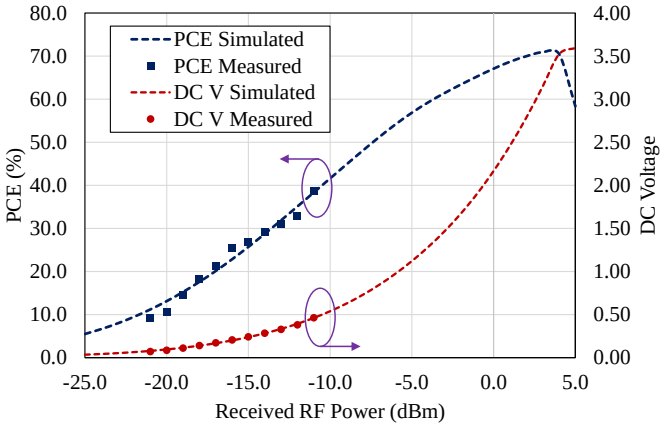

Fig. 8. Simulated and measured PCE and DC voltage output, across a 7 kΩ load, of the rectenna while placed directly on the user's body.

TABLE I
COMPARISON WITH RECENT TEXTILE WEARABLE RECTENNAS

	This work	TAP'20 [3]	TAP'20 [5]	TMTT'18 [17]
Freq (GHz)	**2.41**	0.82	2.45	2.45
Application	**SWIPT**	WPT	WPT	WPT
EH Gain	**6.4 dBi**	0.8 dBi	5.0 dBi	6.3 dBi
Comms. Gain	**5.0 dBi**	None	None	None
Matching Network	**Not needed**	Lumped inductor	Transmission line	Tapered line
Peak PCE	**71%**	58%	70%	64.6%

the measurements to demonstrate the rectenna's output in a real-world use-case. Port 1 (the communications port) was terminated with a 50Ω SMA termination to mimic an active receiver absorbing power while the rectenna is harvesting.

The power received by the rectenna was estimated using an identical textile microstrip patch with a 50Ω feed, connected to the VNA's port. The rectifier output was connected to a 7 kΩ load resistor, the optimal load extracted from simulation. Fig. 8 shows the simulated and measured DC output of the rectenna from a wireless 2.41 GHz CW source. Due to the maximum CW output of 15 dBm from the VNA, the measurements were only performed below −10 dBm. It can be seen that the simulated and measured DC output of the rectifier agree very closely, validating the peak simulated PCE of 71% from 3 dBm of power.

The proposed antenna/rectenna is compared to state-of-art textile antennas and rectennas in Table I. Despite operating as a simultaneous information and power receiver, the proposed antenna achieves state-of-art PCE and radiation properties. Additionally, the size and materials required to realize the antenna are the same as reported low-cost fully-textile antennas, without requiring rigid low-loss PCBs for the rectifier as in [17] or lumped inductors as with [3] and [5].

IV. CONCLUSION

This paper presented a novel dual-port antenna design approach for realizing highly-integrated SWIPT antennas. The

proposed textile antenna is demonstrated for simultaneous communications and energy harvesting in the 2.4 GHz ISM-band while occupying the same area as a standard microstrip patch antenna. The antenna has a 5.0 dB gain and an S_{11} bandwidth covering the 2.4 GHz ISM-band in presence and absence of a human body. The rectenna achieves a high measured PCE approaching 40% at -10 dBm, when measured on-body, and a simulated peak PCE over 70%, with the simulation and measurement showing a very close agreement.

This work will enable new applications of RFEH for both wearable and non-wearable applications combining antenna-rectifier co-design with common antenna designs. Full duplex implementations, multi-band SWIPT antennas, and SWIPT-powered antenna arrays are among the new research streams enabled by this work.

REFERENCES

[1] A. Pellegrini, A. Brizzi, L. Zhang, K. Ali, Y. Hao, X. Wu, C. C. Constantinou, Y. Nechayev, P. S. Hall, N. Chahat, M. Zhadobov, and R. Sauleau, "Antennas and Propagation for Body-Centric Wireless Communications at Millimeter-Wave Frequencies: A Review [Wireless Corner]," *IEEE Antennas Propag. Magazine*, vol. 55 no. 4, pp. 262 – 287, 2013.

[2] L. Corchia, G. Monti, and L. Tarricone, "Wearable Antennas: Non-textile Versus Fully Textile Solutions," *IEEE Antennas and Propagation Magazine*, vol. 61, 2, pp. 71 – 83, 2019.

[3] M. Wagih, A. S. Weddell, and S. Beeby, "Omnidirectional Dual-Polarized Low-Profile Textile Rectenna with over 50% Efficiency for Sub-μW/cm^2 Wearable Power Harvesting," *IEEE Trans. Antennas Propag.*, vol. Early Access, 2020.

[4] G. Monti, L. Corchia, and L. Tarricone, "UHF Wearable Rectenna on Textile Materials," *IEEE Trans. Antennas. Propag.*, vol. 61, 7, pp. 3869 – 3873, 2013.

[5] D. Vital, S. Bhardwaj, and J. L. Volakis, "Textile Based Large Area RF-Power Harvesting System for Wearable Applications," *IEEE Trans. Antennas Propag.*, vol. 68, no. 3, pp. 2323 – 2331, 2019.

[6] M. Wagih, G. S. Hilton, A. S. Weddell, and S. Beeby, "Broadband Millimetre-Wave Textile-based Flexible Rectenna for Wearable Energy Harvesting ," *IEEE Trans. Microw Theory Techn*, vol. Early Access, 2020.

[7] H. Xiaomu, S. Yan, and G. A. E. Vandenbosch, "Wearable Button Antenna for Dual-Band WLAN Applications With Combined on and off-Body Radiation Patterns," *IEEE Trans. Antennas Propag.*, vol. 65 no. 3, pp. 1384 – 1387, 2017.

[8] X. Lu, P. Wang, D. Niyato, D. I. Kim, and Z. Han, "Wireless Networks With RF Energy Harvesting: A Contemporary Survey," *IEEE Communications Surveys & Tutorials*, vol. 17, 2, pp. 757 – 789, 2015.

[9] T. D. P. Perera, D. N. K. Jayakody, S. K. Sharma, S. Chatzinotas, and J. Li, "Simultaneous Wireless Information and Power Transfer (SWIPT): Recent Advances and Future Challenges," *IEEE Communication Surveys and Tutorials*, vol. 20, 1, pp. 264 – 302, 2018.

[10] P. Lu, C. Song, and K. M. Huang, "A Two-Port Multi-Polarization Rectenna with Orthogonal Hybrid Coupler for Simultaneous Wireless Information and Power Transfer (SWIPT)," *IEEE Trans. Antennas Propag.*, vol. Early Access, 2020.

[11] P. Lu, X.-S. Yang, and B.-Z. Wang, "A Two-Channel Frequency Reconfigurable Rectenna for Microwave Power Transmission and Data Communication," *IEEE Trans. Antennas Propag.*, vol. 65 no. 12, pp. 6976 – 6985, 2017.

[12] C. X. Mao, Y. Zhou, Y. Wu, H. Soewardiman, D. H. Werner, and J. S. Jur, "Low-Profile Strip-Loaded Textile Antenna with Enhanced Bandwidth and Isolation for Full-Duplex Wearable Applications," *IEEE Trans. Antennas Propag.*, vol. Early Access, 2020.

[13] M. Wagih, A. S. Weddell, and S. Beeby, "Rectennas for RF Energy Harvesting and Wireless Power Transfer: a Review of Antenna Design [Antenna Applications Corner]," *IEEE Antennas Propag. Mag.*, vol. 62 no. 5, 2020.

[14] H. J. Visser, S. Keyrouz, and A. B. Smolders, "Optimized Rectenna Design," *Wireless Power Transfer*, vol. 2, 1, pp. 44 – 50, 2017.

[15] D. L. Paul, H. Giddens, M. G. Paterson, G. S. Hilton, and J. P. McGeehan, "Impact of Body and Clothing on a Wearable Textile Dual Band Antenna at Digital Television and Wireless Communications Bands," *IEEE Trans. Antennas Propag.*, vol. 61 no. 4, pp. 2188 – 2194, 2013.

[16] K. Palmer and M. van Rooyen, "Simple broadband measurements of balanced loads using a network analyzer," *IEE Transactions on Instrumentation and Measurements*, vol. 55, no. 1, pp. 266 – 272, 2006.

[17] S.-E. Adami, P. Proynov, G. S. Hilton, G. Yang, C. Zhang, D. Zhu, Y. Li, S. P. Beeby, I. J. Craddock, and B. H. Stark, "A Flexible 2.45-GHz Power Harvesting Wristband With Net System Output From -24.3 dBm of RF Power," *IEEE Trans. Microw. Theory Techn.*, vol. 66 no. 1, pp. 380–395, 2018.

Appendix B

Literature Review SoA Comparisons

This appendix presents the tabular comparisons of several antennas, rectifiers, and rectennas reviewed in Chapter 2, based on the different rectenna topologies identified.

Comparisons of the following systems and components are presented:

- UHF rectennas compared based on their impedance matching architecture.
- UHF rectennas compared based on their polarization diversity.
- mmWave antenna designs proposed for rectennas from 20 to 30 GHz.
- mmWave antenna designs proposed for rectennas beyond 30 GHz.
- Fully-integrated CMOS mmWave rectifiers.
- Discrete Schottky-based mmWave rectifiers.
- Printed and flexible mmWave rectifiers.

TABLE B.1: Comparison of rectennas based on their impedance matching architecture

Lit.	**Topology**	Antenna	Matching	Frequency bands (GHz)	Fractional Bandwidth (rect-enna) **FoM**
2018 [11]	A	Narrow-Band Patch	Single-band tapered line	2.45 (single)	4%
2013 [13]	B	Single-band tapes	Single-band LC	0.5, 0.9, 1.8, 2.1	7%, 5%, 3%, 4-5% .
2018 [43]	B and C	Broadband slot, single band slot	T/Pi networks (single diode/band)	0.9, 2, 2.55	15%, 23.7%, 0.07%
2016 [33]	C	Frequency-independent Log-periodic	Transmission-line match	0.55, 0.75, 0.9, 1.8, 2.3	9%*, 3%*, 2.3%, 2.2%, 2.2%
2013 [26]	D	Broadband Yagi-Uda array	8th-order LC (voltage doubler/band)	1.8, 2.1	4%, 3%
2014 [89]	E	High-Q loop	Weighted capacitor bank	0.868	6.9%
2016 [109]	F	High-Z Dipole	N/A	0.55	21.1%
2017 [34]	G	High-Z Multi-band Dipole	N/A	0.95, 1.85-2.4	2%, 30%*

*Bandwidth at $S_{11} < -6dB$

TABLE B.2: Comparison of rectennas based on their polarization diversity

Lit.	Polarization	Antenna and Frequency	Primary Gain (**FoM**)	Secondary Gain (**FoM**)	Bandwidth (MHz)
2018 [11]	a: LP	2.45 GHz Patch	Co-Pol 7.3 dBi	X-Pol -15.2 dBi	50
2018 [143]	b: CP	5.8 GHz Slot	6 dBc	-14 dBc	100
2018 [149]	c: DLP	2.4 GHz Dual-Slot	H-LP 7.45 dBi	V-LP 7.63 dBi	140
2015 [85]	d: DCP	2.4 GHz Slot	7.9 dBc	7.9 dBc	60

TABLE B.3: Comparison of antenna designs proposed for rectennas from 20 to 30 GHz.

Rectenna	Freq.	Antenna Design	Peak Gain (dB)	−3 dB beam-width (°)	Polari-zation	Dim. (mm)	Substr-ate/ Tech-nology
2014 [224]	21 GHz†	Strip dipole	>4	>50	Linear	10×13	RO6002
2014 [220]	24 GHz*	4×4 SIW array	15	≈15	Linear	75×35	Duroid 5880
2014 [76]	24 GHz*	2×2 cavity-backed array	12.6	≈20	Circular	30×30	Duroid 5880
2015 [256]	24 GHz*	Folded dipole	−1	>60	Linear	3.7× 1.2× 0.12	65nm CMOS
2017 [257]	24 and 40 GHz*	DRA on slot an-tenna	−1 at 24 GHz, 0 at 40 GHz	65 at 24 GHz, 360 at 40 GHz	Linear	32× 32× 4.64	DRA on CMOS
2017 [75]	24 GHz*	2×2 mi-crostrip patch array	5	≈30	Linear	12×12	LCP
2019 [234]	22-28 GHz*	2×1 mi-crostrip patch array	NR (<5)	>50	Linear	NR: ≈10×10	Printed FLGR02 (tanδ= 0.03)
2019 [135]	28 GHz*	8×5 Rotman lens array	≈18	80	Linear	55×87	LCP
2020 [358]	24 GHz*	4×4 mi-crostrip patch array	13.8	<20	Linear	60×30**	RO3003
2020 [244]	24 to 40 GHz*	Single an-tipodal Vivaldi	>8 up to 30 GHz	50	Linear	16.5×9.5	Textile (tanδ= 0.026)

*50Ω antenna bandwidth; †complex impedance antenna; ‡simulated only; NR: not reported; **estimated.

TABLE B.4: Comparison of antenna designs proposed for rectennas beyond 30 GHz.

Rectenna	Freq.	Antenna Design	Peak Gain (dB)	−3 dB beam-width (°)	Polari-zation	Dim. (mm)	Substr-ate/ Tech-nology
1992 [204]	35 GHz*	Stripline dipole	NR	NR	Linear	NR: ≈5×3	Duroid
2014 [248]	35 GHz*	4×4 patch	19‡	18	Linear	21.7× 22.6	Duroid 5880
2016 [243]	35 GHz*	Fabry-Perot res-onator	17	NR	Circular	32× 32× 4.64	Wave-guide (air-filled)
2020 [246]	35 GHz*	Wave-guide Fabry-Perot	15.1	≈15	Linear	17.7× 17.7 × 2.2	Wave-guide (air-filled)
2016 [260]	60 GHz*	2×2 Grid array on package	8.9	≈15	Linear	10× 10× 0.5	CCL-HL832 (tanδ= 0.012)
2018 [359]	60 GHz*	8×1 mi-crostrip array	13.3‡	≈20	Linear	18× 7.8× 0.2	Thin film ceramic
2013 [259]	71 GHz*	$\lambda/4$ monopole	NR	NR	Linear	0.94× 0.75	65 nm CMOS
2015 [238]	94 GHz*	Coplanar Bow-tie	3.9‡	≈20	Linear	2× 2× 0.1	Thin film alumina
2018 [360]	94 GHz*	8×8 Mi-crostrip	9	≈25	Linear	7× 15	NPC F220A
2014 [361]	75-110 GHz *‡	Meander dipole	2.28‡	>180	Linear	0.53× 0.91	65 nm CMOS

*50Ω antenna bandwidth; †complex impedance antenna; ‡simulated only; NR: not reported; **estimated.

TABLE B.5: Comparison of CMOS mmWave rectifiers.

Lit.	Freq. (GHz)	Z-match	Process	1 V Sensitivity (dBm)	Max PCE
[258]'14	24	Parallel inductor	180nm	−2	1%*
[256]'15	24	Folded dipole	65nm	−10	NR
[260]'16	60	Transformer balun	40nm	6	28%
[265]'13	62	Series inductor	65nm	$-4^{\dagger}$	7%
[259]'13	71	Series inductor	65nm	5.2	8%

*Calculated from DC voltage across 1 MΩ load; †estimated.

TABLE B.6: Comparison of Schottky-based mmWave rectifiers.

Lit.	Freq. (GHz)	Z-match	Harmonics Termination	1 V Sensitivity	Max PCE
[76]'14	24	L-microstrip	radial stubs at f_0, f_1	9 dBm	37%
[358]'20	24	L-microstrip	radial stubs at f_0, f_1	≈12 dBm*	37%
[251]'13	25.7	Dual-microstrip stubs	NA	NR	≈17%
[204]'92	35	microstrip $\lambda/4$ transformer	Tapered line and shunt stubs LPF	9.2	35%
[243]'16	35	Coplanar stripline	LPF and tapered DC terminals	≈8 dBm	60%
[248]'14	35	L-microstrip	LPF only	≈4 dBm	67%
[238]'15	94	Coplanar stripline	LPF only	<0 dBm*	37.7%

*Calculated from the PCE curve; NR: not reported

TABLE B.7: Comparison of printed and flexible mmWave rectifiers.

Lit.	Frequency (GHz)	10 dBm DC V at Z-Load	Max PCE
[75]'17	24	0.8 V @ 739 Ω	7.6%
[135]'19	28	1.4 V @ 1 kΩ	30%
[234]'19	28	0.7 V @ 750 kΩ	<1%
[358]'20	24 GHz	0.65 V*@200Ω	35%

Bibliography

[1] N. Tesla, "The Transmission of Electrical Energy Without Wires As a Means For Furthering Peace," *Electrical World and Engineer*, pp. 21 – 24, January, 1905.

[2] P. Sparks, "The route to a trillion devices the outlook for iot investment to 2035," https://www.arm.com/-/media/arm-com/company/Investors/Other2017.

[3] W. Brown, "The History of Power Transmission by Radio Waves," *IEEE Trans. Microw. Theory Techn.*, vol. 32, 9, pp. 1230 – 1242, 1984.

[4] P. Grover and A. Sahai, "Shannon meets Tesla: Wireless information and power transfer," in *2010 IEEE International Symposium on Information Theory*, 2010.

[5] J. Garnica, R. A. Chinga, and J. Lin, "Wireless Power Transmission: From Far Field to Near Field," *Proceedings of the IEEE*, vol. 101, 6, pp. 1321 – 1331, 2013.

[6] A. Sharma, V. Singh, T. L. Bougher, and B. A. Cola, "A carbon nanotube optical rectenna," *Nature Nanotechnology*, vol. 10, p. 1027âĂŞ1032, 2015.

[7] X. Lu, P. Wang, D. Niyato, D. I. Kim, and Z. Han, "Wireless Networks With RF Energy Harvesting: A Contemporary Survey," *IEEE Communications Surveys & Tutorials*, vol. 17, 2, pp. 757 – 789, 2015.

[8] T. D. P. Perera, D. N. K. Jayakody, S. K. Sharma, S. Chatzinotas, and J. Li, "Simultaneous Wireless Information and Power Transfer (SWIPT): Recent Advances and Future Challenges," *IEEE Communication Surveys and Tutorials*, vol. 20, 1, pp. 264 – 302, 2018.

[9] B. Clerckx, A. Costanzo, A. Georgiadis, and N. B. Carvalho, "Wireless Power Transmission: From Far Field to Near Field," *IEEE Microw. Mag.*, vol. 19, 6, pp. 69 – 82, 2018.

[10] S. A. Nauroze, J. G. Hester, B. K. Tehrani, W. Su, J. Bito, R. Bahr, J. Kimionis, and M. M. Tentzeris, "Additively Manufactured RF Components and Modules: Toward Empowering the Birth of Cost-Efficient Dense and Ubiquitous IoT Implementations," *Proc. IEEE*, vol. 105, no. 4, pp. 702 – 722, 2017.

[11] S.-E. Adami, P. Proynov, G. S. Hilton, G. Yang, C. Zhang, D. Zhu, Y. Li, S. P. Beeby, I. J. Craddock, and B. H. Stark, "A Flexible 2.45-GHz Power Harvesting Wristband With Net System Output From -24.3 dBm of RF Power," *IEEE Trans. Microw. Theory Techn.*, vol. 66 no. 1, pp. 380–395, 2018.

[12] M. Wagih, A. S. Weddell, and S. Beeby, "Millimeter-Wave Power Harvesting: A Review," *IEEE Open Journal of Antennas and Propagation*, vol. 1, pp. 560 – 578, 2020.

[13] M. Pinuela, P. D. Mitcheson, and S. Lucyszyn, "Ambient RF Energy Harvesting in Urban and Semi-Urban Environments," *IEEE Trans. Microw. Theory Techn.*, vol. 61 no. 7, pp. 2715 – 2726, 2013.

[14] J. Bito, R. Bahr, J. G. Hester, S. A. Nauroze, A. Georgiadis, and M. M. Tentzeris, "A Novel Solar and Electromagnetic Energy Harvesting System With a 3-D Printed Package for Energy Efficient Internet-of-Things Wireless Sensors," *IEEE Trans. Microw. Theory Techn.*, vol. 65 no. 5, pp. 1831 – 1842, 2017.

[15] M. Wagih, A. S. Weddell, and S. Beeby, "Rectennas for RF Energy Harvesting and Wireless Power Transfer: a Review of Antenna Design [Antenna Applications Corner]," *IEEE Antennas Propag. Mag.*, vol. 62 no. 5, pp. 95 – 107, 2020.

[16] P. Koert and J. Cha, "Millimeter wave technology for space power beaming," *IEEE Trans. Mirow Theory Techn.*, vol. 40 no. 6, pp. 1251 – 1258, 1992.

[17] C. R. Valenta and G. D. Durgin, "Harvesting Wireless Power: Survey of Energy-Harvester Conversion Efficiency in Far-Field, Wireless Power Transfer Systems," *IEEE Microw. Mag.*, vol. 15, 4, pp. 108–120, 2014.

[18] G. Marrocco, "The art of UHF RFID antenna design: impedance-matching and size-reduction techniques," *IEEE Antennas Propag. Magazine*, vol. 50, 1, pp. 66 – 79, 2008.

[19] Yi Huang and Kevin Boyle, *Antennas: From Theory to Practice*. West Sussex, United Kingdom: John Wiley & Sons Ltd, 2008.

[20] H. J. Visser and R. J. M. Vullers, "RF Energy Harvesting and Transport for Wireless Sensor Network Applications: Principles and Requirements," *Proc. IEEE*, vol. 101, 6, pp. 1410 – 1423, 2013.

[21] U. Guler and M. Ghovanloo, "Power management in wireless power-sipping devices: A survey," *IEEE Circuits and Systems Magazine*, vol. 17, 4, pp. 64–82, 2015.

[22] S. K. Divakaran, D. D. Krishna, and Nasimuddin, "RF energy harvesting systems: An overview and design issues," *Int. J. RF and Microwave Computer-Aided Engineering*, vol. 29, no. 1, 2018.

[23] T. Soyata, L. Copeland, and W. Heinzelman, "Rf energy harvesting for embedded systems: A survey of tradeoffs and methodology," *IEEE Circuits and Systems Magazine*, vol. 16, 1, pp. 22 – 57, 2016.

[24] M. Cansiza, D. Altinel, and G. K. Kurt, "Efficiency in RF energy harvesting systems: A comprehensive review," *Energy*, vol. 174, pp. 292–309, 2019.

[25] R. Bansal, "Electropollution or Sustainable Energy? [Microwave Surfing]," *IEEE Microw. Mag.*, vol. 11, 7, pp. 20 – 22, 2010.

[26] H. Sun, Y. xin Guo, M. He, and Z. Zhong, "A Dual-Band Rectenna Using Broadband Yagi Antenna Array for Ambient RF Power Harvesting," *IEEE Antennas Wireless Propag. Lett.*, vol. 12, pp. 918 – 921, 2013.

[27] Z. Song and C. R. Sastry, "Passive RF energy harvesting scheme for wireless sensor," Patent US8 552 597B2.

[28] K. Xie, Y.-M. Liu, H.-L. Zhang, and L.-Z. Fu, "Harvest the ambient am broadcast radio energy for wireless sensors," *Journal Electromagnetic Waves and Applications*, vol. 25, 14-15, pp. 2054 – 2065, 2012.

[29] R. J. Vyas, B. B. Cook, Y. Kawahara, and M. M. Tentzeris, "E-WEHP: A Batteryless Embedded Sensor-Platform Wirelessly Powered From Ambient Digital-TV Signals," *IEEE Trans. Microw. Theory Techn.*, vol. 61, 6, pp. 2491 – 2505, 2013.

[30] A. S. Andrenko, X. Lin, and M. Zeng, "Outdoor rf spectral survey: A roadmap for ambient rf energy harvesting," in *TENCON 2015 - 2015 IEEE Region 10 Conference*, 2015.

[31] J. W. Matiko, N. J. Grabham, S. P. Beeby, and M. J. Tudor, "Review of the application of energy harvesting in buildings," *Measurement Science and Technology*, vol. 25, 012002, 2014.

[32] K. Mimis, D. Gibbins, S. Dumanli, and G. T. Watkins, "Ambient RF energy harvesting trial in domestic settings," *IET Microwaves, Antennas & Propagation*, vol. 9, 5, pp. 454 – 462, 2014.

[33] C. Song, Y. Huang, P. Carter, J. Zhou, S. Yuan, Q. Xu, and M. Kod, "A Novel Six-Band Dual CP Rectenna Using Improved Impedance Matching Technique for Ambient RF Energy Harvesting," *IEEE Trans. Antennas Propag.*, vol. 64, 7, pp. 3160 –3171, 2016.

[34] C. Song, Y. Huang, J. Zhou, P. Carter, S. Yuan, Q. Xu, and Z. Fei, "Matching Network Elimination in Broadband Rectennas for High-Efficiency Wireless Power Transfer and Energy Harvesting," *IEEE Transactions on Industrial Electronics*, vol. 64, 5, pp. 3950 – 3961, 2017.

[35] D. Willkomm, S. Machiraju, J. Bolot, and A. Wolisz, "Primary users in cellular networks: A large-scale measurement study," in *2008 3rd IEEE Symposium on New Frontiers in Dynamic Spectrum Access Networks*, 2008.

[36] A. Dolgov, R. Zane, and Z. Popovic, "Power management system for online low power rf energy harvesting optimization," *IEEE Trans. Circuits Systems I: Regular Papers*, vol. 57, 7, pp. 1802–1811, 2010.

[37] E. M. Jung, Y. Cui, T.-H. Lin, X. He, A. Eid, J. G. D. Hester, G. D. Abowd, T. E. Starner, W.-S. Lee, and M. M. Tentzeris, "A Wideband, Quasi-Isotropic, Kilometer-Range FM Energy Harvester for Perpetual IoT," *IEEE Microw. Wireless Compon. Lett*, vol. 30 no. 2, pp. 201 – 204, 2020.

[38] S. N. Daskalakis, R. Correia, G. Goussetis, M. M. Tentzeris, N. B. Carvalho, and A. Georgiadis, "Four-pam modulation of ambient fm backscattering for spectrally efficient low-power applications," *IEEE Trans. Microw. Theory Techn.*, vol. 66 no. 12, pp. 5909 – 5921, 2018.

[39] A. Okba, A. Takacs, and H. Aubert, "Compact rectennas for ultra-low-power wireless transmission applications," *IEEE Trans. Microw. Theory Techn.*, vol. 67, 5, pp. 1697 – 1707, 2019.

[40] X. Gu, L. Grauwin, D. Dousset, S. Hemour, and K. Wu, "Dynamic ambient rf energy density measurements of montreal for battery-free iot sensor network planning," *IEEE Internet of Things Journal*, pp. 1–1, 2021.

[41] L. Chen, B. Milligan, T. Qu, L. Jeevananthan, G. Shaker, and S. Safavi-Naeini, "Cellular wireless energy harvesting for smart contact lens applications [education corner]," *IEEE Antennas and Propagation Magazine*, vol. 60, 5, pp. 108 – 124, 2018.

[42] J. Bito, J. G. Hester, and M. M. Tentzeris, "Ambient RF Energy Harvesting From a Two-Way Talk Radio for Flexible Wearable Wireless Sensor Devices Utilizing Inkjet Printing Technologies," *IEEE Trans. Microw. Theory Techn.*, vol. 63, 12, pp. 4533–4543, 2015.

[43] V. Palazzi, J. Hester, J. Bito, F. Alimenti, C. Kalialakis, A. Collado, P. Mezzanotte, A. Georgiadis, L. Roselli, and M. M. Tentzeris, "A Novel Ultra-Lightweight Multiband Rectenna on Paper for RF Energy Harvesting in the Next Generation LTE Bands," *IEEE Trans. Microw. Theory Techn.*, vol. 66 no. 1, pp. 366 –379, 2018.

[44] K. Mimis, D. R. Gibbins, S. Dumanli, and G. T. Watkins, "The ant and the elephant: ambient RF harvesting from the uplink," *IET Microwaves, Antennas & Propagation*, vol. 11 no. 3, pp. 386 – 393, 2017.

[45] C. R. Valenta and G. D. Durgin, "Rectenna performance under power-optimized waveform excitation," in *2013 IEEE International Conference on RFID (RFID)*, 2013.

[46] G. Breed, "There's Nothing Magic About 50 Ohms," *High Frequency Electronics*, pp. 6 – 7, 2007.

[47] V. Kuhn, C. Lahuec, F. Seguin, and C. Person, "A Multi-Band Stacked RF Energy Harvester With RF-to-DC Efficiency Up to 84%," *IEEE Trans. Microw. Theory Techniq.*, vol. 63, 5, pp. 1768 – 1778, 2015.

[48] T. Matsunaga, E. Nishiyama, and I. Toyoda, "5.8-GHz Stacked Differential Rectenna Suitable for Large-Scale Rectenna Arrays With DC Connection," *IEEE Trans. Antennas Propag.*, vol. 63, 12, pp. 5944 – 5949, 2015.

[49] Y.-J. Ren and K. Chang, "5.8-ghz circularly polarized dual-diode rectenna and rectenna array for microwave power transmission," *IEEE Trans. Microw. Theory Techn.*, vol. 54 no. 4, pp. 1495 – 1502, 2006.

[50] P. Kamalinejad, C. Mahapatra, Z. Sheng, S. Mirabbasi, V. C. M. Leung, and Y. L. Guan, "Novel Design of 2.45-GHz Rectenna Element and Array for Wireless Power Transmission," *IEEE Access*, vol. 7, pp. 28 356 – 28 362, 2019.

[51] A. M. Jie, Nasimuddin, M. F. Karim, and K. T. Chandrasekaran, "A Wide-Angle Circularly Polarized Tapered-Slit-Patch Antenna With a Compact Rectifier for Energy-Harvesting Systems [Antenna Applications Corner]," *IEEE Antennas and Propagation Magazine*, vol. 61, 2, pp. 94 – 111, 2019.

[52] S. Yang and J. Kim, "Wireless power transmission using dipole rectennas made on flexible cellulose membrane," *IET Microwaves, Antennas & Propagation*, vol. 6, 7, pp. 756 – 760, 2012.

[53] S. Shen, Y. Zhang, C.-Y. Chiu, and R. Murch, "An Ambient RF Energy Harvesting System Where the Number of Antenna Ports Is Dependent on Frequency," *IEEE Trans. Microw. Theory Techn.*, vol. 67 no. 9, pp. 3821 – 3832, 2019.

[54] Y. Tawk, J. Costantine, F. Ayoub, and C. G. Christodoulou, "A Communicating Antenna Array with a Dual-Energy Harvesting Functionality [Wireless Corner]," *IEEE Antennas and Propagation Magazine*, vol. 60, 2, pp. 132 – 144, 2018.

[55] J.-K. Huang, W.-T. Hung, T.-H. Cheng, and S.-Y. Chen, "A 2.45-GHz high-efficiency loop-shaped PIFA rectenna for portable devices and wireless sensors," in *2015 IEEE International Symposium on Antennas and Propagation & USNC/URSI National Radio Science Meeting*, 2015.

[56] C. Liu, Y.-X. Guo, H. Sun, and S. Xiao, "Design and Safety Considerations of an Implantable Rectenna for Far-Field Wireless Power Transfer," *IEEE Trans. Antennas Propag.*, vol. 62, 11, pp. 5798 – 5806, 2014.

[57] T. Sakamoto, Y. Ushijima, E. Nishiyama, M. Aikawa, and I. Toyoda, "5.8-GHz Series/Parallel Connected Rectenna Array Using Expandable Differential Rectenna Units," *IEEE Trans. Antennas Propag.*, vol. 61, 9, pp. 4872 – 4875, 2013.

[58] J. Zhang, X. Bai, W. Han, B. Zhao, L. Xu, and J. Wei, "The design of radio frequency energy harvesting and radio frequencyâĂŘbased wireless power transfer system for batteryâĂŘless selfâĂŘsustaining applications," *International Journal of RF and Microwave Computer-Aided Engineering*, vol. 29, 1, pp. 1–13, 2018.

[59] Y. Shi, Y. Fan, Y. Li, L. Yang, and M. Wang, "An Efficient Broadband Slotted Rectenna for Wireless Power Transfer at LTE Band," *IEEE Trans. Antennas Propag.*, vol. Early Access, pp. 1 – 1, 2018.

[60] M.-J. Nie, X.-X. Yang, G.-N. Tan, and B. Han, "A compact 2.45-ghz broadband rectenna using grounded coplanar waveguide," *IEEE Antennas Wireless Propag. Lett.*, vol. 14, pp. 986 – 989, 2015.

[61] Z. Harouni, L. Cirio, L. Osman, A. Gharsallah, and O. Picon, "A dual circularly polarized 2.45-ghz rectenna for wireless power transmission," *IEEE Antennas Wireless Propag. Lett.*, vol. 10, pp. 306 – 309, 2011.

[62] V. Palazzi, M. D. Prete, and M. Fantuzzi, "Scavenging for Energy: A Rectenna Design for Wireless Energy Harvesting in UHF Mobile Telephony Bands," *IEEE Microw. Mag.*, vol. 18, 1, pp. 91 – 99, 2017.

[63] M. Mattsson, C. I. Kolitsidas, and B. L. G. Jonsson, "Dual-Band Dual-Polarized Full-Wave Rectenna Based on Differential Field Sampling," *IEEE Antennas Wireless Propag. Lett.*, vol. 17, 6, pp. 956 – 959, 2018.

[64] B. L. Pham and A.-V. Pham, "Triple bands antenna and high efficiency rectifier design for rf energy harvesting at 900, 1900 and 2400 mhz," in *2013 IEEE MTT-S International Microwave Symposium Digest (MTT)*, 2013.

[65] S. Shen, C.-Y. Chiu, and R. D. Murch, "A Dual-Port Triple-Band L-Probe Microstrip Patch Rectenna for Ambient RF Energy Harvesting," *IEEE Antennas Wireless Propag. Lett.*, vol. 16, pp. 3071 – 3074, 2017.

[66] M. Wagih, A. S. Weddell, and S. Beeby, "Millimeter-Wave Textile Antenna for On-Body RF Energy Harvesting in Future 5G Networks," in *2019 IEEE Wireless Power Transfer Conference (WPTC)*, 2019.

[67] R. M. E. Khosht, M. A. E. Feshawy, M. A. E. Shorbagy, M. N. Farag, A. E. E. Said, H. F. Hammad, and A. T. Abdel-Hamid, "A foldable textile-based broadband archimedean spiral rectenna for rf energy harvesting," in *2016 16th Mediterranean Microwave Symposium (MMS)*, 2016.

[68] J. Hagerty, F. Helmbrecht, W. McCalpin, R. Zane, and Z. Popovic, "Recycling ambient microwave energy with broad-band rectenna arrays," *IEEE Trans. Microw. Theory Techn.*, vol. 52, 3, pp. 1014 – 1024, 2002.

[69] M. Arrawatia, M. S. Baghini, and G. Kumar, "Broadband Bent Triangular Omnidirectional Antenna for RF Energy Harvesting," *IEEE Antennas Wireless Propag. Lett.*, vol. 15, pp. 36 – 39, 2015.

[70] M. Fantuzzi, D. Masotti, and A. Costanzo, "A Novel Integrated UWBâĂŞUHF One-Port Antenna for Localization and Energy Harvesting," *IEEE Trans. Antennas Propag.*, vol. 63, 9, pp. 3839 – 3848, 2015.

[71] S. Shen, C.-Y. Chiu, and R. D. Murch, "Multiport Pixel Rectenna for Ambient RF Energy Harvesting," *IEEE Trans. Antennas Propag.*, vol. 66, 2, pp. 644 –656, 2018.

[72] Z. Hameed and K. Moez, "A 3.2 V -15 dBm Adaptive Threshold-Voltage Compensated RF Energy Harvester in 130 nm CMOS," *IEEE Transactions on Circuits and Systems I: Regular Papers*, vol. 62, 4, pp. 948 – 958, 2015.

[73] H. Sun and W. Geyi, "A New Rectenna With All-Polarization-Receiving Capability for Wireless Power Transmission," *IEEE Antennas Wireless Propag. Lett.*, vol. 15, pp. 814 – 817, 2016.

[74] J. Kimionis, M. Isakov, B. S. Koh, A. Georgiadis, and M. M. Tentzeris, "3D-Printed Origami Packaging With Inkjet-Printed Antennas for RF Harvesting Sensors," *IEEE Trans. Microw. Theory Techn.*, vol. 63, 12, pp. 4521 – 4532, 2015.

[75] J. Bito, V. Palazzi, J. Hester, R. Bahr, F. Alimenti, P. Mezzanotte, L. Roselli, and M. M. Tentzeris, "Millimeter-wave ink-jet printed RF energy harvester for next generation flexible electronics," in *2017 IEEE Wireless Power Transfer Conference (WPTC)*, 2017.

[76] S. Ladan, A. B. Guntupalli, and K. Wu, "A High-Efficiency 24 GHz Rectenna Development Towards Millimeter-Wave Energy Harvesting and Wireless Power Transmission," *IEEE Trans. Circuits And Systems*, vol. 61, 12, pp. 3358 – 3366, 2014.

[77] Y.-S. Chen and C.-W. Chiu, "Maximum Achievable Power Conversion Efficiency Obtained Through an Optimized Rectenna Structure for RF Energy Harvesting," *IEEE Trans. Antennas Propag.*, vol. 65, 5, pp. 2305 – 2317, 2017.

[78] S. Chandravanshi, S. S. Sarma, and M. J. Akhtar, "Design of Triple Band Differential Rectenna for RF Energy Harvesting," *IEEE Trans. Antennas Propag.*, vol. 66, 6, pp. 2716 – 2726, 2018.

[79] H. Sun and W. Geyi, "A New Rectenna Using Beamwidth-Enhanced Antenna Array for RF Power Harvesting Applications," *IEEE Antennas Wireless Propag. Lett.*, vol. 16, pp. 1451 – 1454, 2016.

[80] C. Song, Y. Huang, J. Zhou, J. Zhang, S. Yuan, and P. Carter, "A High-Efficiency Broadband Rectenna for Ambient Wireless Energy Harvesting," *IEEE Trans. Antennas Propag.*, vol. 63, 8, pp. 3486–3495, 2015.

[81] D. Wang, X. A. Nghiem, and R. Negra, "Design of a 57% bandwidth microwave rectifier for powering application," in *2014 IEEE Wireless Power Transfer Conference*, 2014.

[82] Q. Awais, Y. Jin, H. T. Chattha, M. Jamil, H. Qiang, and B. A. Khawaja, "A Compact Rectenna System With High Conversion Efficiency for Wireless Energy Harvesting," *IEEE Access*, vol. 6, pp. 35 857 – 35 866, 2018.

[83] C. Song, Y. Huang, P. Carter, J. Zhou, S. D. Joseph, and G. Li, "Novel Compact and Broadband Frequency-Selectable Rectennas for a Wide Input-Power and Load Impedance Range," *IEEE Trans. Antennas Propag.*, vol. 66, 7, pp. 3306 – 3316, 2018.

[84] A. Z. Ashoor and O. M. Ramahi, "Polarization-Independent Cross-Dipole Energy Harvesting Surface," *IEEE Trans. Microw. Theory Techn.*, vol. 67 no. 3, pp. 1130 –1137, 2019.

[85] J.-H. Chou, D.-B. Lin, K.-L. Weng, and H.-J. Li, "All Polarization Receiving Rectenna With Harmonic Rejection Property for Wireless Power Transmission," *IEEE Trans. Antennas Propag.*, vol. 62, 10, pp. 5242 – 5249, 2014.

[86] T. S. Almoneef, F. Erkmen, and O. M. Ramahi, "Harvesting the Energy of Multi-Polarized Electromagnetic Waves," *Scientific Reports*, vol. 7, pp. 3354 – 3356, 2017.

[87] H. Takhedmit, L. Cirio, S. Bellal, D. Delcroix, and O. Picon, "Compact and efficient 2.45 GHz circularly polarised shorted ring-slot rectenna," *Electronics Letters*, vol. 48, 5, pp. 253 – 254, 2015.

[88] M. A. Abouzied, K. Ravichandran, and E. Sanchez-Sinencio, "A fully integrated reconfigurable self-startup rf energy-harvesting system with storage capability," *IEEE Journal of Solid-State Circuits*, vol. 52, 3, pp. 704 – 719, 2017.

[89] M. Stoopman, S. Keyrouz, H. J. Visser, K. Philips, and W. A. Serdijn, "Co-design of a cmos rectifier and small loop antenna for highly sensitive rf energy harvesters," *IEEE Journal of Solid-State Circuits*, vol. 49 no. 3, pp. 622 – 634, 2014.

[90] J. Kang, S. Rao, P. Chiang, and A. Natarajan, "Design and Optimization of Area-Constrained Wirelessly Powered CMOS UWB SoC for Localization Applications," *IEEE Trans. Microw. Theory Techn.*, vol. 64, 4, pp. 1042 – 1054, 2016.

[91] V. Marian, B. Allard, C. Vollaire, and J. Verdier, "Strategy for microwave energy harvesting from ambient field or a feeding source," *IEEE Transactions on Power Electronics*, vol. 27, 11, pp. 4481 – 4491, 2012.

[92] U. Muncuk, te Kubra Alemdar, J. D. Sarode, and K. R. Chowdhury, "Multiband Ambient RF Energy Harvesting Circuit Design for Enabling Batteryless Sensors and IoT," *IEEE Internet of Things Journal*, vol. 5, 4, pp. 2700 –2714, 2018.

[93] S. Shieh and M. Kamarei, "Fast Start-Up RF Energy Harvester Design for GSM-900 Uplink Band," *IEEE Transactions on Circuits and Systems II: Express Briefs*, vol. 66, 4, pp. 582 – 586, 2019.

[94] P. Lu, K. Huang, Y. Yang, F. Cheng, and L. Wu, "Frequency Reconfigurable Rectenna with an Adaptive Matching Stub for Microwave Power Transmission," *IEEE Antennas Wireless Propag. Lett.*, vol. Early Access, pp. 1 – 1, 2019.

[95] S. M. Asif, J. Hansen, M. S. Khan, S. D. Walden, M. O. Jensen, B. D. Braaten, and D. L. Ewert, "Design and In Vivo Test of a Batteryless and Fully Wireless Implantable Asynchronous Pacing System," *IEEE Transactions on Biomedical Engineering*, vol. 63, 5, pp. 1070 – 1081, 2018.

[96] W. Lin, R. W. Ziolkowski, and J. Huang, "Electrically Small, Low Profile, Highly Efficient, Huygens Dipole Rectennas for Wirelessly Powering Internet-of-Things (IoT) Devices," *IEEE Trans. Antennas Propag.*, vol. Early access, 2019.

[97] K. R. Sadagopan, J. Kang, Y. Ramadass, and A. Natarajan, "A cm-Scale 2.4-GHz Wireless Energy Harvester With NanoWatt Boost Converter and Antenna-Rectifier Resonance for WiFi Powering of Sensor Nodes," *IEEE Journal of Solid-State Circuits*, vol. 53, 12, pp. 3396 – 3406, 2018.

[98] M.-C. Tang, H. Wang, and R. W. Ziolkowski, "Design and Testing of Simple, Electrically Small, Low-Profile, Huygens Source Antennas With Broadside Radiation Performance," *IEEE Trans. Antennas Propag.*, vol. 64, 11, pp. 4607 – 4617, 2016.

[99] A. Y.-S. Jou, H. Pajouhi, R. Azadegan, and S. Mohammadi, "A cmos integrated rectenna for implantable applications," in *2016 IEEE MTT-S International Microwave Symposium (IMS)*, 2016.

[100] H. Rahmani and A. Babaakhani, "A 434 mhz dual-mode power harvesting system with an on-chip coil in 180 nm cmos soi for mm-sized implants," in *2018 IEEE MTT-S International Microwave Symposium (IMS)*, 2018.

[101] B. Zhao, N.-C. Kuo, B. Liu, Y.-A. Li, L. Iotti, and A. M. Niknejad, "A 5.8ghz power-harvesting 116μmx116μm "dielet" near-field radio with on-chip coil antenna," in *2018 IEEE International Solid - State Circuits Conference - (ISSCC)*, 2018.

[102] Y. Sun, D. Li, and A. Babakhani, "A wirelessly-powered i.460hz transmitter with on-chip antennas in i80nm cmos," in *2018 IEEE International Solid - State Circuits Conference - (ISSCC)*, 2018.

[103] P. V. Nikitin and K. V. S. Rao, "Antennas and Propagation in UHF RFID Systems," in *2008 IEEE International Conference on RFID*, 2008.

[104] J. Yi, W.-H. Ki, and C.-Y. Tsui, "Analysis and Design Strategy of UHF Micro-Power CMOS Rectifiers for Micro-Sensor and RFID Applications," *IEEE Trans. Circuits And Systems*, vol. 54 no. 1, pp. 153 – 166, 2007.

[105] L. Grasso, G. Sorbello, E. Ragonese, and G. Palmisano, "Codesign of Differential-Drive CMOS Rectifier and Inductively Coupled Antenna for RF Harvesting," *IEEE Trans. Microw. Theory Techn.*, vol. 68 no. 1, pp. 365 – 376, 2020.

[106] J. McSpadden, L. Fan, and K. Chang, "Design and experiments of a high-conversion-efficiency 5.8-GHz rectenna," *IEEE Trans. Microw. Theory Techn.*, vol. 46, 12, pp. 2053 – 2060, 1998.

[107] H.-T. Zhong, X.-X. Yang, C. Tan, and K. Yu, "Triple-band polarization-insensitive and wide-angle metamaterial array for electromagnetic energy harvesting," *Appl. Phys. Lett.*, vol. 109, pp. 1 – 4, 2016.

[108] H.-T. Zhong, X.-X. Yang, X.-T. Song, Z.-Y. Guo, and F. Yu1, "Wideband metamaterial array with polarization-independent and wide incident angle for harvesting ambient electromagnetic energy and wireless power transfer," *Appl. Phys. Lett.*, vol. 111, pp. 1 – 4, 2017.

[109] H. Miyagoshi, K. Noguchi, K. Itoh, and J. Ida, "High-impedance wideband folded dipole antenna for energy harvesting applications," in *2014 International Symposium on Antennas and Propagation Conference Proceedings*, 2014.

[110] F. Erkmen, T. S. Almoneef, and O. M. Ramahi, "Electromagnetic Energy Harvesting Using Full-Wave Rectification," *IEEE Trans. Microw. Theory Techn.*, vol. 65, 5, pp. 1843 – 1851, 2017.

[111] H. J. Visser, S. Keyrouz, and A. B. Smolders, "Optimized Rectenna Design," *Wireless Power Transfer*, vol. 2, 1, pp. 44 – 50, 2017.

[112] A. Takacs, H. Aubert, and S. Charlot, "Ultra-compact ku band rectenna," in *2015 IEEE MTT-S International Microwave Symposium*, 2015.

[113] S. Preradovic and N. Karmakar, "Chipless millimeter wave identification (mmid) tag at 30 ghz," in *2011 41st European Microwave Conference*, 2011.

[114] T. S. Almoneefa and O. M. Ramahi, "Metamaterial electromagnetic energy harvester with near unity efficiency," *Appl. Phys. Lett.*, vol. 106, pp. 1 – 4, 2015.

[115] L. Li, X. Zhang, C. Song, W. Zhang, T. Jia, and Y. Huang, "Compact Dual-Band, Wide-Angle, Polarization-Angle-Independent Rectifying Metasurface for Ambient Energy Harvesting and Wireless Power Transfer," *IEEE Trans. Microw. Theory Techn.*, vol. Early Access, DOI: 10.1109/TMTT.2020.3040962, 2020.

[116] Z. He, H. Lin, and C. Liu, "Codesign of a Schottky Diode's and Loop Antenna's Impedances for Dual-Band Wireless Power Transmission," *IEEE Antennas Wireless Propag. Lett.*, vol. 19 no. 10, pp. 1813 – 1817, 2020.

[117] C. A. Balanis, "Antenna Theory: Analysis and Design. Third Edition," *Wiley Interscience*, pp. 84 – 85, 2005.

[118] N. Shinohara and H. Matsumoto, "Experimental study of large rectenna array for microwave energy transmission," *IEEE Trans. Microw. Theory Techn.*, vol. 46, 3, pp. 261 – 268, 1998.

[119] Y. Song, J. Wang, and X. Luo, "Design of a high gain quasi-yagi antenna and array for rectenna," in *2017 IEEE International Symposium on Antennas and Propagation & USNC/URSI National Radio Science Meeting*, 2017.

[120] N. P. Basta, E. A. Falkenstein, and Z. Popovic, "Bow-tie rectenna arrays," in *2015 IEEE Wireless Power Transfer Conference (WPTC)*, 2015.

[121] T. S. Almoneef, F. Erkmen, M. A. Alotaibi, and O. M. Ramahi, "A New Approach to Microwave Rectennas Using Tightly Coupled Antennas," *IEEE Trans. Antennas Propag.*, vol. 66, 4, pp. 1714 – 1724, 2018.

[122] Y. Liu, K. Huang, Y. Yang, and B. Zhang, "A Low-Profile Lightweight Circularly Polarized Rectenna Array Based on Coplanar Waveguide," *IEEE Antennas Wireless Propag. Lett.*, vol. 17, 9, pp. 1659 – 1663, 2018.

[123] Y. Yang, L. Li, J. Li, Y. Liu, B. Zhang, H. Zhu, and K. Huang, "A Circularly Polarized Rectenna Array Based on Substrate Integrated Waveguide Structure With Harmonic Suppression," *IEEE Antennas Wireless Propag. Lett.*, vol. 17, 4, pp. 684 – 688, 2018.

[124] D.-Y. Kim, J. W. Lee, T. K. Lee, and C. S. Cho, "Design of SIW Cavity-Backed Circular-Polarized Antennas Using Two Different Feeding Transitions," *IEEE Trans. Antennas Propag.*, vol. 59, 4, pp. 1398 – 1403, 2011.

[125] G. Q. Luo, X. H. Zhang, L. X. Dong, W. J. Li, and L. L. Sun, "A Gain Enhanced Cavity Backed Slot Antenna using High Order Cavity Resonance," *Journal of Electromagnetic Waves and Applications*, vol. 25, pp. 1273 – 1279, 2011.

[126] O. Bjorkqvist, O. Dahlberg, G. Silver, C. Kolitsidas, O. Quevedo-Teruel, and B. Jonsson, "Wireless Sensor Network Utilizing Radio-Frequency Energy Harvesting for Smart Building Applications [Education Corner]," *IEEE Trans. Microw. Theory Techn.*, vol. 60, 5, pp. 124 – 136, 2018.

[127] Y.-S. Chen and J.-W. You, "A Scalable and Multidirectional Rectenna System for RF Energy Harvesting," *IEEE Transactions on Components, Packaging and Manufacturing Technology*, vol. 8, 12, pp. 2060 – 2072, 2018.

[128] D. H. N. Bui, T.-P. Vuong, J. Verdier, B. Allard, and P. Benech, "Design and Measurement of 3D Flexible Antenna Diversity for Ambient RF Energy Scavenging in Indoor Scenarios," *IEEE Access*, vol. 7, pp. 17 033 – 17 044, 2019.

[129] H. Sun and W. Geyi, "A New Rectenna Using Beamwidth-Enhanced Antenna Array for RF Power Harvesting Applications," *IEEE Antennas Wireless Propag. Lett.*, vol. 16, pp. 1451 – 1454, 2016.

[130] Y.-Y. Hu and S. Sun, "Dual-polarized and multi-beam cross-mesh array antenna for rf energy harvesting applications," in *2018 IEEE International Symposium on Antennas and Propagation & USNC/URSI National Radio Science Meeting*, 2018.

[131] Y.-Y. Hu, S. Sun, H. Xu, and H. Sun, "Grid-Array Rectenna With Wide Angle Coverage for Effectively Harvesting RF Energy of Low Power Density," *IEEE Trans. Microw. Theory Techn.*, vol. 67, 1, pp. 402 – 413, 2019.

[132] E. Vandelle, D. H. N. Bui, T.-P. Vuong, G. Ardila, K. Wu, and S. Hemour, "Harvesting Ambient RF Energy Efficiently With Optimal Angular Coverage," *IEEE Trans. Antennas Propag.*, vol. 67, 3, pp. 1862 – 1873, 2019.

[133] K. T. Chandrasekaran, N. Nasimuddin, A. Alphones, and M. F. Karim, "Compact circularly polarized beamâĂŘswitching wireless power transfer system for ambient energy harvesting applications," *Int. J. RF and Microw Computer-Aided Engineering*, vol. 29, no. 1, pp. 1 – 10, 2017.

[134] D.-J. Lee, S.-J. Lee, I.-J. Hwang, W.-S. Lee, and J.-W. Yu, "Hybrid Power Combining Rectenna Array for Wide Incident Angle Coverage in RF Energy Transfer," *IEEE Trans. Microw. Theory Techn.*, vol. 65, 9, pp. 3409 – 3418, 2017.

[135] A. Eid, J. Hester, and M. M. Tentzeris, "A Scalable High-Gain and Large-Beamwidth mm-Wave Harvesting Approach for 5G-powered IoT," in *2019 IEEE MTT-S International Microwave Symposium (IMS)*, 2019.

[136] A. Eid, J. Hester, and E. M. Tentzeris, "Rotman Lens-Based Wide Angular Coverage and High Gain Semi-Passive Architecture for Ultra-Long Range mm-wave RFIDs," *IEEE Antennas Wireless Propag. Lett.*, vol. 19 no. 11, pp. 1943 – 1947, 2020.

[137] X. Quan and R. Li, "A Broadband Dual-Polarized Omnidirectional Antenna for Base Stations," *IEEE Trans. Antennas Propag.*, vol. 61, 2, pp. 943 – 947, 2013.

[138] Y. Cui, R. Li, and H. Fu, "A Broadband Dual-Polarized Planar Antenna for 2G/3G/LTE Base Stations," *IEEE Trans. Antennas Propag.*, vol. 62, 9, pp. 4836 – 4840, 2014.

[139] K. R. Mahmoud and A. M. Montaser, "Performance of Tri-Band Multi-Polarized Array Antenna for 5G Mobile Base Station Adopting Polarization and Directivity Control," *IEEE Access*, vol. 6, pp. 8682 – 8694, 2018.

[140] M. Ali, G. Yang, and R. Dougal, "Miniature Circularly Polarized Rectenna With Reduced Out-of-Band Harmonics," *IEEE Antennas Wireless Propag. Lett.*, vol. 5, pp. 107 – 110, 2006.

[141] T.-C. Yo, C.-M. Lee, C.-M. Hsu, and C.-H. Luo, "Compact Circularly Polarized Rectenna With Unbalanced Circular Slots," *IEEE Trans. Antennas Propag.*, vol. 56, 3, pp. 882 – 886, 2008.

[142] J. Heikkinen and M. Kivikoski, "A novel dual-frequency circularly polarized rectenna," *IEEE Antennas Wireless Propag. Lett.*, vol. 2, pp. 330 – 333, 2003.

[143] Y. Yang, L. Li, J. Li, Y. Liu, B. Zhang, H. Zhu, and K. Huang, "A Circularly Polarized Rectenna Array Based on Substrate Integrated Waveguide Structure With Harmonic Suppression," *IEEE Antennas Wireless Propag. Lett.*, vol. 17, 4, pp. 684 – 688, 2018.

[144] R. Rasshofer, M. Thieme, and E. Biebl, "Circularly Polarized Millimeter-wave Rectenna on Silicon Substrate," *IEEE Microw. Theory Techniq. Trans.*, vol. 46, 5, pp. 715 – 718, 1998.

[145] S. B. Vignesh, Nasimuddin, and A. Alphones, "Stubs-integrated-microstrip antenna design for wide coverage of circularly polarised radiation," *IET Microwaves, Antennas & Propagation*, vol. 11, no. 4, pp. 444 – 449, 2017.

[146] X. Lou and G.-M. Yang, "A Dual Linearly Polarized Rectenna Using Defected Ground Structure for Wireless Power Transmission," *IEEE Microwave and Wireless Components Letters*, vol. 28, 9, pp. 828 – 830, 2018.

[147] F. Erkmen, T. S. Almoneef, and O. M. Ramahi, "Dual linear polarized cavity-backed patch rectenna with DC power management network for optimized wireless RF power transfer," *Microwave and Optimcal Technology Letters*, vol. 60, 3, pp. 713 – 717, 2017.

[148] H. Zhang, S.-P. Gao, W. Wu, and Y.-X. Guo, "Uneven-to-Even Power Distribution for Maintaining High Efficiency of Dual-Linearly Polarized Rectenna," *IEEE Microwave and Wireless Components Letters*, vol. 28, 12, pp. 1119 – 1121, 2018.

[149] H. Sun and W. Geyi, "A New Rectenna With All-Polarization-Receiving Capability for Wireless Power Transmission," *IEEE Antennas Wireless Propag. Lett.*, vol. 15, pp. 814 – 817, 2015.

[150] Z.-C. Hao, K.-K. Fan, and H. Wang, "A Planar Polarization-Reconfigurable Antenna," *IEEE Antennas Wireless Propag. Lett.*, vol. 65, 4, pp. 1624 – 1632, 2018.

[151] B. Ghaderi, V. Nayyeri, M. Soleimani, and O. M. Ramahi, "Multi-polarisation electromagnetic energy harvesting with high efficiency," *IET Microwaves, Antennas & Propagation*, vol. 12, 15, pp. 2271 – 2275, 2018.

[152] S. Keyrouz, G. Perotto, and H. J. Visser, "Frequency selective surface for radio frequency energy harvesting applications," *IET Microwaves, Antennas & Propagation*, vol. 8, 7, pp. 523 – 531, 2014.

[153] M. Fantuzzi, M. D. Prete, D. Masotti, and A. Costanzo, "Quasi-isotropic rf energy harvester for autonomous long distance iot operations," in *2017 IEEE MTT-S International Microwave Symposium (IMS)*, 2017.

[154] A. Georgiadis, G. V. Andia, and A. Collado, "Rectenna design and optimization using reciprocity theory and harmonic balance analysis for electromagnetic (EM) energy harvesting," *IEEE Antennas Wireless Propag. Lett.*, vol. 9, pp. 444 – 446, 2017.

[155] P. S. Hall and Y. Hao, "Antennas and propagation for body centric communications," in *2006 First European Conference on Antennas and Propagation*, 2006.

[156] D. L. Paul, H. Giddens, M. G. Paterson, G. S. Hilton, and J. P. McGeehan, "Impact of Body and Clothing on a Wearable Textile Dual Band Antenna at Digital Television and Wireless Communications Bands," *IEEE Trans. Antennas Propag.*, vol. 61 no. 4, pp. 2188 – 2194, 2013.

[157] A. Meredov, K. Klionovski, and A. Shamim, "Screen-Printed, Flexible, Parasitic Beam-Switching Millimeter-Wave Antenna Array for Wearable Applications," *IEEE Open Journal of Antennas and Propagation*, vol. 1, pp. 2 – 10, 2020.

[158] K. Turbic, L. M. Correia, and M. Beko, "A Channel Model for Polarized Off-Body Communications With Dynamic Users," *IEEE Trans. Antennas Propag.*, vol. 67 no. 11, pp. 7001 – 7013, 2019.

[159] N. Chahat, M. Zhadobov, S. A. Muhammad, L. L. Coq, and R. Sauleau, "60-GHz Textile Antenna Array for Body-Centric Communications," *IEEE Trans. Antennas Propag.*, vol. 61 no. 4, pp. 1816 – 1824, 2013.

[160] P. Sambandam, M. Kanagasabai, R. Natarajan, M. G. N. Alsath, and S. Palaniswamy, "Miniaturized Button like WBAN Antenna for Off body Communication," *IEEE Trans. Antennas Propag.*, vol. 68 no. 7, pp. 5228 – 5235, 2020.

[161] P. B. Samal, P. J. Soh, and G. A. E. Vandenbosch, "UWB All-Textile Antenna With Full Ground Plane for Off-Body WBAN Communications," *IEEE Trans. Antennas Propag.*, vol. 62 no. 1, pp. 102 – 108, 2014.

[162] G.-P. Gao, C. Yang, B. Hu, R.-F. Zhang, and S.-F. Wang, "A Wearable PIFA With an All-Textile Metasurface for 5 GHz WBAN Applications," *IEEE Antennas Wireless Propag. Lett.*, vol. 18, no. 2, pp. 288 – 292, 2019.

[163] C. Mendes and C. Peixeiro, "On-Body Transmission Performance of a Novel Dual-Mode Wearable Microstrip Antenna," *IEEE Trans. Antennas Propag.*, vol. 66 no. 9, pp. 4872 – 4877, 2018.

[164] N. Chahat, M. Zhadobov, L. L. Coq, and R. Sauleau, "Wearable Endfire Textile Antenna for On-Body Communications at 60 GHz," *IEEE Antennas Wireless Propag. Lett.*, vol. 11, pp. 799 – 802, 2012.

[165] A. Alemaryeen and S. Noghanian, "On-Body Low-Profile Textile Antenna With Artificial Magnetic Conductor," *IEEE Trans. Antennas Propag.*, vol. 67 no. 6, pp. 3649 – 3656, 2019.

[166] M. SÃďrestÃűniemi, C. Pomalaza-RÃąez, T. Kumpuniemi, M. HÃďmÃďlÃďinen, R. Kovacs, and J. Iinatti, "Measurement Data-Based Study on the Intrabody Propagation in the Presence of the Sternotomy Wires and Aortic Valve Implant," *IEEE Trans. Antennas Propag.*, vol. 67 no. 8, pp. 4989 – 5001, 2019.

[167] C. Mendes and C. Peixeiro, "A Dual-Mode Single-Band Wearable Microstrip Antenna for Body Area Networks," *IEEE Antennas Wireless Propag. Lett.*, vol. 16, pp. 3055 – 3058, 2017.

[168] M. K. Magill, G. A. Conway, and W. G. Scanlon, "Circularly Polarized Dual-Mode Wearable Implant Repeater Antenna With Enhanced Into-Body Gain," *IEEE Trans. Antennas Propag.*, vol. 68 no. 5, pp. 3515 – 3524, 2020.

[169] K. Zhang, Z. H. Jiang, W. Hong, and D. H. Werner, "A Low-Profile and Wideband Triple-Mode Antenna for Wireless Body Area Network Concurrent On-/Off-Body Communications," *IEEE Trans. Antennas Propag.*, vol. 68 no. 3, pp. 1982 – 1994, 2020.

[170] H. Xiaomu, S. Yan, and G. A. E. Vandenbosch, "Wearable Button Antenna for Dual-Band WLAN Applications With Combined on and off-Body Radiation Patterns," *IEEE Trans. Antennas Propag.*, vol. 65 no. 3, pp. 1384 – 1387, 2017.

[171] J. Tak, S. Woo, J. Kwon, and J. Choi, "Dual-Band Dual-Mode Patch Antenna for On-/Off-Body WBAN Communications," *IEEE Antennas Wireless Propag. Lett.*, vol. 15, pp. 1384 – 1387, 2015.

[172] X. Y. Zhang, H. Wong, T. Mo, and Y. F. Cao, "Dual-Band Dual-Mode Button Antenna for On-Body and Off-Body Communications," *IEEE Trans. Biomed. Circuits Sys.*, vol. 11 no. 4, pp. 933 – 941, 2017.

[173] R. Masood, C. Person, and R. Sauleau, "A Dual-Mode, Dual-Port Pattern Diversity Antenna for 2.45-GHz WBAN," *IEEE Antennas Wireless Propag. Lett.*, vol. 16, pp. 1064 – 1067, 2016.

[174] R. B. V. B. Simorangkir, Y. Yang, L. Matekovits, and K. P. Esselle, "Dual-Band Dual-Mode Textile Antenna on PDMS Substrate for Body-Centric Communications," *IEEE Antennas Wireless Propag. Lett.*, vol. 16, pp. 677 – 680, 2016.

[175] C.-X. Mao, D. Vital, D. H. Werner, Y. Wu, and S. Bhardwaj, "Dual-Polarized Embroidered Textile Armband Antenna Array With Omnidirectional Radiation for On-/Off-Body Wearable Applications," *IEEE Trans. Antennas Propag.*, vol. 68 no. 4, pp. 2575 – 2584, 2020.

[176] X. Tong, C. Liu, X. Liu, H. Guo, and X. Yang, "Switchable ON-/OFF-Body Antenna for 2.45 GHz WBAN Applications," *IEEE Trans. Antennas Propag.*, vol. 66 no. 2, pp. 967 – 971, 2018.

[177] S. J. Chen, D. C. Ranasinghe, and C. Fumeaux, "A Robust Snap-On Button Solution for Reconfigurable Wearable Textile Antennas," *IEEE Trans. Antennas Propag.*, vol. 66 no. 9, pp. 4541 – 4551, 2018.

[178] G. Monti, L. Corchia, and L. Tarricone, "UHF Wearable Rectenna on Textile Materials," *IEEE Trans. Antennas. Propag.*, vol. 61, 7, pp. 3869 – 3873, 2013.

[179] D. Vital, S. Bhardwaj, and J. L. Volakis, "Textile Based Large Area RF-Power Harvesting System for Wearable Applications," *IEEE Trans. Antennas Propag.*, vol. 68, no. 3, pp. 2323 – 2331, 2019.

[180] K. W. Lui, O. H. Murphy, and C. Toumazou, "A Wearable Wideband Circularly Polarized Textile Antenna for Effective Power Transmission on a Wirelessly-Powered Sensor Platform," *IEEE Trans. Antennas Propag.*, vol. 61 no. 7, pp. 3873 – 3876, 2013.

[181] J. A. Estrada, E. Kwiatkowski, A. LÃşpez-Yela, M. BorgoÃśÃşs-GarcÃŋa, D. Segovia-Vargas, T. Barton, and Z. PopoviÄĞ, "An RF-Harvesting Tightly-Coupled Rectenna Array Tee-Shirt with Greater than Octave Bandwidth," *IEEE Trans. Microw. Theory Techniq.*, vol. 68 no. 9, pp. 3908 – 3919, 2020.

[182] G. Ginestet, N. Brechet, J. Torres, E. Moradi, L. Ukkonen, T. BjÃűrninen, and J. Virkki, "Embroidered Antenna-Microchip Interconnections and Contour Antennas in Passive UHF RFID Textile Tags," *IEEE Antennas Wireless Propag. Lett.*, vol. 16, pp. 1205 – 1208, 2016.

[183] M. Wagih, Y. Wei, A. Komolafe, R. Torah, and S. Beeby, "Reliable UHF Long-Range Textile-Integrated RFID Tag Based on a Compact Flexible Antenna Filament," *Sensors*, vol. 20 (12), p. 3435, 2020.

[184] T. Acti, A. Chauraya, S. Zhang, W. G. Whittow, R. Seager, J. C. Vardaxoglou, and T. Dias, "Embroidered Wire Dipole Antennas Using Novel Copper Yarns," *IEEE Antennas Wireless Propag. Lett.*, vol. 14, pp. 638 – 641, 2014.

[185] M. Wagih, Y. Wei, and S. Beeby, "Flexible 2.4 GHz Sensor Node for Body Area Networks with a Compact High-Gain Planar Antenna," *IEEE Antennas Wireless Propag. Lett.*, vol. 17, 12, pp. 49 – 53, 2018.

[186] H. Xiaomu, S. Yan, and G. A. E. Vandenbosch, "Wearable Button Antenna for Dual-Band WLAN Applications With Combined on and off-Body Radiation Patterns," *IEEE Trans. Antennas Propag.*, vol. 65, 3, pp. 1384 – 1387, 2017.

[187] J. Tak and J. Choi, "An All-Textile Louis Vuitton Logo Antenna," *IEEE Antennas Wireless Propag. Lett.*, vol. 14, pp. 1211 – 1214, 2015.

[188] G. Monti, L. Corchia, E. D. Benedetto, and L. Tarricone, "Wearable logo-antenna for GPS-GSM-based tracking systems," *IET Microwaves, Antennas & Propagation*, vol. 10, 12, pp. 1332 – 1338, 2016.

[189] S. H. Nguyen, N. Ellis, and R. Amirtharajah, "Powering smart jewelry using an rf energy harvesting necklace," in *2016 IEEE MTT-S International Microwave Symposium (IMS)*, 2016.

[190] W. G. Whittow, A. Chauraya, J. C. Vardaxoglou, Y. Li, R. Torah, K. Yang, S. Beeby, and J. Tudor, "Inkjet-Printed Microstrip Patch Antennas Realized on Textile for Wearable Applications," *IEEE Antennas Wireless Propag. Lett.*, vol. 13, pp. 71–74, 2014.

[191] S.-E. Adami, D. Zhu, Y. Li, E. Mellios, B. H. Stark, and S. Beeby, "A 2.45 GHz rectenna screen-printed on polycotton for on-body RF power transfer and harvesting," in *2015 IEEE Wireless Power Transfer Conference (WPTC)*, 2015.

[192] Y. Li, R. Torah, S. Beeby, and J. Tudor, "Fully direct-write dispenser printed dipole antenna on woven polyester cotton fabric for wearable electronics applications," *Electronics Letters*, vol. 51, 17, pp. 1306 – 1308, 2015.

[193] S. Lemey, S. Agneessens, and H. Rogier, "Wearable smart objects: Microwaves propelling smart textiles: A review of holistic designs for wireless textile nodes," *IEEE Microw. Mag.*, vol. 19, 6, pp. 83–100, 2018.

[194] N. F. M. Aun, P. J. Soh, A. A. Al-Hadi, M. F. Jamlos, G. A. Vandenbosch, and D. Schreurs, "Revolutionizing wearables for 5g: 5g technologies: Recent developments and future perspectives for wearable devices and antennas," *IEEE Microw. Mag.*, vol. 18, 3, pp. 108 – 124, 2017.

[195] K. N. Paracha, S. K. A. Rahim, P. J. Soh, and M. Khalily, "Wearable antennas: A review of materials, structures, and innovative features for autonomous communication and sensing," *IEEE Access*, vol. 7, 2019.

[196] M.-Q. Lee and S. Nam, "An accurate broadband measurement of substrate dielectric constant," *IEEE Microwave and Guided Wave Letters*, vol. 6, 4, pp. 168 – 170, 1996.

[197] Basics of Measuring the Dielectric Properties of Materials. [Online]. Available: http://literature.cdn.keysight.com/litweb/pdf/5989-2589EN.pdf

[198] Measurement of Dielectric Material Properties-Application Note. [Online]. Available: https://cdn.rohde-schwarz.com/pws/dl_downloads/dl_application/00aps_undefined/RAC-0607-0019_1_5E.pdf

[199] F. Declercq, H. Rogier, and C. Hertleer, "Permittivity and loss tangent characterization for garment antennas based on a new matrix-pencil two-line method," *IEEE Trans. Antennas Propag.*, vol. 56, 8, pp. 2548 – 2554, 2008.

[200] D. Cottet, J. Grzyb, T. Kirstein, and G. Troster, "Electrical characterization of textile transmission lines," *IEEE Transactions on Advanced Packaging*, vol. 26, 2, pp. 182 – 190, 2003.

[201] S. Sankaralingam and B. Gupta, "Determination of Dielectric Constant of Fabric Materials and Their Use as Substrates for Design and Development of Antennas for Wearable Applications," *IEEE Transactions on Instrumentation and Measurement*, vol. 59, 12, pp. 3122 – 3130, 2010.

[202] V. Milanovic, M. Gaitan, J. Marshall, and M. Zaghloul, "CMOS foundry implementation of Schottky diodes for RF detection," *IEEE Transactions on Electron Devices*, vol. 43, 12, pp. 2210 – 2214, 1996.

[203] U. Karthaus and M. Fischer, "Fully integrated passive UHF RFID transponder IC with 16.7-/spl mu/W minimum RF input power," *IEEE Journal of Solid-State Circuits*, vol. 38, 10, pp. 1602 – 1608, 2003.

[204] T.-W. Yoo and K. Chang, "Theoretical and experimental development of 10 and 35 GHz rectennas," *IEEE Trans. Mirow Theory Techn.*, vol. 40, 6, pp. 1259 – 1266, 1992.

[205] J. Semple, D. G. Georgiadou, G. Wyatt-Moon1, G. Gelinck, and T. D. Anthopoulos, "Flexible diodes for radio frequency (RF) electronics: a materials perspective," *Semiconductor Science and Technology*, vol. 32, 2017.

[206] M. K. Matters-Kammerer, L. Tripodi, R. van Langevelde, J. Cumana, and R. H. Jansen, "RF Characterization of Schottky Diodes in 65-nm CMOS," *IEEE Trans. Electron Devices*, vol. 57 no. 5, pp. 1063 – 1068, 2010.

[207] S. Ladan and K. Wu, "Nonlinear Modeling and Harmonic Recycling of Millimeter-Wave Rectifier Circuit," *IEEE Trans. Microw. Theory Techn.*, vol. 63, 3, pp. 937 – 944, 2015.

[208] L. Xia, J. Cheng, N. E. Glover, and P. Chiang, "0.56 V, -20 dBm RF-Powered, Multi-Node Wireless Body Area Network System-on-a-Chip With Harvesting-Efficiency Tracking Loop," *IEEE Journal of Solid-State Circuits*, vol. 49, 6, pp. 1345 – 1355, 2014.

[209] J. F. Dickson, "On-chip high-voltage generation in MNOS integrated circuits using an improved voltage multiplier technique," *IEEE Journal of Solid-State Circuits*, vol. 11, 3, pp. 374 – 378, 1976.

[210] G. Papotto, F. Carrara, and G. Palmisano, "A 90-nm cmos threshold-compensated rf energy harvester," *IEEE Journal of Solid-State Circuits*, vol. 46 no. 9, pp. 1985 – 1997, 2011.

[211] G. Papotto, F. Carrara, A. Finocchiaro, and G. Palmisano, "A 90-nm CMOS 5-Mbps Crystal-Less RF-Powered Transceiver for Wireless Sensor Network Nodes," *IEEE Journal of Solid-State Circuits*, vol. 49, 2, pp. 335 – 346, 2014.

[212] P. T. Theilmann, C. D. Presti, D. J. Kelly, and P. M. Asbeck, "A μW Complementary Bridge Rectifier With Near Zero Turn-on Voltage in SOS CMOS for Wireless Power Supplies," *IEEE Transactions on Circuits and Systems I: Regular Papers*, vol. 59, 9, pp. 2111 – 2124, 2012.

[213] S. Oh and D. D. Wentzloff, "A -32dbm sensitivity rf power harvester in 130nm cmos," in *2012 IEEE Radio Frequency Integrated Circuits Symposium*, 2012.

[214] A. S. Almansouri, J. Kosel, and K. N. Salama, "A Dual-Mode Nested Rectifier for Ambient Wireless Powering in CMOS Technology," *IEEE Trans. Microw. Theory Techn.*, vol. 68 no. 5, pp. 1754 – 1762, 2016.

[215] C. H. P. Lorenz, S. Hemour, W. Li, Y. Xie, J. Gauthier, P. Fay, and K. Wu, "Breaking the Efficiency Barrier for Ambient Microwave Power Harvesting With Heterojunction Backward Tunnel Diodes," *IEEE Trans. Microw. Theory Techn.*, vol. 63, 12, pp. 4544 – 4555, 2015.

[216] S. Hemour, Y. Zhao, C. H. P. Lorenz, D. Houssameddine, Y. Gui, C.-M. Hu, and K. Wu, "Towards Low-Power High-Efficiency RF and Microwave Energy Harvesting," *IEEE Trans. Microw. Theory Techn.*, vol. 62, 4, pp. 965 – 976, 2014.

[217] M. Yasir, M. Aldrigo, M. Dragoman, A. Dinescu, M. Bozzi, S. Iordanescu, and D. Vasilache, "Integration of Antenna Array and Self-Switching Graphene Diode for Detection at 28 GHz," *IEEE Electron Device Lett.*, vol. 40, 4, pp. 628 – 631, 2019.

[218] X. Zhang, J. Grajal, J. L. Vazquez-Roy, U. Radhakrishna, X. Wang, W. Chern, L. Zhou, Y. Lin, P.-C. Shen, X. Ji, X. Ling, A. Zubair, Y. Zhang, H. Wang, M. Dubey, J. Kong, M. Dresselhaus, and T. Palacios, "Two-dimensional MoS2-enabled flexible rectenna for Wi-Fi-band wireless energy harvesting," *Nature*, vol. 566, pp. 368–372, 2019.

[219] V. Rizzoli, A. Lipparini, A. Costanzo, F. Mastri, C. Cecchetti, A. Neri, and D. Masotti, "State-of-the-art harmonic-balance simulation of forced nonlinear microwave

circuits by the piecewise technique," *IEEE Trans. Microw. Theory Techn.*, vol. 40, 1, pp. 12 – 28, 1992.

[220] S. Ladan, "Simultaneous wireless power transmission and data communication."

[221] J. Akkermans, M. van Beurden, G. Doodeman, and H. Visser, "Analytical models for low-power rectenna design," *IEEE Antennas Wireless Propag. Lett.*, vol. 2, pp. 187 – 190, 2005.

[222] M. A. Karami and K. Moez, "Systematic Co-Design of Matching Networks and Rectifiers for CMOS Radio Frequency Energy Harvesters," *IEEE Trans. Circuits and Systems I: Regular Papers*, vol. Early Access, pp. 1 – 14, 2019.

[223] E. F. Silva, A. G. Neto, and C. Peixeiro, "Fast and Accurate Rectenna Design Method," *IEEE Antennas Wireless Propag. Lett.*, vol. Early Access, pp. 1 – 1, 2019.

[224] A. Takacs, H. Aubert, S. Fredon, L. Despoisse, and H. Blondeaux, "Microwave Power Harvesting for Satellite Health Monitoring," *IEEE Trans. Microw. Theory Techn.*, vol. 62, 4, pp. 1090–1098, 2014.

[225] T. Q. V. Hoang, E. SÃľguenot, F. Ferrero, J.-L. Dubard, P. Brachat, and J.-L. Desvilles, "3D Voltage Pattern Measurement of a 2.45 GHz Rectenna," *IEEE Trans. Antennas Propag.*, vol. 61, 6, pp. 3354 – 3356, 2013.

[226] H. Sun and W. Geyi, "Optimum Design of Wireless Power Transmission Systems in Unknown Electromagnetic Environments," *IEEE Access*, vol. 5, pp. 20 198 – 20 206, 2017.

[227] Q. Chen, Z. Liu, Y. Cui, H. Cai, and X. Chen, "A 915-MHz Far-Field Energy Harvester With 22-dBm Sensitivity and 3-V Output Voltage Based on Antenna-and- Rectifier Codesign," *IEEE Microw. Wireless Compon. Lett*, vol. 29 no. 8, pp. 557 – 559, 2019.

[228] H. Sun, Y. xin Guo, M. He, and Z. Zhong, "Design of a High-Efficiency 2.45-GHz Rectenna for Low-Input-Power Energy Harvesting," *IEEE Antennas Wireless Propag. Lett.*, vol. 11, pp. 929–932, 2012.

[229] Y. Zhang, S. Shen, C. Y. Chiu, and R. Murch, "Hybrid RF-Solar Energy Harvesting Systems Utilizing Transparent Multiport Micromeshed Antennas," *IEEE Trans. Microw. Theory Techn.*, vol. 67 no. 11, pp. 4534 – 4546, 2019.

[230] Y. Huo, X. Dong, and W. Xu, "5g cellular user equipment: From theory to practical hardware design," *IEEE Access*, vol. 5, 2017.

[231] I. A. Hemadeh, K. Satyanarayana, M. El-Hajjar, and L. Hanzo, "Millimeter-Wave Communications: Physical Channel Models, Design Considerations, Antenna Constructions, and Link-Budget," *IEEE Communications Surveys & Tutorials*, vol. 20, 2, pp. 870 – 913, 2017.

[232] S. F. Jilani, M. O. Munoz, Q. H. Abbasi, and A. Alomainy, "Millimeter-Wave Liquid Crystal Polymer Based Conformal Antenna Array for 5G Applications," *IEEE Antennas Wireless Propag. Lett.*, vol. 18, 1, pp. 84, 88, 2019.

[233] I. Nasr, R. Jungmaier, A. Baheti, D. Noppeney, J. S. Bal, M. Wojnowski, E. Karagozler, H. Raja, J. Lien, I. Poupyrev, and S. Trotta, "A Highly Integrated 60 GHz 6-Channel Transceiver With Antenna in Package for Smart Sensing and Short-Range Communications," *IEEE J. Solid-State Circuits*, vol. 51 no. 8, pp. 2066 – 2076, 2016.

[234] T.-H. Lin, S. N. Daskalakis, A. Georgiadis, and M. M. Tentzeris, "Achieving fully autonomous system-on-package designs: An embedded-on-package 5g energy harvester within 3d printed multilayer flexible packaging structures," in *2019 IEEE MTT-S International Microwave Symposium (IMS)*, 2019.

[235] T. A. Khan, A. Alkhateeb, and R. W. Heath, "Millimeter Wave Energy Harvesting," *IEEE Trans. Wireless Communications*, vol. 15, 9, pp. 6048 – 6062, 2016.

[236] T. Yoo and K. Chang, "35 GHz integrated circuit rectifying antenna with 33efficiency," *Electronics Lett.*, vol. 27 no. 23, p. 2117, 1992.

[237] P. Koert and J. Cha, "35 and 94 ghz rectifying antenna systems," in *SPS 91 - Power from space: Proceedings of the 2nd International Symposium*, 1991.

[238] S. Hemour, C. H. P. Lorenz, and K. Wu, "Small-footprint wideband 94 GHz rectifier for swarm micro-robotics," in *2015 IEEE MTT-S International Microwave Symposium*, 2015.

[239] G. Nikandish, R. B. Staszewski, and A. Zhu, "Breaking the Bandwidth Limit: A Review of Broadband Doherty Power Amplifier Design for 5G," *IEEE Microw. Mag.*, vol. 21, no. 4, pp. 57 – 75, 2020.

[240] J. Charthad, N. Dolatsha, A. Rekhi, and A. Arbabian, "System-Level Analysis of Far-Field Radio Frequency Power Delivery for mm-Sized Sensor Nodes," *IEEE Trans. Circuits And Systems*, vol. 63 no. 2, pp. 300 – 311, 2016.

[241] P. Bailey and N. Worthington, "History and applications of haarp technologies: the high frequency active auroral research program," in *IECEC-97 Proceedings of the Thirty-Second Intersociety Energy Conversion Engineering Conference (Cat. No.97CH6203)*, 1997.

[242] A. Riaz, M. Awais, M. M. Farooq, and W. T. Khan, "A single cell dual band rectifier at millimeter-wave frequencies for future 5g communications," in *2019 49th European Microwave Conference (EuMC)*, 2019.

[243] H. Mei, X. Yang, B. Han, and G. Tan, "High-efficiency microstrip rectenna for microwave power transmission at Ka band with low cost," *IET Microwave Antennas and Propagation*, vol. 10 no. 15, pp. 1648–1655, 2016.

[244] M. Wagih, G. S. Hilton, A. S. Weddell, and S. Beeby, "Broadband Millimetre-Wave Textile-based Flexible Rectenna for Wearable Energy Harvesting ," *IEEE Trans. Microw Theory Techn*, vol. 68 no. 11, pp. 4960 – 4972, 2020.

[245] E. Lier, "Review of Soft and Hard Horn Antennas, Including Metamaterial-Based Hybrid-Mode Horns," *IEEE Antennas and Propagation Magazine*, vol. 52 no. 2, pp. 31 – 39, 2018.

[246] Q. Chen, Z. Liu, Y. Cui, H. Cai, and X. Chen, "A Metallic Waveguide-Integrated 35-GHz Rectenna With High Conversion Efficiency," *IEEE Microw. Wireless Compon. Lett*, vol. Early access, p. 10.1109/LMWC.2020.3002163, 2020.

[247] D. M. Pozar, "Microstrip antennas," *Proc. IEEE*, vol. 80 no. 1, pp. 79 – 91, 1992.

[248] A. Mavaddat, S. H. M. Armaki, and A. R. Erfanian, "Millimeter-Wave Energy Harvesting Using 4x4 Microstrip Patch Antenna Array," *IEEE Antennas Wireless Propag. Lett.*, vol. 14, pp. 515 – 518, 2014.

[249] M. Bozzi, A. Georgiadis, and K. Wu, "Review of substrate-integrated waveguide circuits and antennas," *IET Microwave Antennas and Propagation*, vol. 5, 8, pp. 909 – 920, 2011.

[250] L. Yan, W. Hong, G. Hua, J. Chen, K. Wu, and T. J. Cui, "Simulation and experiment on SIW slot array antennas," *IEEE Microwave and Wireless Components Letters*, vol. 14, 9, pp. 446 – 448, 2004.

[251] A. Collado and A. Georgiadis, "24 ghz substrate integrated waveguide (siw) rectenna for energy harvesting and wireless power transmission," in *IEEE MTT-S International Microwave Symposium Digest (MTT)*, 2013.

[252] G.-N. Tan, X.-X. Yang, H. Mei, and Z.-L. Lu, "Study on Millimeter-Wave Vivaldi Rectenna and Arrays with High Conversion Efficiency," *Int. J. Antennas Propag.*, vol. 2016, Article ID 1897283, 2016.

[253] R. Moro, S. Agneessens, H. Rogier, A. Dierck, and M. Bozzi, "Textile Microwave Components in Substrate Integrated Waveguide Technology," *IEEE Trans. Microw. Theory Techn.*, vol. 63, 2, pp. 422 – 432, 2015.

[254] L. Alonso-Gonzalez, S. Ver-Hoeye, C. Vazquez-Antuna, M. Fernandez-Garcia, and F. L.-H. Andres, "On the Techniques to Develop Millimeter-Wave Textile Integrated Waveguides Using Rigid Warp Threads," *IEEE Trans. Microw. Theory Techn.*, vol. 66, 2, pp. 751 – 761, 2018.

[255] Y. P. Zhang and D. Liu, "Antenna-on-Chip and Antenna-in-Package Solutions to Highly Integrated Millimeter-Wave Devices for Wireless Communications," *IEEE Trans. Antennas Propag.*, vol. 57 no. 10, pp. 2830 – 2841, 2009.

[256] M. Tabesh, N. Dolatsha, A. Arbabian, and A. M. Niknejad, "A Power-Harvesting Pad-Less Millimeter-Sized Radio," *IEEE Journal of Solid-State Circuits*, vol. 50, 4, pp. 962 – 977, 2015.

[257] P. Burasa, T. Djerafi, N. G. Constantin, and K. Wu, "On-Chip Dual-Band Rectangular Slot Antenna for Single-Chip Millimeter-Wave Identification Tag in Standard CMOS Technology," *IEEE Trans. Antennas Propag.*, vol. 65 no. 8, pp. 3858 – 3868, 2017.

[258] H. Dagan, A. Shapira, A. Teman, A. Mordakhay, S. Jameson, E. Pikhay, V. Dayan, Y. Roizin, E. Socher, and A. Fish, "A low-power low-cost 24 ghz rfid tag with a c-flash based embedded memory," *IEEE Journal of Solid-State Circuits*, vol. 49 no. 9, pp. 1942 – 1957, 2014.

[259] H. Gao, M. K. Matters-Kamrnerer, P. Harpe, D. Milosevic, U. Johannsen, A. van Roermund, and P. Baltus, "A 71ghz rf energy harvesting tag with 8% efficiency for wireless temperature sensors in 65nm cmos," in *2013 IEEE Radio Frequency Integrated Circuits Symposium (RFIC)*, 2013.

[260] M. Nariman, F. Shirinfar, A. P. Toda, S. Pamarti, A. Rofougaran, and F. D. Flaviis, "A Compact 60-GHz Wireless Power Transfer System," *IEEE Trans. Microw. Theory Techn.*, vol. 64, no. 8, pp. 2664 – 2677, 2016.

[261] H.-K. Chiou and I.-S. Chen, "High-Efficiency Dual-Band On-Chip Rectenna for 35- and 94-GHz Wireless Power Transmission in 0.13-um CMOS Technology," *IEEE Trans. Microw. Theory Techn.*, vol. 58, 12, pp. 3598 – 3606, 2010.

[262] R. Garg and A. S. Natarajan, "A 28-ghz low-power phased-array receiver front-end with 360 rtps phase shift range," *IEEE Trans. Microw. Theory Techn.*, vol. 65 no. 11, pp. 4703 – 4714, 2017.

[263] S. Lim and T. Itoh, "60-ghz retrodirective array system with efficient power management," in *2006 European Microwave Conference*, 2006.

[264] B. Kapilevich, V. Shashkin, B. Litvak, G. Yemini, A. Etinger, D. Hardon, and Y. Pinhasi, "W-Band Rectenna Coupled With Low-Barrier Mott Diode," *IEEE Microw. Wireless Compon. Lett*, vol. 26 no. 8, pp. 637 – 639, 2016.

[265] H. Gao, D. M. Leenaerts, and P. Baltus, "A 62 GHz inductor-peaked rectifier with 7% efficiency," in *2013 IEEE Radio Frequency Integrated Circuits Symposium (RFIC)*, 2013.

[266] C. A. Balanis, "Batteryless mm-Wave Wireless Sensors," *Springer*, 2018.

[267] S. Ladan, S. Hemour, and K. Wu, "Towards Millimeter-Wave High-Efficiency Rectification for Wireless Energy Harvesting," in *2013 IEEE International Wireless Symposium (IWS)*, 2013.

[268] B. T. Malik, V. Doychinov, S. A. R. Zaidi, I. D. Robertson, N. Somjit, and R. Richardson, "Flexible Rectennas for Wireless Power Transfer to Wearable Sensors at 24 GHz," in *2019 Research, Invention, and Innovation Congress*, 2019.

[269] D. D. Marco, K. Drissi, N. Delhote, O. Tantot, P.-M. Geffroy, S. Verdeyme, and T. Chartier, "Dielectric properties of pure alumina from 8 GHz to 73 GHz," *Journal of the European Ceramic Society*, vol. 36, May 2016, pp. 3355 – 3361, 2016.

[270] E. Shi, E. Centeno, R. Figueroa, C. Qi, and G. Durgin, "A Rectenna Using Copper Foil on Glass to Reduce Cost of Space Solar Power," in *2019 IEEE Wireless Power Transfer Conference (WPTC)*, 2019.

[271] P. He, D. Zhao, L. Liu, J. Xu, Q. Zheng, C. Yu, and X. You, "A W-Band 2 x 2 Rectenna Array With On-Chip CMOS Switching Rectifier and On-PCB Tapered Slot Antenna for Wireless Power Transfer," *IEEE Trans. Microw. Theory Techn.*, 2020, Early Access, DOI: 10.1109/TMTT.2020.3032971.

[272] B. S. Cook, B. Tehrani, J. R. Cooper, and M. M. Tentzeris, "Multilayer Inkjet Printing of Millimeter-Wave Proximity-Fed Patch Arrays on Flexible Substrates," *IEEE Antennas Wireless Propag. Lett.*, vol. 12, pp. 1351 – 1354, 2013.

[273] M. Ur-Rehman, N. A. Malik, X. Yang, Q. H. Abbasi, Z. Zhang, and N. Zhao, "A Low Profile Antenna for Millimeter-Wave Body-Centric Applications," *IEEE Trans. Antennas Propag.*, vol. 65 no. 12, pp. 6329 – 6337, 2017.

[274] R. Hoffman, "Handbook of Microwave integrated Circuits," *Artech House*, 1987.

[275] David M. Pozar, *Microwave Engineering 4th Edition.* NJ, United States: John Wiley & Sons Inc, 2011.

[276] H. T. Friis, "A note on a simple transmission formula," in *Proceedings of the I.R.E. and Waves and Electrons*, 1946.

[277] H.-W. Son and S. P. Pyo, "Design of RFID tag antennas using an inductively coupled feed," *Electronics Letters*, vol. 41 no. 18, pp. 994 – 996, 2005.

[278] G. Zamora, S. Zuffanelli, F. Paredes, F. Martin, and J. Bonache, "Design and Synthesis Methodology for UHF-RFID Tags Based on the T-Match Network," *IEEE Trans. Microw. Theory Techn.*, vol. 61 no. 12, pp. 4090 – 4098, 2013.

[279] J. Liang, C. Chiau, X. Chen, and C. Parini, "Study of a printed circular disc monopole antenna for uwb systems," *IEEE Trans. Antennas Propag.*, vol. 53, no. 11, pp. 3500 – 3504, 2005.

[280] C. Niamien, S. Collardey, A. Sharaiha, and K. Mahdjoubi, "Compact Expressions for Efficiency and Bandwidth of Patch Antennas Over Lossy Magneto-Dielectric Materials," *IEEE Antennas Wireless Propag. Lett.*, vol. 10, pp. 63 – 66, 2011.

[281] N.-W. Liu, L. Zhu, W.-W. Choi, and J.-D. Zhang, "A Low-Profile Differentially Fed Microstrip Patch Antenna With Broad Impedance Bandwidth Under Triple-Mode Resonance," *IEEE Antennas Wireless Propag. Lett.*, vol. 17 no. 8, pp. 1478 – 1482, 2018.

[282] T. Ohira, "Power Efficiency and Optimum Load Formulas on RF Rectifiers Featuring Flow-Angle Equations," *IEICE Electronics Express*, vol. 10 no. 11, pp. 1 – 9, 2013.

[283] C. R. Valenta, M. M. Morys, and G. D. Durgin, "Theoretical Energy-Conversion Efficiency for Energy-Harvesting Circuits Under Power-Optimized Waveform Excitation," *IEEE Trans. Microw. Theory Techn.*, vol. 63 no. 5, pp. 1758 – 1767, 2015.

[284] C. R. Valenta, "Microwave-energy harvesting at 5.8 ghz for passive devices."

[285] C. A. Balanis, "Antenna Theory: Analysis and Design. Third Edition," *Wiley Interscience*, pp. 84 – 85, 2005.

[286] J. C. McLaughlin and K. L. Kaiser, ""Deglorifying" the Maximum Power Transfer Theorem and Factors in Impedance Selection," *IEEE Trans. Education*, vol. 50 no. 3, pp. 251 – 255, 2007.

[287] H. J. Visser, "Design Considerations for Low-Power, High-Sensitivity Rectennas," in *The 8th European Conference on Antennas and Propagation*, 2014.

[288] M. Wagih, O. Cetinkaya, B. Zaghari, A. S. Weddell, and S. Beeby, "Real-World Performance of Sub-1 GHz and 2.4 GHz Textile Antennas for RF-Powered Body Area Networks," *IEEE Access*, vol. 8, pp. 133 746 – 133 756, 2020.

[289] M. Wagih, A. S. Weddell, and S. Beeby, "Omnidirectional Dual-Polarized Low-Profile Textile Rectenna with over 50% Efficiency for Sub-μW/cm^2 Wearable Power Harvesting," *IEEE Trans. Antennas Propag.*, vol. Early Access, 2020.

[290] C. X. Mao, Y. Zhou, Y. Wu, H. Soewardiman, D. H. Werner, and J. S. Jur, "Low-Profile Strip-Loaded Textile Antenna with Enhanced Bandwidth and Isolation for Full-Duplex Wearable Applications," *IEEE Trans. Antennas Propag.*, vol. 68 no. 9, pp. 6527 – 6537, 2020.

[291] A. R. Guraliuc, M. Zhadobov, G. Valerio, N. Chahat, and R. Sauleau, "Effect of textile on the propagation along the body at 60 ghz," *IEEE Trans. Antennas Propag.*, vol. 62, 3, pp. 1489 – 1494, 2014.

[292] K. Yang, R. Torah, Y. Wei, S. Beeby, and J. Tudor, "Waterproof and durable screen printed silver conductive tracks on textiles," *Textile Research Journal*, vol. 83, pp. 2023 – 2031, 2013.

[293] A. Komolafe, R. Torah, Y. Wei, H. NunesâĂŘmatos, M. Li, D. Hardy, T. Dias, M. Tudor, and S. Beeby, "Integrating flexible filament circuits for eâĂŘtextile applications," *Advanced Materials Technologies*, vol. 4, no. 7, 2019.

[294] R. Seager, A. Chauraya, S. Zhang, W. Whittow, and Y. Vardaxoglou, "Flexible radio frequency connectors for textile electronics," *Electronics Letters*, vol. 49, no. 22, pp. 1371 – 1373, 2013.

[295] J. W. Massey and A. E. Yilmaz, "Austinman and austinwoman: High-fidelity, anatomical voxel models developed from the vhp color images," in *2016 38th Annual International Conference of the IEEE Engineering in Medicine and Biology Society (EMBC)*, 2016.

[296] C. Domnik, S. Husges, and C. Degen, "Frugal Energy Harvesting: Microwave Energy Radiated Into the Environment From Wireless Networks," *IEEE Microw. Mag.*, vol. 9, 5, pp. 454 – 462, 2014.

[297] M. Wagih, A. S. Weddell, and S. Beeby, "Characterizing and Modelling Non-Linear Rectifiers for RF Energy Harvesting," in *2019 PowerMEMS*, 2019.

[298] J. Kimionis, A. Collado, M. M. Tentzeris, and A. Georgiadis, "Octave and Decade Printed UWB Rectifiers Based on Nonuniform Transmission Lines for Energy Harvesting," *IEEE Trans. Microw. Theory Techn.*, vol. 65, no. 11, pp. 4326 – 4334, 2017.

[299] J. Myers, A. Savanth, R. Gaddh, D. Howard, P. Prabhat, and D. Flynn, "A Subthreshold ARM Cortex-M0+ Subsystem in 65 nm CMOS for WSN Applications with 14 Power Domains, 10T SRAM, and Integrated Voltage Regulator," *IEEE Journal of Solid-State Circuits*, vol. 51, 1, pp. 31 – 44, 2016.

[300] M. Wagih, A. S. Weddell, and S. Beeby, "High-Efficiency Sub-1 GHz Flexible Compact Rectenna based on Parametric Antenna-Rectifier Co-Design," in *2020 IEEE/MTT-S International Microwave Symposium (IMS)*, 2020.

[301] M. Wagih, G. S. Hilton, A. S. Weddell, and S. Beeby, "2.4 GHz Wearable Textile Antenna/Rectenna for Simultaneous Information and Power Transfer," in *2021 15th European Conference on Antennas and Propagation*, 2021.

[302] ——, "Dual-Band Dual-Mode Textile Antenna/Rectenna for Simultaneous Wireless Information and Power Transfer (SWIPT)," *IEEE Trans. Antennas Propag.*, 2021.

[303] D. Vital, S. Bhardwaj, and J. L. Volakis, "A 2.45 GHz RF Power Harvesting System Using Textile-Based Single-Diode Rectennas," in *2019 IEEE MTT-S International Microwave Symposium (IMS)*, 2019.

[304] A. S. Almansouri, M. H. Ouda, and K. N. Salama, "A cmos rf-to-dc power converter with 86% efficiency and -19.2-dbm sensitivity," *IEEE Trans. Microw. Theory Techn.*, vol. 66, 5, pp. 2409 – 2415, 2018.

[305] P. Lu, C. Song, and K. M. Huang, "A Two-Port Multi-Polarization Rectenna with Orthogonal Hybrid Coupler for Simultaneous Wireless Information and Power Transfer (SWIPT)," *IEEE Trans. Antennas Propag.*, vol. 68 no. 10, pp. 6893 – 6905, 2020.

[306] C. A. Balanis, "Antenna Theory: Analysis and Design. Third Edition," *Wiley Interscience*, pp. 830 – 833, 2005.

[307] K. Palmer and M. van Rooyen, "Simple broadband measurements of balanced loads using a network analyzer," *IEE Transactions on Instrumentation and Measurements*, vol. 55, no. 1, pp. 266 – 272, 2006.

[308] S. N. Daskalakis, G. Goussetis, S. D. Assimonis, M. M. Tentzeris, and A. Georgiadis, "A uW Backscatter-Morse-Leaf Sensor for Low-Power Agricultural Wireless Sensor Networks," *IEEE Sensors J.*, vol. 18 no. 1, pp. 7889 – 7898, 18.

[309] A. Meredov, K. Klionovski, and A. Shamim, "Screen-Printed, Flexible, Parasitic Beam-Switching Millimeter-Wave Antenna Array for Wearable Applications," *IEEE Open Journal of Antennas and Propagation*, vol. 1, 2020.

[310] D. Ghodgaonkar, O. Gandhi, and M. Iskander, "Complex permittivity of human skin in vivo in the frequency band 26.5-60 GHz," in *IEEE Antennas and Propagation Society International Symposium*, 2000.

[311] W. Sun, Y. Li, Z. Zhang, and Z. Feng, "Broadband and Low-Profile Microstrip Antenna Using Strip-Slot Hybrid Structure," *IEEE Antennas Wireless Propag. Lett.*, vol. 16, pp. 3118 – 3121, 2017.

[312] J. Yin, Q. Wu, C. Yu, H. Wang, and W. Hong, "Broadband Symmetrical E-Shaped Patch Antenna With Multimode Resonance for 5G Millimeter-Wave Applications," *IEEE Trans. Antennas Propag.*, vol. 67 no. 7, pp. 4474 – 4483, 2019.

[313] 5G Spectrum Positions. [Online]. Available: www.gsma.com/spectrum/wp-content/uploads/2019/02/5G-Spectrum-Positions-InfoG.pdf

[314] A. R. Guraliuc, M. Zhadobov, O. D. Sagazan, and R. Sauleau, "Solid Phantom for Body-Centric Propagation Measurements at 60 GHz," *IEEE Trans. Microw. Theory Techn.*, vol. 62 no. 6, pp. 1373 – 1380, 2014.

[315] M. Wagih, G. S. Hilton, A. S. Weddell, and S. Beeby, "Higher-Order Mode Broadband Textile-Based Microstrip Antenna for Compact Wearable Millimeter-Wave Wireless Power Transfer," *IEEE Open Journal of Antennas and Propagation*, (Under Review).

[316] H. Chen, Y. Shao, Y. Zhang, C. Zhang, and Z. Zhang, "A Low-Profile Broadband Circularly Polarized mmWave Antenna With Special-Shaped Ring Slot," *IEEE Antennas Wireless Propag. Lett.*, vol. 18, 7, pp. 1492 – 1496, 2019.

[317] N. Chahat, M. Zhadobov, L. L. Coq, S. I. Alekseev, and R. Sauleau, "Characterization of the Interactions Between a 60-GHz Antenna and the Human Body in an Off-Body Scenario," *IEEE Trans. Antennas Propag.*, vol. 60 no. 12, pp. 5958 – 5965, 2012.

[318] H. Sun, H. He, and J. Huang, "Polarization-Insensitive Rectenna Arrays With Different Power Combining Strategies," *IEEE Antennas Wireless Propag. Lett.*, vol. 19, 3, pp. 492 – 496, 2020.

[319] T. X. Tran, W. Wang, S. Luo, and K. C. Teh, "Nonlinear Energy Harvesting for Millimeter Wave Networks With Large-Scale Antennas," *IEEE Trans. Veh. Technol.*, vol. 67 no. 10, pp. 9488 – 9498, 2018.

[320] X. Gu, L. Guo, S. Hemour, and K. Wu, "Optimum Temperatures for Enhanced Power Conversion Efficiency (PCE) of Zero-Bias Diode-Based Rectifiers," *IEEE Trans. Microw. Theory Techn.*, vol. Early access, pp. 1 – 1, 2020.

[321] S. Hemour, Y. Zhao, C. H. P. Lorenz, D. Houssameddine, Y. Gui, C.-M. Hu, and K. Wu, "Towards Low-Power High-Efficiency RF and Microwave Energy Harvesting," *IEEE Trans. Microw. Theory Techn.*, vol. 62 no. 4, pp. 965 – 976, 2014.

[322] FCC. Revision of Part 15 of the Commission's Rules to Permit Unlicensed National Information Infrastructure (U-NII) Devices in the 5 GHz Band. [Online]. Available: https://www.fcc.gov/document/5-ghz-u-nii-ro

[323] G. R. MacCartney, S. Deng, and T. S. Rappaport, "Indoor Office Plan Environment and Layout-Based mmWave Path Loss Models for 28 GHz and 73 GHz," in *2016 IEEE 83rd Vehicular Technology Conference (VTC Spring)*, 2016.

[324] M. Moosazadeh, S. Kharkovsky, J. T. Case, and B. Samali, "Improved Radiation Characteristics of Small Antipodal Vivaldi Antenna for Microwave and Millimeter-Wave Imaging Applications," *IEEE Antennas Wireless Propag. Lett.*, vol. 16, pp. 1961 – 1964, 2017.

[325] Y. Rajavi, M. Taghivand, K. Aggarwal, A. Ma, and A. S. Y. Poon, "An rf-powered fdd radio for neural microimplants," *IEEE Journal of Solid-State Circuits*, vol. 52, no. 5, pp. 1221 – 1229, 2017.

[326] S. Yang, J. Yin, H. Yi, W.-H. Yu, P.-I. Mak, and R. P. Martins, "A 0.2-V Energy-Harvesting BLE Transmitter With a Micropower Manager Achieving 25% System Efficiency at 0-dBm Output and 5.2-nW Sleep Power in 28-nm CMOS," *IEEE Journal of Solid-State Circuits*, vol. 54, no. 5, pp. 1351 – 1362, 2019.

[327] M. Taghivand, K. Aggarwal, Y. Rajavi, and A. S. Y. Poon, "An Energy Harvesting 2x2 60 GHz Transceiver With Scalable Data Rate of 38=2450 Mb/s for Near-Range Communication," *IEEE Journal of Solid State Circuits*, vol. 50, 8, pp. 1889 – 1902, 2015.

[328] F. Bolos, J. Blanco, A. Collado, and A. Georgiadis, "RF Energy Harvesting From Multi-Tone and Digitally Modulated Signals," *IEEE Trans. Microw. Theory Techn.*, vol. 64, no. 6, pp. 1918 – 1927, 2016.

[329] S. Yong, J. Shi, and S. Beeby, "Wearable Textile Power Module Based on Flexible Ferroelectret and Supercapacitor," *Energy Technology*, vol. 7 (5), pp. 2284 – 2291, 2018.

[330] K. Dong, Y.-C. Wang, J. Deng, Y. Dai, S. L. Zhang, H. Zou, B. Gu, B. Sun, and Z. L. Wang, "A Highly Stretchable and Washable All-Yarn Based Self-Charging Knitting Power Textile Composed of Fiber Triboelectric Nanogenerators and Supercapacitors," *ACS Nano*, vol. 11, pp. 9490–9499, 2017.

[331] A. Okba, D. Henry, A. Takacs, and H. Aubert, "Autonomous RFID Sensor Node Using a Single ISM Band for Both Wireless Power Transfer and Data Communication," *Sensors*, vol. 19 (15), p. 3330, 2019.

[332] S. D. Assimonis, S.-N. Daskalakis, and A. Bletsas, "Sensitive and Efficient RF Harvesting Supply for Batteryless Backscatter Sensor Networks," *IEEE Trans. Microw. Theory Techn.*, vol. 64 no. 4, pp. 1327 – 1338, 2016.

[333] M. Wagih, N. Hillier, S. Yong, A. S. Weddell, and S. Beeby, "Rf-powered wearable energy harvesting and storage module based on e-textile coplanar waveguide rectenna and supercapacitor," *IEEE Open Journal of Antennas and Propagation*, vol. 2, pp. 302 – 314, 2021.

[334] M. Wagih, A. S. Weddell, and S. Beeby, "Sub-1 GHz Flexible Concealed Rectenna Yarn for High-Efficiency Wireless-Powered Electronic Textiles," in *2020 European Conference on Antennas and Propagation (EuCAP)*, 2020.

[335] M. Wagih, N. Hillier, S. Yong, A. S. Weddell, and S. Beeby, "Wearable E-Textile Wireless RF Power Supply based on a Textile Supercapacitor and a Flexible Rectenna Filament," in *2020 IEEE Int. Conf. Flexible and Printable Sensors Systems*, 2020.

[336] M. Li, R. Torah, N. M. Helga, Y. Wei, S. Beeby, M. Tudor, and K. Yang, "Integration and testing of a three-axis accelerometer in a woven e-textile sleeve for wearable movement monitoring," *Sensors*, vol. 20 (18), p. 5033, 2020.

[337] W. Zhao, K. Choi, S. Bauman, Z. Dilli, T. Salter, and M. Peckerar, "A radio-frequency energy harvesting scheme for use in low-power ad hoc distributed networks," *IEEE Trans. Circuits And Systems*, vol. 59 no. 9, pp. 573 – 577, 2012.

[338] P. Li, Z. Long, and Z. Yang, "RF Energy Harvesting for Battery-Less and Maintenance-Free Condition Monitoring of Railway Tracks," *IEEE Internet of Things Journal*, vol. Early Access, p. DOI: 10.1109/JIOT.2020.3023475, 2020.

[339] Y. H. Jung, Y. Qiu, S. Lee, T.-Y. Shih, Y. Xu, R. Xu, J. Lee, A. A. Schendel, W. Lin, J. C. Williams, N. Behdad, and Z. Ma, "A Compact Parylene-Coated WLAN Flexible Antenna for Implantable Electronics," *IEEE Antennas Wireless Propag. Lett.*, vol. 17, 12, 2018.

[340] A. Eid, J. Hester, J. Costantine, Y. Tawk, A. H. Ramadan, and M. M. Tentzeris, "A Compact Source-Load Agnostic Flexible Rectenna Topology for IoT Devices," *IEEE Trans. Antennas Propag.*, vol. Early Access, pp. 1 – 1, 2019.

[341] M. Wagih, A. S. Weddell, and S. Beeby, "Meshed High-Impedance Matching Network-Free Rectenna Optimized for Additive Manufacturing," *IEEE Open Journal of Antennas and Propagation*, vol. 1, pp. 615 – 626, 2020.

[342] D. Balsamo, O. Cetinkaya, A. R. Arreola, S. C. B. Wong, G. V. Merrett, and A. S. Weddell, "A Control Flow for Transiently Powered Energy Harvesting Sensor Systems," *IEEE J. Sensors*, vol. 20 no. 18, pp. 10 687 – 10 695, 2020.

[343] A. Bakytbekova, T. Q.Nguyen, C. Huynh, K. N. Salama, and A. Shamima, "Fully printed 3D cube-shaped multiband fractal rectenna for ambient RF energy harvesting," *Nano Energy*, vol. 53, pp. 587 – 595, 2018.

[344] W. Lin and R. W. Ziolkowski, "Electrically Small Huygens CP Rectenna With a Driven Loop Element Maximizes Its Wireless Power Transfer Efficiency," *IEEE Trans. Antennas Propag.*, vol. 68 no. 11, pp. 540 – 545, 2020.

[345] ——, "Electrically Small, Single-Substrate Huygens Dipole Rectenna for Ultra-Compact Wireless Power Transfer Applications," *IEEE Trans. Antennas Propag.*, vol. Early Access, pp. 1 – 5, 2020.

[346] Y. Zheng, Z. He, Y. Gao, and J. Liu, "Direct Desktop Printed-Circuits-on-Paper Flexible Electronics," *Scientific Reports*, vol. 3, 2013.

[347] B. S. Cook and A. Shamim, "Inkjet Printing of Novel Wideband and High Gain Antennas on Low-Cost Paper Substrate," *IEEE Trans. Antennas Propag.*, vol. 60, 9, pp. 4148 – 4156, 2012.

[348] M. Wagih, "Direct-Write Dispenser Printing for Rapid Antenna Prototyping on Thin Flexible Substrates," in *2020 European Conference on Antennas and Propagation (EuCAP)*, 2020.

[349] Z. J. Silva, C. P. Hunter, C. R. Valenta, and G. D. Durgin, "2.5 GHz Meshed Inset-Fed Patch Antenna," in *2019 IEEE International Symposium on Antennas and Propagation and USNC-URSI Radio Science Meeting*, 2019.

[350] Z. J. Silva, C. R. Valenta, and G. Durgin, "Optically Transparent Antennas : A Survey of Transparent Microwave Conductor Performance and Applications," *IEEE Antennas Propag. Magazine*, vol. Early Access, 2020.

[351] R. Yazdani, M. Yousefi, H. Aliakbarian, H. Oraizi, and G. A. E. Vandenbosch, "Miniaturized Triple-Band Highly Transparent Antenna," *IEEE Trans. Antennas Propag.*, vol. 62, no. 4, pp. 712 – 718, 2009.

[352] Z. J. Silva, C. R. Valenta, and G. D. Durgin, "Design and Characterization of Meshed Microstrip Transmission Lines," in *IEEE International Microwave Symposium*, 2019.

[353] P. D. Tung and C. W. Jung, "Optically Transparent Wideband Dipole and Patch External Antennas Using Metal Mesh for UHD TV Applications," *IEEE Trans. Antennas Propag.*, vol. 68 no. 3, pp. 1907 – 1917, 2020.

[354] H. jiang Ni, J. gang Liu, Z. he Wang, and S. yong Yang, "A review on colorless and optically transparent polyimide films: Chemistry, process and engineering applications," *Journal of Industrial and Engineering Chemistry*, vol. 28, 25, pp. 16 – 27, 2015.

[355] A. T. Castro and S. K. Sharma, "Inkjet-Printed Wideband Circularly Polarized Microstrip Patch Array Antenna on a PET Film Flexible Substrate Material," *IEEE Antennas Wireless Propag. Lett.*, vol. 17 no. 1, pp. 176 – 179, 2018.

[356] A. S. M. Sayem, R. B. V. B. Simorangkir, K. P. Esselle, and R. M. Hashmi, "Development of Robust Transparent Conformal Antennas Based on Conductive

Mesh-Polymer Composite for Unobtrusive Wearable Applications," *IEEE Trans. Antennas Propag.*, vol. 67 no. 12, pp. 7216 – 7224, 2019.

[357] J. Zhu, Z. Hu, C. S. N. Yi, Z. Yu, Z. Liu, S. Liu, M. Wang, M. G. Dexheimer, J. Yang, and H. Chengad, "Stretchable wideband dipole antennas and rectennas for RF energy harvesting," *Materials Today Physics*, vol. 18, p. 100377, 2021.

[358] B. T. Malik, V. Doychinov, A. M. Hayajneh, S. A. R. Zaidi, I. D. Robertson, and N. Somjit, "Wireless Power Transfer System for Battery-Less Sensor Nodes," *IEEE Access*, pp. 95 878 – 958 877, 2020.

[359] C. Hannachi, S. Boumaiza, and S. O. Tatu, "A Highly Sensitive Broadband Rectenna for Low Power Millimeter-wave Energy Harvesting Applications," in *2018 IEEE Wireless Power Transfer Conference (WPTC)*, 2018.

[360] K. Matsui, K. Fujiwara, Y. Okamoto, Y. Mita, H. Yamaoka, H. Koizumi, and K. Komurasaki, "Development of 94GHz microstrip line rectenna," in *2018 IEEE Wireless Power Transfer Conference (WPTC)*, 2018.

[361] N. Weissman, S. Jameson, and E. Socher, "W-band cmos on-chip energy harvester and rectenna," in *2014 IEEE MTT-S International Microwave Symposium (IMS2014)*, 2014.